Design of a Compact Heat Exchanger Used in a Methanation Plant and Produced by Additive Manufacturing

BY

JULIEN ROUX
B.S., Politecnico di Torino, Turin, Italy, 2014

THESIS

Submitted as partial fulfillment of the requirements
for the degree of Master of Science in Mechanical Engineering
in the Graduate College of the
University of Illinois at Chicago, 2016

Chicago, Illinois

Defense Committee:

Suresh K. Aggarwal, Chair and Advisor
Kenneth Brezinsky
Massimo Santarelli, Politecnico di Torino

This thesis is dedicated to my parents Cristina and Aldo, for their never ending faith in the value of education and their full support throughout my whole academic career.

ACKNOWLEDGMENTS

I would like to thank the following:

- My parents Cristina and Aldo, for their enthusiastic support throughout my time at university and for their encouragements in difficult moments, my sister Anna, because she has always pushed me to do my best and my grandmother Francesca, for teaching me the value of work.
- My research supervisors Dr. Massimo Santarelli and Dr. Suresh K. Aggarwal, for their guidance during the development of this thesis.
- Research fellow Federico Monaco and PhD. candidate Domenico Ferrero for their precious technical assistance.
- Lynn Thomas, for helping throughout the whole graduation process.
- All the organizations and individuals that have kindly granted me the permission to use proprietary material in this thesis.

JR

PREFACE

My purpose for developing this thesis, consisting in the design of a compact high-temperature heat exchanger to be used in a methanation plant, can be summarized as follows:

1. After a second-year *Thermodynamics and Fundamentals of Heat Transfer* course where I was first introduced to heat exchangers, during a M.Sc. first year *Advanced Engineering Thermodynamics* class, I was asked to size a *tube and shell* heat exchanger from scratch. In that same course, I learnt the continuum mechanics and understood that the Navier-Stokes equations represent the basis of *Computational Fluid Dynamics*. However, because of time constraints and due to the difficulties related with the set-up of CFD simulations, I decided to carry out the heat exchanger sizing by implementing on *Microsoft Excel* a faster $\varepsilon - NTU$ based iterative design procedure.

   In conclusion, the heat exchanger design by means of CFD tools object of this thesis somehow represents the perfect conclusion of a formative path began several years ago.

2. At home, observing the photovoltaic solar panels during very sunny days, I used to wonder how to efficiently avoid to waste the off-peak electrical power produced by renewable energy resources. This explains my interest for the *Power-to-Gas* methanation technology, which allows to convert the power excess into easily stored methane.

TABLE OF CONTENTS

TABLE OF CONTENTS (continued)

CHAPTER **PAGE**

TABLE OF CONTENTS (continued)

CHAPTER **PAGE**

LIST OF TABLES

LIST OF TABLES (continued)

LIST OF FIGURES

LIST OF FIGURES (continued)

LIST OF FIGURES (continued)

FIGURE **PAGE**

LIST OF FIGURES (continued)

LIST OF FIGURES (continued)

LIST OF FIGURES (continued)

LIST OF ABBREVIATIONS

AM	Addictive Manufacturing
BC	Boundary Condition
CAD	Computer-Aided-Design
CFD	Computational Fluid Dynamics
CHE	Compact Heat Exchanger
DMLS	Direct Metal Laser Sintering
DOF	Degree of Freedom
EU	European Union
FLT	First Law of Thermodynamics
GMRES	Generalized Minimum Residual Method
KMT	Kinetic Molecular Theory
HE	Heat Exchanger
HELMETH	Integrated High-Temperature Electrolysis and Methanation for Effective Power to Gas Conversion
HT	High Temperature
HTE	High Temperature Electrolysis
IC	Initial Condition

LIST OF ABBREVIATIONS (continued)

ITD	Inlet Temperature Difference
MRS	Mesh Refinement Study
NIST	National Institute of Standards and Technology
ntu	Individual Side Number of Transfer Units
NTU	Total Number of Transfer Units
P2G	Power-to-Gas
PDE	Partial Differential Equation
PFHE	Plate-Fins Heat Exchanger
PHE	Plate Heat Exchanger
RAM	Random Access Memory
RES	Renewable Energy Sources
RU	Reactant Utilization
SI	International System of Units
SLM	Selective Laser Melting
SNG	Substitute Natural Gas
SOEC	Solid Oxide Electrolyser Cell
SOFC	Solid Oxide Fuel Cell
TFHE	Tube-Fins Heat Exchanger
USD	US Dollar

LIST OF SYMBOLS

a	Fin width
A	Heat transfer area
A_0	Free-flow area
A_{fr}	Frontal area
b	Plates spacing
C	Heat capacity rate
c_p	Constant pressure specific heat
c_v	Constant volume specific heat
C^*	Heat capacity rates ratio
D_H	Hydraulic diameter
E	Elongation
$\dot{E}$	Flow power
e_c	Specific kinetic energy
E_c	Kinetic energy
e_p	Specific potential energy
E_p	Potential energy
f	Fanning friction factor

LIST OF SYMBOLS (continued)

f_s	Finned to total heat transfer area ratio
g_c	Proportionality constant in Newtons second law
G	Mass velocity
h	Heat transfer coefficient
	Specific enthalpy
H_0	Total enthalpy
H	Heat exchanger height
i	SOEC current
j	Colburn factor
k	Boltzmann's constant
K_C	Pressure loss entrance coefficient
K_E	Pressure loss exit coefficient
l_s	Fin length
L	Heat exchanger length
$\dot{m}$	Mass flow rate
M	Molar mass
N_C	Number of cold fluid passages
N_H	Number of hot fluid passages

LIST OF SYMBOLS (continued)

N_w	Number of plates
p_0	Environmental pressure
p	Pressure
	Pitch
Pr	Prandtl number
$\mathbf{q}$	Heat flux vector
q	Specific heat power
$\mathbf{Q}$	Volumetric heat source
Q	Heat power
R	Elastic gas constant
Re	Reynolds number
$R_{P0.2}$	Yield strength
R_u	Universal gas constant
R_U	Ultimate strength
s	Minimum free-flow width
t	Time
	Fin semi-height
t_w	Plate thickness

LIST OF SYMBOLS (continued)

T	Temperature
u	Velocity vector
U	Internal energy
	Overall heat transfer coefficient
U_0	Total internal energy
$\dot{V}$	Volumetric flow rate
x	Mass fraction
y	Molar fraction
v	Specific volume
V	Heat exchanger volume
V_C	Control volume
W	Heat exchanger width
W_t	Mechanical power
α	Heat transfer area to HE volume ratio
β	Surface area density
γ	Specific heats ratio
Δ	Approach point temperature difference
ε	Heat exchanger effectiveness

LIST OF SYMBOLS (continued)

	Lennard-Jones energy minimum
η_f	Fin efficiency
η_o	Overall finned surface efficiency
η_y	Polytropic compressor efficiency
λ	Thermal conductivity
μ	Dynamic viscosity
ν	Kinematic viscosity
ρ	Density
σ	Free-flow to frontal area ratio
	Lennard-Jones average collision diameter
τ	Viscous stress tensor
	Residence time
Ω	Collision integral
∇	Nabla operator

LIST OF SUBSCRIPTS

1	Cold mixture
2	Hot mixture
b	Bulk
c	Cold mixture
CFD	Computational Fluid Dynamics
f	Fin
h	Hot mixture
HE	Heat exchanger
id	Ideal
in	Inlet
I	First stage
II	Second stage
l	Longitudinal
lim	Limit
m	Mean
max	Maximum
min	Minimum

LIST OF SUBSCRIPTS (continued)

mix	Mixture
out	Outlet
SIM	Simulation
t	Transversal
tot	Total
v	Volume
w	Wall

SUMMARY

As the fraction of power produced by renewable energy sources (RES) continues to rapidly increase, it becomes mandatory to devise systems allowing to efficiently store the off-peak power produced by the highly volatile RES for later use.

One of the most promising solutions is represented by *Power-to-Gas*(P2G) technology, which converts the excess of electrical power from renewables into methane, a commercial gaseous fuel that can be easily stored for later consumption. In a P2G, a hot gaseous mixture of water steam and carbon dioxide under pressure is fed to a high temperature electrolysis module (SOEC) where it gets converted to carbon monoxide and hydrogen, which are subsequently reacted to methane in a methanation module.

For such a system to work efficiently, it is necessary that the gaseous mixture enters the SOEC at sufficiently high temperature. The present study aims precisely at designing a compact heat exchanger (CHE) to heat the inlet mixture to the required temperature of 850 $°C$. In order to maximize the P2G plant efficiency, it is crucial to thermally integrate its various components and this explains the choice of a HE regenerative layout, in which the hot mixture of H_2, CO, CH_4, H_2O and CO_2 exiting from SOEC provides the necessary heat to bring the cold mixture of H_2O and CO_2 to the required temperature before it enters the SOEC.

The first part of the thesis involves the definition of the operative environment and the derivation of all the quantities needed for the subsequent design activity. This includes, after clarifying the role of this heat exchanger within the European HELMETH project, specifying the

3-D manufacturing technology (DMLS) and building material (Inconel 718), the computation of the cold and hot side mixture compositions and mass flow rates, along with the related thermo-physical properties, and finally the HE limit outlet temperatures.

The second section focuses instead on the numerical design of the heat exchanger. After selecting a suitable HE design, inclusive of the construction type, the flow configuration and the fin geometry, the device is designed from scratch using two alternative approaches, namely (i) an iterative procedure based on the renowned $\varepsilon - NTU$ method and (ii) *Computational Fluid Dynamics* (CFD) tools.

The final heat exchanger design follows an optimization procedure aimed at maximizing the device thermo-hydraulic performances and compactness index, quantities which are then benchmarked with other notable heat exchanger typologies so to highlight the design soundness. In this context, the benefits of using CFD tools relative to simpler semi-empirical methods for heat exchangers design are also discussed.

Finally, the possibility of *functionalizing* the heat exchanger, which involves the design of special catalytic surfaces able to simultaneously transfer heat and catalyze exothermal methanation reactions, is explored. In particular, it is demonstrated that by adopting a two-stages layout, featuring first a low temperature *functionalized* device followed by a *classical* heat exchanger, it is possible to boost the cold side outlet temperature, therefore yielding at a higher P2G plant overall efficiency.

CHAPTER 1

INTRODUCTION

It is very well known that the power produced by the most promising renewable energy sources (RES), such as wind and solar power, is highly volatile, showing remarkable daily and seasonal fluctuations. Already today, RES power plants are stopped if the electricity generation is above the demand. Only in 2010, as much as 150 GWh of renewable electricity was waisted in Germany [1]. This trend is expected to further extend, because the share of power produced by renewable means is steadily increasing [2], as required by the *EU Renewable Energy Directive*, which aims at fulfilling at least 20 % of the total European energy needs with renewables by 2020 (3.5 PWh) [3].

Energy storage, allowing to temporally postpone the consumption, drastically reduces the energy losses due to off-peak power [1; 4; 5; 6]. At the same time, it makes energy available when the environmental conditions are such (no wind, clouds, snow) that not enough power can be produced by renewable means. This evidently allows for a smoother load balancing of the energy grid and for the merging of the traditionally separated energy sectors of electricity, gas and mobility [3].

At present, as shown in Figure 1 [1], it exists several different energy storage technologies. They differ mainly in terms of the amount of energy that can be stored and of their characteristic discharge time, i.e. the time-frame during which energy is available.

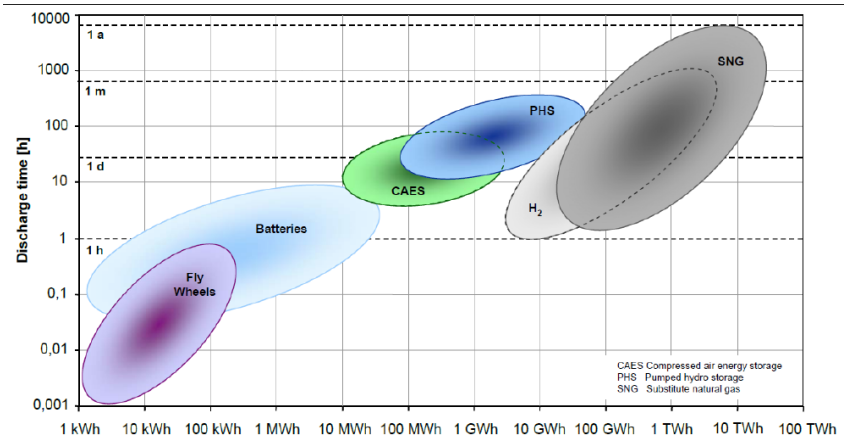

Figure 1: Comparison between different energy storage solutions performances

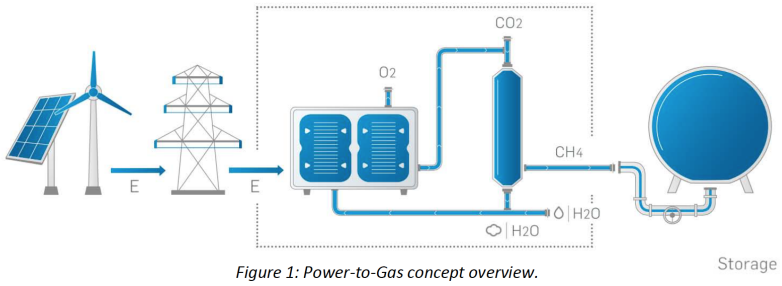

Figure 1: Power-to-Gas concept overview.

Figure 2: Power-to-Gas concept overview

Power-to-Gas(P2G) technology, consisting in the conversion of electrical power into gas fuels as schematically shown in Figure 2 [1], offers the best performances, exhibiting virtually unlimited storage capacity and a discharge time of years. Neither mechanical systems, such as flywheels, nor electrochemical devices, such as batteries, can evidently compete with P2G for industrial applications.

Whatever the fuel produced, it is necessary to preliminary split the water molecule into hydrogen and oxygen. This chemical reaction, shown in Equation 1.1, is known as *electrolysis reaction* and it requires an external energy supply to happen which, in this context, would be represented by the excess power produced by RES [7; 8].

$$H_2O \rightarrow H_2 + \frac{1}{2}O_2 \tag{1.1}$$

The hydrogen can be then either directly used or combined with carbon dioxide CO_2 to produce methane, as suggested by the *Sabatier* reaction shown in Equation 1.2 [9; 10].

$$CO_2 + 4H_2 \rightarrow CH_4 + 2H_2O \tag{1.2}$$

Both hydrogen and synthetic natural gas (SNG) are effective storage means, but the latter is gaining momentum because of the following advantages over hydrogen:

- Bigger storage capacity
- Higher discharge time
- SNG is fully compatible with the existing pipeline network and storage infrastructure. Hydrogen, instead, cannot exceed the 5 % as volume fraction and would then require additional distribution facilities [10].

Figure 3: HELMETH logo

1.1 HELMETH

It is in such an energetic context that the European Union (EU), considering P2G strategical and complementary to the energy production by renewable sources, has decided to invest on this technology co-financing the HELMETH[1] project. More precisely, HELMETH is regarded as a proof of concept of a highly efficient Power-to-Gas (P2G) technology that uses methane as chemical storage [1; 4].

Traditional P2G plants, using alkaline or PEM (Proton Exchange Membrane) electrolyser modules, have an efficiency lower than 50 %, comparable with that of traditional thermoelectric powerhouses. HELMETH, targeting much higher efficiencies, above 85 %, is naturally a more interesting paradigm from an industrial and scientific standpoint [10; 11; 12]. Such high efficiencies are enabled by the following factors:

1. Electrolysis is carried out in innovative, high-temperature *Solid Oxide Electrolyser Cells* (SOEC), Figure 4 [1], whose typical operative temperature falls in the range 800-850 $°C$.
2. Thermal integration, i.e. the highly exothermal methanation reactions partially balance the electrolysis endothermal processes.

---

[1]Integrated High-Temperature Electrolysis and Methanation for Effective Power to Gas Conversion

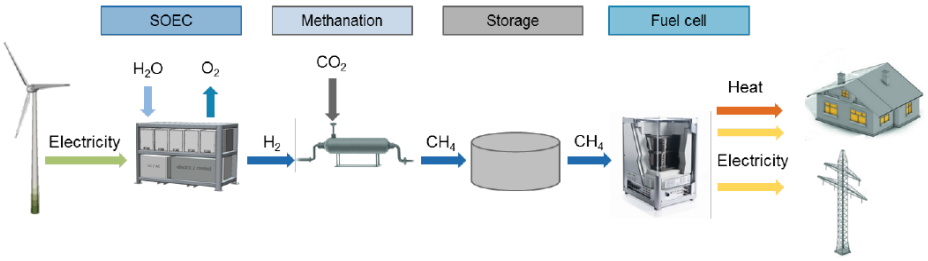

Figure 4: SOEC role in a P2G plant

Co-electrolysis (CE), thanks to its higher SNG output, allows to further improve P2G efficiency [10]. In an electrolytic cell only water molecules are split into its elementary components, with hydrogen then being forced to react with carbon dioxide to produce methane. On the contrary, considering co-electrolysis, both water and carbon dioxide are fed to the SOEC to obtain a mixture of hydrogen, carbon monoxide, methane and residual reactants, known as *syngas*, which is then directly fed to the methanator [13].

1.1.1 Heat exchanger

HELMETH focuses mainly on electrolysis, as the final objective is designing, producing and testing an experimental plant inclusive of SOEC and methanation modules. However, quoting the official project call, "*co-electrolysis shall be investigated as a further parameter toward the overall system efficiency optimization*"[1]. This is the reason why the object of design of this thesis, an optimized high-temperature compact heat exchanger, is precisely at the service of a co-electrolysis P2G plant, whose layout is schematically represented in Figure 5.

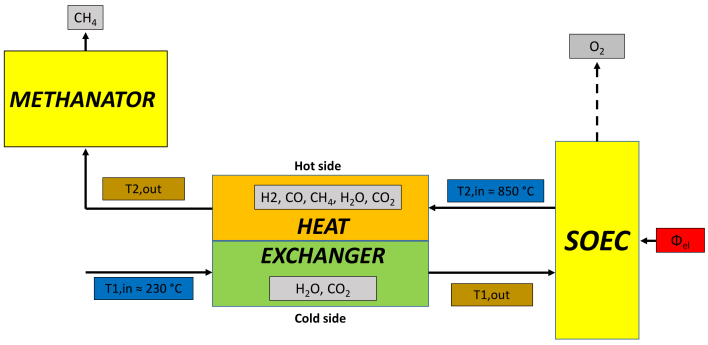

Figure 5: Reference plant layout for the heat exchanger design

The heat exchanger role is to heat up the SOEC inlet mixture, including both water steam H_2O and carbon dioxide CO_2, to a temperature as close as possible to the SOEC operative point (850 $°C$). The thermal source used to heat up this cold mixture is the SOEC cathodic outlet mixture, i.e. the syngas itself. This regenerative approach is coherent with HELMETH philosophy of thermal integration, which aims at minimizing the external energy supply Φ_{el} by exploiting internal heat sources.

Because of this regenerative layout, the cold and hot heat exchanger mass flow rates are evidently coupled and a function of the working point of the SOEC. The immediate consequence is that it will not be possible to increase the heat transfer by simply increasing the hot side mass flow rate, but it will be rather necessary to enhance the heat exchanger effectiveness.

Hereafter follows a brief description of the SOEC working principle, which will allow to better understand the nature of the mass flow rates functional coupling.

1.1.2 Solid oxide electrolyser cell

An electrolyser is an electrochemical cell that undergoes a redox reaction when an external electrical energy supply is provided [14]. Whatever the specific design, there are usually three main components: an electrolyte and two electrodes, acting respectively as cathode and anode. As previously hinted at, electrolysis can be currently performed by one of the following three different technologies [7]:

1. Alkaline electrolysers
2. Proton Exchange Membrane (PEM) electrolysers
3. Solid Oxide Electrolyser Cells (SOEC)

The first two technologies are sufficiently mature to be commercially available, while SOEC is an innovative and promising technology that is still under development [10].

In alkaline electrolysers, the electrodes are immersed into a liquid alkaline electrolyte, notably aqueous solutions of potassium or sodium hydroxide, and operate at a temperature around 60-90 $°C$. In a PEM, a solid polymer electrolyte, electrically insulating the electrodes, is responsible for the protons conduction and for the subsequent separation of product gases. This technology, with respect to alkaline electrolysers, allows for higher current densities and operative pressures, while operating in a similar temperature range (40–80 $°C$) [10].

While both these technologies are examples of low-temperature electrolysers, Solid Oxide Electrolyser Cells operate at higher temperatures, precisely in the range 700-900 $°C$. Their main advantages over competitive technologies are the high efficiency and the low operating

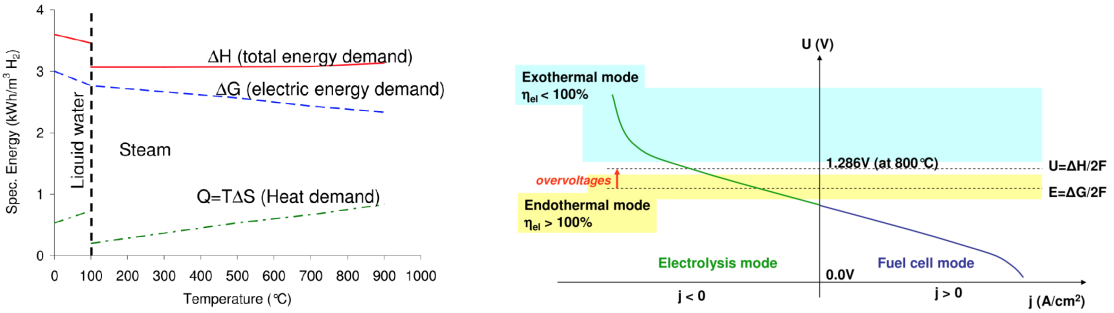

(a) Electrolysis energy demand as a function of temperature

(b) Operation modes of a SOEC

Figure 6: SOEC energy demand

cost. As suggested by name (SOEC), the electrolyte material is solid oxide or ceramic, in most cases electrolyte zirconia ZrO_2 stabilized with yttria (Y_2O_3) [7; 15].

A SOEC can be thought as a Solid Oxide Fuel Cell (SOFC) running in regenerative mode to achieve the electrolysis of water or the co-electrolysis of a mixture of water and carbon dioxide. In principle a SOFC could be reverted to work as SOEC. In practice, a given fuel cell is usually optimized for operating in one mode and it is not always possible or convenient to use it as SOEC. The SOEC specifically used within HELMETH is being developed by one of the industrial partners of the project, the German company *Sunfire Gmbh* [4]. This unit, whose nominal operative temperature is 850 $°C$, will be able to operate efficiently at high pressure (up to about 15 bar) and to support CO_2 co-electrolysis [16].

Performing electrolysis is an energy-demanding task, because it is necessary to break the chemical bonds of thermodynamically stable molecules such as water and carbon dioxide. The

reason why high-temperature electrolysis is more efficient than low-temperature is precisely because of the reduced required electric energy supply shown in Figure 6 (a) [1]. In fact, at high temperatures, as a consequence of the more favorable thermodynamic and electrochemical kinetic conditions, the required Gibbs free energy is lower and it is possible to increment the energy fraction provided by heat, either coming from external sources or produced by Joule effect within the stack itself [10].

Figure 6 (b) shows the three different operation modes of a SOEC [1]:

1. Thermoneutral

   The electrolysis heat demand $Q = T \cdot \Delta S$ equals the heat released by Joule effect within the cell. Since the cell voltage is exactly equal to the thermoneutral, the net heat flux is zero and the electric efficiency is exactly 100 %.

2. Exothermal

   Because of a cell voltage over the thermoneutral, the electric energy input exceeds the enthalpy of reaction, determining an overall positive heat flux and an electric efficiency lower than 100 %.

3. Endothermal

   The cell voltage being lower than the thermoneutral, the electric energy input stays below the reaction enthalpy, meaning that heat must be supplied to the system for isothermal operation and that the electric efficiency is above 100 %.

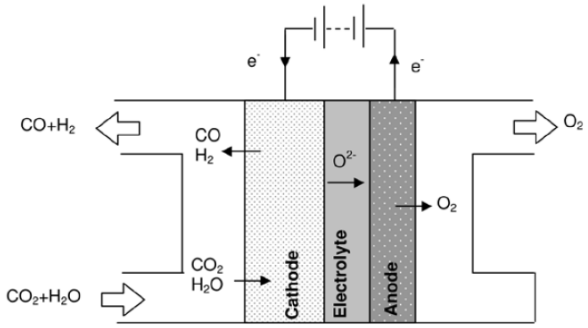

Figure 7: Co-Electrolysis

After having considered the issues related to energy and thermal management of a SOEC, it is worth understanding better which are the electrochemical reactions taking place in the SOEC, as shown in Figure 7 [1]. Basically, water and carbon dioxide are reduced at the cathode, according to Equation 1.3, while oxygen, after being conducted trough the electrolyte, is oxidated at the anode according to Equation 1.4 [7; 11]. Overall, the co-electrolysis equation can be summarized as displayed in Equation 1.5.

$$x\,CO_2 + y\,H_2O + 4e^- \rightarrow x\,CO + y\,H_2 + 2O^{2-} \tag{1.3}$$

$$2O^{2-} \rightarrow O_2 + 4e^- \tag{1.4}$$

$$x\,CO_2 + y\,H_2O \rightarrow x\,CO + y\,H_2 + =_2 \tag{1.5}$$

Theoretically, the cathode outlet mixture should include only pure hydrogen and carbon monoxide. In reality, since the SOEC reactant utilization (RU) cannot be unitary and is usually

bounded to a value of 70 % for thermal management reasons, side-chemical reactions, such as the water-gas shift reaction shown in Equation 1.6, can happen [10]. As a consequence, among the products there are also fractions of water and carbon dioxide, i.e. of unreacted reactants.

$$\mathrm{H_2O + CO \rightleftharpoons H_2 + CO_2} \tag{1.6}$$

Finally, in a pressurized SOEC or while using a high RU, the exothermic methanation reactions shown in Equation 1.7 and Equation 1.8 can become relevant, in spite of the fact that they are not thermodynamically favored at high temperatures. In fact, Figure 8 [10] proves that the methane fraction can be as high as 10 % when the system is pressurized at about 30 bars. In co-electrolysis plants, also because of the formation of methane already in the SOEC, the final SNG fraction is higher than in electrolysis plants and the overall efficiency is consequently higher.

$$\mathrm{CO + 3\,H_2 \rightleftharpoons CH_4 + H_2O} \qquad \Delta\bar{h}^0_{298K} = -206\frac{kJ}{mol} \tag{1.7}$$

$$\mathrm{CO_2 + 4\,H_2 \rightleftharpoons CH_4 + 2\,H_2O} \qquad \Delta\bar{h}^0_{298K} = -165\frac{kJ}{mol} \tag{1.8}$$

In conclusion, considering a co-electrolysis SOEC, the cathode mixture is likely to include, beyond the expected products, i.e. hydrogen H_2 and carbon monoxide CO, also water H_2O, carbon dioxide CO_2 and methane CH_4.

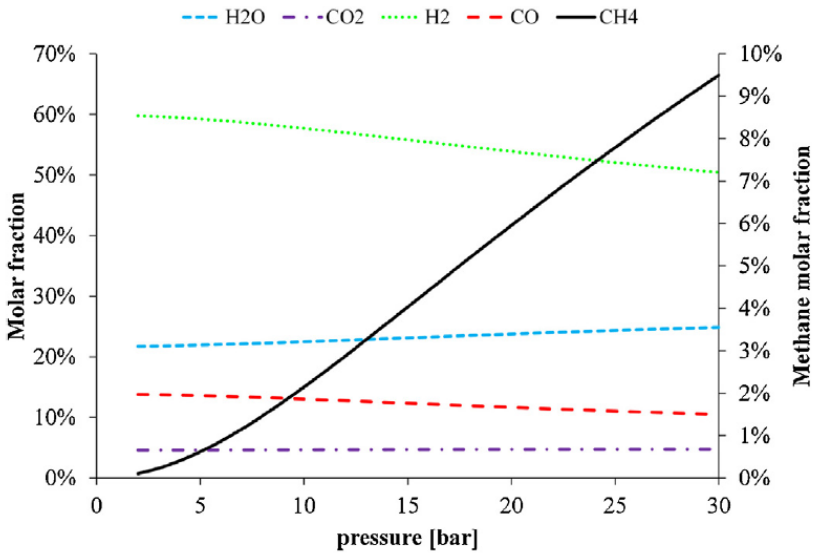

Figure 8: SOEC cathode composition as a function of pressure

1.1.3 Methanator

After having clarified the role and the operation of both the heat exchanger and the SOEC within the co-electrolysis P2G plant shown in Figure 5, it is worth concluding this initial overview by briefly describing the methanation module as well.

The syngas obtained at the SOEC outlet, flowing through the heat exchanger, is cooled down from a temperature of 850 $°C$ to about 250 $°C$ [1]. In a methanation unit, the newly formed carbon monoxide CO and the residual carbon dioxide CO_2 are hydrogenated to methane following the Ni-catalyzed exothermal Sabatier reactions, Equation 1.7 and Equation 1.8, previously introduced [9; 17].

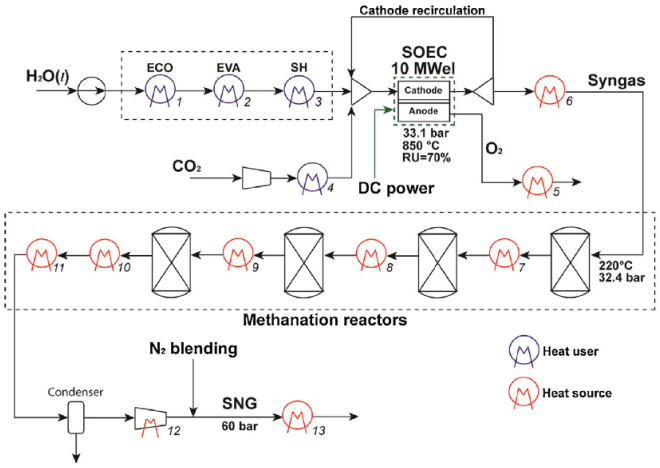

Figure 9: Co-electrolysis detailed plant layout

The reference technology considered to model the methanation section is Haldor-Topse TREMP™ (*Topse Recycle Energy-efficient Methanation Process*). This multiple adiabatic fixed bed reactors methanation module, schematically represented in Figure 9 [1], exploiting a combination of non-Ni and Ni catalysts, allows an inlet temperature as low as 220 $°C$ [18]. Remembering the regenerative nature of the plant of Figure 5, it is evident that this condition favors heat transfer in the heat exchanger, allowing the achievement of higher effectiveness.

The syngas composition is crucial to achieve high methanation conversion rates. More precisely, the stoichiometric feed ratio of the reactants must meet the constraint displayed in Equation 1.9 [18].

$$FR = \frac{[H_2] - [CO_2]}{[CO] + [CO_2]} = 3 \tag{1.9}$$

This equation allows to account for the simultaneous presence of carbon monoxide and dioxide. In fact, solving this equation imposing a null carbon monoxide concentration, it follows a hydrogen to carbon dioxide ratio of 4, i.e. precisely what prescribed by the stoichiometric reaction shown in Equation 1.8. Vice-versa, solving considering a null carbon dioxide concentration, it follows a hydrogen to carbon dioxide ratio of 3, i.e. exactly what suggested by Equation 1.7.

Because of the exothermic nature of Sabatier reactions, if it true that high temperature is a penalizing factor from a thermodynamic standpoint, it is also renowned that it enhances the reaction kinetics, as the reaction rate monotonically increases with the temperature [14].

Moreover, according to *Le Châtelier's principle*, the reactions in which the number of moles decreases passing from reactants to products are favored at high-pressures [14]. Within HELMETH, in order to maximize the production of SNG, the whole plant, i.e. pipes, HE, SOEC and methanator, is pressurized at 15 bar. Traditionally, only the methanator is maintained under pressure and the mixture is pressurized only downstream of the SOEC, resulting in remarkably high compression costs. Using even higher pressure would boost methane production, but at present the SOEC are not able to withstand pressures higher than 15 bar.

Taking all the above factors into account, it is possible to understand why Figure 9 features several high-pressure (15 bar) methanation reactors connected in series with intermediate cooling. This is the only way to reach methane concentrations sufficiently high, i.e. above 90 %, to meet the requirements for SNG direct introduction into the national distribution grid [19].

CHAPTER 2

ADDICTIVE MANUFACTURING

Coherently with the innovative spirit of HELMETH, heat exchangers will be produced by a relatively new technology such as *Addictive Manufacturing* (AM). The term AM, in reality an umbrella term given to all those technologies that manufacture parts by adding material layer by layer, is opposed to the traditional subtractive processes, where material is instead removed. AM also refers to a class of technologies allowing to automatically construct solid parts starting from digital CAD data.

Whatever the specific AM technology used, the procedure to follow in order to obtain the final object of design starting from a digital CAD file includes the following steps, graphically summarized in Figure 10.

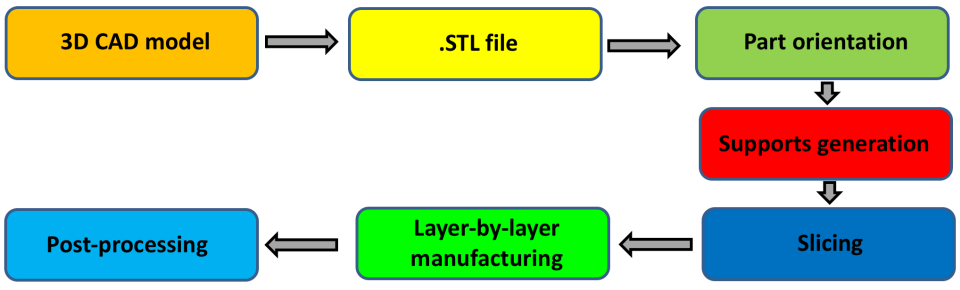

Figure 10: Addictive Manufacturing steps

```
solid
 facet normal  0.121   0.380  -0.917
  outer loop
    vertex    1.5000  1.8882  0.0511
    vertex    1.5000  2.2500  0.2010
    vertex    1.9302  1.9783  0.1450
   endloop
  endfacet
 facet normal  0.175   0.175  -0.969
  outer loop
    vertex    1.9302  1.9783  0.1450
    vertex    1.8882  1.5000  0.0511
    vertex    1.9302  1.8882  0.0511
   endloop
  endfacet
     ...
endsolid
```

(a) Numerical representation by triangles normal and vertices

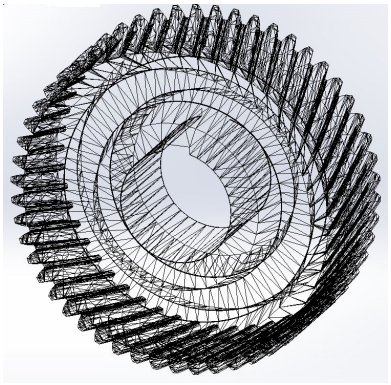

(b) Graphical representation of an unstructured triangulated surface

Figure 11: .STL files

1. Triangularization of the CAD file to produce a standard .STL file, which describes raw unstructured triangulated surfaces by the unit normal and the triangles vertices, as shown in Figure 11.

2. Import of the .STL file on the AM machine software, where:

   - The file is checked, to avoid manufacturing errors due to inverted normals or gaps.
   - The part is oriented.
   - Depending on the orientation, supports could be generated.
   - The geometry is sliced, i.e. subdivided into thin layers.

3. Physical manufacturing of the 3D object layer by layer.

4. If necessary, post-processing operations, such as cleaning, finishing, support removal and strengthening or stress-relieving heat treatments.

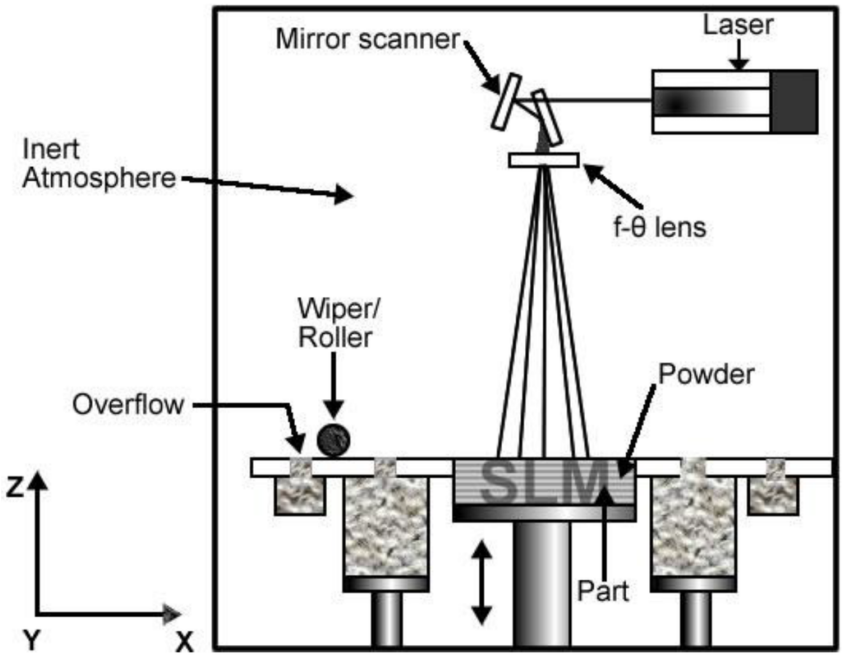

Figure 12: SLM building process

The specific AM technology used in this context, generally referred to as *Selective Laser Melting* (SLM) or as *Direct Metal Laser Sintering* (DMLS), is hereafter shortly described, highlighting its working principle, its points of strength and the limitations to take into account during the design process.

2.1 Direct Metal Laser Sintering

Selective laser melting is an AM technology, invented in 1995 at the *Fraunhofer Institute ILT* (Germany), that uses 3D CAD data as a digital information source and a laser beam to selectively melt fine metal powder and build up fully-dense parts layer-by-layer. The machine is usually equipped with a 200W Yb fiber continuum laser having a beam focus of 0.1 mm [20].

According to Yadroitsev et al. (2015), the process parameters influencing the quality of the sintered metallic object are, in order of importance, the laser power density, the powder layer thickness, the scanning speed and finally the powder particle size [21].

SLM manufacturing process starts with the deposition of a layer of metal powder on the building platform by a re-coater blade, as shown in Figure 12 [22]. The laser beam melts the powder according to the slice geometry tracing the cross-section. After irradiation, the platform is lowered by a vertical distance equal to the layer thickness and the sequence is repeated until completion of the part [23].

After the deposition of each new layer, the direction of the core area scan lines is usually rotated by 67°. At the end of the building process, the platform with the part is subjected to a thermal treatment for stress relieving and finally the part can be removed from the platform.

Having clarified the working principle of SLM, hereafter follows a short analysis of the advantages and disadvantages associated with AM.

2.2 Advantages and Drawbacks

Addictive Manufacturing is by-now renowned for enabling fast, flexible and cost-effective productions directly from electronic data. Its most relevant advantage is undoubtedly the design freedom, which makes it possible to realize non modular geometries of whatever complexity. The term *Design for AM* indicates precisely this new and different method of conceiving parts, free of the compromises imposed by process limitations. In terms of heat exchanger design, this freedom enables to optimize the HE thermo-mechanical performances by customizing the fin shapes, as proved by Figure 13 [24], rather than using a traditional fin geometry.

Another remarkable feature of AM, thanks to the possibility of realizing hollow components, is the production of lightweight structures. Material can in fact be deposited only where necessary for structural reasons, resulting in both cost and weight savings, which have made this technology particularly appealing for aerospace applications.

Furthermore, AM often allows to build the final device in one piece instead of having to go through assembly processes. For instance, the operative pressure of plate-fin heat exchangers, traditionally manufactured by welding or brazing together fins and plates, has long been limited by the weakness of the soldered joint. A monolith heat exchanger design produced by DMLS allows to substantially improve the HE mechanical properties.

Finally, it is worth highlighting that an object produced by AM, being already *net shape* or *near net shape*, barely requires any post-processing.

AM advantages are not limited to the product, but extend to the manufacturing process as well. In fact, AM eliminates the need for special tools and fixtures. One machine enables the production of unlimited different shapes and geometries. Even more importantly, differently from subtractive processes, the manufacturing time and cost depend only on the product size and not on its complexity.

Needless to say, AM comes also with some disadvantages, notably:

- If the time-to-market is shorter than for traditional manufacturing process, the actual building time can be higher because each layer is very thin and the laser scanning speed is limited.

- The machines reduced building volume, usually not exceeding a 30 cm cube, limits AM application field to small products.
- The scarcity of building materials types.
- The need for support structures in case of overhanging geometries.
- The surface roughness *Ra*, related to the powder granulometry, is high and often requires finishing post-processing operations.
- Residual stresses.

Knowing AM strengths and weaknesses, it is worth shortly assessing how this technology has been so far applied to the heat exchangers industry.

2.3 AM Applications to Heat Exchangers

At present, the industrial use of AM for serial production is still not a standard manufacturing method. However, because of the many innovation possibilities enabled by AM, it is likely that the industrial manufacturing paradigm will rapidly evolve toward a mix of addictive and subtractive processes. AM advantages, as highlighted by Pham and Gault back in 1997 [25; 26], are not limited to the technical realm, as AM is also expected to cut new product costs by up to 70 % and the time to market by 90 %.

The theme of thermal devices fabrication by AM has already been explored in scientific literature. M. Wong et al. have repeatedly investigated the performances of heat sinks using optimized fin shapes produced by SLM [24; 27; 28]. S. Tsopanos et al. have proved the advantages of AM micro cross-flow heat exchangers in terms of thermal performance and compactness

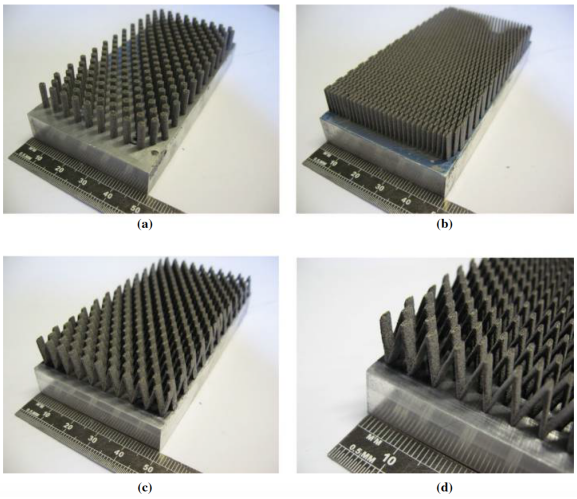

Figure 13: Different fin designs produced by SLM

[29]. Thompson et al. have characterized the design of a titanium alloy CHE built by SLM [30]. Finally, M. Norfolk and H. Johnson have focused on the use of ultrasonic sheet lamination (UAM) as an alternative to DMLS for the solid-state manufacturing of heat exchangers [31].

In addition to the academic interest toward AM, there is strong evidence that whole industrial segments are actively investigating the use of this technology for serial production. EOS, a German producer of addictive manufacturing systems, has manufactured several HE prototypes to show the level of geometric complexity achievable through DMLS [32]. M. Fuller, founder of *Conflux Technology*, is producing by AM innovative and ultra-compact heat exchangers for automotive applications, a market which is valued at nearly 12 USD billions [33]. Because of the extreme lightweight of parts manufactured by AM, the aerospace industry is investing in this technology as well: A. Muley, in 2007, has analyzed advanced HE for aircraft engines

TABLE I: DIMENSIONS OF THE DMLS MACHINE BUILDING VOLUME

L [cm]	W [cm]	H [cm]	$V_{max}[dm^3]$
25	25	21.5	13.438

use [34], while in 2015 *3D Systems* has signed a 1.3 USD millions partnership with Honeywall international for the production of an innovative aircraft heat exchanger [35].

In conclusion, even though AM tools are not an industrial standard yet, both academic and commercial institutions are investing this innovative technology. As AM is rapidly gaining momentum, the choice of using it for heat exchangers manufacture within HELMETH project appears motivated from both a technical and commercial standpoint. Hereafter the machine actually used to realize the heat exchanger and the building material, i.e. Inconel 718, properties are briefly analyzed.

2.4 EOS DMLS Machine

Within HELMETH, the DMLS machine used for the heat exchangers manufacture is the EOSINT M270 *Xtended* [36], represented in Figure 14.

One of the main limitations of this specific machine and of AM technology in general is the reduced size of the building volume, whose linear dimensions, shown in Table I, never exceed 25 cm. The building chamber is filled with nitrogen, an inert gas, which limits the metal particles oxidation at high temperature.

The machine performances are strongly related to the material being used. Considering Inconel 718, the following technical specifications apply:

Figure 14: EOSINT M 270 system for Direct Metal Laser Sintering (DMLS), source: EOS.

- Minimum viable wall thickness of 0.2 mm.
- Maximum accuracy of 40 μm.
- Minimum layer thickness of 20 μm and maximum of 100 μm.
- Surface roughness before polishing of 4-6.5 μm.
- Maximum building rate of 4 $\frac{mm^3}{s}$.

In conclusion, the most important limitations to be taken into account while designing the heat exchanger are the minimum wall thickness (0.2 mm) and the minimum horizontal plate thickness (1 mm).

TABLE II: INCONEL 718 ALLOYING ELEMENTS MASS FRACTIONS

Ni	Cr	Nb	Mo	Ti	Al	Co	Cu
$50 \div 55$	$17 \div 21$	$4.75 \div 5$	$2.8 \div 3$	$0.65 \div 1.15$	$0.2 \div 0.8$	< 1	< 0.3

2.5 Inconel 718 Thermo-Mechanical Properties

Traditional heat-exchanger materials include aluminum, perfectly suitable for low-temperature devices thanks to its high thermal conductivity, steel, the most commonly used building material because of its strength and limited cost, and finally special alloys for particular applications. The high-temperature corrosive operative environment of a P2G plant demands precisely such a super-alloy, Inconel 718. Inconel is a family of austenite nickel-chromium-based super-alloys, first developed in the 1940s at *Wiggin Alloys*, UK [37]. Different Inconels have very diverse compositions, but nickel is always predominant with chromium as second main element. Inconel 718, whose precise composition is shown in Table II, is particularly rich in niobium and aluminum and has a theoretical density of 8.15 g/cm^3.

Inconel alloys are traditionally employed under extreme operative conditions, characterized by high temperature, elevated pressures and presence of corrosive fluids. Inconel 718 resistance to oxidation and corrosion, enhanced by the addition of aluminum, derives from the formation of a thick and stable passivated oxide layer that protects the surface from further attacks. Inconel 718 also retains mechanical properties over a wide temperature range and is therefore commonly employed in high-temperature applications were traditional materials such as aluminum and steel would suffer of creep. Inconel properties are the consequence of heat treatments having the

double objective of maximizing the precipitation of strengthening particles and to tune the grain size [38], as bigger grains perform better in terms of creep resistance. Inconel 718 outstanding weldability guarantees the possibility of joining together different components, such as the heat exchanger core and its distribution system, without the risk of post-welding cracking.

Finely tuning SLM operative parameters, notably the laser power density and the scanning speed, it is possible to obtain almost fully dense Inconel 718 components, with a relative density close to 99.8 % of the theoretical one. Such a low porosity level determines final properties similar to the nominal ones.

2.5.1 Experimental results

The final material properties of a device depend on which manufacturing technique has been adopted. In literature, there is a wide array of studies about selective laser melted Inconel 718 properties [39] [40]. However, for the sake's of accuracy, this material has been experimentally characterized at Politecnico di Torino (2015) in terms of thermal conductivity and mechanical properties [38]. Figure 15 (a) [38] shows the granulometry distribution of the Inconel 718 special powder optimized for processing on EOS M systems [41].

Figure 15 (b) shows that Inconel 718 thermal conductivity λ, which for metals can be explained by means of free electrons motion, monotonically increases with temperature. Thermal conductivity values, ranging from 11 $^{W}/_{m \cdot K}$ at ambient temperature to 25 $^{W}/_{m \cdot K}$ at 900 $^{\circ}C$, because of the high mass fraction of low conductivity nickel, are comparable with those of stainless steels and are instead substantially lower than those of aluminum alloys.

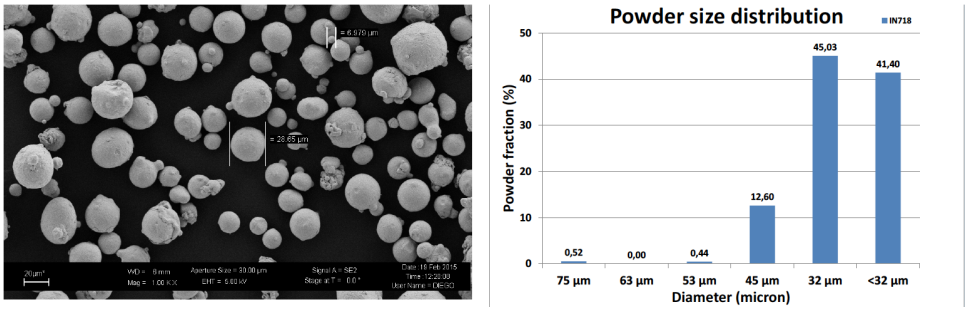

(a) Powder granulometry

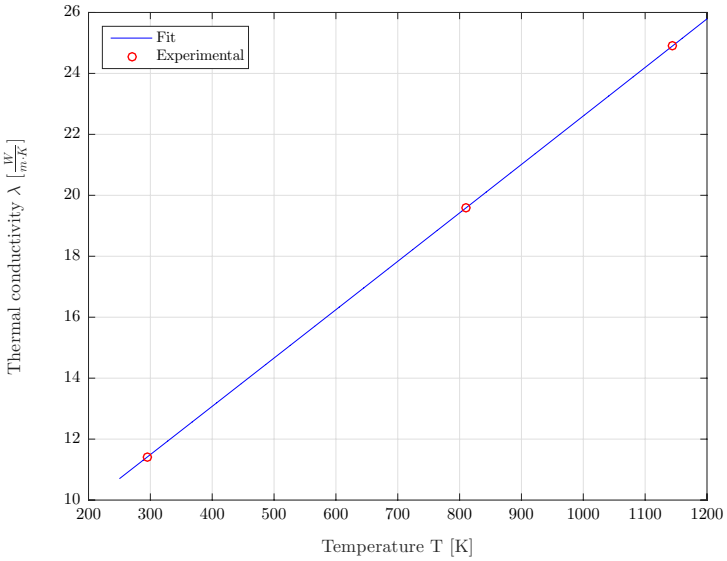

(b) Thermal conductivity λ as a function of temperature

Figure 15: Inconel 718

As previously anticipated while introducing Inconel alloys, this material is able to retain exceptional strengths at high temperatures. Figure 16 (a) highlights how, at temperatures as high as 1000 $°C$, the yield resistance is still about 1000 MPa. Finally, Figure 16 (b) shows that Inconel 718 increment in elongation at high temperatures is limited.

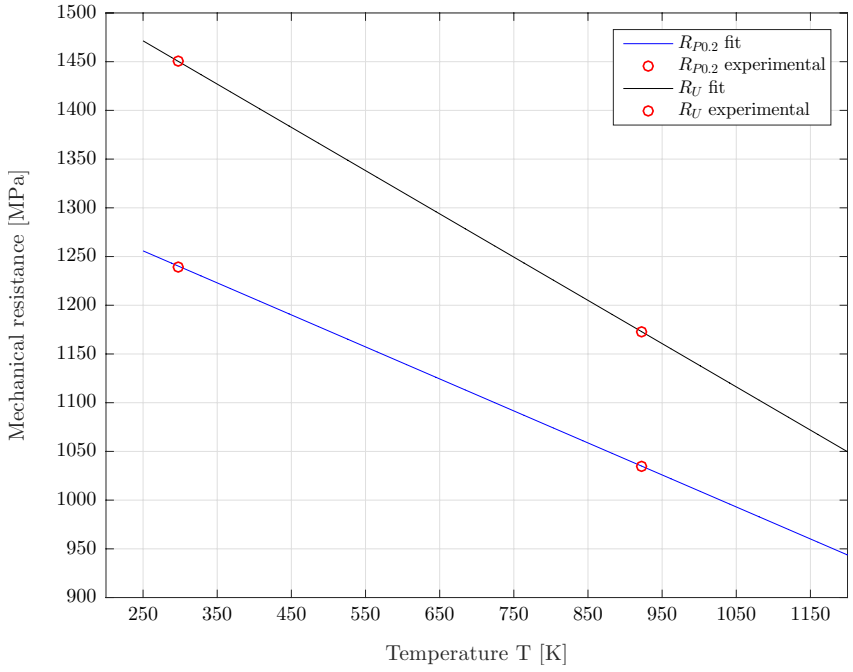

(a) Yield strength $R_{P0.2}$ and ultimate strength R_U

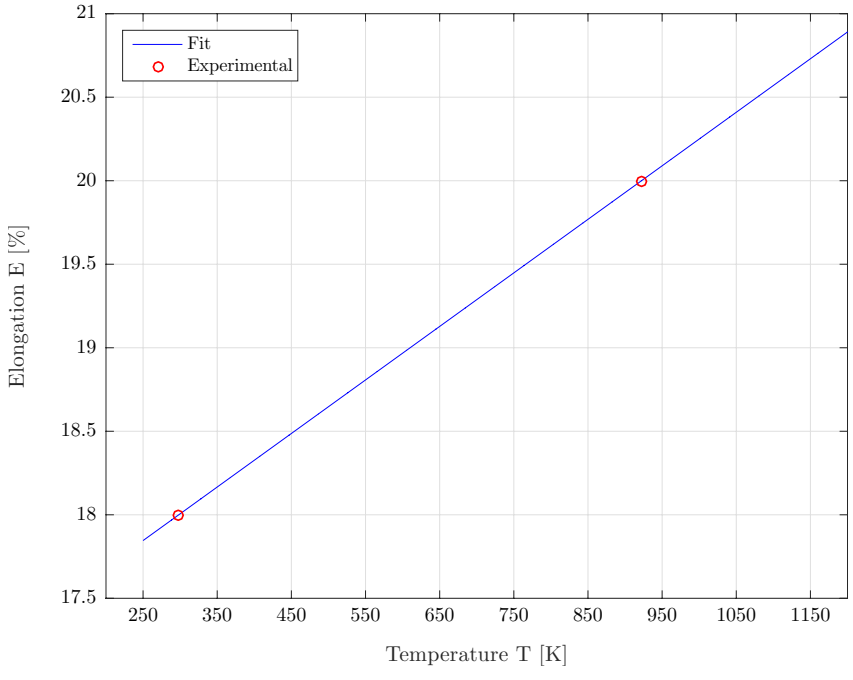

(b) Elongation E

Figure 16: Inconel 718 mechanical properties as a function of temperature

CHAPTER 3

MIXTURES COMPOSITIONS AND MASS FLOW RATES

3.1 Mixtures Compositions

The final objective of a P2G plant being the production of SNG, the composition of the mixture entering the methanator needs to be such to maximize the methane production. As it has been explained in Chapter 1, in a co-electrolysis plant the SOEC is uniquely responsible for the water vapor H_2O and carbon dioxide CO_2 inlet mixture conversion into a hydrogen H_2 and carbon monoxide CO rich syngas. From now on, for the sake's of conciseness, the SOEC inlet mixture will be referred to as *mixture 1*, while the SOEC outlet mixture will be indicated by *mixture 2*. Knowing the nominal operative conditions of the SOEC, summarized in Table III, it is therefore possible to determine the precise composition of mixtures 1 and 2, whose role, according to Figure 5, is functional for the heat exchanger design.

To this aim, the SOEC has been modeled on *Aspen Plus* as a dimensionless component. This simulation model, graphically shown in Figure 17 and referred to a 150 kWe P2G plant,

TABLE III: SOEC NOMINAL OPERATIVE CONDITIONS

p $[bar]$	T $[°C]$	RU [/]	FR [/]	i [kA]	V [V]
15	850	0.70	3	100	1.47

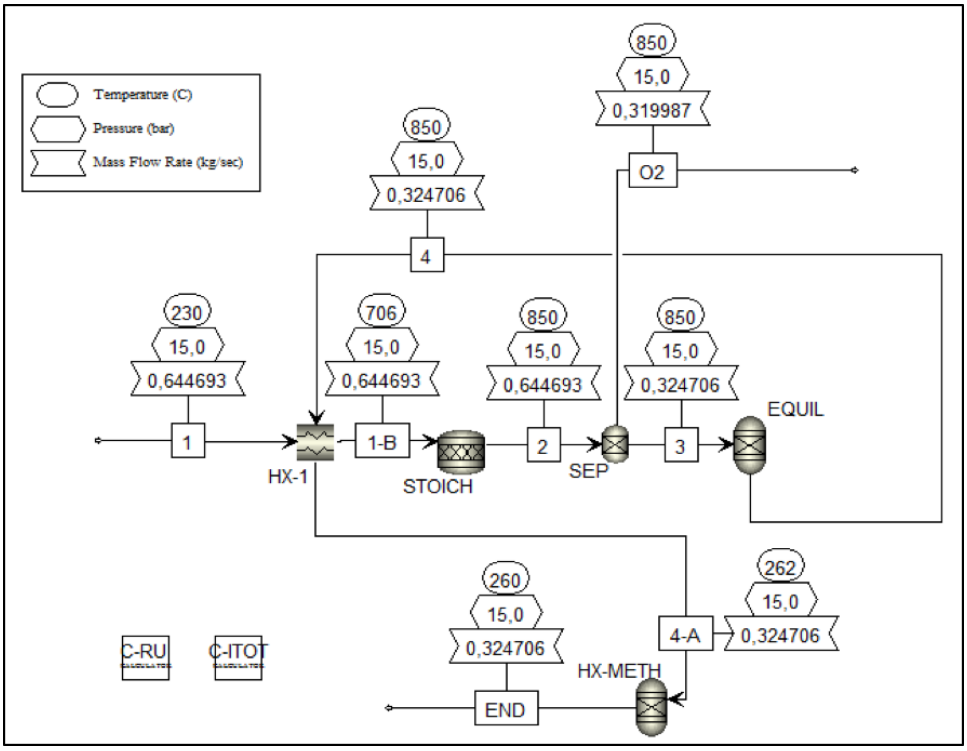

Figure 17: *Aspen Plus* co-electrolysis SOEC model

complemented by the suitable boundary conditions hereafter listed, allows to derive the molar fractions y_i of each mixture component.

1. SOEC inlet components: H_2O, CO_2
2. SOEC outlet components: H_2, CO, CH_4, H_2O, CO_2
3. Chemical equilibrium (Equation 1.5 and Equation 1.6)
4. Electro-chemical equilibrium (Equation 1.3 and Equation 1.4)
5. SOEC operative pressure: 15 bar

TABLE IV: MIXTURE 1 COMPOSITION: MOLAR AND MASS FRACTIONS

	H_2O	CO_2
y_i	0.8250	0.1750
x_i	0.6585	0.3415

6. SOEC nominal working temperature: 850 $°C$
7. Reactant utilization rate: $RU = 70\ \%$
8. Feed ratio: 3 (Equation 1.9)
9. SOEC current i: 100 kA
10. Thermoneutral voltage: 1.47 V

Knowing the molar fractions y_i, using Equation 3.1 to Equation 3.3, it is possible to calculate the mass fractions x_i as well. The simulation output, i.e. mixtures 1 and 2 compositions, is reported in Table IV and Table V.

$$\dot{V}_i = y_i \cdot \dot{V} \tag{3.1}$$

$$\dot{m}_i = \dot{V}_i \cdot M_i \tag{3.2}$$

$$x_i = \frac{\dot{m}_i}{\dot{m}_{tot}} \tag{3.3}$$

From a thermodynamic standpoint, it takes an infinite time to reach chemical equilibrium. Since in reality the residence time in a SOEC is finite, the simulation results, derived imposing

TABLE V: MIXTURE 2 COMPOSITION: MOLAR AND MASS FRACTIONS

	H_2O	CO_2	CO	H_2	CH_4
y_i	0.2860	0.0530	0.1070	0.5300	0.0240
x_i	0.4319	0.1956	0.2513	0.0889	0.0322

the equilibrium, are not coherent with the actual non-equilibrium conditions. However, a comparison between simulation and experimental compositions (Politecnico di Torino, 2014) has shown negligible numerical discrepancies, thus validating the use of *Aspen Plus* as a tool for preliminary compositions assessment.

It is important to highlight that as the objective is determining a composition, i.e. a dimensionless quantity, and as the SOEC is modeled as 0-D, the numerical value assigned to the inlet and outlet total flow rates $\dot{V}_1$ and $\dot{V}_2$ does not influence the final results. The mass flow rates used in the *Aspen Plus* simulation and shown in Figure 17 are therefore different from the ones actually considered while designing the heat exchanger.

As a final remark, it is noteworthy to highlight how the simultaneous presence of carbon monoxide CO and dioxide CO_2 determines a water to carbon dioxide ratio, $^{H_2O}/_{CO_2} = 4.714$, higher than the stoichiometric values of 3 and 4 respectively suggested by Equation 1.7 and Equation 1.8. From a mathematical standpoint, this is the consequence of fixing the feed ratio value. Calculating this parameter, according to Equation 1.9 and using the newly derived compositions, yields at a value of 2.98, completely coherent with the imposed input value of 3.

3.2 Mass Flow Rates Ratio

Because of the regenerative layout shown in Figure 5, where the SOEC acts as coupling element between the hot and cold side of the heat exchanger, the HE mass flow rates are evidently not independent. More precisely, provided that the SOEC operative conditions do not vary, the mass flow rates ratio is constant. Since at the SOEC anode some oxygen is routed away and since mass conservation, under steady-state conditions, can be expressed as the mass flow rate balance shown in Equation 3.4, the HE hot side mass flow rate 2 is always lower than the cold side mass flow rate 1.

$$\dot{m}_1 = \dot{m}_{SOEC} = \dot{m}_2 + \dot{m}_{O_2} \tag{3.4}$$

Depending on the operative conditions of the SOEC, the mixtures compositions and therefore the amount of oxygen routed away change and so does the ratio K_M between the hot side and cold side mass flow rates. Having fixed the SOEC nominal working point, Table III, and derived the corresponding mixtures compositions, Table IV and Table V, it is possible to work out a numerical value for this ratio, whose importance is crucial for the heat exchanger design.

Each side total mass flow rate, Equation 3.5, because of mass conservation law, is trivially the sum of the individual mixture components mass flow rates.

$$\dot{m}_{tot} = \sum_{i=1}^{N} \dot{m}_i = \sum_{i=1}^{N} M_i \cdot \dot{V}_i \tag{3.5}$$

Knowing both the cold and hot mass flow rates, it is straightforward to calculate the ratio K_M according to its definition shown in Equation 3.6.

$$K_M = \frac{\dot{m}_2}{\dot{m}_1} = 0.5042 \tag{3.6}$$

In conclusion, from a heat transfer standpoint the crucial information is that the hot side mass flow rate is approximately half of the one flowing through the cold side.

3.3 Mass Flow Rates

After having clarified and quantified the HE mass flow rates coupling, it is evident that only one information, precisely the cold side mass flow rate $\dot{m}_1$, needs to be specified as model input. Since co-electrolysis is an endothermic[1] process, this flow rate is directly proportional to the electrical power absorbed by the SOEC.

Remembering that HELMETH is an experimental project [1], it has been chosen to size the heat exchanger for a SOEC electrical input of 20 kWe[2]. The corresponding cold side mass flow rate of 3 g/s has been calculated scaling the values provided by *Giglio et al.* in [10] relative to the SOEC electrical power. Table VI reports the mass flow rates $\dot{m}_1$ and $\dot{m}_2$ actually selected for the subsequent heat exchanger design and sizing procedure. It is useful to remember once

---

[1]The term *endothermic*, in its most general meaning, describes a process that requires an external energy supply, in most cases, but not always, in the form of heat.

[2]A part from the experimental nature of HELMETH, another good reason to use a small geometric model is to limit the CFD computational requirements.

TABLE VI: HEAT EXCHANGER MASS FLOW RATES AND MASS FLOW RATES RATIO

$\dot{m}_1 \left[\frac{g}{s}\right]$	K_M [/]	$\dot{m}_2 \left[\frac{g}{s}\right]$
3.000	0.5042	1.513

more that, even if the actual plant (20 kWe) is smaller than the one simulated on *Aspen Plus* (150 kWe), the compositions previously derived do not change.

Finally, it is noteworthy to mention that changing the mass flow rates defined in Table VI does not imply a complete HE re-design. In fact, it is sufficient to rescale the frontal area, and particularly the free-flow area, to accommodate a larger flow rate.

CHAPTER 4

FLUIDS THERMO-PHYSICAL PROPERTIES

4.1 Definition

Thermo-physical properties include all those properties, function of temperature, pressure and composition, that affect heat transfer and storage. As solid mechanical properties are necessary for a sound structural design, so the knowledge of thermo-physical fluid properties is essential for an effective heat exchanger thermal design. Excluding density, most properties, while strongly depending on temperature T, are only weakly influenced by moderate pressures p. This, along with the difficulty in gathering experimental data at high pressures, is the reason why most analytical correlations available in literature take into account only temperature induced property variations. Experimental data retrieved from the NIST Chemistry WebBook [42] and produced by the *Material Measurement Laboratory* have confirmed that the thermo-physical properties sensitivity to pressure is minimal. In the models used hereafter pressure induced effects will therefore be neglected, unless specified otherwise.

The following thermo-physical properties of interest for the heat exchanger design will be analyzed:

- Density $\boldsymbol{\rho}$ $\left[\frac{kg}{m^3}\right]$: mass per unit of material volume.
- Constant pressure specific heat $\boldsymbol{c_p}$ $\left[\frac{J}{kg \cdot K}\right]$: amount of heat per unit of mass required to raise the temperature by one degree Celsius at constant pressure.

- Constant volume specific heat $\boldsymbol{c_v}$ $\left[\frac{J}{kg \cdot K}\right]$: amount of heat per unit of mass required to raise the temperature by one degree Celsius at constant volume.
- Heat capacity ratio or adiabatic index $\boldsymbol{\gamma}$ [/]: dimensionless ratio of constant pressure specific heat c_p to constant volume specific heat c_v.

$$\gamma = \frac{c_p}{c_v} \tag{4.1}$$

- Specific enthalpy $\boldsymbol{h}$ $\left[\frac{J}{kg}\right]$: sum of the specific internal energy u and of the product of pressure and specific volume v of the system.

$$h = u + p \cdot v = u + \frac{p}{\rho} \tag{4.2}$$

- Thermal conductivity $\boldsymbol{\lambda}$ $\left[\frac{W}{m \cdot K}\right]$: ability of a material to conduct heat.
- Thermal diffusivity $\boldsymbol{\alpha}$ $\left[\frac{m^2}{s}\right]$: ability of a material to conduct thermal energy relative to its ability to store it.

$$\alpha = \frac{\lambda}{\rho \cdot c_p} \tag{4.3}$$

- Dynamic viscosity $\boldsymbol{\mu}$ $[Pa \cdot s]$: measure of the force needed to overcome internal friction in a fluid. Non-SI units of measure, notably the *Poise* ($1P = 0.1\ Pa \cdot s$) are usually preferred.

- Kinematic viscosity or momentum diffusivity $\boldsymbol{\mu}$ $\left[\frac{m^2}{s}\right]$: ratio of dynamic viscosity to density. Again, non-SI units of measure, notably the *Stoke* $\left(1St = 10^{-4}\ \frac{m^2}{s}\right)$ are usually preferred.

$$\nu = \frac{\mu}{\rho} \tag{4.4}$$

- Prandtl number $\boldsymbol{Pr}$ [/]: dimensionless quantity defined as the ratio of momentum diffusivity to thermal diffusivity.

$$\mathrm{Pr} = \frac{\nu}{\alpha} = \frac{c_p \cdot \mu}{\lambda} \tag{4.5}$$

As highlighted by Bruce E. Poling et al. in [43], while, for the sake's of accuracy, it would be desirable to characterize every material experimentally, because of time and cost requirements the designer is often forced to estimate the required material properties. Experimental data are particularly scarce for multicomponent mixtures, due to the countless number of possible different components combinations. Kinetic Molecular Theory (KMT), born at the beginning of the nineteenth century and experimentally validated during the twentieth century, is today the standard method used to estimate thermo-physical properties. KMT is precisely the approach adopted hereafter.

Among the five gaseous species composing the mixtures, whose compositions have been defined in Table IV and Table V, flowing through the heat exchanger, only water H_2O is liquid

at atmospheric pressure. In the change of state from liquid to vapor, water thermo-physical properties vary substantially. Due to this difference in the behavior of water with respect to the other mixture components, it has been decided to evaluate water properties an approach alternative to KMT. In fact, water properties, as result of extensive experimental campaigns, are very well-known and accessible through the renowned *Mollier's Diagram*. Entering this chart with two state variables, in most cases pressure p and temperature T, allows to derive all the remaining thermo-physical and thermodynamic properties for both liquid water and steam. A virtual MATLAB version of the *Mollier's Diagram* known as *XSteam*, written by Magnus Holmgren [44] and compliant with IAPWS IF-97 standard, will be systematically used to retrieve steam properties.

The approach used to derive mixture properties is interpolative, meaning that it requires the knowledge of all the individual component properties. Therefore, these will be addressed first and only in a second moment the properties of each multicomponent gaseous mixture will be assessed.

4.2 Individual Mixtures Components Properties

4.2.1 Density

As previously hinted at, density is the only property that is strongly pressure dependent. Since under the operative conditions of the heat exchanger compressibility factor Z of the gaseous species above listed is almost unitary [43], it is not worth using real gas models. The simpler ideal gas equation of state, Equation 4.6, derived experimentally by E. Clapeyron (1834) and microscopically using KMT by R. Clausius (1857), will be used to calculate the density ρ as

TABLE VII: MIXTURES COMPONENTS MOLAR MASSES AND ELASTIC CONSTANTS

	H_2O	CO_2	CO	H_2	CH_4
M $\left[\frac{g}{mol}\right]$	18.0153	44.0095	28.0101	2.01588	16.0425
R $\left[\frac{J}{K \cdot mol}\right]$	461.52	188.92	296.83	4124.48	518.27

a function of temperature T and pressure p, as shown in Equation 4.7. It is worth remembering that the specific volume v, because of its definition as a volume per unit of mass, is trivially the density ρ reciprocal.

$$p \cdot v = R \cdot T \tag{4.6}$$

$$\rho = \frac{p}{R \cdot T} \tag{4.7}$$

The quantity R, first used in Equation 4.6 and computed according to Equation 4.8, is the elastic gas constant, which is defined as the ratio of the universal gas constant ($R_u = 8,314.46\left[\frac{J}{K \cdot kmol}\right]$) to the molar mass M of the chemical specie. Table VII reports the molar masses and the elastic constants for every mixtures component.

$$R = \frac{R_u}{M} \tag{4.8}$$

TABLE VIII: MIXTURES COMPONENTS SHOMATE COEFFICIENTS

	CO_2	CO	CH_4	H_2
A	24.99735	25.56759	-0.703029	33.066178
B	55.18696	6.096130	108.4773	-11.363417
C	-33.69137	4.054656	-42.52157	11.432816
D	7.948387	-2.671301	5.862788	-2.772874
E	-0.136638	0.131021	0.678565	-0.158558
F	-403.6075	-118.0089	-76.84376	-9.980797
H	-393.5224	-110.5271	- 74.87310	0.0

It is worth remembering that the ideal gas equation is not valid for water vapor. Steam density will therefore be retrieved using the *Mollier's diagram*.

4.2.2 Constant pressure specific heat

Over time, the scientific community has developed several models to calculate the constant pressure specific heat c_p [42; 45; 46]. After having numerically verified that these fits yield at coherent results, it has been decided to adopt the model proposed by NIST [47] and shown in Equation 4.9.

$$c_p = A + B \cdot t + C \cdot t^2 + D \cdot t^3 + \frac{E}{t^2} \tag{4.9}$$

In this equation the parameter t is simply an absolute temperature normalized by a factor thousand, i.e. $t = {}^{T}/_{1000}$, while the literal factors A to E, known as Shomate coefficients, have been taken from [47]. The numerical values for each mixture component are shown in Table VIII.

It is important to remember that these coefficients are referred to the atmospheric temperature. However, the results obtained at higher pressures are accurate within 10 % because of the weak influence of pressure on the constant pressure specific heat c_p.

Again, the absence of data for water in Table VIII is related to the choice of using the more precise *Mollier's Diagram*.

4.2.3 Specific enthalpy

Considering a generic fluid, specific enthalpy can be expressed trough Equation 4.10 [48]. Introducing the volumetric expansion coefficient β, defined in Equation 4.12, Equation 4.10 is equivalent to Equation 4.11. Both equations describe the enthalpy dependence on temperature and pressure in terms of variations from a reference condition $(h, T, p)_{ref}$.

$$h = h_{T_{ref}} + \int_{T_{ref}}^{T} c_p \, dT + \int_{p_{ref}}^{p} \frac{1}{\rho} \cdot \left[1 + \frac{T}{\rho} \cdot \left(\frac{\partial \rho}{\partial T}\right)_p\right] dp \tag{4.10}$$

$$h = h_{T_{ref}} + \int_{T_{ref}}^{T} c_p \, dT + \int_{p_{ref}}^{p} \frac{1 - \beta \cdot T}{\rho} \, dp \tag{4.11}$$

$$\beta = \frac{1}{v} \cdot \left(\frac{\partial v}{\partial T}\right)_p = -\frac{1}{\rho} \cdot \left(\frac{\partial \rho}{\partial T}\right)_p \tag{4.12}$$

Considering the volumetric expansion coefficient β definition and remembering the initial hypothesis of validity of the ideal gas law, Equation 4.6, Equation 4.10 and Equation 4.11 can be simplified, because of the pressure dependent term going to zero, yielding at Equation 4.13.

It is interesting to notice that neglecting the pressure effects and modeling the fluid as an ideal gas produce exactly the same results.

$$h - h_{T_{ref}} = \int_{T_{ref}}^{T} c_p \, dT \tag{4.13}$$

Substituting the expression for the constant pressure specific heat previously derived, Equation 4.9, into Equation 4.13, yields at Equation 4.14, where the variable t has the same meaning as before [47]. Since this equation provides only specific enthalpy variations, in order to obtain an absolute quantity it is convenient to define a nil enthalpic value at the reference temperature of 298.15 K. The final expression for specific enthalpy calculation is therefore Equation 4.15.

$$h - h_{298K} = A \cdot t + B \cdot t^2 + C \cdot t^3 + D \cdot t^4 - \frac{E}{t} + F - H \tag{4.14}$$

$$h = A \cdot t + B \cdot t^2 + C \cdot t^3 + D \cdot t^4 - \frac{E}{t} + F - H \tag{4.15}$$

4.2.4 Dynamic viscosity

Kinetic Molecular Theory (KMT), allowing to explain the gas macroscopic properties starting from the submicroscopic particles random motion, is the theoretical foundation for any temperature-dependent viscosity model. Viscosity and thermal conductivity, because they cannot be measured in conditions of thermodynamic equilibrium and are intrinsically defined in non-equilibrium situations, i.e. momentum or heat transfer, are remarkable examples of transport properties.

Chapman and Enskog theory (1917) [49], building on simpler models based on elementary kinetic theory, improves viscosity estimates by taking into account the effects of intermolecular forces. Even though the model assumptions would restrict its applicability field to mono-atomic gases at low pressures and high temperatures, i.e. to ideal gases, this model yields at satisfactory results even when used with polyatomic gases [43].

Equation 4.16 is the first-order Chapman-Enskog viscosity equation, where M is the molar mass of the gas, σ is the average collision diameter and $\Omega_v(T^*)$ is the temperature-dependent collision integral.

$$\eta = \frac{26.69 \cdot \sqrt{M \cdot T}}{\sigma^2 \cdot \Omega_v} \tag{4.16}$$

T^* is a dimensionless temperature which depends on the intermolecular potential chosen. Considering the most frequently used *12-6 Lennard-Jones* potential [50], T^* is defined in Equation 4.17, where k is Boltzmanns constant and ε is the pair-potential energy minimum. *Lennard-Jones* coefficients for every mixture component, excepted water, are collected in Table IX.

$$T^* = \frac{k \cdot T}{\varepsilon} \tag{4.17}$$

In 1972, Neufeld proposed a new expression, Equation 4.18, for the calculation of the collision integral $\Omega_v(T^*)$. Based on the coefficients shown in Table X, this equation has been selected because it allows an easy computer implementation of the viscosity model.

TABLE IX: MIXTURES COMPONENTS LENNARD-JONES COEFFICIENTS

	CO_2	CO	H_2	CH_4
σ	3.941	3.690	2.827	3.758
$\frac{\varepsilon}{k}$	195.2	91.7	59.7	148.6

TABLE X: NEUFELD COEFFICIENTS

A	B	C	D	E	F
1.16145	0.14874	0.52487	0.77320	2.16178	2.43787

$$\Omega_v(T^*) = A(T^*)^{-B} + C \cdot e^{-D(T^*)} + E \cdot e^{-F(T^*)} \tag{4.18}$$

4.2.5 Thermal conductivity

Gaseous thermal conductivity, being a transport property as viscosity, can be derived using Kinetic Molecular Theory (KMT). Eucken extended existing models to polyatomic gases by decoupling the contributions due to translational and internal degrees of freedom [43]. This resulted in Equation 4.19, whose left-member is traditionally referred to as *Eucken factor*.

$$\frac{\lambda \cdot M}{\eta \cdot c_v} = 1 + \frac{9/4}{c_v/R} \tag{4.19}$$

Combining Equation 4.19 with the previous definition of viscosity, Equation 4.16, it is possible to derive Equation 4.20, a final expression for the calculation of thermal conductivity as a function of temperature.

$$\lambda = \left[0.115 + 0.354 \cdot \frac{c_p}{R}\right] \cdot \frac{0.08322}{\sigma^2 \cdot \Omega_v(T^*)} \cdot \sqrt{\frac{T}{M}} \tag{4.20}$$

4.3 Mixtures Properties

Mixture 1, whose precise composition in terms of molar and mass fractions is shown in Table IV, is a binary mixture of water H_2O and carbon dioxide CO_2. Mixture 2, whose composition is detailed in Table V, is instead a quinary mixture of water H_2O, carbon dioxide CO_2, carbon monoxide CO, hydrogen H_2 and methane CH_4.

As anticipated, an interpolative approach requiring the knowledge of the individual components properties will be used to derive the multicomponent mixtures thermo-physical properties.

4.3.1 Density

The density ρ of a mixture is calculated through Equation 4.21, which can be derived by simply reminding the definition of density and molar fraction y.

$$\rho_{mix} = \sum_{i=1}^{N} y_i \cdot \rho_i \tag{4.21}$$

Figure 18 shows a non-linear density reduction with temperature for both mixtures. Since the individual component densities are calculated using the linear idea gas law Equation 4.6, the non-linearity is clearly introduced by the coexistence of more components.

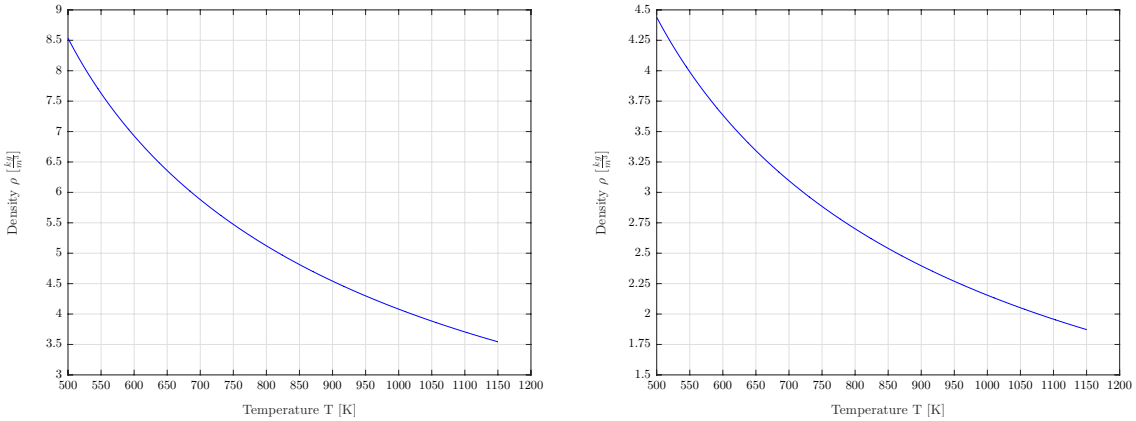

(a) Mixture 1 (b) Mixture 2

Figure 18: Mixtures density ρ as a function of temperature

4.3.2 Constant pressure specific heat

The constant pressure specific heat c_p of a mixture is computed using Equation 4.22, basically a weighted average of individual components c_p against their mass fractions x_i.

$$c_{p,mix} = \sum_{i=1}^{N} x_i \cdot c_{p,i} \tag{4.22}$$

The constant pressure specific heat minimum around 650 K shown in Figure 19 for both mixtures is likely to be due to the presence of water. In fact, since liquid water has a much higher constant pressure specific heat than steam, moving away from saturated liquid conditions, i.e. increasing the temperature above the saturation limit for a pressure of 15 bar ($T_{sat} = 471.45\ K$), determines a decrement in the c_p. However, this effect is counterbalanced by the monotonic

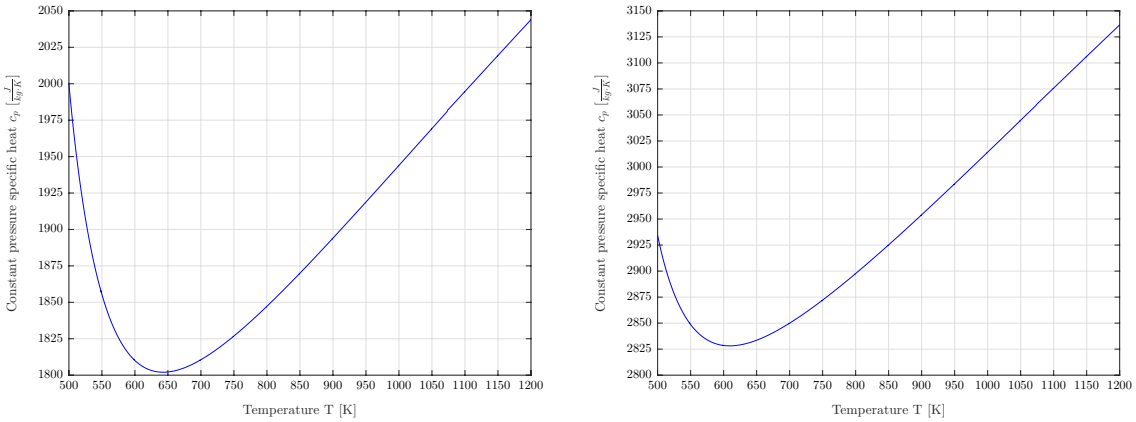

(a) Mixture 1 (b) Mixture 2

Figure 19: Mixtures constant pressure specific heat c_p as a function of temperature

c_p increment with temperature explained by Equation 4.9. The combination of these opposite trends accounts for the presence of the minimums in Figure 19.

From a numerical standpoint, it is interesting to highlight that mixture 2 has a constant pressure specific heat which is almost 50 % higher than the one of mixture 1, no matter the temperature. The reason lies in the fact that the second mixture is very rich in hydrogen, whose c_p is extremely high. It is almost worthless to precise how this disparity in terms of constant pressure specific heats has profound implications in terms of heat transfer capability and therefore of heat exchanger performances.

4.3.3 Heat capacity ratio

Remembering the initial hypothesis of ideal gas and extending it to the mixtures, the heat capacity ratio γ, also known as adiabatic index, is calculated in Equation 4.23 based on its

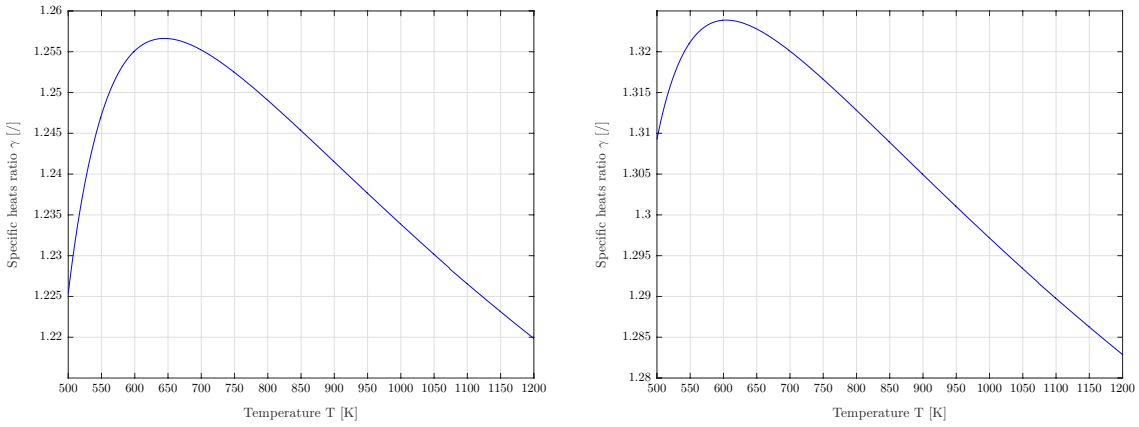

(a) Mixture 1 (b) Mixture 2

Figure 20: Mixtures specific heats ratio γ as a function of temperature

definition as the ratio of constant pressure c_p and constant volume c_v specific heats. Due to Mayer's equation ($R = c_p - c_v$), γ can only assume values higher than one.

$$\gamma_{mix} = \frac{c_p}{c_v} = \frac{c_p}{c_p - R} \tag{4.23}$$

The mixture elastic constant R can be computed by Equation 4.8 using as M the mixture molar mass calculated according to Equation 4.24.

$$M_{mix} = \sum_{i=1}^{N} y_i \cdot M_i \tag{4.24}$$

The adiabatic indexes behavior represented in Figure 20 is coherent with the constant pressure specific heat trend. In fact, where c_p is minimum, γ is maximum, as analytically

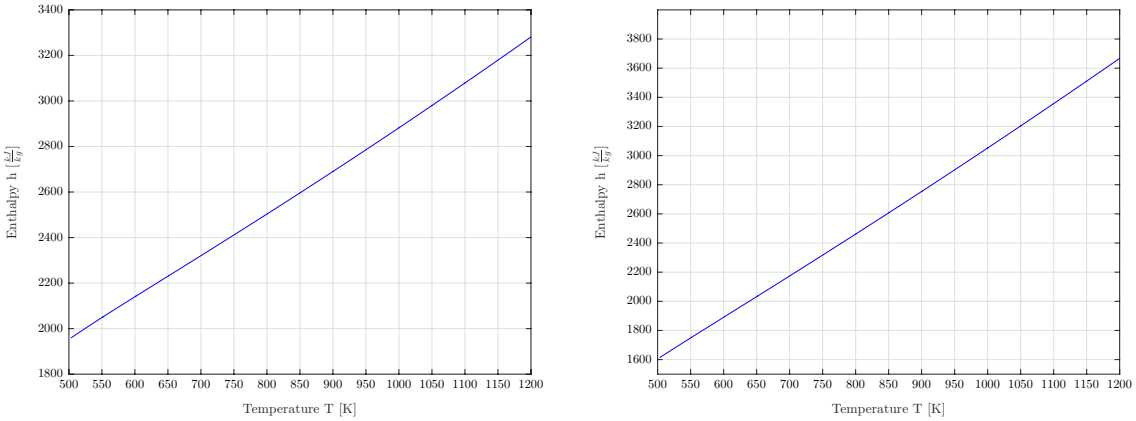

(a) Mixture 1 (b) Mixture 2

Figure 21: Mixtures enthalpy h as a function of temperature

suggested by Equation 4.23. In spite of the apparently sharp shape of Figure 20, the numerical value of the adiabatic indexes is almost constant over a wide range of temperatures, with relative variations lower than 4 % for both mixtures.

4.3.4 Specific enthalpy

The specific enthalpy h of a mixture is computed using Equation 4.25, basically a weighted average of individual components h_i against their mass fractions x_i.

$$h_{mix} = \sum_{i=1}^{N} x_i \cdot h_i \tag{4.25}$$

Even though Figure 21 seems to suggest a linear increment of specific enthalpy with temperature, in reality the behavior is non linear. In fact, since h has been defined as the the integral over temperature of the c_p and considering the non-linear c_p behavior shown in Figure 19, the

slope of the curve should not be constant. As a matter of fact, zooming the original MATLAB plot it is possible to spot the non-linearity, which is barely visible in Figure 21 because of the c_p reduced variations.

4.3.5 Viscosity

4.3.5.1 Dynamic viscosity

The dynamic viscosity of a mixture could be derived using an interpolative approach extending the Chapman and Enskog viscosity model [49]. However, this approach is very complicated and not worth for this application. In fact, good viscosity estimations can be obtained even using simplified approaches, such as Wilke's equation (1950), shown in Equation 4.26, which, neglecting second-order effects, drastically reduces the computational load [43].

$$\mu_{mix} = \sum_{i=1}^{N} \frac{\mu_i}{1 + \sum\limits_{\substack{k=1 \\ k \neq i}}^{N} \left(\frac{y_j}{y_i}\right) \cdot \Phi_{ij}} \tag{4.26}$$

The interaction factor Φ_{ij}, defined in Equation 4.27, allows to take into account the mutual interactions between two of the N mixture components, defined by the subscripts i and j respectively.

$$\Phi_{ij} = \frac{\left[1 + \left(\frac{\mu_i}{\mu_j}\right)^{0.25} \cdot \left(\frac{M_j}{M_i}\right)^{0.25}\right]^2}{\sqrt{8 \cdot \left(1 + \frac{M_i}{M_j}\right)}} \tag{4.27}$$

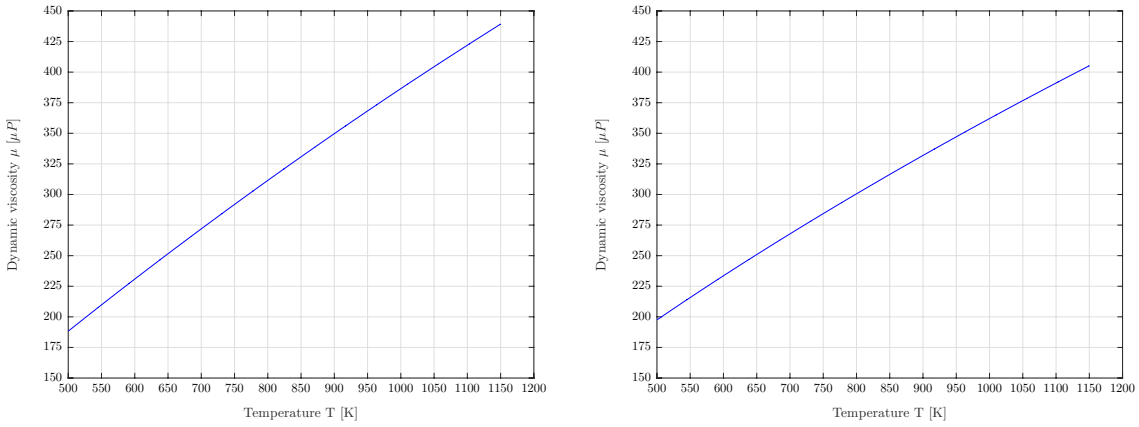

(a) Mixture 1 (b) Mixture 2

Figure 22: Mixtures dynamic viscosity μ as a function of temperature

As it is possible to appreciate in Figure 22, dynamic viscosity μ increment with temperature is substantially linear for both mixtures. Also, viscosities numerical values are similar for mixtures 1 and 2.

4.3.5.2 Kinematic viscosity

Kinematic viscosity ν, defined in Equation 4.4 as an index of momentum diffusivity, is plotted in Figure 23 for both mixtures. ν monotonically increases with temperature, but not as linearly as the dynamic viscosity μ because of non linear behavior of density ρ. Moreover, always because of density effects, mixture 2 is about three times more viscous than mixture 1.

4.3.6 Thermal conductivity

The thermal conductivity λ of a mixture is calculated according to Mason and Saxena (1958) Equation 4.28 using an approach similar to the one used for viscosity [43]. It is noteworthy

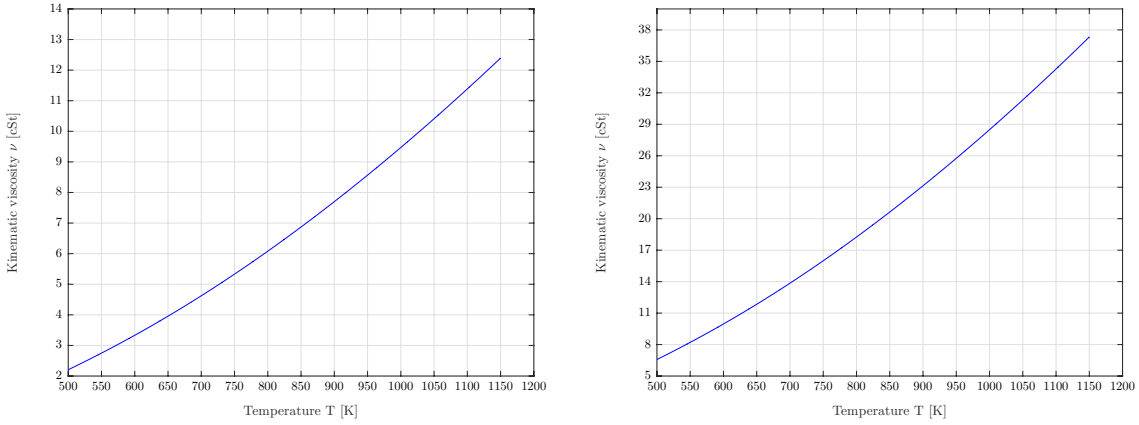

(a) Mixture 1 (b) Mixture 2

Figure 23: Mixtures kinematic viscosity ν as a function of temperature

to highlight that exactly the same interaction factors Φ_{ij}, introduced for and dependent on viscosity, are required to derive the thermal conductivity. This confirms that both quantities, respectively related to momentum and heat transfer, in quality of transport properties can be modeled in similar ways.

$$\lambda = \sum_{i=1}^{N} \frac{\lambda_i}{1 + \sum\limits_{\substack{k=1 \\ k \neq i}}^{N} \left(1.065 \cdot \frac{X_j}{X_i}\right) \cdot \Phi_{ij}} \tag{4.28}$$

The plots in Figure 24 suggest that thermal conductivity λ increases quasi-linearly with temperature for both mixtures. As for kinematic viscosity, mixture 2 thermal conductivity is about twice as big as the one of mixture 1.

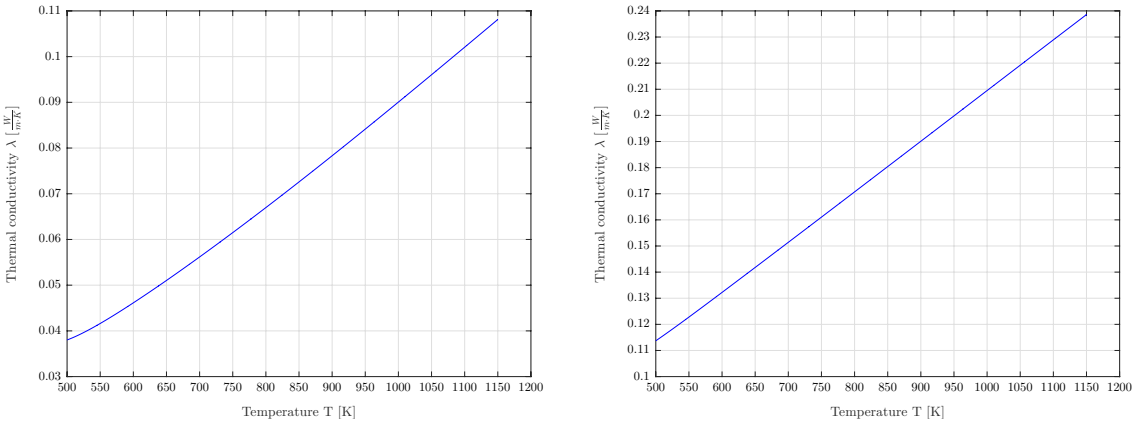

(a) Mixture 1 (b) Mixture 2

Figure 24: Mixtures thermal conductivity λ as a function of temperature

4.3.7 Prandtl number

Prandtl number has been introduced as a dimensionless quantity describing the fluid capability of transmitting momentum (kinematic viscosity ν) relative to heat (thermal diffusivity α). Low Prandtl numbers are associated with thick velocity boundary layers and thin thermal boundary layers; vice-versa for high Pr values.

With the constant pressure specific heat c_p, the dynamic viscosity μ and the thermal conductivity λ finally available for each mixture, Prandtl number can be easily calculated according to its definition, Equation 4.5.

The two mixtures temperature sensitivity is completely different. In fact, while for mixture 1, as shown in Figure 25 (a), the Prandtl number steadily decreases with temperature, mixture 2, plotted in Figure 25 (b), has a point of minimum around 600 K. However, in spite of the

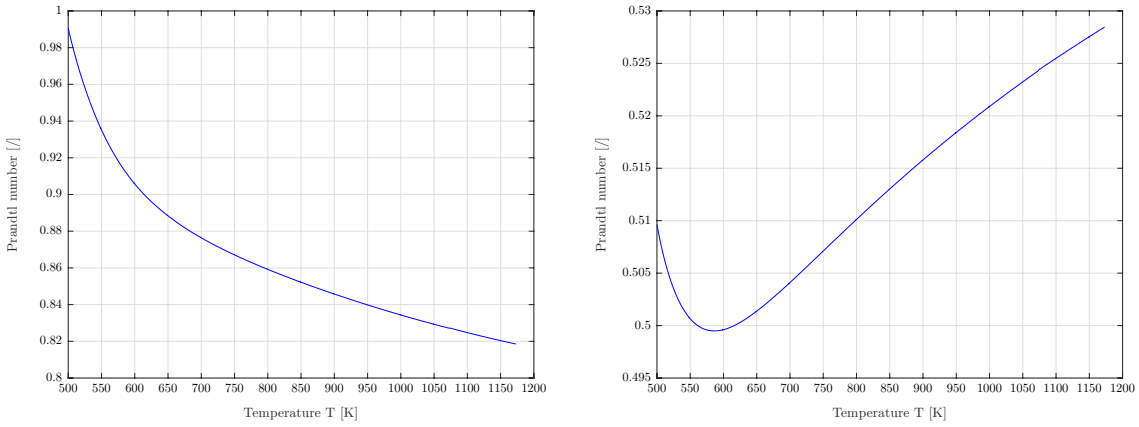

(a) Mixture 1 (b) Mixture 2

Figure 25: Mixtures Prandtl number Pr as a function of temperature

apparently sharp Pr curve for mixture 2, the numerical value is almost constant over a wide range of temperatures,with relative variations lower than 5 %. As a final remark, it is important to highlight that for both mixtures Prandtl number is always lower than one. This behavior is typical of many gaseous systems and implies that heat is transferred more effectively than momentum.

CHAPTER 5

INPUT DATA FOR HEAT EXCHANGER DESIGN

5.1 Cold Mixture Inlet Temperature

As shown in Table IV, the mixture flowing through the cold side of the heat exchanger is a binary mixture of water vapor H_2O and carbon dioxide CO_2. These two components need to be mixed before entering the heat exchanger. Hereafter mixture 1 inlet temperature will be derived assuming an isenthalpic mixing.

5.1.1 Water inlet temperature

Water saturation temperature at a pressure of 15 bar amounts to 198.30 $°C$ [44]. The processes of liquid water compression, heating and vaporization, even if relevant from a plant thermal integration standpoint, are not of direct interest for the heat exchanger design. Therefore, the water inlet temperature of 198.30 $°C$ will be regarded as an exogenous variable.

5.1.2 Carbon dioxide inlet temperature

In order to derive the carbon dioxide inlet temperature, a simple gas compression model featuring a two-stage polytropic compressive process without intercooling has been implemented. Considering commercial machines, at least 2 compression stages are required to reach the operative pressure of 15 bar. Intercooling aims at reducing the required mechanical work by cooling down the fluid after each compression, so to approach the most energy-efficient scenario of an isothermal compression [51]. Considering the specificity of this application, where the ultimate

TABLE XI: CARBON DIOXIDE COMPRESSION PROCESS

$p_{in}[bar]$	$p_{fin}[bar]$	$\beta[/]$	$\eta_y[/]$	$\gamma_{CO_2}[/]$	$T_{in}[K]$	$T_{fin}[K]$
1.0	15.0	15.0	0.80	1.294	293.15	632.56

aim of a heat exchanger is increasing mixture 1 temperature as much as possible, it is not convenient to introduce additional components such as intercoolers. In fact, if it is unquestionable that with such a set-up the compression work is higher, it is also true that the greater energetic expense, directly contributing to the cold fluid heating, is not wasted.

Table XI gathers the data related to the carbon dioxide compression process. The adiabatic index γ is the carbon dioxide average value over the range of temperature $20 \div 500\ ^{\circ}C$. Without referring to any actual datasheet, considering that usual polytropic efficiencies η_y fall in the range $70 \div 85$ %, the compressor polytropic efficiency has been estimated to be 80 %. The total compression ratio, defined in Equation 5.1 as the final to initial pressure ratio, has been equally split between the two compression stages, Equation 5.2, as this is the configuration that minimizes the external mechanical work [51].

$$\beta_{tot} = \frac{p_{fin}}{p_{in}} \tag{5.1}$$

$$\beta_1 = \beta_2 = \sqrt{\beta_{tot}} \tag{5.2}$$

Starting from the polytropic equation[1], Equation 5.4 [51], where m is the polytropic index[2], it is possible to derive the ratio between the final and the initial temperature for each compression stage, as shown in Equation 5.5

$$T \cdot p^{\frac{1-m}{m}} = const \tag{5.4}$$

$$\frac{T_{fin}}{T_{in}} = \beta^z \tag{5.5}$$

where the factor z is defined as:

$$z = \frac{\gamma - 1}{\gamma} \cdot \frac{1}{\eta_{pol}} \tag{5.6}$$

Remembering that there are two compression stages, the carbon dioxide final temperature at a pressure of 15 bar can be calculated according to Equation 5.7 and is equal to 359.4 $°C$.

$$T_{CO_2,fin} = T_{CO_2,in} \cdot (\beta^z)^2 = T_{CO_2,in} \cdot (\beta_{tot})^z \tag{5.7}$$

---

[1]T denotes an absolute temperature measured in degree Kelvin

[2]For a compressor, the polytropic index m is related to the adiabatic index γ through the polytropic efficiency η_y by Equation 5.3

$$\eta_y = \frac{m}{m-1} \cdot \frac{\gamma - 1}{\gamma} \tag{5.3}$$

5.1.3 Isenthalpic mixing process

With both water H_2O and carbon dioxide CO_2 at the same pressure of 15 bar, these two components can be blended in a proportion such to obtain exactly the composition defined in Table IV. However, since H_2O and CO_2 have different inlet temperatures, the final temperature after mixing is still unknown and has to be derived by applying the *First Law of Thermodynamics* (FLT), which in its most general expression reads as Equation 5.8.

$$\underbrace{q}_{1} - \overbrace{W_t}^{2} = \underbrace{\frac{d}{dt}\Big(U + E_c + E_p + p_0 \cdot V\Big)_{VC}}_{3} + \overbrace{\sum_{k=1}^{NC} \dot{m}_k \cdot (h + e_c + e_p)_k}^{4} \tag{5.8}$$

Within Equation 5.8 it is possible to recognize the 4 following main terms:

1. Thermal power exchanged with the environment.
2. Mechanical power exchanged with the environment.
3. Internal, kinetic, potential and deformation energy variations in the control volume due to transients.
4. Enthalpy, kinetic and potential energy variations due to mass transport trough the NC fluid ports of the open system.

Considering a specific thermodynamic system, the FLT can be greatly simplified. Since at this stage of design the main interest lies in the steady state behavior, the transient term can be neglected thus zeroing the third term in Equation 5.8. The mixer is then supposed to be adiabatic, meaning that no heat is lost toward the external environment ($q = 0$). This is

naturally an approximation, but a well designed insulation allows to minimize these losses and validate the hypothesis of adiabatic system. Moreover, since in a mixer there is no production of mechanical power, because of the absence of moving parts like blades of turbines, the corresponding contribution W_t is also nil.

Because of the reduced dimensions of this device, regardless of its orientation, i.e. horizontal or vertical, the specific gravitational potential energy variations e_p are orders of magnitude lower than specific enthalpy variations h. A similar line of thought, remembering that under laminar flow regime the order of magnitude for velocity is units of meters per second, leads to neglect also the specific kinetic energy variations e_k.

Based on the above hypothesis, Equation 5.8 reduces to the much simpler Equation 5.9, which is basically an enthalpic balance.

$$0 \approx \sum_{k=1}^{NC} \dot{m}_k \cdot h_k \tag{5.9}$$

Specifying Equation 5.9 for the binary mixture of water and carbon dioxide, remembering that under steady state conditions mass fractions x_i can be equivalently defined as ratio of masses m or mass flow rates $\dot{m}_i$ as shown in Equation 5.13, it is straightforward to derive an explicit expression for the cold mixture enthalpy Equation 5.12. In Equation 5.10 incoming mass flow rates, according to thermodynamic conventions, have been considered negative while outgoing ones positive.

$$\dot{m}_1 \cdot h_1 - \dot{m}_{H_2O} \cdot h_{H_2O} - \dot{m}_{CO_2} \cdot h_{CO_2} \tag{5.10}$$

$$\dot{m}_1 \cdot h_1 = \dot{m}_{H_2O} \cdot h_{H_2O} + \dot{m}_{CO_2} \cdot h_{CO_2} \tag{5.11}$$

$$h_1 = x_{H_2O} \cdot h_{H_2O} + x_{CO_2} \cdot h_{CO_2} \tag{5.12}$$

$$x_i = \frac{m_i}{m_{tot}} \equiv \frac{\dot{m}_i}{\dot{m}_{tot}} \tag{5.13}$$

According to the *Gibb's Phase Rule*[1], the number of state variables necessary and sufficient to fully determine the thermodynamic state of a binary gaseous mixture is three. One of them being the composition, knowing two other quantities, such as pressure p and specific enthalpy h, it is possible to derive every remaining state variable. In particular, the following iterative procedure allows to numerically define the mixture temperature at the isenthalpic mixing process conclusion:

1. Make a reasonable guess for the solution temperature T_{trial}.

2. Calculate the mixture enthalpy at that temperature $h(T_{trial})$.

---

[1]For non-reactive multi-component heterogeneous systems in thermodynamic equilibrium, the number of thermodynamic degrees of freedom F is related to the number of components C and to the number of phases P according to Equation 5.14 [14]

$$F = C - P + 2 \tag{5.14}$$

3. Calculate the enthalpy absolute and relative errors ε_a and ε_r as:

$$\varepsilon_a = h - h_{trial} \tag{5.15}$$

$$\varepsilon_r = \frac{\varepsilon_a}{h} \tag{5.16}$$

4. Compare the relative error ε_r with the tolerance t, a measure of the relative accuracy of the result. If this is lower than the tolerance, then the iterative procedure is over. If not, the next step, in order to guarantee the converge of the iterative procedure, depends on the sign of the relative error:

   - If the error is positive, the initial temperature guess was too low and must be incremented of a factor dT before beginning a new iterative step.
   - If it is negative, the initial guess was too high and must be decremented of the same factor dT.

Decreasing the correction factor dT enough, the accuracy of the result can be as high as desired. However, because of the uncertainties associated to the enthalpic model described by Equation 4.11, from a physical standpoint it is completely meaningless to use too much of a strict tolerance t. In conclusion, the implementation of this iterative procedure on MATLAB with an accepted relative error of 0.5 % returns a temperature of 230.35 $°C$.

TABLE XII: HEAT EXCHANGER NOMINAL INLET TEMPERATURES AND PRESSURES

$T_{1,in}[^\circ C]$	$T_{2,in}[^\circ C]$	$p_{1,in}[bar]$	$p_{2,in}[bar]$
230.35	850	15.0	≈ 15.0

5.2 Heat Exchanger Inlet Pressures and Temperatures

Table XII summarizes the inlet temperatures and pressures for both the heat exchanger sides. The cold side mixture, as a result of the isenthalpic mixing process above described, enters the HE at a temperature of about 230 $^\circ C$. The hot side mixture, instead, flows in at the SOEC nominal operative temperature of 850 $^\circ C$.

Concerning the pressures, while the cold side inlet pressure is exactly 15 bar, the hot side inlet pressure is for sure lower because of the pressure drops in the heat exchanger and in the SOEC. As a matter of fact, a pressure difference is always required to generate a flow and this explains why, in real fluid devices, pressure losses are unavoidable. However, since the pressure drops in both the HE and in the SOEC are expected to be small with respect to the absolute pressure, their effect on fluid properties can be neglected. In conclusion, even the hot side inlet pressure will be considered equal to 15 bar.

CHAPTER 6

HEAT EXCHANGER LIMIT PERFORMANCE

6.1 Simulation Accuracy as Design Tool

Simulation is the imitation of the operation of a real-world process or system over time (J. Banks et al., 2001) [52; 53]. Simulation implies the set-up of a model that allows to describe and represents the behavior of a real system. Because of the consolidated trend featuring a steady increment in the computational power per unit of cost, computer simulations have become a widely used instrument for the mathematical modeling of many systems. However, due to the number of hypothesis underlying a virtual model, the validity and accuracy of a simulation are continuously questioned, as highlighted by Sargent (2011):

> Simulation models are increasingly being used to solve problems and to aid in decision-making. The developers and users of these models, the decision makers using information obtained from the results of these models, and the individuals affected by decisions based on such models are all rightly concerned with whether a model and its results are "correct". ([54; 55])

The only way to trust the results of a simulation is to verify and validate the underlying model. While verification is a process aimed at confirming that the virtual model is correctly implemented with respect to the conceptual model, validation assesses the accuracy of the model's representation of the real system [54; 55].

These general considerations about simulation apply even to the specific case of heat exchanger design. If it is undoubtedly true that only prototyping the device and physically testing it can definitively validate a design obtained trough simulation, it is also true that there are several verification and validation steps that can consolidate a design credibility.

1. Taking the two fluid domains as separate control volumes, by applying the *First Law of Thermodynamics* (FLT) it is straightforward to compute the HE limit outlet temperatures. This information, which relies on the universally valid physical principle of energy conservation, can be absolutely trusted and used as a benchmark to validate the following, more complicate models results. It is in fact trivial to understand that if a simulation suggests a cold side outlet temperature higher than the limit one derived by applying the FLT, there must be an error in the simulation set-up.

2. Using several different models and comparing the results also helps to validate a simulation result. For this reason, even if the final heat exchanger design will be obtained using Computational Fluid Dynamics (CFD) tools, a simpler model relying on the by-now consolidated $\varepsilon - NTU$ method will also be implemented. In fact, the importance of the geometrical design obtained applying this latter method is two-fold. First, it helps creating the geometrical model used within the first CFD simulation. Second, it serves as benchmark for the thermodynamic results and the HE performances obtained by CFD tools.

3. Considering a CFD model, it is possible to indirectly validate the simulation results by:

(a) Check that the physical principles of mass and energy conservation are respected from a numerical standpoint.

(b) Perform a mesh refinement study (MRS), to prove the physical results independence from the computational grid.

4. Compare the simulation set-up and results with similar studies existing in the scientific literature.

After having clarified how the issue of simulations accuracy will be managed toward the final aim of obtaining a credible heat exchanger design, in the following of this chapter the HE outlet limit temperatures will be derived by applying the FLT.

6.2 Heat Exchanger Limit Outlet Temperatures

6.2.1 Energy conservation

As previously hinted at, in order to determine the HE outlet temperatures it is necessary to apply the *First Law of Thermodynamics*, reported in its most general form in Equation 6.1, to each individual fluid domain.

$$\underbrace{q}_{1} - \overbrace{W_t}^{2} = \underbrace{\frac{d}{dt}\Big(U + E_c + E_p + p_0 \cdot V\Big)_{VC}}_{3} + \overbrace{\sum_{k=1}^{NC} \dot{m}_k \cdot (h + e_c + e_p)_k}^{4} \tag{6.1}$$

While designing a heat exchanger from scratch, the main target is transferring the required amount of heat among the two fluids. In other words, what really matters is the device stationary behavior and, consequently, the transient terms labeled by number 3 can be neglected.

With arguments similar to the ones used while analyzing the mixer, it is possible to conclude that the specific potential e_p and kinetic e_k energies are negligible with respect to the specific enthalpy h. The heat exchanger will be treated as perfectly adiabatic: heat is not dispersed toward the surrounding environment but only transferred from the hot to the cold fluid trough the solid, conductive wall. The thermal power q has therefore opposite signs and the same module considering the two fluid control volumes.

Based on these considerations, Equation 6.1 can be simplified to Equation 6.2, which is the reference equation used for the determination of the HE outlet temperatures.

$$q \approx \sum_{k=1}^{NC} \dot{m}_k \cdot h_k \tag{6.2}$$

Specifying Equation 6.2 for the cold and hot fluid domains yields respectively at Equation 6.3 and Equation 6.4. Knowing the HE heat duty q, the outlet enthalpy h_{out} derivation follows straightforwardly from Equation 6.5 and Equation 6.6.

$$q = \dot{m}_1 \cdot h_{1,out} - \dot{m}_1 \cdot h_{1,in} \tag{6.3}$$

$$-q = \dot{m}_2 \cdot h_{2,out} - \dot{m}_2 \cdot h_{2,in} \tag{6.4}$$

$$h_{1,out} = h_{1,in} + \frac{q}{\dot{m}_1} \tag{6.5}$$

$$h_{2,out} = h_{2,in} - \frac{q}{\dot{m}_2} \tag{6.6}$$

As previously noted, for gaseous binary mixtures the knowledge of two thermodynamic variables beyond the mixture composition, such as pressure p and specific enthalpy h, allows to derive whatever other state variable and in particular the temperature T. The same iterative procedure used in Chapter 5 can be then exploited to determine the HE outlet temperatures, once that the heat duty and consequently the outlet enthalpies are available.

6.2.2 Heat exchanger effectiveness ε definition

When dealing with heat exchangers, it is usual to introduce a quantity known as effectiveness ε and defined in Equation 6.7 as the ratio between the actual heat transfer q and the maximum thermodynamically allowed heat transfer q_{max}.

$$\varepsilon = \frac{q}{q_{max}} \tag{6.7}$$

As the HE performance is benchmarked directly with the thermodynamic limit, the value of the effectiveness ε is absolute and independent from the specific heat exchanger design. In order to reach a unitary effectiveness, a heat exchanger needs to have an infinite heat transfer area, which implies an infinite size and an infinite weight. In practice, real heat exchanger effectiveness is always lower than 1.

The maximum heat transfer, defined in Equation 6.8, is physically bounded by the fluid having the lower heat capacity rate $C_{min} = (\dot{m} \cdot c_p)_{min}$. In fact, was it the other way around, the fluid with the lower heat capacity rate would not have been able to absorb or release the thermal power required by the other fluid. The inlet temperature difference ITD, whose

mathematical definition is provided in Equation 6.9, is simply the difference between the hot and cold inlet temperatures.

$$q_{max} = C_{min} \cdot ITD \tag{6.8}$$

$$ITD = T_{hot,in} - T_{cold,in} = T_{2,in} - T1_{1in} \tag{6.9}$$

6.2.3 Fluid limiting the heat transfer

It is worth proving analytically which is the fluid side limiting the heat transfer. The mass flow rates ratio, derived in Chapter 3, is such to suggest that the limiting fluid is the hot one. However, to confirm this guess, it is necessary to calculate also the constant pressure specific heats ratio. This way, the individual heat capacity rates as well as the heat capacity rates ratio C^* can be calculated according to Equation 6.10 and Equation 6.11 respectively.

$$C = \dot{m} \cdot c_p \tag{6.10}$$

$$C^* = \frac{C_{min}}{C_{max}} \tag{6.11}$$

By now, it is plain that for any assigned heat exchanger effectiveness, it is possible to calculate in sequence the corresponding heat duty q, the individual side outlet temperatures and consequently the respective mean temperatures. It is important to highlight that calculating

the mean temperature taking the arithmetical mean as shown in Equation 6.12 is an approximation, because in reality heat is not transferred linearly along the heat exchanger length. Even calculating a mean temperature weighted over the fluid volume is conceptually misleading, because of temperature induced density variations. The mean temperature should instead be computed weighting the temperature field over the fluid mass distribution. However, since these last two definitions are of no practical use during the design phase, the mean temperatures will be approximated using Equation 6.12 and the constant pressure specific heats c_p will be evaluated at such temperatures.

$$T_m = \frac{T_{in} + T_{out}}{2} \tag{6.12}$$

Figure 26 graphically proves that the ratio between hot and cold constant pressure specific heat is monotonically decreasing with the effectiveness ε but always bigger than one. Moreover, the numerical variability is so small to be negligible: the c_p ratio can be safely considered constant and equal to 1.6.

With such an information available and remembering that the hot side mass flow rate is about half of the cold one, it follows a heat capacity rates ratio approximately equal to 0.8. This value confirms the initial assumption that the hot side is the one limiting the heat transfer.

Figure 27, representing the heat capacity rates ratio C^* as a function of ε and practically obtained by scaling Figure 26 relative to the mass flow rates ratio, shows that, in spite of the monotonically decreasing trend, C^* oscillates around the previously estimated value of 0.8.

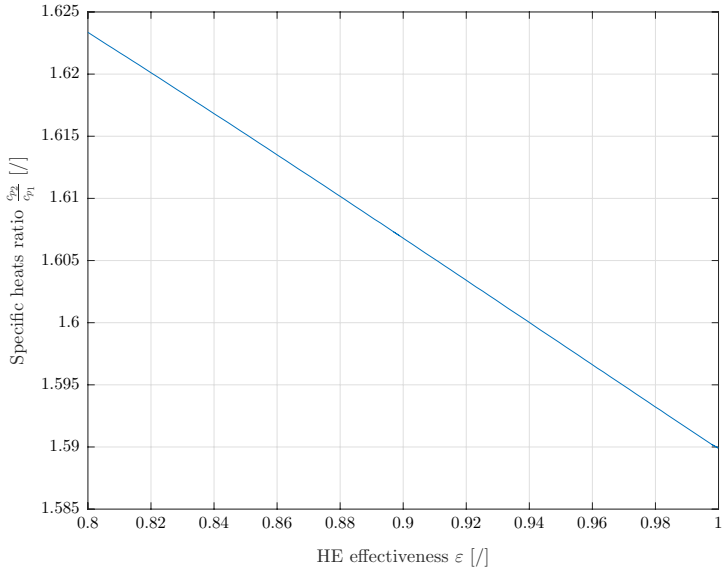

Figure 26: Constant pressure specific heats ratio $\left(\frac{c_{p_2}}{c_{p_1}}\right)$ as a function of the HE effectiveness ε

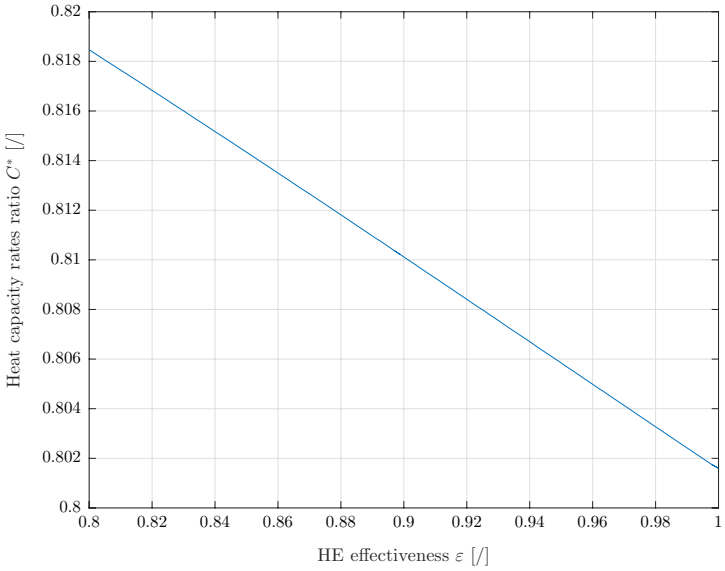

Figure 27: Heat capacity rates ratio C^* as a function of HE effectiveness ε

This plot numerically confirms that, whatever the HE effectiveness, the limiting side is always the hot one.

6.2.4 Outlet temperatures as a function of ε

Because of the dependence of the thermal power q on the HE effectiveness ε expressed in Equation 6.13, by solving Equation 6.4 and Equation 6.6 for temperature it is possible to directly plot the outlet temperatures as a function of the heat exchanger effectiveness.

$$q = q_{max} \cdot \varepsilon \tag{6.13}$$

Since both the minimum heat capacity rate C_{min} and the ITD are constant, the maximum possible heat transfer rate q_{max} is constant as well, which means that the temperature versus effectiveness plot should be linear. Figure 28 (a) confirms the expected linear behavior, while Figure 28 (b) focuses on the region where ε is higher than 90 %, as these are the target values for a high-performance HE.

These plots are useful to rapidly gain an understanding of the system performance, by:

- Determining the heat exchanger effectiveness ε corresponding to the desired cold side outlet temperature.
- Finding the actual heat exchanger effectiveness ε given an outlet temperature.
- Assessing the accuracy of simulations by checking that the outlet temperature for cold and hot side are coherent one with each other, i.e. by verifying energy conservation law.

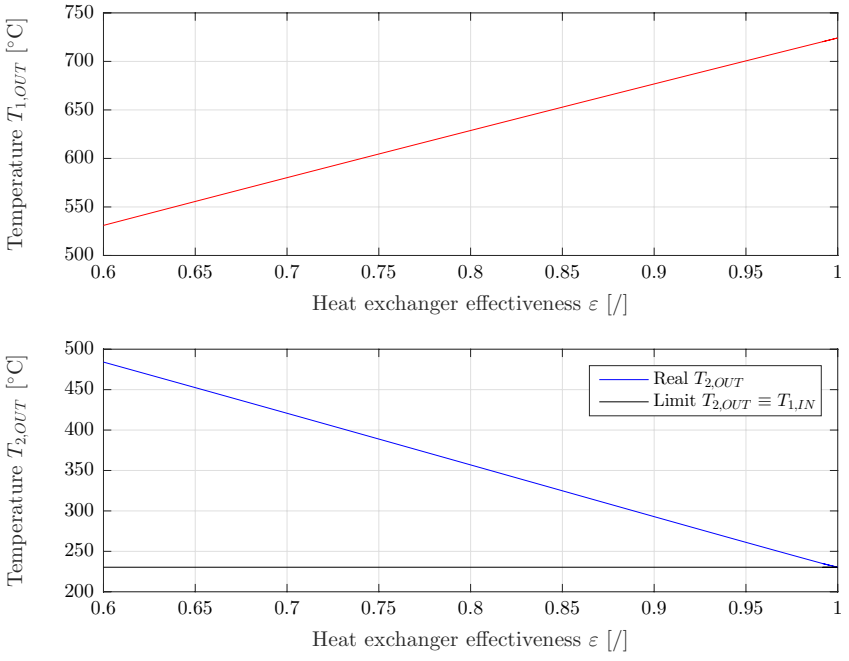

(a) Overview: $0.60 \leq \varepsilon \leq 1.00$

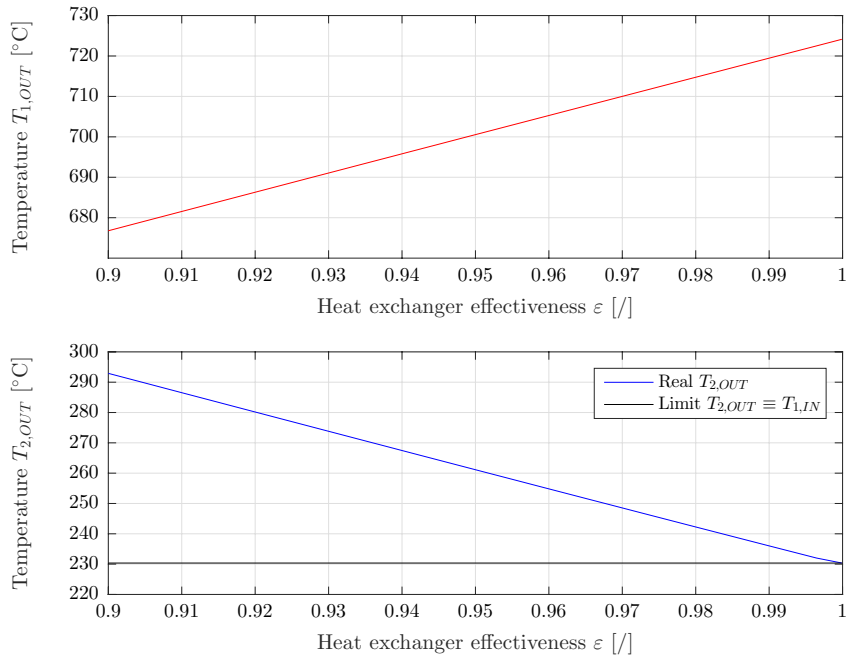

(b) Detail: $0.90 \leq \varepsilon \leq 1.00$

Figure 28: HE outlet temperatures as a function of the effectiveness ε

TABLE XIII: HEAT EXCHANGER LIMIT OUTLET TEMPERATURES

ε [/]	$T_{1,OUT}$ [°C]	$T_{2,OUT}$ [°C]
1.0	724.17	230.35

- Finding out graphically the maximum thermodynamically allowed cold side outlet temperature $T_{1,out,lim}$

6.2.5 Outlet temperatures absolute limit

Imposing a unitary heat exchanger effectiveness in Equation 6.13, it is possible to analytically derive the maximum thermodynamically allowed cold side outlet temperature.

Since the hot side is the limiting side, it is expected that with a unitary effectiveness ε its outlet temperature $T_{2,out}$ coincides with the inlet temperature of the cold side $T_{1,in}$. Table XIII precisely validates the hypothesis about the hot side and indicates a temperature of 724.17 °C as maximum possible cold side outlet temperature.

Exactly the same result can be read graphically in Figure 28 (b), thus confirming the coherence between graphical and analytical approaches.

CHAPTER 7

HEAT EXCHANGER REFERENCE DESIGN SELECTION

As clarified in Chapter 1, the object of design of this thesis is a high temperature heat exchanger in the context of a P2G plant. Before venturing any further in the choice of the suitable HE constructive typology and configuration, it is worth providing a precise definition of such a thermal device.

A widely accepted *heat exchanger* (HE) definition reads as a device used to transfer thermal energy between two or more fluids at different temperatures and in thermal contact [56; 57]. HE are applied in a limitless variety of industries, including automotive, energy, aerospace, electronic, food and chemical. In the United States alone, the heat exchangers industry is worth several USD billions and, worldwide, there are hundreds of companies engaged in the manufacture of a wide array of heat exchangers [57].

Before tackling the proper HE design and sizing, this chapter aims at identifying the heat exchanger reference design, in terms of construction type, flow configuration and fin geometry, that best suits the needs of a P2G plant.

7.1 Heat Exchangers Classification

Due to the huge number of existing designs and to the many variables involved, selecting an optimal typology of heat exchanger can be as challenging as designing it. Important factors to be taken into account while choosing a HE include:

- Minimum and maximum operative pressures
- Pressure drops
- Thermal performance
- Minimum and maximum working temperature
- Constructive materials

Needless to say, the only way to select the most suitable heat exchanger typology among the countless existing designs is by comparing the design requirements with the features of each HE constructive type. Considering the specific application field of a co-electrolysis P2G plant, the technical specifications for the heat exchanger serving the SOEC can be summarized as:

1. Capacity to maintain cold and hot gaseous mixtures separated.
2. Extreme thermal performance, motivated by the required 500 $^{\circ}C$ temperature increment on the cold side and by the fact that gases have very low heat transfer coefficients.
3. Resistance to temperatures higher than 850 $^{\circ}C$.
4. Capacity to withstand moderate pressures, up to 30 bar.
5. Compactness.

Considering the HE classification criteria proposed by Shah in [57], a heat exchanger meeting these technical requirements can be classified as a/an:

- **Two-fluids HE**: there are only two mixtures involved in the heat transfer process.

- **Indirect contact HE**: the cold and the hot fluids remain unmixed.
- **Direct transfer HE** or **recuperator**: energy is continuously transferred from the hot to the cold domain rather than being stored and released through the heat exchanger matrix as it happens in regenerators.
- **Convective single-phase HE**: the fluids remain gaseous during the whole heat transfer process. Since there is no phase transition, such a device is also referred to as *sensible* HE. Most of the heat transfer can be explained through convective mechanisms, with radiation playing only a marginal role.
- **Compact HE** (CHE): the heat transfer surface area density β is higher than 700 $^{m^2}/_{m^3}$.

This preliminary classification allows to substantially reduce the pool of suitable heat exchanger designs. In the following section, after a brief overview of the most commonly used HE typologies, a reference heat exchanger construction is selected for later use during the HE proper sizing activity.

7.2 Heat Exchanger Reference Construction

In terms of construction type, recuperators can be broadly subdivided into the four following families [57; 58; 59; 60]:

1. Shell & Tube, Figure 29 (a)
2. Plates, Figure 29 (b) [61]
3. Extended surface

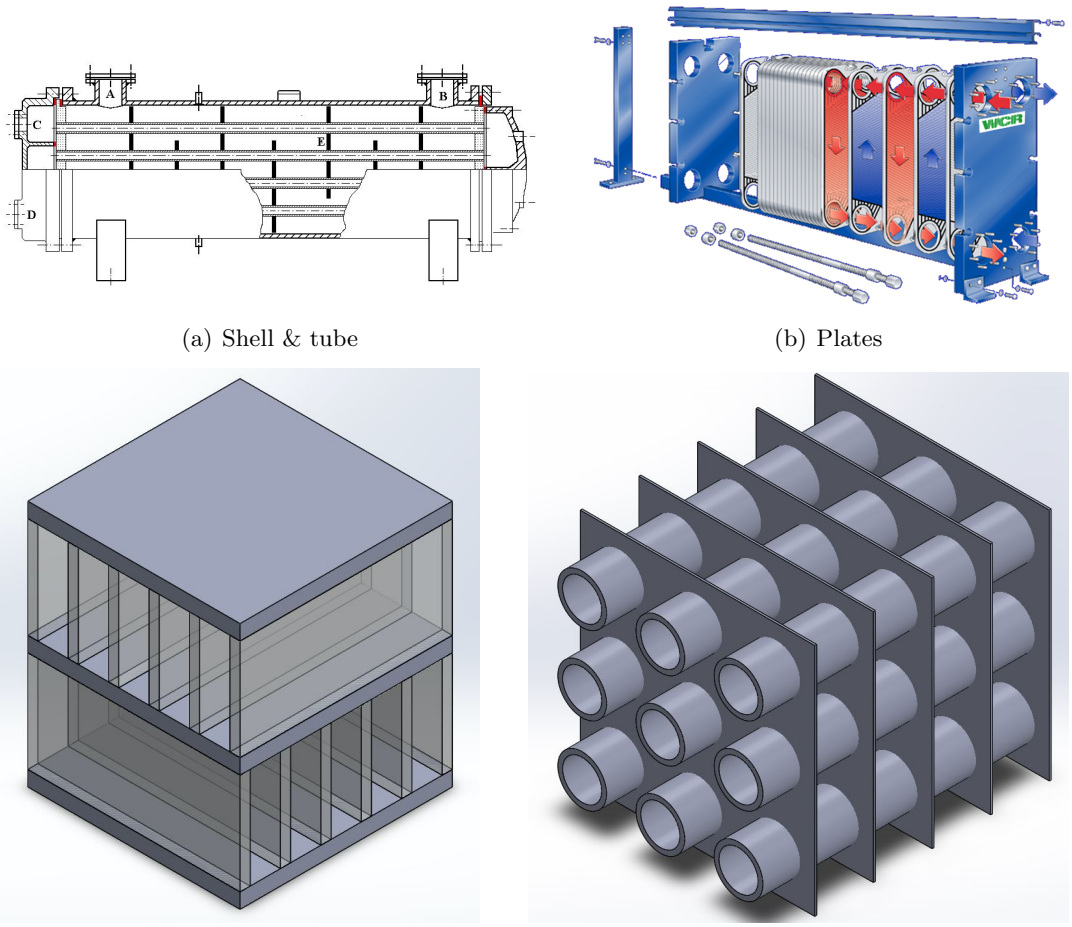

(a) Shell & tube

(b) Plates

(c) Plate-fins

(d) Tube-fins

Figure 29: Main heat exchangers constructive types

(a) Plate-fins, Figure 29 (c)

(b) Tube-fins, Figure 29 (d)

It is worth highlighting that, after decades of experimentations and HE design, for each of the four families graphically represented in Figure 29 it exists a variety of different configura-

tions, optimized for particular applications. As previously explained, the selection of a specific construction is the result of a comparison between the design specifications and the peculiar features of each HE typology.

Shell & Tube heat exchangers, widely used for industrial applications, consist of a large pressure vessel, called *shell*, with a bundle of tubes inside it. This geometry allows to withstand very high pressures and is easily serviceable. However, this class of HE, beyond not being suitable for AM, features a very low compactness index β, which makes it inadequate for the application object of analysis.

"Plate heat exchangers (PHE) use metal plates to transfer heat between two fluids [and, thanks to their much] larger surface area" [62], have an higher compactness index than a shell & tube design. Unfortunately, because of the reduced thickness of each plate, this family of HE is not appropriate for pressurized applications and is therefore unsuitable as reference layout for a 15 bar HE.

Extended surface heat exchangers name is indicative of their high heat transfer area, the result of the addition of fins attached to the heat exchanger primary surface. As a consequence, the compactness index β is much higher than for shell & tube and PHE, as shown in Figure 30 [57]. Beyond increasing the HE total heat transfer area, fins also allow to enhance the heat transfer coefficient h and, ultimately, the transferred thermal power.

Plate-fin (PFHE) and tube-fin (TFHE) geometries are the two most common types of extended surface heat exchangers [57; 63]. From a geometrical standpoint, as evidenced by Figure 31 [64; 65], "plate-fin heat exchangers consist of finned chambers separated by flat plates

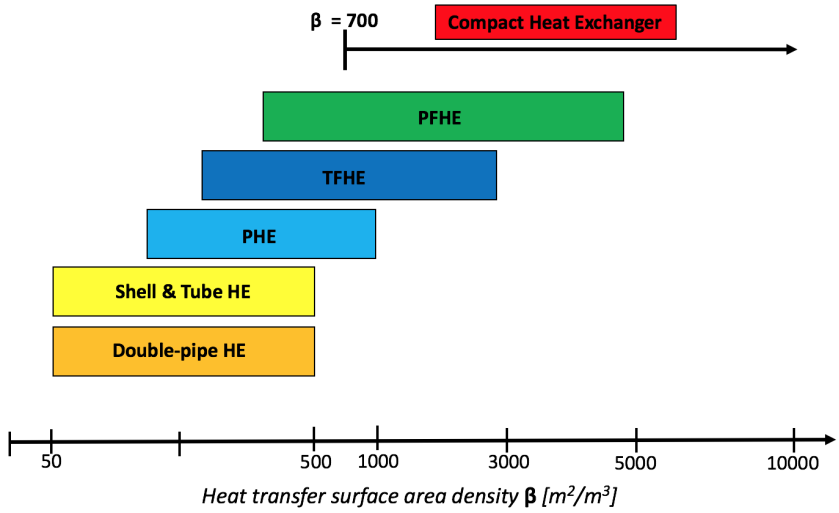

Figure 30: Surface area density β for various heat exchanger designs

and route fluids through alternating hot and cold passages" [64]. Heat is sequentially transferred from the hot side fins to the separator plate and finally, trough another array of fins, reaches the cold side. In a tube-fins heat exchanger, fins are generally arranged on the tubes outside, but they may be used on the inner surface as well in order to balance the two side thermal resistances and improve the heat exchanger effectiveness [57].

PFHE surface area density β, which can be as high as 5000 $^{m^2}/_{m^3}$, is almost twice the one reachable using a TFHE design [57]. Another remarkable quality of PFHE relative to TFHE is the unlimited flexibility in terms of fin design, which allows to use different fins for each fluid side and to fit any particular envelope shape. Even though it already exists a variety of different fin geometries, notably plain, wavy, offset, perforated and louver fins, but, as a matter of fact, thanks to AM technology, it is possible to build even new and optimized fin shapes.

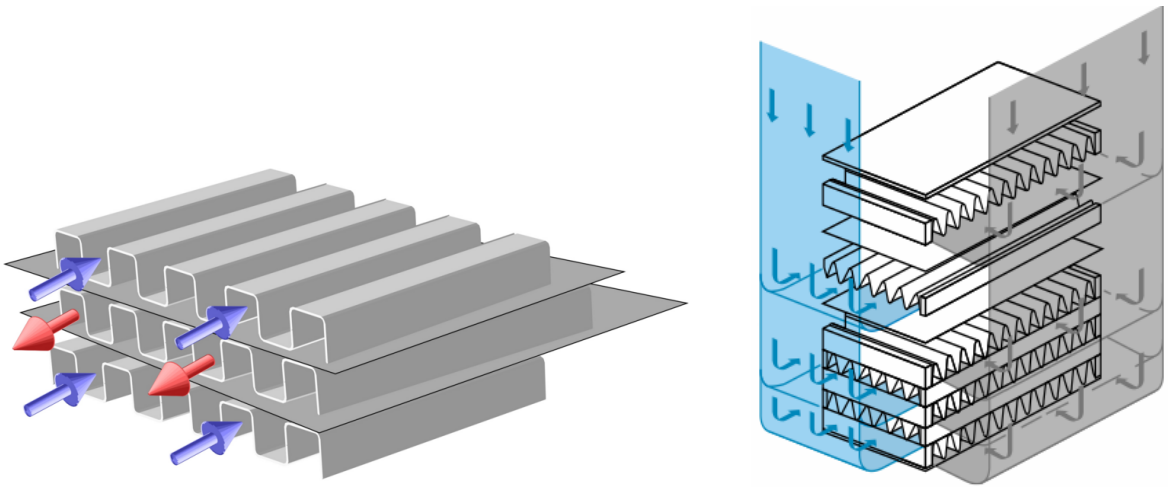

(a) Counter-flow (b) Cross-flow

Figure 31: Plate-fins heat exchanger configurations

In conclusion, because of its superior performances relative to the others HE typology, the plate-fins heat exchanger design will be selected as reference construction type. In the following section, the various PFHE flow configurations are first analyzed and then the most performing one is selected as reference configuration for later use during the HE proper sizing activity.

7.3 Heat Exchanger Reference Configuration

For a two-fluids PFHE, it exists the following 3 basic flow configurations [66], schematically represented in Figure 32:

1. **Parallel-flow**: fluids flow in the same direction
2. **Counter-flow**: fluid flow in opposite directions
3. **Cross-flow**: fluids flow orthogonally one to each other

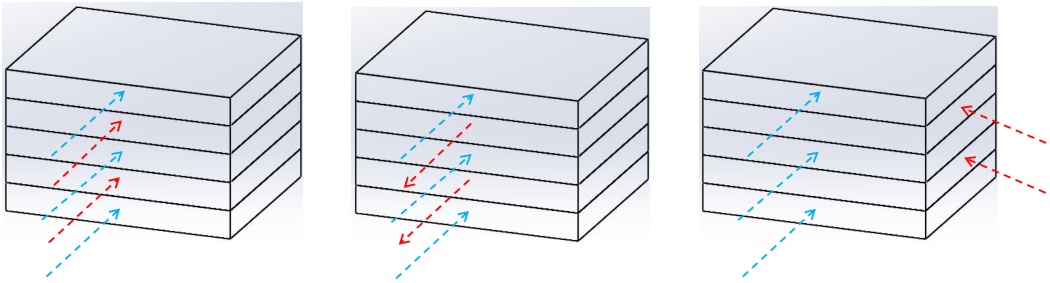

(a) Parallel-flow (b) Counter-flow (c) Cross-flow

Figure 32: Plate-fins heat exchanger configurations

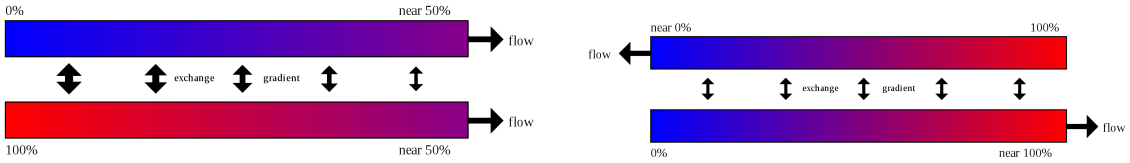

(a) Parallel-flow (b) Counter-flow

Figure 33: Hot-cold temperature difference along the heat exchanger length for different HE configurations

In order to meet the extremely high HE thermal requirements, it is necessary to select the most performing among these three flow configuration. Adopting a counter-flow configuration, the temperature difference between hot and cold fluids along the heat exchanger length is substantially more constant than using a parallel-flow configuration, which translates in a enhanced heat transfer. Hereafter, the renowned $\varepsilon - NTU$ method is introduced and used to justify this intuitive result, graphically represented in Figure 33.

7.3.1 $\varepsilon - NTU$ method

The $\varepsilon - NTU$ method for heat exchanger analysis, introduced by London and Seban in 1942 [63], today is probably the most widespread HE thermal design tool. The name of this method is indicative of two of the three main parameters used to evaluate heat exchanger performances. The effectiveness ε has already been introduced in Chapter 6 and defined in Equation 6.7. The acronym NTU stands for *Number of Transfer Units* and is defined in Equation 7.1 as the ratio between the overall thermal conductance UA and the smaller heat capacity rate C_{min}. NTU is clearly related to the effective heat transfer area A, which is in turn proportional to the HE overall dimensions. Because of this connection, $\varepsilon - NTU$ method has been successfully used to implement HE sizing procedures [57; 63]. The last parameter, not included in the method name, is the heat capacity rates ratio C^*, introduced in Chapter 6 and defined in Equation 6.11.

$$NTU = \frac{UA}{C_{min}} \tag{7.1}$$

In literature there is a wide array of available $\varepsilon - NTU$ correlations allowing to compare the performances of different HE [57; 66]. All of them are mathematical relations linking the effectiveness ε of a particular HE configuration to its NTU and, through C^*, to the fluid properties. Figure 34 3-D plot graphically represents the functional relationship expressed in Equation 7.2, highlighting how each of the three variables is a function of both the remaining two. In the following, 2-D plots will be preferred because they allow an easier understanding of the effect of each individual variable on the other two.

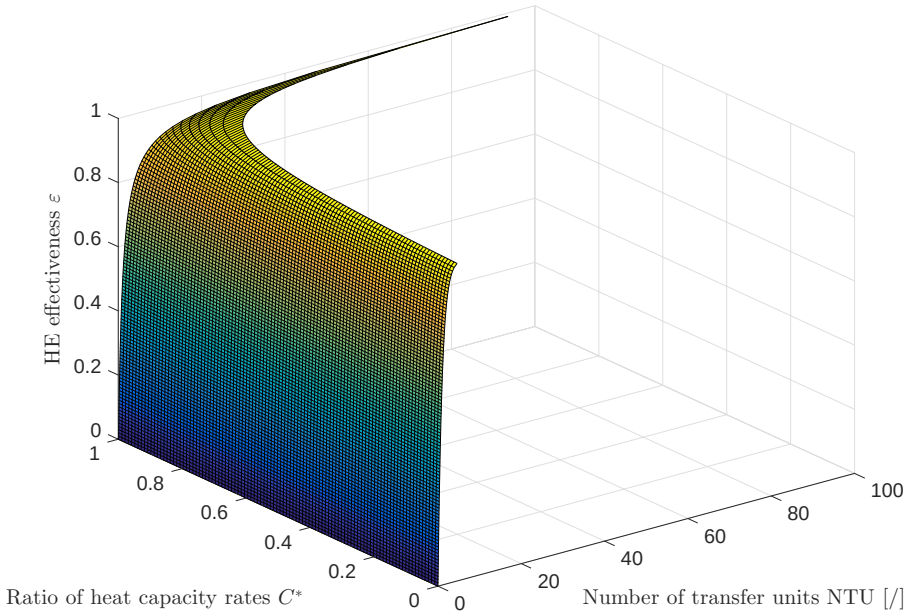

Figure 34: 3-D representation of $\varepsilon - NTU$ correlation for a counterflow PFHE

$$\varepsilon = f(HE\ configuration, NTU, C^*) \tag{7.2}$$

Figure 35 (a) shows the effect of the heat capacity rates ratio C^* on the $\varepsilon - NTU$ curves. The best results, i.e. high effectiveness with low NTU, corresponding to a high heat transfer in a reduced space, are achieved when C^* tends to zero. This situation happens when a fluid changes physical state, as its constant pressure specific heat c_p and consequently its heat capacity rate C tend to infinite. On the contrary, when two fluids have very similar heat capacity rates, the heat transfer area required to reach the target effectiveness increases exponentially.

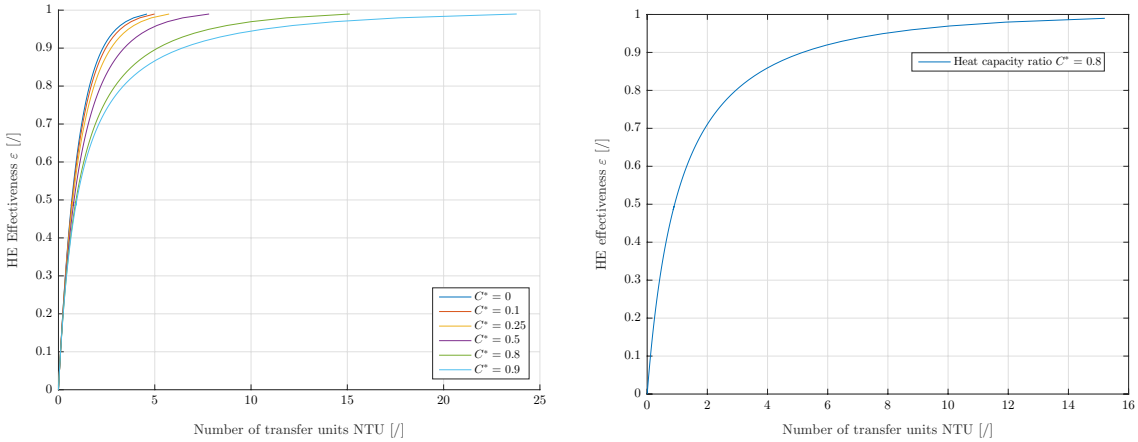

(a) For different heat capacity rates ratio C^* (b) For $C^* = 0.8$

Figure 35: HE effectiveness ε as a function of NTU

As derived in Chapter 6, the heat capacity rates ratio C^* for the heat exchanger object of design is approximately equal to 0.8. Considering the results of Figure 35 (a), it is evident that such a value of C^* does not help toward the HE dimensions minimization, as confirmed by Figure 35 (b), which proves that NTU must be greater than 5 in order to reach effectivenesses higher than 90 %.

The $\varepsilon - NTU$ method introduced in this section will be hereafter used to analytically assess the thermal superiority of the counter-flow configuration relative to the parallel-flow and cross-flow configurations.

7.3.2 Effectiveness for different heat exchanger configurations

$\varepsilon - NTU$ correlations for parallel-flow, counter-flow and cross-flow HE are respectively shown in Equation 7.3, Equation 7.4 and Equation 7.5 [48; 57].

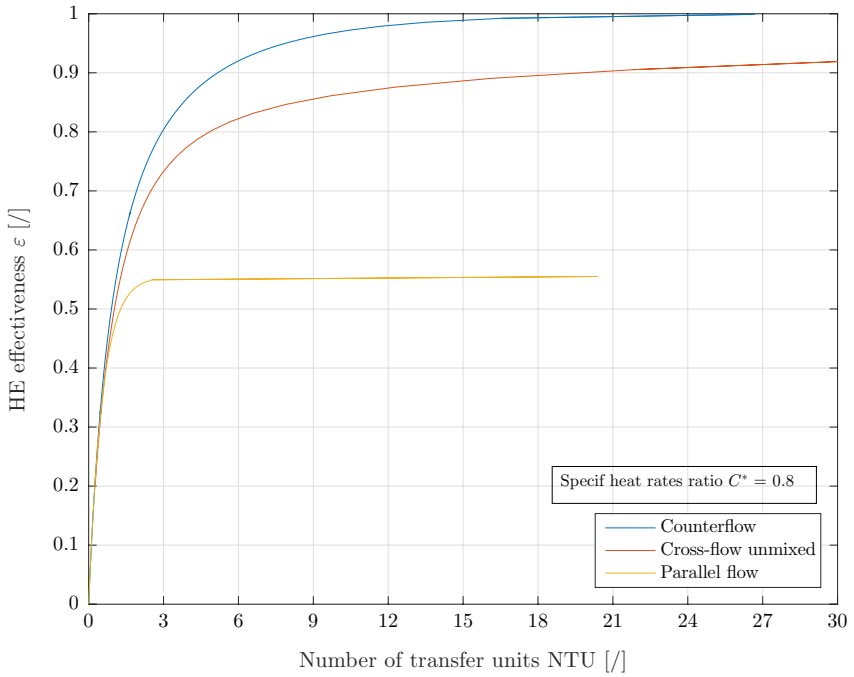

Figure 36: HE effectiveness ε as a function of NTU for different HE configurations

$$\varepsilon = \frac{1 - exp[-NTU \cdot (1 + C^*)]}{1 + C^*} \tag{7.3}$$

$$\varepsilon = \frac{1 - exp[-NTU \cdot (1 - C^*)]}{1 - C^* \; exp[-NTU \cdot (1 - C^*)]} \tag{7.4}$$

$$\varepsilon = 1 - exp\left[\frac{NTU^{0.22}}{C^*} \; exp\big[- C^* \cdot NTU^{0.78} - 1\big]\right] \tag{7.5}$$

Figure 36, obtained by plotting these equations parametrized with a heat capacity rates ratio C^* of 0.8, confirms the initial intuition that the counter-flow configuration is the most performing one. In fact, such a configuration yields at the highest possible effectiveness ε, very close to limit unitary value, while requiring the minimum heat transfer area A. Moreover, it allows to obtain very high effectiveness even when the heat capacity rates ratio C^* assumes unfavorable values such as 0.8.

Observing Figure 36, it is also evident that the parallel-flow configuration effectiveness is inherently bounded to a value which is function of the heat capacity rates ratio C^* through Equation 7.3. As a matter of fact, this flow configuration allows to achieve high HE effectivenesses only when the C^* is almost nil, i.e. when one of the fluid changes phase.

Finally, the cross-flow configuration performances are intermediate between the extreme cases of parallel and counter-flow. In fact, cross-flow heat exchangers allow to achieve effectiveness almost as high as for counter-flow HE, but requiring a substantially higher NTU, which corresponds to larger heat transfer areas A.

The main disadvantage associated with a counterflow configuration is the complexity of headers design, due to the fact that inlets and outlets are situated on the same geometrical surface. This is often the main reason behind the choice of a cross-flow configuration, whose thermal performance are still satisfactory and whose header design is substantially simpler. However, a cross-flow configuration is not sufficiently performing to meet the extremely high HE thermal requirements, which demands instead the selection of a counter-flow configuration.

7.4 Heat Exchanger Reference Fin Geometry

As anticipated in Chapter 6, even if the final heat exchanger design will be obtained using Computational Fluid Dynamics (CFD) tools, a simpler HE model relying on the by-now consolidated $\varepsilon - NTU$ method will also be implemented as a tool to compare the results and validate the CFD simulations.

A variety of fin geometries can be applied to the counter-flow plate-fin heat exchanger reference design above discussed. While the CFD tools described in Chapter 9 allow to freely simulate the effects of whatever fin shape, the $\varepsilon - NTU$ based analytical approach developed in Chapter 8 requires the selection of a more traditional fin geometry, whose behavior has already been experimentally assessed and for which correlations are available in literature. According to Shah (1985), it is possible to discern the following three main classes of fins [57], graphically represented in Figure 37 [65]:

1. Plain and straight
2. Plain but wavy
3. Interrupted

Remembering one more time the requirement of exceptional HE thermal performances, the first two basic layouts are immediately excluded, leaving room to the more performing designs belonging to the third category, notably perforated, louver and offset-strip fins. Because of their excellent performances and of the abundance of semi-empirical correlations in literature

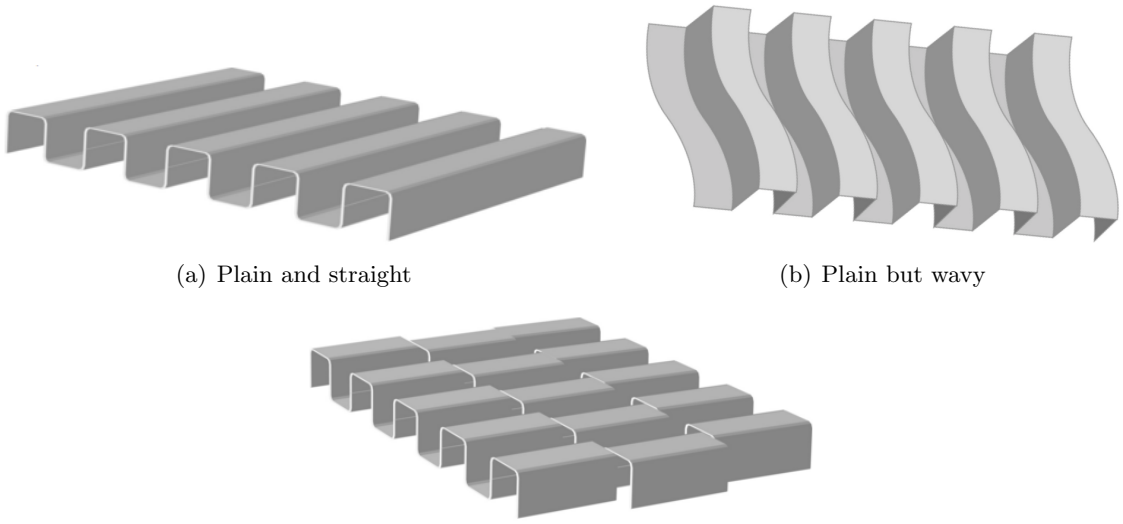

(a) Plain and straight

(b) Plain but wavy

(c) Interrupted

Figure 37: Main fin categories

[57; 67; 68; 69], offset-strip fins, also known as serrated fins and shown in Figure 37 (c), will be hereafter adopted as standard fin geometry.

In conclusion, an Inconel 718 counter-flow plate-fin heat exchanger is selected as reference design for the following HE sizing activity. Moreover, offset-strip fins will be the reference layout in Chapter 8, while fin geometry is willingly left unspecified for the CFD design tackled in Chapter 9, where new fin shapes will be designed and optimized.

CHAPTER 8

HEAT EXCHANGER PRELIMINARY SIZING

This chapter focuses on the development of an analytical, $\varepsilon - NTU$ based, heat exchanger sizing procedure and on the description of the results whereby produced. As explained in Chapter 6, the ultimate aim is the comparison of this model output with the results obtained by CFD tools in Chapter 9, so to prove the consistency and the validity of the heat exchanger definitive design.

8.1 Preliminary Concepts

In this section the general approach used to design the heat exchanger is clarified, followed by the definition of the sizing procedure inputs and in particular of the reference offset-strip fin geometry.

8.1.1 Design approach

Whatever the problem that needs to be solved, including design, it has to be well posed, meaning that the set of design requirements, the free variables and the boundary conditions must be known a priori and such to produce a unique solution. When sizing a heat-exchanger from scratch, there are two viable approaches:

1. Design by trial and error
2. Direct sizing procedure

The first approach consists in choosing the heat exchanger geometrical dimensions, based either on a reasonable guess or on previous designs, and then rating its performances. In the unlikely case that the design requirements are immediately met, the sizing procedure is over. Otherwise, another geometric configuration has to be produced and rated, until the functional requirements are met.

The principal inconvenient of trial and error is that the designer lacks any clue on which direction to change the geometry iteration after iteration, making it impossible to gain a deep understanding of each parameter effect on the final result. This design methodology can be effective and faster than a direct sizing procedure only for simple systems, for which the effect of geometric modifications can be easily guessed. On the contrary, dealing with complex systems, a trial and error approach can become very time expensive and can even fail to find a solution.

A direct sizing procedure, instead, relies upon an extensive knowledge of the system object of design, precisely in the form of a set of equations relating the system variables. This approach, a part from being faster, determines a deeper understanding of each parameter influence on the final result and therefore allows to refine, improve and optimize the definitive design.

Since for the type of heat exchanger selected in Chapter 7, a counterflow offset-strip fins PFHE, such a set of equations exists in literature [57; 67; 68; 69], the direct approach, because of its numerous advantages, will be preferred. Specifically, the PFHE sizing procedure hereafter employed, based on the $\varepsilon - NTU$ method and first introduced in 1988 by R.K. Shah [57], allows to determine the heat exchanger core dimensions, in terms of length L and frontal area A_{fr}.

Due to the extensive amount of calculations required by this approach and to its iterative nature, demanding multiple iterations to achieve numerical convergence, the whole sizing procedure will be implemented on a numerical computing environment like, specifically on MATLAB.

8.1.2 Design requirements

As hinted at in the introduction, for the sizing problem to be well posed, the design requirements must be clearly defined. In fact, only with well defined objectives it is possible to validate the iterative design procedure convergence.

When dealing with heat exchangers, there are always three main targets:

1. Thermal performance
2. Pressure drops
3. Dimensions

The first design requirement consists in building a device capable of completely transferring the thermal power required to heat up the cold fluid to the desired temperature. The thermal variables include the HE heat duty q, the cold and hot side outlet temperatures, $T_{1,out}$ and $T_{2,out}$, and finally the heat exchanger effectiveness ε. Fixing one of these 4 quantities automatically determines the remaining three because of energy conservation law. For HE, it is common to establish the thermal target in terms of effectiveness ε. The thermal power and the outlet temperatures can be then easily obtained following the approach exposed in Chapter 6, in particular through Equation 6.13, Equation 6.5 and Equation 6.6. From a numerical standpoint, the HE effectiveness must be at least equal to 95 %.

The second target is met by maintaining the pressure drops below an imposed limit value, which within HELMETH is established to 10 *mbar* for both fluid sides. It is crucial to understand that, while pressure drops must be kept as low as possible to reduce the pumping power, it is impossible to sustain an internal flow without having a pressure difference inducing it.

Unfortunately, these first two requirements are conflicting one with each other, as an improvement in thermal performances generally determines an increment in pressure losses and, vice-versa, a reduction of pressure drops commonly leads to a heat transfer worsening. Therefore, the final design will be the result of a compromise allowing to meet both requirements at the same time.

Finally, the HE dimensions are usually addressed in terms of compactness by imposing a target surface area density β, defined in Equation 8.1 as the ratio between the heat transfer area and the volume between plates. Since the heat transfer area A is directly proportional to the number of transfer units NTU and this is, in turn, related to the target heat exchanger effectiveness ε by Equation 7.4, imposing a value for β indirectly determines the heat exchanger volume. Remembering that PFHE typical values of surface area density range between 1000 and 5000 $^{m^2}/_{m^3}$ and taking into account the manufacturing constraints imposed by AM, in particular the minimum plate thickness of 1 mm, a target compactness value of 3500 $^{m^2}/_{m^3}$ has been selected.

$$\beta = \frac{A}{V_{plates}} \tag{8.1}$$

TABLE XIV: HEAT EXCHANGER DESIGN REQUIREMENTS

ε [/]	$\Delta p_{1,lim}$ $[mbar]$	$\Delta p_{2,lim}$ $[mbar]$	β $\left[\frac{m^2}{m^3}\right]$
0.95	10.0	10.0	3600

Table XIV summarizes the thermal, mechanical and volumetric design requirements target values used in the following sizing procedure.

8.1.3 Additional model input data

A part from the design requirements target values, the sizing procedure requires the following additional input data in order to derive the heat exchanger dimensions:

1. Mixtures composition
2. Mixtures mass flow rates
3. Mixtures thermo-physical properties
4. Mixtures inlet temperatures
5. Solid thermal properties
6. Offset-strip fin geometric parameters

All of these quantities, except the offset-strip fin geometry, whose definition follows hereafter, have already been defined in previous Chapters 2 to 5 and are therefore available to be inputted into the iterative sizing procedure. It is important to remember that the thermo-physical properties of each mixture are referred to a temperature which is the arithmetical mean of the inlet and outlet temperatures.

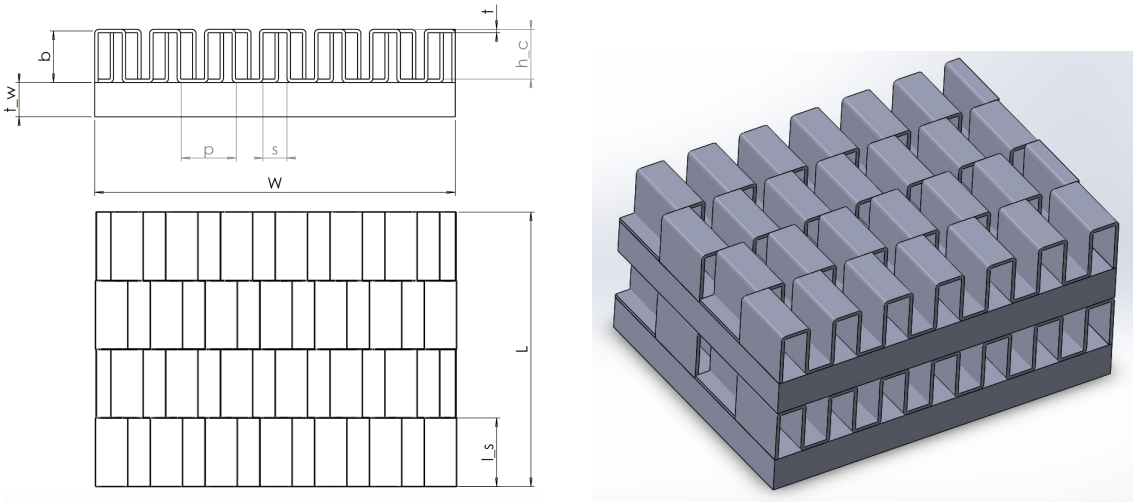

(a) 2-D view (b) 3-D view

Figure 38: Offset-strip fin geometry

8.1.4 Offset-strip fin geometry

Offset-strip fins, whose geometry is schematically represented in Figure 38, have been selected because of their remarkable heat transfer capability and due to the availability of analytical expressions to evaluate their performance. In later stages of design, while using CFD tools, fin geometry will be modified to further improve the HE performances and reduce the considerable pressure drops associated with offset-strip fins.

The independent geometrical parameters defining offset-strip fins are:

1. The fin thickness t
2. The fin length l_s
3. The transversal fin pitch p_t
4. The plates spacing b
5. The plates thickness t_w

Considering the specific geometry shown in Figure 38, starting from the independent parameters above listed, it is possible to derive other useful geometrical quantities, namely:

- The free flow width: difference between the transversal fin pitch and the fin thickness.

$$s = p_t - t \tag{8.2}$$

- The free flow height: difference between the plates distance and the fin thickness.

$$h_c = b - t \tag{8.3}$$

- The effective length for fin-efficiency calculation.

$$l = \frac{b}{2} - t \tag{8.4}$$

Other important quantities defined in [57] for offset-strip fins are:

- The hydraulic diameters D_H: equivalent flow diameter for non-circular channels.

$$\begin{aligned} D_{H1} &= \frac{4 \cdot s_1 \cdot h_{c1} \cdot l_{s1}}{2 \cdot [s_1 \cdot l_{s1} + h_{c1} \cdot l_{s1} + h_{c1} \cdot t_1] + s_1 \cdot t_1} \\ D_{H2} &= \frac{4 \cdot s_2 \cdot h_{c2} \cdot l_{s2}}{2 \cdot [s_2 \cdot l_{s2} + h_{c2} \cdot l_{s2} + h_{c2} \cdot t_2] + s_2 \cdot t_2} \end{aligned} \tag{8.5}$$

- The heat transfer area to heat exchanger volume ratio α.

$$\alpha_1 = \frac{b_1}{b_1 + b_2 + 2 \cdot t_W} \cdot \beta_1$$
$$\alpha_2 = \frac{b_2}{b_1 + b_2 + 2 \cdot t_W} \cdot \beta_2 \tag{8.6}$$

- The free flow to frontal area ratio σ.

$$\sigma_1 = \frac{D_{H1}}{4} \cdot \alpha_1$$
$$\sigma_2 = \frac{D_{H2}}{4} \cdot \alpha_2 \tag{8.7}$$

- The finned to total heat transfer area ratio f_s.

$$f_s = \frac{A_f}{A} \tag{8.8}$$

The hydraulic diameter D_H definition provided in Equation 8.5 has been derived using the so-called *unitary cell approach*, which consists in considering just one flow channel to infer an expression for D_H explicitly depending on the channel geometry. The hydraulic diameter values

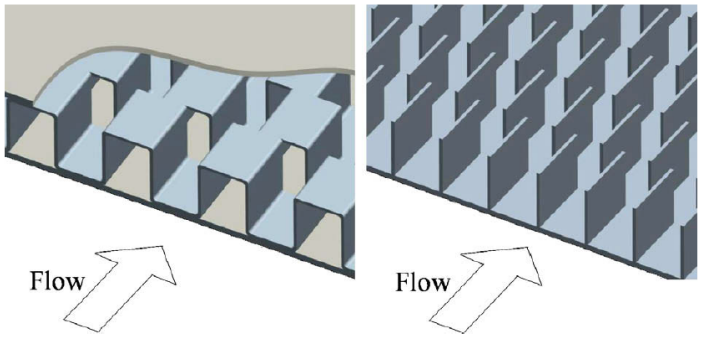

Figure 39: Offset-strip fin geometry modification

calculated using this local approach are in most cases consistent with the ones derived from the standard definition of hydraulic diameter shown in Equation 8.9.

$$D_H = \frac{4A_0 \cdot L}{A} \tag{8.9}$$

Thanks to the HE manufacturing by AM, it is possible to improve the traditional offset-strip fin geometry as shown in Figure 39 [24]. In fact, since the fins will be built layer-by-layer rather than using shaped metal sheets welded to the plates, the flat part connecting adjacent fins can be eliminated. This modification requires the redefinition of some of the quantities previously introduced, in particular:

- The free flow height.

$$h_c \equiv b \tag{8.10}$$

- The effective fin length.

$$l = \frac{b}{2} \tag{8.11}$$

- The hydraulic diameters D_H.

$$D_{H1} = \frac{4 \cdot s_1 \cdot h_{c1} \cdot l_{s1}}{2 \cdot [s_1 \cdot l_{s1} + h_{c1} \cdot l_{s1} + h_{c1} \cdot t_1]}$$
$$D_{H2} = \frac{4 \cdot s_2 \cdot h_{c2} \cdot l_{s2}}{2 \cdot [s_2 \cdot l_{s2} + h_{c2} \cdot l_{s2} + h_{c2} \cdot t_2]} \tag{8.12}$$

8.2 Basis of thermo-hydraulics

This section aims at introducing and describing theoretical concepts whose role is crucial in the definition of the heat exchanger iterative sizing procedure object of the next section. In particular, hereafter the fundamental thermo-hydraulic dimensionless numbers are defined, an expression for the calculation of the pressure losses in a HE is derived and finally the cardinal core mass velocity equation is introduced.

8.2.1 Dimensionless numbers definition

While designing heat exchangers, because of the nonlinear relationships between geometrical and operative quantities, is it not convenient to use absolute parameters to assess heat transfer and pressure drops. Dimensionless numbers are instead preferred, as they allow to extend experimental results to heat exchangers having a similar geometry but a different size.

Hereafter follows a definition of the dimensionless groups required for carrying out the HE sizing procedure.

Reynolds number *Re*, defined in Equation 8.13 as the ratio between inertia and viscous forces, is a good indicator of flow regimes. When inertia forces prevail over viscous forces, Reynolds number is high and the corresponding flow is turbulent. Vice-versa, in low Reynolds number laminar flows viscosity is the dominant term.

$$Re = \frac{\rho \cdot v \cdot D_H}{\mu} = \frac{G \cdot D_H}{\mu} \tag{8.13}$$

While Reynolds number is descriptive of the flow conditions, Prandtl number *Pr*, introduced in Chapter 4 and defined in Equation 4.5 as the ratio between the fluid momentum diffusivity ν and the thermal diffusivity α, characterizes a specific fluid.

$$Pr = \frac{\mu \cdot c_p}{\lambda} = \frac{\nu}{\alpha}$$

The Fanning friction factor *f*, defined in Equation 8.14 as the ratio of wall shear stress τ_w to the flow kinetic energy per unit volume [57], is a dimensionless number used as local parameter in continuum mechanics calculations.

$$f = \frac{\tau_w}{(\rho \cdot u_m^2)/2g_c} \tag{8.14}$$

Experimental evidence has proved that Fanning factor f is related to wall friction generated pressure drops Δp through Equation 8.15. The friction factor dependence on the flow channel

geometry is a function of Reynolds number, being strong for laminar flows and, vice-versa, rather weak under turbulent flow regimes [57].

$$f = \frac{g_c \cdot \rho}{G^2} \cdot \frac{D_H}{2L} \cdot \Delta p \tag{8.15}$$

For an offset-strip fins geometry, the Fanning factor f can be calculated using the semi-empirical correlation, valid for $120 \leq Re \leq 10,000$ and $0.5 \leq Pr \leq 15$, derived by Manglik and Bergles reported in Equation 8.16 [69]. Figure 40 (a) shows the Fanning factor sensitivity to the fin thickness t and length l_s and to the free flow width s and height h_c.

$$\begin{aligned} f = 9.6243 \cdot Re^{-0.7422} \cdot \left(\frac{s}{h_c}\right)^{-0.1856} \cdot \left(\frac{t}{l_s}\right)^{0.3053} \cdot \left(\frac{t}{s}\right)^{-0.2659} \\ \times \left[1 + 7.669 \times 10^{-8} \cdot Re^{4.429} \cdot \left(\frac{s}{h_c}\right)^{0.920} \cdot \left(\frac{t}{l_s}\right)^{3.767} \cdot \left(\frac{t}{s}\right)^{0.236}\right]^{0.1} \end{aligned} \tag{8.16}$$

The Colburn factor j, defined in Equation 8.17, is the result of a modification of the Stanton number St that makes it virtually independent from the particular fluid considered, provided that the fluid Prandtl number belongs to the prescribed range $0.5 \leq Pr \leq 15$.

$$j = St \cdot Pr^{\frac{2}{3}} = \frac{Pr^{\frac{2}{3}}}{G \cdot c_p} \cdot h \tag{8.17}$$

The physical interpretation is similar to the one attributed to the Stanton number, defined in Equation 8.18 as the ratio of convected heat transfer (per unit duct surface area) to the

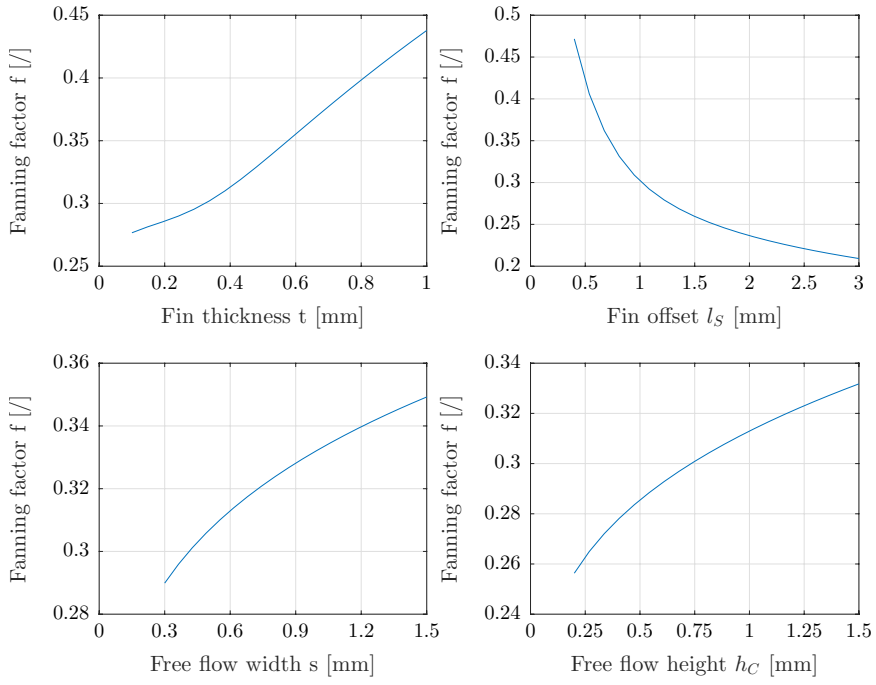

(a) Fanning friction factor

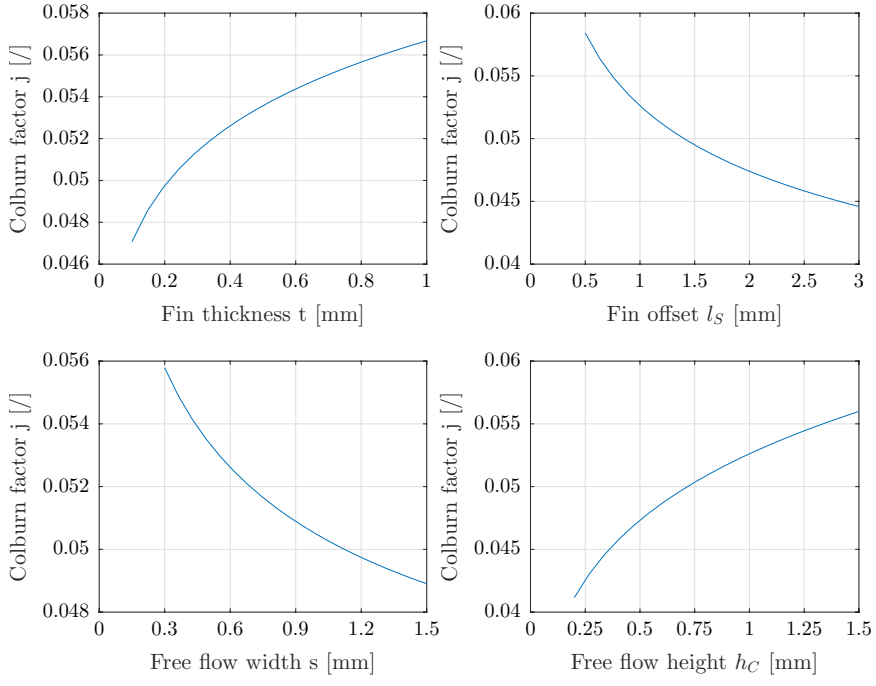

(b) Colburn factor

Figure 40: Dimensionless factors sensitivity to the fin geometry

enthalpy rate change of the fluid reaching the wall temperature (per unit of flow cross-sectional area) [57].

$$St = \frac{h}{G \cdot c_p} \tag{8.18}$$

An advantage of Colburn factor relative to Nusselt number is that its behavior as a function of Reynolds number is similar to the one exhibited by Fanning factor. This means that, even if both factor individually are *Re* dependent, their ratio is almost independent from the flow regime. The Colburn factor j can be related to the HE individual side number of transfer units ntu as proved by equation Equation 8.19.

$$ntu = \frac{\eta_o \cdot h \cdot A}{\dot{m} \cdot c_p} = \eta_o \cdot \frac{h}{G \cdot c_p} \cdot \frac{A}{A_0} = \eta_o \cdot j \cdot Pr^{-\frac{2}{3}} \cdot \frac{A}{A_0} = \eta_o \cdot j \cdot Pr^{-\frac{2}{3}} \cdot \frac{4L}{D_H} \tag{8.19}$$

As for the friction factor *f*, it exists a formula (Manglik & Bergles, 1995), reported in Equation 8.20, allowing the calculation of the Colburn factor j for an offset-strip fin geometry [69]. Figure 40 (b) graphically shows Colburn factor sensitivity to the fin geometry.

$$\begin{aligned} j = 0.6522 \cdot Re^{-0.5403} \cdot \left(\frac{s}{h_c}\right)^{-0.1541} \cdot \left(\frac{t}{l_s}\right)^{0.1499} \cdot \left(\frac{t}{s}\right)^{-0.0678} \\ \times \left[1 + 5.269 \times 10^{-5} \cdot Re^{1.340} \cdot \left(\frac{s}{h_c}\right)^{0.504} \cdot \left(\frac{t}{l_s}\right)^{0.456} \cdot \left(\frac{t}{s}\right)^{-1.055}\right]^{0.1} \end{aligned} \tag{8.20}$$

8.2.2 Pressure drops calculation

Pressure losses Δp need to be determined as accurately as possible because of their functional and economical importance. In fact, on one side pressure drops are responsible for the fluid flow and affect the heat transfer, on the other, because of the direct proportionality to the fluid pumping power evidenced by Equation 8.21, they determine the pumping costs.

$$P_P = \frac{\dot{m}}{\rho \cdot \eta_P} \cdot \Delta p \tag{8.21}$$

It is possible to distinguish two major pressure drop contributions, namely:

1. Core pressure drops
2. Pressure drops in flow distribution devices (headers, pipes, nozzles)

It is important to highlight one more time that for a heat exchanger to accomplish its task, i.e. transfer heat from the hot to the cold fluid, there must be a pressure difference that forces the fluid flow over the heat transfer surfaces. If core pressure drops can be then regarded as functional losses, the second type of pressure drops cannot and therefore needs to be minimized by a proper design of the flow distribution system. Moreover, not only pressure drops in the headers increase the plant operative costs, they also cause non uniformities in the fluid flow, thus seriously affecting the HE performances.

For a PFHE, pressure drops in the headers, due to the fluid sudden contraction at the core inlet and expansion at the core outlet, represent the main losses in flow distribution devices.

Core pressure drops can be instead explained in terms of wall friction, with relevant secondary factors being:

- The form drag, particularly important for interrupted fins as these determine the fluid detachment in correspondence of the fin leading and trailing edges.
- Momentum effects, i.e. changes of pressure driven by temperature-induced density variations.

Equation 8.23 proves that it is possible to interpret the total pressure drops described in Equation 8.22 as the product between a dimensionless coefficient a and a term having the dimensions of a pressure and proportional to the square of the core mass velocity G. Hereafter follows a brief description of each of the four individual terms contributing, according to Equation 8.24, to the total pressure loss coefficient a.

$$\Delta p = \Delta p_{inlet} + \Delta p_{core} + \Delta p_{outlet} \tag{8.22}$$

$$\Delta p = a \cdot \frac{G^2}{2 g_c \cdot \rho_{in}} \tag{8.23}$$

$$a = a_{inlet} + a_{outlet} + a_{momentum} + a_{friction} \tag{8.24}$$

The inlet pressure loss coefficient definition shown in Equation 8.25 highlights the strong dependence on the free flow to frontal area ratio σ, both directly and through the entrance coefficient K_C.

$$a_{inlet} = \left(1 - \sigma^2 + K_C(\sigma)\right) \tag{8.25}$$

In correspondence of the outlet section the flow expansion determines the pressure rise described by Equation 8.26, which is again strongly depend on the free flow to frontal area ratio σ, both directly and through the exit coefficient K_E. In general the magnitude of inlet and outlet effects is similar and, due to their opposite signs, the two effects almost completely balance out.

$$a_{outlet} = -\left(1 - \sigma^2 - K_E(\sigma)\right) \cdot \left(\frac{\rho_{in}}{\rho_{out}}\right) \tag{8.26}$$

The entrance and exit pressure loss coefficients K_C and K_E can be derived graphically using experimental plots [57] of the type shown in Figure 41. This specific plot refers to a PFHE having rectangular flow channels. Among the multitude of curves corresponding to different flow regimes, it has been chosen the one corresponding to a infinite Reynolds number because the flow is locally very well mixed due to the frequent boundary layer interruptions.

As previously anticipated, pressure losses due to momentum effect are mainly due to density variations, Equation 8.27, and can become relevant for devices characterized by a high temperature differences between the inlet and the outlet.

$$a_{momentum} = 2 \cdot \left(\frac{\rho_{in}}{\rho_{out}} - 1\right) \tag{8.27}$$

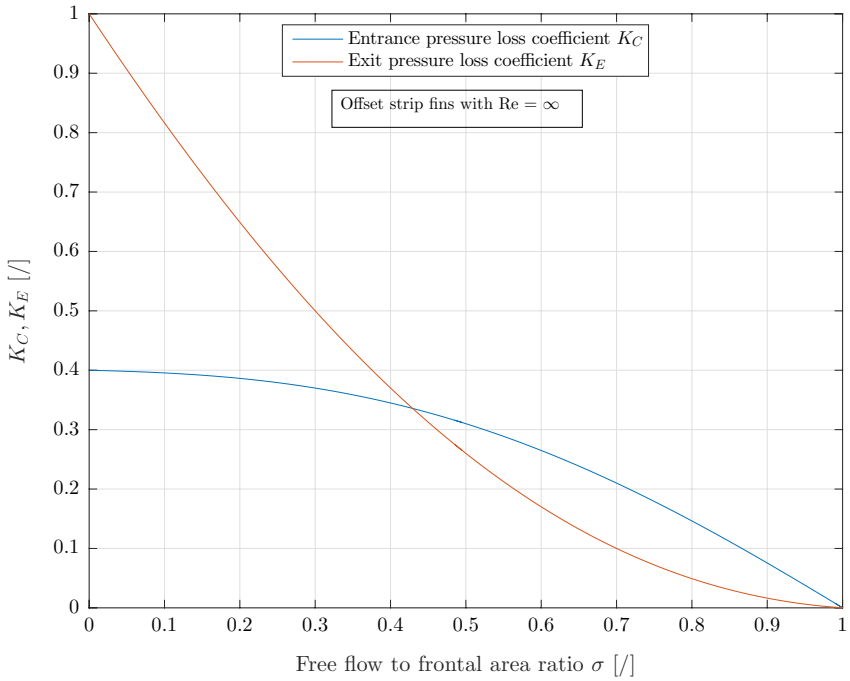

Figure 41: Entrance and exit pressure loss coefficients

Finally, Equation 8.28 states the dependence of wall friction pressure losses from the core length L, the flow passage hydraulic diameter D_H and the Fanning friction factor f. The mean density ρ_m can be calculated through Equation 8.29 as the specific volumes average reciprocal.

$$a_{friction} = f_c \cdot \frac{4L}{D_H} \cdot \left(\frac{\rho_{in}}{\rho_m} - 1\right) \tag{8.28}$$

$$\frac{1}{\rho_m} = \frac{1}{2} \cdot \left(\frac{1}{\rho_{in}} + \frac{1}{\rho_{out}}\right) \tag{8.29}$$

Equation 8.30 combines all the previous effects in the single dimensionless factor a, which can be then substituted into Equation 8.23 to obtain the physical pressure drops.

$$a = \left[\left(1 - \sigma^2 + K_C\right) + 2 \cdot \left(\frac{\rho_{in}}{\rho_{out}} - 1 \right) + f_c \cdot \frac{4L}{D_H} \cdot \left(\frac{\rho_{in}}{\rho_m} - 1 \right) - \left(1 - \sigma^2 - K_E\right) \cdot \left(\frac{\rho_{in}}{\rho_{out}} \right) \right] \quad (8.30)$$

As a final remark, it is wise to highlight how the wall friction term is generally the main contribution, being responsible for more than 90 % of the total pressure losses in many compact heat exchangers. Entrance and exit pressure drops become instead relevant only when the free flow area is small with respect to the frontal area, i.e. when σ is small. This typically happens when the flow passages are small while the plates and fins are relatively thick.

8.2.3 Core mass velocity equation

As previously hinted at, the ultimate aim of the sizing procedure is to derive the heat exchanger core dimensions while simultaneously meeting both thermal and pressure drop requirements. The core mass velocity equation, first proposed by Kays and London in 1998 [60], coupling the heat duty with the pressure drops and exploiting this information to derive the mass velocity G, allows to close the iterative HE design loop. Hereafter, the core mass velocity equation will be derived and its role within the sizing procedure explained.

Having already defined the heat exchanger configuration, its effectiveness ε and the heat capacity rates ratio C^*, the number of required transfer units NTU can be calculated by means of the counterflow $\varepsilon - NTU$ correlation defined in Equation 7.4.

Neglecting wall and fouling resistance, the overall conductance can be written as in Equation 8.31. This equation can be modified so to include both the overall NTU and individual sides ntu_1 and ntu_2, as shown in Equation 8.32.

$$\frac{1}{UA} = \frac{1}{\left(\eta_o \cdot h \cdot A\right)_1} + \frac{1}{\left(\eta_o \cdot h \cdot A\right)_2} \tag{8.31}$$

$$\frac{1}{NTU} = \frac{1}{ntu_1 \cdot \left(\frac{C_1}{C_{min}}\right)} + \frac{1}{ntu_2 \cdot \left(\frac{C_2}{C_{min}}\right)} \tag{8.32}$$

Since both mixtures are gaseous, the thermal resistances have the same order of magnitude, meaning that the overall and individual sides number of transfer units are related by Equation 8.33.

$$ntu_1 \approx ntu_2 \approx 2NTU \tag{8.33}$$

Reminding Equation 8.19, relating the individual sides ntu with the Colburn factor, isolating the term $\left({}^{4L}/_{D_H}\right)$ and substituting it in the pressure drops equation previously derived, Equation 8.23, the derivation of the core mass velocity equation, displayed in Equation 8.34 and complemented by Equation 8.35, is concluded.

$$G = \sqrt{\frac{\Delta p \cdot 2g_c \cdot \rho_{in}}{b}} \tag{8.34}$$

$$b = \left[\left(1-\sigma^2+K_C\right)+2\cdot\left(\frac{\rho_{in}}{\rho_{out}}-1\right)+\left(\frac{f}{j}\right)\cdot ntu\cdot\eta_o\cdot Pr^{\frac{2}{3}}\cdot\left(\frac{\rho_{in}}{\rho_m}-1\right)-\left(1-\sigma^2-K_E\right)\cdot\left(\frac{\rho_{in}}{\rho_{out}}\right)\right] \quad (8.35)$$

The power of the core mass velocity equation lies in the fact that it does not require the knowledge of individual Fanning and Colburn factors, which are function of the Reynolds number Re, but only of their ratio $\left(f/j\right)$, which is only weakly dependent on Re. As it will be clarified in the next section, the fact that through this equation it is possible to estimate the mass velocity G even without knowing precisely the flow regime is of crucial importance for sizing the heat exchanger.

8.3 Iterative Sizing Procedure

This section aims at describing in detail the iterative sizing procedure that leads to the numerical definition of the actual heat exchanger core dimensions and at introducing a tool to validate the procedure results.

8.3.1 Main algorithm

Being able to calculate the Fanning and and the Colburn factors, using respectively Equation 8.16 and Equation 8.20, it is possible to calculate their ratio, which is fairly independent from the flow regime as shown in Figure 42, and then its average value over a reasonable range of Reynolds numbers, according to Equation 8.36.

$$\left(\frac{f}{j}\right)_m = \frac{\sum_{i=1}^{N}\left(\frac{f}{j}\right)_i}{N} \quad (8.36)$$

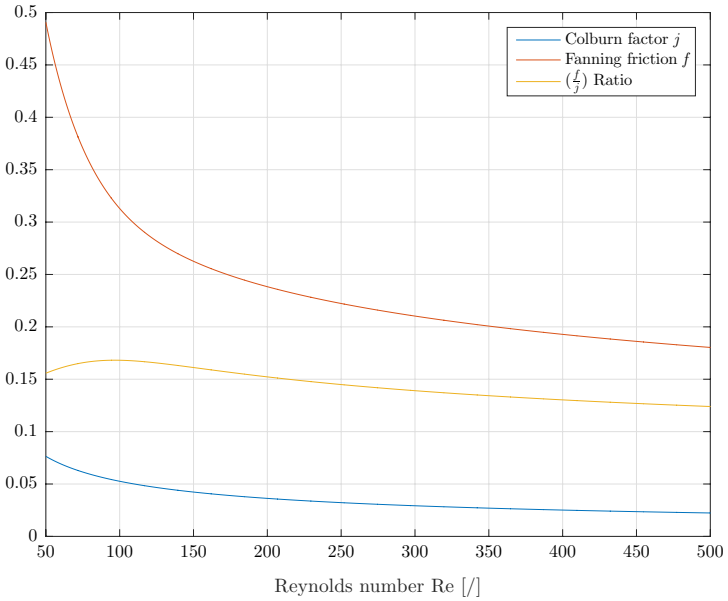

Figure 42: Fanning and Colburn factors as a function of Reynolds number

Introducing this ratio into a simplified version of the core mass velocity equation, Equation 8.37, which takes into account only the effect of pressure drops due to wall friction, it is possible to compute a first-trial value for the mass velocity G. The pressure drop Δp imposed in Equation 8.37 is precisely the limit pressure drop specified as a design requirement. Knowing G, the actual Reynolds number Re calculation, based on its definition, Equation 8.13, becomes straightforward and with such an information available the Colburn and Fanning factors can be locally re-calculated through Equation 8.16 and Equation 8.20.

$$G = \sqrt{2g_c \cdot \rho_m \cdot Pr^{-\frac{2}{3}} \cdot \eta_o \cdot \frac{\Delta p}{ntu} \cdot \left(\frac{j}{f}\right)_m} \tag{8.37}$$

The heat transfer coefficient h follows from the definition of the Colburn factor, as shown in Equation 8.38.

$$h = \frac{G \cdot c_p}{Pr^{\frac{2}{3}}} \cdot j \tag{8.38}$$

It is then straightforward to calculate the fin parameter m, the fin efficiency η_f and finally the overall surface efficiency η_o, using respectively Equation 8.39, Equation 8.40 and Equation 8.41, in which λ_f denotes the fin thermal conductivity and f_s the finned to total heat transfer area ratio.

$$m = \sqrt{\frac{2h}{\lambda_f \cdot t} \cdot \left(1 + \frac{t}{l_s}\right)} \tag{8.39}$$

$$\eta_f = \frac{\tanh(m \cdot l)}{m \cdot l} \tag{8.40}$$

$$\eta_o = 1 - (1 - \eta_f) \cdot f_s \tag{8.41}$$

Neglecting the fouling resistance and, only during this first iteration round, the wall resistance, the overall heat transfer coefficient U can be computed according to Equation 8.42.

$$U = \frac{1}{\frac{1}{(\eta_{o1} \cdot h_1)} + \left(\frac{\alpha_1}{\alpha_2}\right) \cdot \frac{1}{(\eta_{o2} \cdot h_2)}} \tag{8.42}$$

The heat transfer area A for one of the two sides can be then extrapolated directly from the NTU definition, Equation 8.43, with the second area being scaled, as displayed in Equation 8.44, with respect to the heat transfer area to HE volume coefficients α.

$$A_1 = \frac{NTU \cdot C_{min}}{U_1} \tag{8.43}$$

$$A_2 = \frac{\alpha_2}{\alpha_1} \cdot A_1 \tag{8.44}$$

The free flow area A_0 follows directly from the core mass velocity G definition according to Equation 8.45.

$$A_0 = \frac{\dot{m}}{G} \tag{8.45}$$

Since the ratio between the free flow and the frontal area, depending only on the channel geometry, is already available, based on its definition it is finally possible to derive the heat exchanger frontal area A_{fr} using Equation 8.46.

$$A_{fr} = \frac{A_0}{\sigma} \tag{8.46}$$

For a counter-flow heat exchanger, the frontal area must be the same for both fluid sides, i.e. $A_{fr1} = A_{fr2}$. However, it is likely that because of numerical errors the areas calculated by

Equation 9.21 are not equal. If this is the case, the bigger area has to be chosen for following calculations.

In absence of further constraints, of spacial, manufacturing or economic nature, there is no reason not to prefer a square frontal section, in which case the heat exchanger side can be computed as in Equation 8.47.

$$S = \sqrt{A_{fr}} \tag{8.47}$$

With both the heat transfer and the free flow areas available, the last HE significant dimension, its flow length L, can be derived starting from the hydraulic diameter D_H definition, as shown in Equation 8.48.

$$L = \frac{D_H \cdot A}{4A_0} \tag{8.48}$$

Again, as for the heat exchanger frontal area, it is possible that the length L calculated using data referred to the cold side differs from the one obtained using information related to the hot side. Since the HE length L must be unique, the higher value has to be selected.

Finally, the heat exchanger volume needs to be calculated because of the limited building volume, reported in Table I, of the AM machine used to manufacture it. If the actual volume calculated by Equation 8.49 is bigger than the limit one, the HE has to be completely redesigned.

$$V = A_{fr} \cdot L = S^2 \cdot L \tag{8.49}$$

The sizing algorithm introduced above can be improved by correcting the isothermal Fanning friction factor definition, so that it takes into account the effect of temperature variability along the HE length. According to Shah (1985), under laminar flow conditions the corrected Fanning factor can be calculated by means of Equation 8.50, where T_w denotes the wall temperature, calculated using Equation 8.51, T_m is the fluid mean temperature, available from the thermal balance, and finally R_i labels each fluid thermal resistance, computed from Equation 8.52. The coefficient m assumes a different value depending on the fluid being heated, $m = 1.9$ or being cooled, $m = 0.81$.

$$f_c = f \cdot \left(\frac{T_w}{T_{m1}} \right)^m \tag{8.50}$$

$$T_w = \frac{T_{m1} + \left(\frac{R_1}{R_2}\right) \cdot T_{m2}}{1 + \left(\frac{R_1}{R_2}\right)} \tag{8.51}$$

$$R = \frac{1}{\eta_o \cdot h \cdot A} \tag{8.52}$$

The design procedure ends when both thermal and pressure drop requirements are met simultaneously. Figure 43 schematically clarifies the type of closed loop control implemented to verify this convergence condition.

In detail, convergence is controlled by comparing the actual pressure drops Δp, calculated using previously derived Equation 8.23, with the design requirement Δp_{lim}. If these two values are in agreement, then the sizing procedure is concluded. Otherwise, it is necessary to start

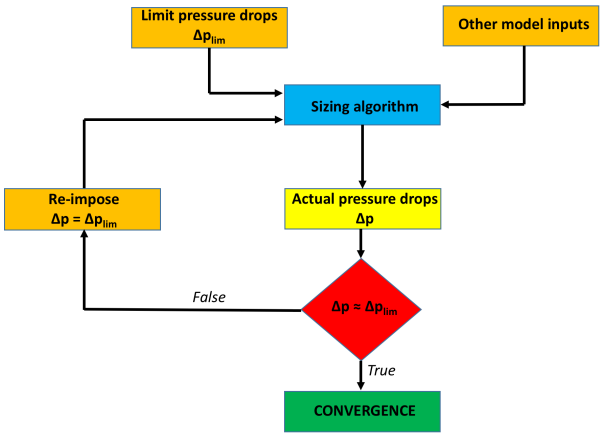

Figure 43: HE sizing procedure convergence closed loop control

a new iteration by re-imposing the limit pressure drops Δp_{lim} in the mass velocity calculation defined by Equation 8.37. The procedure then continues exactly as during the first iteration and ends again with a check performed on the pressure drops. This iterative algorithm is expected to converge within a few iterations.

The main difference between the first iteration round and the next ones is that, since in the following iterations preliminary HE dimensions are available, it is possible to modify the overall heat transfer coefficient Equation 8.42 including the effect of wall resistance, thus producing Equation 8.53. In fact, especially with relatively thick fins and plates, this contribution may be relevant and substantially improve the heat exchanger design.

$$\frac{1}{UA} = \frac{1}{(\eta_o \cdot h \cdot A)_1} + R_w + \frac{1}{(\eta_o \cdot h \cdot A)_2} \tag{8.53}$$

Because of its thermal conductive nature, the wall resistance can be calculated as shown in Equation 8.54, where A_w is the wall area, defined in Equation 8.55, t_w is the wall thickness, available as input parameter, and finally λ_w is the wall thermal conductivity.

$$R_w = \frac{t_w}{A_w \cdot \lambda_w} \tag{8.54}$$

$$A_w = 2 \cdot (N_p + 1) \cdot L \cdot S \tag{8.55}$$

A HE configuration where the outermost flow channels are occupied by cold mixture evidently allows to minimize the heat losses toward the environment. Therefore, indicating the number of hot passages by $N_H = N_p$, the number of cold passages is $N_C = N_p + 1$ and the number of plates is $N_w = 2N_C$. The quantity N_p can be then derived by means of Equation 8.56 knowing the plate thickness t_w, the cold and hot side plate distances b_1 and b_2 and the HE height. Due to the hypothesis of square frontal section, height and width assume equal values derived using Equation 8.47. The *ceil* operator ensures that the number of fluid passages is an entire number.

$$N_p = ceil\left[\frac{S - b_2 + 2t_w}{b_1 + b_2 + 2t_w}\right] \tag{8.56}$$

8.3.2 Heat exchanger definitive size and characteristics

The dimensions obtained by applying the sizing procedure presented in the previous section, being the result of numerical calculations, do not allow to practically manufacture the heat exchanger. In fact, to this aim, it is necessary that the HE actual dimensions, namely the length L, the width W and the height H, are an integer multiple of the fin dimensions. Hereafter the computed dimensions, denoted by the subscript c, will be slightly modified in order to meet this manufacturing requirement.

The heat exchanger length L must be a multiple of the fin length l_s. After having determined the number of fin rows Z_l by means of Equation 8.57, it is possible to obtain the HE actual length using Equation 8.58.

$$Z_l = ceil\left[\frac{L_c}{l_s}\right] \tag{8.57}$$

$$L = Z_l \cdot l_s \tag{8.58}$$

Similarly, the heat exchanger height H must be compatible with the plates spacing b and thickness t_w. After having calculated the quantity N_p using Equation 8.56 and remembering that $N_H = N_p$, $N_C = N_p + 1$ and $N_w = 2N_C$, the HE actual height can be derived by means of Equation 8.59.

$$H = N_c \cdot b_1 + N_h \cdot b_2 + N_w \cdot t_w \tag{8.59}$$

Finally, the heat exchanger width W must be a multiple of the fin pitch p. After having determined the number of flow channels Z_t composing each HE *layer* using Equation 8.61, the HE actual width can be calculated by means of Equation 8.61. In conclusion, even if because of manufacturing constraints the heat exchanger frontal area shape, defined in Equation 8.62, is not exactly square anymore, the height to width aspect ratio is still almost unitary.

$$Z_t = ceil\left[\frac{L_c}{p}\right] \tag{8.60}$$

$$W = Z_t \cdot p \tag{8.61}$$

$$A_{fr} = W \cdot H \tag{8.62}$$

Having already derived the number of fin rows Z_l and the number of flow channels per layer Z_t, the number of fins per row n and per channel N_f can be calculated using Equation 8.63 and Equation 8.64 respectively.

$$n = Z_t + 1 \tag{8.63}$$

$$N_f = n \cdot Z_l \tag{8.64}$$

The primary, secondary and total heat transfer area of each HE passage follow according to Equation 8.65, Equation 8.66 and Equation 8.67 respectively.

$$A_p = 2L \cdot W - N_f \cdot (2t \cdot l_s) + 2b \cdot L \tag{8.65}$$

$$A_s = N_f \cdot (2h_c \cdot l_s + 2h_c \cdot t) \tag{8.66}$$

$$A_t = A_p + A_s \tag{8.67}$$

The total heat transfer area is simply the product of each passage area A_t by the fluid number of passages, as shown in Equation 8.68 for the cold side. Substituting N_C with N_H, exactly the same equation can be used for the hot side.

$$A = N_C \cdot A_t \tag{8.68}$$

Considering the geometry of a counterflow PFHE, the total free flow area can be evidently computed as shown in Equation 8.69. Finally, the HE total volume and the volume between two consecutive plates can be computed by means of Equation 8.70 and Equation 8.71 respectively.

$$A_0 = Z_t \cdot Nc \cdot A_{0,cell} = Z_t \cdot Nc \cdot (s \cdot b) \tag{8.69}$$

$$V = W \cdot H \cdot L \tag{8.70}$$

$$V_p = W \cdot L \cdot b \tag{8.71}$$

After having completely defined the heat exchanger final geometry, it is important to re-calculate the quantities initially used as input for the HE sizing procedure, in order to check that the numerically designed HE features are coherent with the model inputs. The sizing procedure is valid only provided that the values of the quantities hereafter re-calculated coincide, at least approximately, with those initially used as model input.

1. The finned to total area ratio f_s.

$$f_s = \frac{A_f}{A_t} \tag{8.72}$$

2. The surface area density β.

$$\beta = \frac{A}{V_p} \tag{8.73}$$

3. The heat transfer area to HE volume ratio α.

$$\alpha = \frac{A}{V} \tag{8.74}$$

4. The hydraulic diameter D_H.

$$D_H = \frac{4A_0 \cdot L}{A} \tag{8.75}$$

8.4 Results

After having defined the model inputs and the expected outputs and detailed how the HE sizing procedure works and how it is possible to check its convergence first and its validity second, the present section is completely devoted to the numerical results analysis. While the first part focuses on the parametric sweep study outcomes, in the second part follows an accurate description of what is deemed to be the heat exchanger optimum design.

8.4.1 Parametric sweep study

A parametric sweep is a study where all the parameters are kept constant except one, which, assuming several different discrete values, reveals the system sensitivity to this particular parameter. In some regards, performing a parametric sweep is equivalent to numerically calculate the partial derivatives of a multi-variable function, whose equation is not explicitly available because hidden in a long MATLAB script.

The quantities selected for this parametric sweep study include most of the parameters defining the HE geometry, the surface area density β, the effectiveness ε and the cold side mass flow rate $\dot{m}_1$.

While setting up a parametric sweep study, a part from choosing the swept parameters, it is also necessary to define some meaningful output variables allowing to measure the system performance variations as a function of the different values assumed by the swept variable. To this aim, it is not possible to select parameters proportional to the HE thermal performances and pressure drops, because these quantities, in quality of model inputs, do not vary during the parametric sweep study.

A smarter choice, taking into account that one of the design objectives is the minimization of the heat exchanger dimensions, consists in selecting the HE length L, its side S and its volume V as output variables. Hereafter, the Reynolds number variability as a function of the swept parameters will be also assessed, in order to gain a better understanding of the HE flow regimes. In fact, since the validity of some of the correlations used in the sizing procedure is restricted to laminar flows only, it is crucial to verify that the flow never becomes turbulent.

8.4.1.1 Outcomes

Plates spacing

Figure 44 (a) shows that increasing the plates spacing b, while keeping constant all the other quantities and in particular the mass flow rate $\dot{m}$ and the plate thickness t_w, determines a reduction of the frontal area surface A_{fr}. This effect is likely to be due to the higher available free flow area. At the same time, because of the thicker fluid layers, heat transfer from the plates to the fins and to the fluid is worsened and, as a result, the HE length L necessary the achieve the target HE effectiveness increases. Even if distancing more the plates minimizes the HE volume V, it is not convenient to increase the plates spacing b beyond 1.5 mm as the gain then tends asymptotically to zero.

Figure 44 (b) suggests a monotonically increasing trend for the Reynolds number Re, probably motivated by the higher hydraulic diameter D_H resulting from the incremented plate spacing. However,with the Reynolds number fluctuating around values of about hundred, it is evident that the flow regime remains laminar for whatever plates spacing.

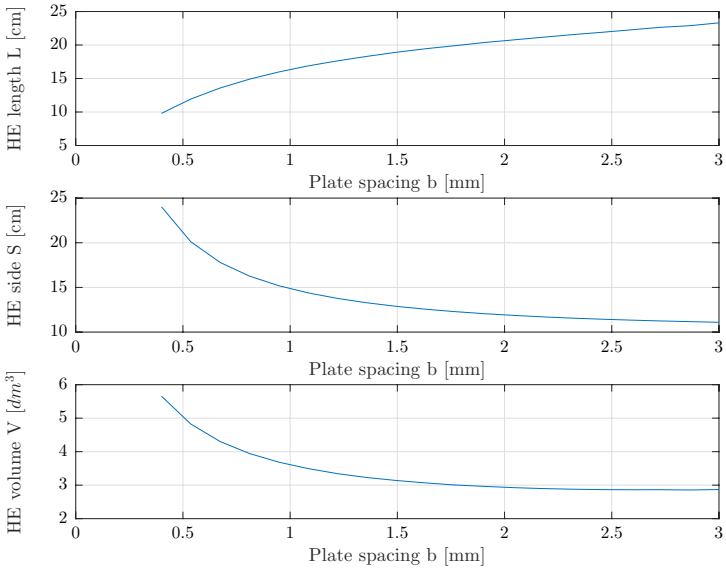

(a) Heat exchanger dimensions

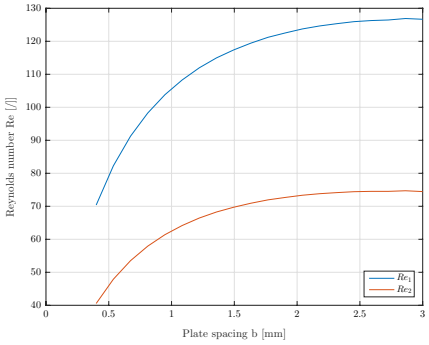

(b) Flow regime

Figure 44: Effect of plates distance b

Fin length

Figure 45 (a) highlights that adopting longer fins, while only marginally reducing of the required frontal area A_{fr}, determines the HE length L to increase of as much as 300 %. Consequently, also the HE volume V monotonically grows with the fin length l_s. The explanation lies in the fact that long fins, reducing the frequency of fluid detachment, worsen the heat transfer. At the same time, this configuration reduces the pressure drops per unit of length, thus allowing, in spite of the higher mass velocities G, due to the smaller frontal area A_{fr}, and of the longer HE, to maintain the total pressure drops below the limit threshold of 10 mbar.

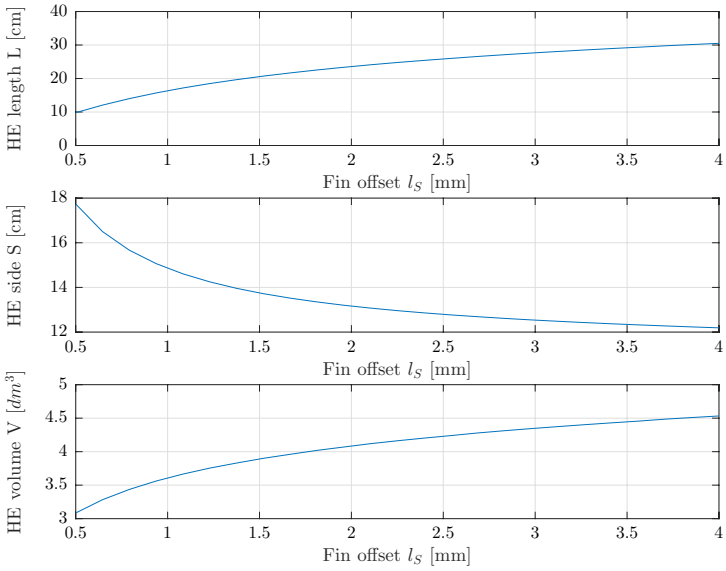

(a) Heat exchanger dimensions

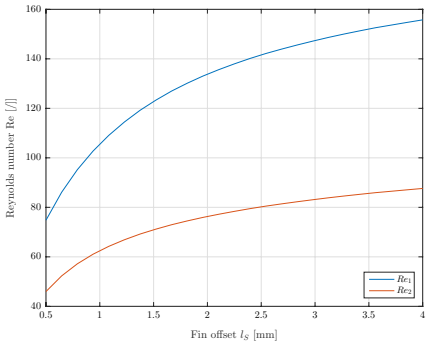

(b) Flow regime

Figure 45: Effect of the fin length l_s

The increasing Reynolds number trend represented in Figure 45 (a) can be explained remembering that, according to Equation 9.46, longer fins determine larger hydraulic diameters D_H and consequently higher Reynolds numbers.

Free flow width

Increasing the free flow width s, while keeping constant all the remaining parameters and in particular the mass flow rate $\dot{m}$, the free flow area A_0 increases and, as a consequence, as confirmed by Figure 46 (a), the HE side S decreases. However, because of the thicker fluid domain between two fins, the worsened heat transfer determines a remarkable increment of

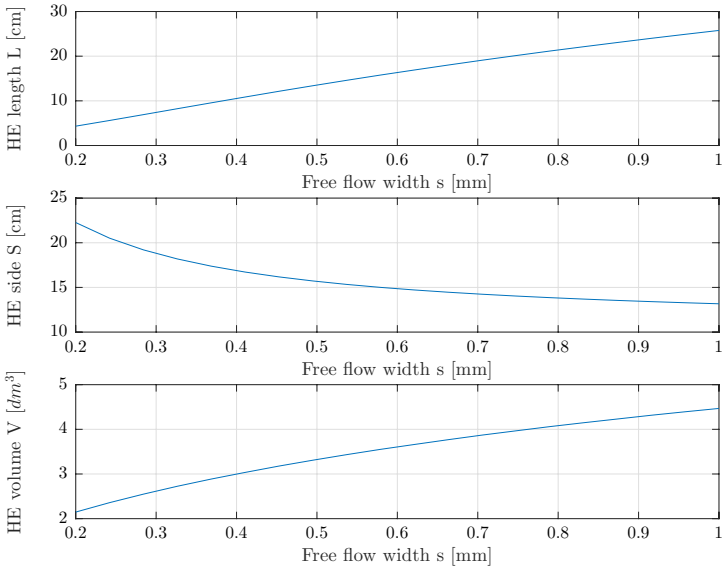

(a) Heat exchanger dimensions

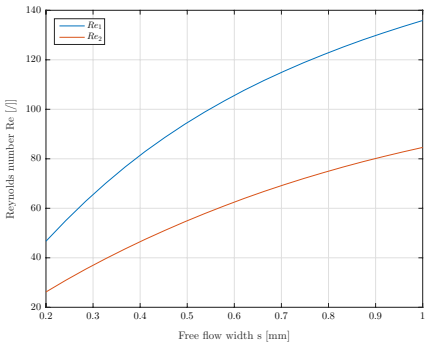

(b) Flow regime

Figure 46: Effect of the free flow width s

the HE length L. Overall, the monotonically increasing trend for the heat exchanger volume V suggests that it is convenient to prefer small values of free flow width s.

The monotonically increasing trend for the Reynolds number Re shown in Figure 46 (b) can be explained reminding that, according to Equation 9.46, higher free flow areas boost the hydraulic diameter D_H which, in turn, pushes the Reynolds number toward higher values.

Fin thickness

According to Figure 47, thicker fins lead to shorter heat exchangers, likely because of the higher volume of conductive material that enhances heat transfer. The frontal area A_{fr} increment, due to the lower free flow to frontal area ratio σ, does not balance out the reduction

in length, so that the overall effect of increasing the fin thickness t is a decrement of the HE volume V.

In terms of flow regime, Figure 47 suggests a reduction of the Reynolds number Reusing thicker fins, which is likely to be due to a drop of the hydraulic diameter D_H triggered by lower values of the free flow area A_0.

The fin thickness effects have been tested for two different values of free flow width s, $s = 0.4\ mm$ and $s = 0.8\ mm$. Comparing these two cases, it is possible to confirm the results previously discussed referring to Figure 46, namely that narrower free flow widths cause the HE to be shorter, wider and the Reynolds number to be lower.

Plate thickness

It is intuitive that incrementing the plate thickness t_w does not induce any positive effect beyond improving the heat exchanger mechanical resistance. In fact, as proved in Figure 48 (a), both the HE length L and side S, and consequently the volume V, monotonically increase using thicker plates. As suggested by Equation 8.54, the plate thermal resistance linearly increases with its thickness and therefore, compatibly with the manufacturing constraints introduced by DMLS, it is convenient to keep this parameter as low as possible. Figure 48 (b) shows that the plate thickness effect on the flow regime is, as expected, totally negligible.

Surface area density

Since the surface area density β is an index of compactness, the expectation, confirmed by Figure 49 (a), is that higher β values produce a decrement of the HE volume V. The monotonically increasing trend of the HE length L is somehow misleading, since from a numerical

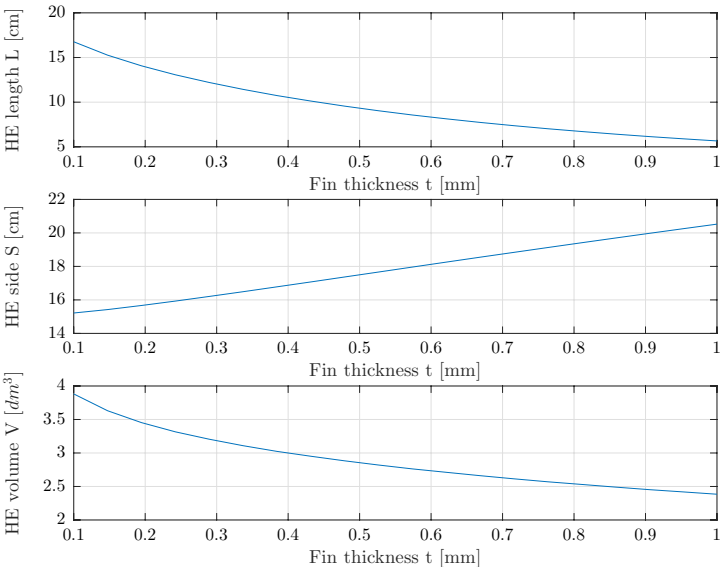

(a) Heat exchanger dimensions (s = 0.4 mm)

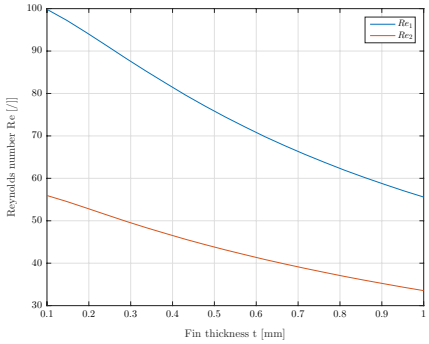

(b) Flow regime (s = 0.4 mm)

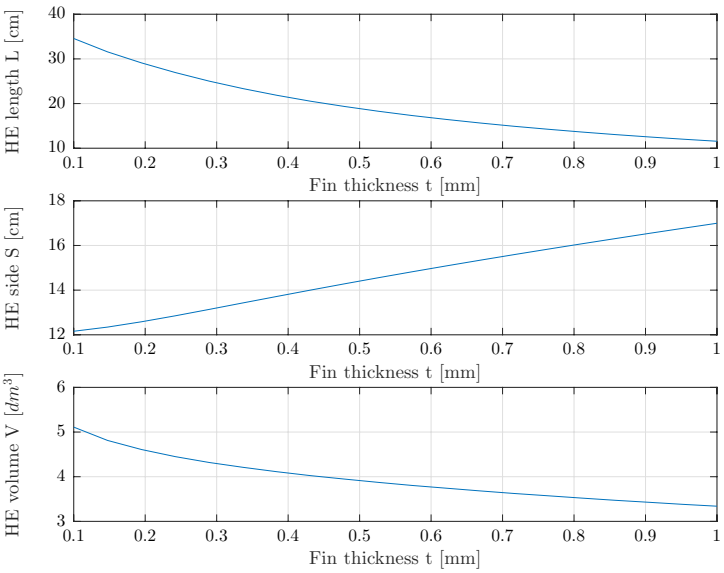

(c) Heat exchanger dimensions (s = 0.8 mm)

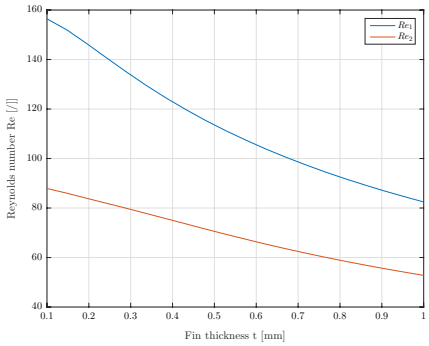

(d) Flow regime (s = 0.8 mm)

Figure 47: Effect of the fin thickness t

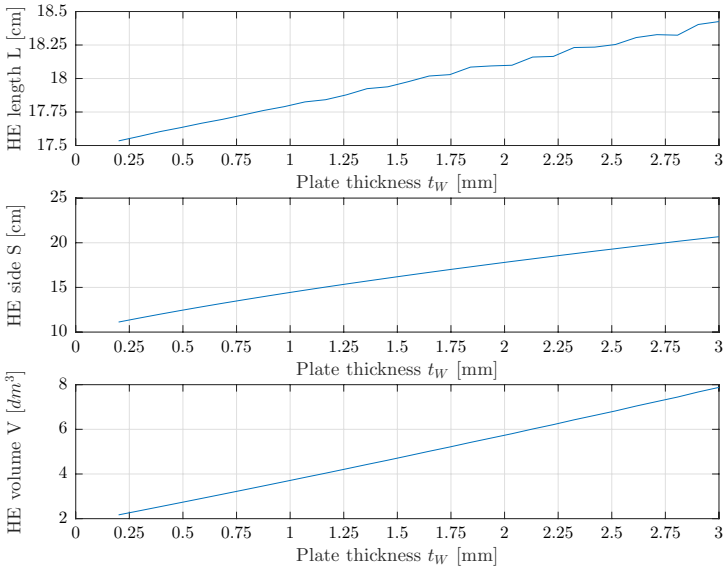

(a) Heat exchanger dimensions

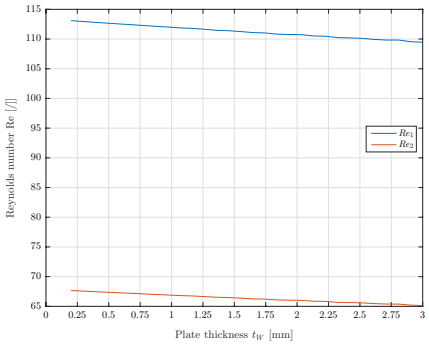

(b) Flow regime

Figure 48: Effect of the plate thickness t_w

standpoint this value remains substantially constant regardless of the compactness index. The remarkable reduction of HE frontal area A_{fr} can be explained by reminding, Equation 8.7, the direct proportionality between the compactness index β and the free flow to frontal area ratio σ. As for the plate thickness, the surface area density effect on the flow regime, shown in Figure 49 (b), is completely negligible.

Cold side mass flow rate

Finally, Figure 50 shows that the heat exchanger length L is virtually independent from the cold mass flow rate $\dot{m}_1$. This result strengthens the impression, derived analyzing previous plots, that the HE length is somehow related to the thermal requirement, while the HE frontal

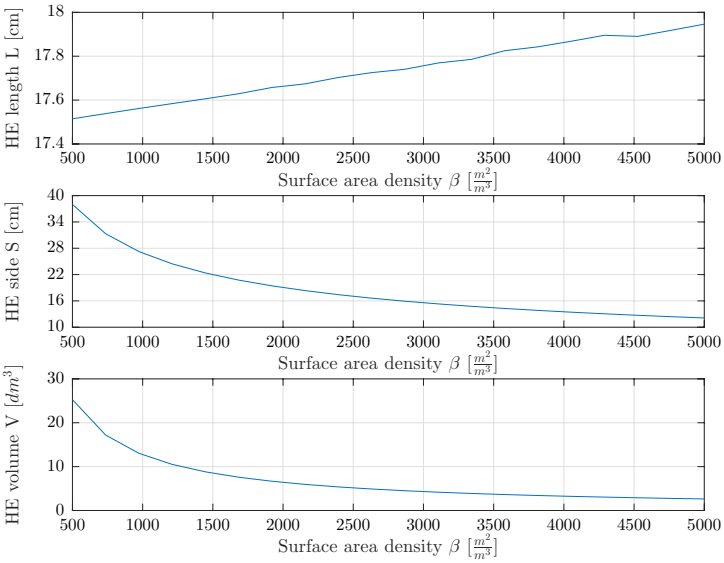

(a) Heat exchanger dimensions

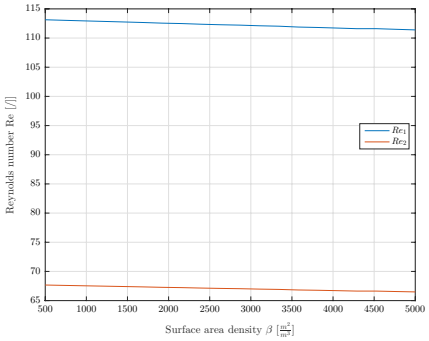

(b) Flow regime

Figure 49: Effect of the surface area density β

area A_{fr} is proportional to the mass flow rate. As the mass flow rate is incremented, also the HE frontal area and the volume linearly increase. Since the mass flow rate has absolutely no effects in terms of Reynolds number, its plot has not been reported.

Effectiveness

Figure 51 confirms that by demanding to the HE better thermal performances and consequently higher effectivenesses ε, the HE length L increases non-linearly, tending to infinite values approaching a unitary effectiveness. Since also HE frontal area A_{fr} follows a similar trend, also the HE volume V is a monotonically increasing function of the HE heat duty.

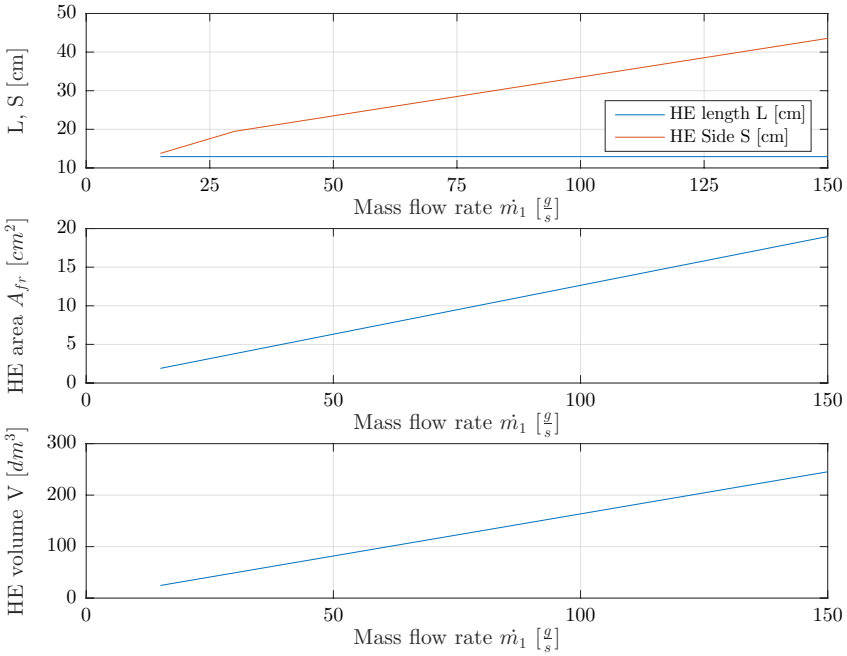

Figure 50: Cold side mass flow rate $\dot{m}_1$ effect on the heat exchanger dimensions

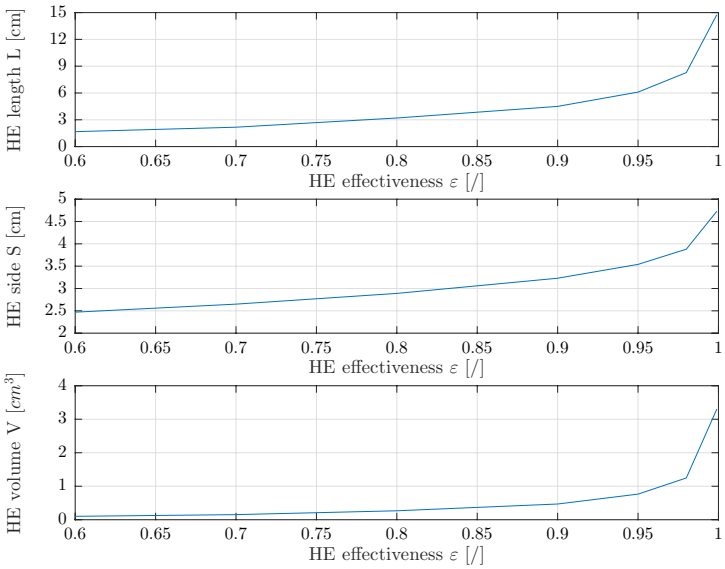

Figure 51: Effect of effectiveness on the heat exchanger dimensions

TABLE XV: PARAMETRIC SWEEP STUDY RESULTS

	b [mm]	t_w [mm]	l_s [mm]	t [mm]	s [mm]	β [/]
L	↑	↑	↑	↓	↑	↑
S	↓	↑	↓	↑	↓	↓
V	↓	↑	↑	↓	↑	↓

The sign of the arrow refers to the effect on the HE dimensions, i.e. length L [cm], side S [cm] and volume V [dm^3], produced by an increment of the column heading parameter.

Conclusions

The effects of each individual parameter on the heat exchanger dimensions are collected in Table XV, while the main parametric sweep study outcomes are hereafter summarized as:

1. As Reynolds number Re never exceed the value of hundred, the flow regime remains always laminar. The procedure used to derive these results, which relies on some correlations valid only under laminar regimes, is therefore adequate and coherent with the physical reality of the design problem.
2. The heat exchanger volume can be minimized adopting close and thin plates, short and large fins, a reduced free flow width and a high surface area density.
3. While the heat exchanger length is independent from the mass flow rate, the frontal area and volume are directly proportional to this quantity.

TABLE XVI: HEAT EXCHANGER INDEPENDENT DESIGN PARAMETERS

Side	b [mm]	t [mm]	l_s $[mm]$	p_t $[mm]$	β $\left[\frac{m^2}{m^3}\right]$	t_w $[mm]$	f_s [/]
Cold	1.2	0.3	2.0	0.8	3600	1.0	0.75
Hot	1.2	0.3	2.0	0.8	3600	1.0	0.75

TABLE XVII: HEAT EXCHANGER DEPENDENT DESIGN VARIABLES

Side	ρ_{fin} $\left[\frac{fin}{m}\right]$	s [mm]	h_c $[mm]$	l [mm]	D_H $[mm]$	α $\left[\frac{m^2}{m^3}\right]$	σ [/]
Cold	1250	0.5	1.2	0.6	0.64	982	0.157
Hot	1250	0.5	1.2	0.6	0.64	982	0.157

8.4.2 Heat exchanger optimum design

Since the sizing procedure previously described is such to automatically satisfy both the thermal and pressure drops requirements, the optimum heat exchanger design coincides with the one having minimum dimensions. Pursuing this objective and considering as design guide the parametric sweep study outcomes above derived, it has been possible to define what is deemed to be the best combination of HE independent design parameters. These and the corresponding dependent variables are respectively represented in Table XVI and Table XVII.

As previously anticipated, the sizing procedure is expected to converge within a few iterations. Figure 52 confirms that 3 iterations are sufficient to obtain results that are sensibly stable and coherent with the design requirements.

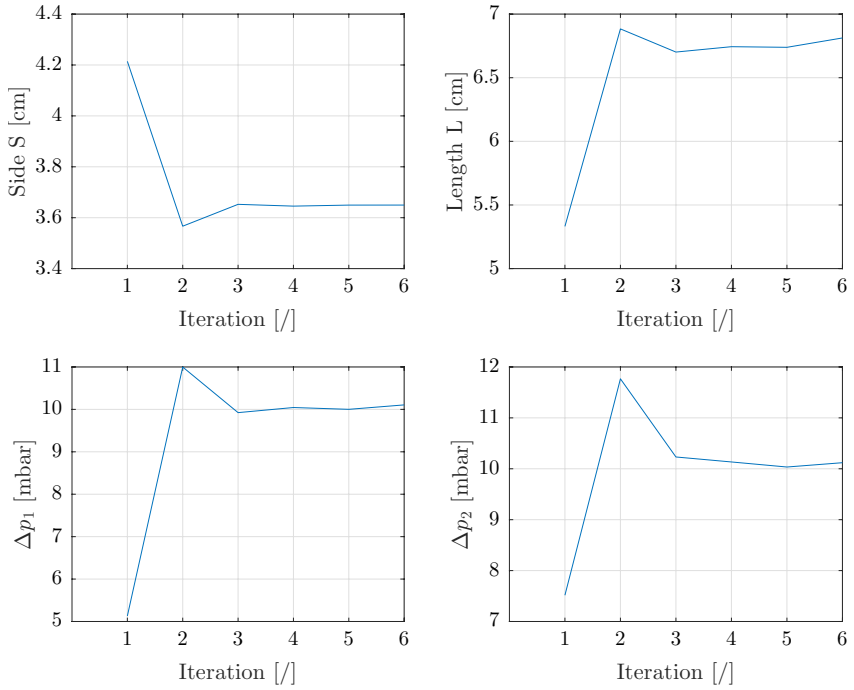

Figure 52: Convergence of the heat exchanger MATLAB sizing procedure

In fact, the actual pressure drops value is substantially coincident with the imposed limit of 10 *mbar* for both HE sides. The square frontal area side S amounts to about 36.5 mm, while the length L is approximately equal to 68 mm. It is important to remember that these geometric values are only temporary, because the HE definitive dimensions, in order to guarantee the device manufacturability, must be an integer multiple of the fin dimensions. Following the procedure introduced earlier in this chapter, it is possible to derive the HE actual dimensions listed in Table XVIII. The HE length L remains unchanged, while width W and height H only slightly changes, so that the frontal section aspect ratio remains still almost unitary.

TABLE XVIII: HEAT EXCHANGER FINAL DIMENSIONS

L [mm]	W [mm]	H [mm]	A_{fr} $[cm^2]$	$A_{0,c}$ $[cm^2]$	$A_{0,h}$ $[cm^2]$	V $[cm^3]$
68.0	37.1	38.4	14.25	2.21	1.93	96.9

TABLE XIX: SIZING PROCEDURE INPUT AND OUTPUT COMPARISON

	σ_1 [/]	σ_2 [/]	f_s [/]	β $\left[\frac{m^2}{m^3}\right]$	α_1 $\left[\frac{m^2}{m^3}\right]$	α_2 $\left[\frac{m^2}{m^3}\right]$	D_H [mm]
Input	0.157	0.157	0.75	3600	982	982	0.64
Output	0.155	0.136	0.73	4000	969	848	0.62
$\Delta\%$	1.3	13.3	2.7	11.1	1.32	13.6	3.2

Knowing the exact heat exchanger geometry and applying the procedure previously described in this same chapter, it is straightforward to re-calculate the quantities initially used as input for the HE sizing procedure, in order to check that the numerically designed HE features are coherent with the model inputs. The results of this operation, shown in Table XIX, are in substantial agreement with the ones inputted into the MATLAB model, therefore allowing to definitively validate this heat exchanger design.

In spite of the more than satisfactory results produced by the by-now familiar $\varepsilon - NTU$ based sizing procedure and of the remarkable solution accuracy proved by Table XIX, it is worth reminding that the final heat exchanger design will be derived only in the next chapter

by means of CFD tools, which, not being bounded to any semi-empirical geometry dependent correlations, allow to truly optimize the fin shapes and ultimately the HE design.

In conclusion, the function of this model is two-fold. First, the optimum heat exchanger design above described is a valuable starting point for CFD simulations. Second, the results obtained earlier in this chapter will be exploited to validate, by comparison, the CFD results which, because of their purely numerical nature, are often not adherent to the physical reality of the problem.

CHAPTER 9

HEAT EXCHANGER CFD DESIGN

In this chapter, the heat exchanger optimum design obtained in Chapter 8 will be challenged and optimized by means of *Computational Fluid Dynamics* (CFD) tools. Simulations will be implemented on COMSOL Multiphysics [70], an interactive environment for modeling and simulating scientific and engineering problems. After a first introductory part about the set-up of CFD simulations, the results whereby obtained will be described and the definitive heat exchanger design will be benchmarked against other possible designs. Finally, the outcomes produced in Chapter 8 by applying a $\varepsilon - NTU$ based design method will be compared with the CFD results hereafter derived.

9.1 Design Methods Comparison

CFD is the discipline of simulating fluid systems using modeling and numerical methods. While CFD describes the HE physical domain as a 3-D distributed parameters system, $\varepsilon - NTU$ method condenses all the information into a simpler 0-D lumped parameters model.

A CFD simulation, solving for the temperature and pressure scalar fields and for the vectorial velocity distribution over the whole 3-D model, generates an incredible amount of data. If this level of spacial detail is indeed useful for local design optimization, it is not required to gage at a glance the HE performances. This is why lumped quantities are often derived starting from the exhaustive spacial variables distribution, thus enabling the comparison of different designs.

In short, results post-processing, allowing to extract the useful information and visualize the solution in an effective way, is of crucial importance while dealing with CFD simulations.

CFD most important advantage over the thermo-hydraulic design procedure introduced in previous Chapter 8 is the complete freedom to change the model inputs, in terms of geometry, materials and physics of the problem. Naturally, this flexibility comes with some inconveniences as well, notably the need for high computational power and the possibly long solving time. Because of these factors, while it is possible to run an iterative MATLAB procedure on a personal computer, it is usually unfeasible to solve a complex CFD model on the same machine. Also, changing the simulation input implies time-consuming operations such as the production of new CAD files and their discretization. In other words, while being very flexible, CFD tools are also very resource demanding, both in terms of hardware and solving time.

On the contrary, the lean $\varepsilon - NTU$ based method allows to rapidly obtain a solution. Because of the reduced number of underlying equations and of their algebraic nature, such a thermo-hydraulic design procedure could be solved even by hand-calculations, evidencing how the solving time and the required computational power associated with a MATLAB implementation are really risible.

The results obtained by a $\varepsilon - NTU$ based design procedure, because of their reliance on semi-empirical correlation, are accurate within 15-20 %. As of 2006, according to R.K. Shah [63], in spite of the significant improvements of CFD analysis, this design tool did not yet allow to predict CHE performances within 5 %. In 2011, Aslam Bhutta et al. have instead stated that, thanks to the rapid spreading of CFD as a design tool, the accuracy has sensibly improved

and is now of "acceptable quality" [71]. In short, both design methods are still facing accuracy problems, which means that for industrial applications prototyping and experimental testing are still mandatory.

Based on the above considerations, the choice of using, in this thesis, both design procedures in sequence can be better understood: the light and versatile $\varepsilon - NTU$ based method provides a preliminary design in a rapid and cost-effective way, which is then fed as input to the more accurate, but also resource-demanding, CFD simulations.

9.2 CFD Model

A typical CFD simulation includes the following steps:

1. Geometry generation
2. Physics definition
3. Mesh generation
4. Solver set-up and numerical solution
5. Post-processing

This section aims precisely at illustrating the physics involved in the simulation of a heat exchanger, at introducing the concept of computational grid or *mesh*, at describing the solvers available on COMSOL Multiphysics and finally at defining the simulation model in terms of geometry, boundary and initial conditions.

9.2.1 Physics

Heat exchangers have been defined in Chapter 7 as devices used to transfer thermal energy between two or more fluids at different temperatures and in thermal contact. Hereafter the equations describing heat transfer and fluid flow physics will be therefore introduced.

It is renown that the fluid flow is governed by the Navier-Stokes equations [48; 72], which are an expression of the physical principles of mass, Equation 9.1, momentum, Equation 9.2, and energy conservation, Equation 9.3.

$$\frac{\partial \rho}{\partial t} + \nabla \cdot (\rho\, \mathbf{u}) = 0 \tag{9.1}$$

$$\rho \cdot \left(\frac{\partial \mathbf{u}}{\partial t} + \mathbf{u} \cdot \nabla \mathbf{u} \right) = -\nabla p + \nabla \cdot \boldsymbol{\tau} + \mathbf{F} \tag{9.2}$$

$$\rho\, c_p \left(\frac{\partial T}{\partial t} + (\mathbf{u} \cdot \nabla) T \right) = -(\nabla \cdot \mathbf{q}) + \boldsymbol{\tau} : \mathbf{S} - \frac{T}{\rho} \frac{\partial \rho}{\partial T}\bigg|_p \left(\frac{\partial p}{\partial t} + (\mathbf{u} \cdot \nabla)\, p \right) + \mathbf{Q} \tag{9.3}$$

The meaning of the previously undefined variables introduced in the Navier-Stokes equation is the following:

- $\mathbf{u}$ $\left[\frac{m}{s}\right]$: velocity vector.
- $\boldsymbol{\tau}$ [Pa]: viscous stress tensor.
- $\mathbf{F}$ $\left[\frac{N}{m^3}\right]$: volume force vector.
- $\mathbf{q}$ $\left[\frac{W}{m^2}\right]$: heat flux vector.
- $\mathbf{Q}$ $\left[\frac{kg}{m^3}\right]$: volumetric heat sources.
- $\mathbf{S}$ $\left[\frac{1}{s}\right]$: strain rate tensor.

The strain rate tensor $\mathbf{S}$ is defined as:

$$\mathbf{S} = \frac{1}{2}\Big(\nabla\mathbf{u} + (\nabla\mathbf{u})^T\Big) \tag{9.4}$$

Generally speaking, energy conservation is stated through the *First Law of Thermodynamics* (FLT), which in integral form can be written as in Equation 9.5, where U_0 is the total internal energy, H_0 is the total enthalpy and W is the mechanical work.

$$\frac{d}{dt}\int_\Omega \rho \cdot U_0 \, dV + \oint_{\partial\Omega} \Big(\rho\mathbf{u}H_0 - \lambda\nabla T - \boldsymbol{\tau}\mathbf{u}\Big) \cdot \mathbf{n} \, d\Omega = Q + W \tag{9.5}$$

However, since internal energy U and enthalpy H are not easily measured nor conveniently used in simulations, this law is usually rewritten using the absolute temperature T as independent variable, thus producing the so-called *heat equation*, shown in Equation 9.3. In Comsol Multiphysics, the integral Equation 9.5 is therefore never used while solving, but only as global post-processing quantity, so to allow the user to check if energy conservation has been numerically respected [72; 73].

Since momentum is a vectorial quantity, the Navier-Stokes equation allow to solve for 5 unknowns, namely the 3 components of the velocity field $\mathbf{u}$, the pressure p and the temperature T. Then, it is evident that to close the equations system, the following additional constitutive equations need to be added:

- The viscous stress tensor $\boldsymbol{\tau}$ expression depends on the fluid nature. Since gaseous mixtures can be idealized as Newtonian fluids[1], the viscous stress tensor can be expressed as in Equation 9.6, where μ is the dynamic viscosity.

$$\boldsymbol{\tau} = 2\mu\mathbf{S} - \frac{2}{3}\mu(\nabla \cdot \mathbf{u})\mathbf{I} \tag{9.6}$$

- Heat transfer by conduction is commonly described through the *Fourier's equation*, shown in Equation 9.7, where λ denotes the material thermal conductivity. Conduction is the only heat transfer mode through solid Inconel 718, while in the fluid domains both conductive and convective mechanisms are active. Radiative heat tranfer is supposed to be negligible[2].

$$\mathbf{q} = -\lambda\nabla T \tag{9.7}$$

- Once that temperature and pressure are known, the ideal gas law, represented one more time in Equation 9.8, allows to determine the density field. It is worth reminding that the fluid specific volume v is the reciprocal of density ρ.

---

[1] *Newtonian fluids* are defined as fluids whose viscosity is function of the state variables but not of flow velocity [43].

[2] This assumption is justified by the fact that the introduction of radiative heat transfer, while just marginally affecting the heat exchanger design, results in an exponential increment of the required computational power [74]. In fact, radiation introduces non-local couplings between the nodes, which results in a relatively dense system matrix whose solution calculation is substantially more resource-demanding.

$$p \cdot v = R \cdot T \tag{9.8}$$

As stated in Chapter 6, while designing a heat exchanger attention is focused on its steady-state behavior, i.e. on whether the device is capable of effectively transferring thermal power. As a consequence, all the time-dependent terms disappear, yielding at the simpler stationary differential form of the Navier-Stokes equations shown in Equation 9.9, Equation 9.10 and Equation 9.11.

$$\nabla \cdot (\rho \mathbf{u}) = 0 \tag{9.9}$$

$$\rho \mathbf{u} \cdot \nabla \mathbf{u} = -\nabla p + \nabla \cdot \boldsymbol{\tau} + \mathbf{F} \tag{9.10}$$

$$\rho \, c_p \big(\mathbf{u} \cdot \nabla\big) T = -\big(\nabla \cdot \mathbf{q}\big) + \boldsymbol{\tau} : \mathbf{S} - \frac{T}{\rho} \frac{\partial \rho}{\partial T}\bigg|_p \big(\mathbf{u} \cdot \nabla\big) p + \mathbf{Q} \tag{9.11}$$

Although the Navier-Stokes equations are theoretically valid regardless of the flow regime, COMSOL Multiphysics provides different modules for laminar and turbulent flows [70]. In fact, directly solving the Navier-Stokes equations for high Reynolds numbers (DNS, *Direct Numerical Simulation*) would be an extremely resource-demanding task because the whole range of spatial turbulence need to be explored. In practice, turbulent flows are preferentially described by using

a simplified set of equations, notably the RANS (*Reynolds-Averaged Navier-Stokes*) equations combined with a turbulence model such as the $K - \varepsilon$ [70].

Based on the results produced by the preliminary heat exchanger design object of Chapter 8, which suggested a laminar flow regime, the steady state Navier-Stokes equations above derived are the ones actually used by COMSOL Multiphysics and specifically by the *Conjugated Heat Transfer Module*, which combines together heat transfer and laminar flow [70; 75].

9.2.2 Mesh

Numerical analysis tools demand the subdivision of the geometric model into small subdomains, often called elements or cells. The *mesh*, or grid, is defined as the collection of all these elements. The purpose of the mesh is twofold [76]:

1. It allows to write, in a discretized form, a set of equations for each cell. These element-referred equations, assembled in a unique stiffness matrix, form an algebraic system which needs to be solved.
2. It enables the representation of the solution field.

During both operations, solving and representing the solution, the fact that the meshed model is not exactly equal to the original geometry determines an approximation error. It is intuitive that a finer mesh leads to a better subdivision of complex geometries and thus allows to reduce such an error. In order to obtain a reliable computational grid, the geometric CAD model itself must be of high quality. To this aim, W. Frei suggests to perform a *defeaturing* operation on the CAD file imported from another software, in order to get rid of geometric details not relevant for the simulation purposes [77].

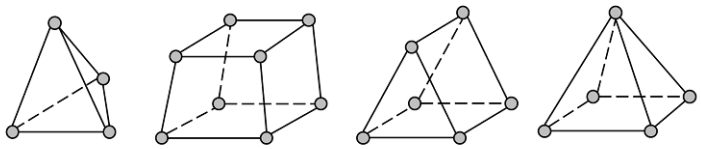

Figure 53: Typologies of 3-D mesh elements [Image credit: COMSOL]

It exists four types of 3-D meshing elements, as represented in Figure 53: tetrahedrals, hexahedrals, prisms and pyramids [76]. The free tetrahedrals, because they allow to mesh geometries of any shape, are by far the most used ones and they represent the default choice on most softwares, including COMSOL Multiphysics.

Another type of mesh commonly used is the boundary layer mesh. This is particularly useful to solve for the velocity field at the interface between fluid and solid, where a no-slip wall boundary condition is usually applied and therefore there is a strong gradient to be resolved. In this regions, the solution, while varying slowly in the tangential direction, changes rapidly in a direction normal to the wall. As a consequence, it is convenient to use elements having a very high aspect ratio, i.e. long and very thin.

It is of crucial importance to make clear that the solution is computed exclusively at the nodes. The final 3-D distribution is derived interpolating the nodal values using suitable basis functions, also known as *Lagrangian* polynomials, whose order generally determines the solution accuracy. However, there are exceptions: using second order Lagrangian elements *P2* is not effective while dealing with convection dominated problems, i.e. having a high *Péclet* number.

This case, characteristic of flow fields, is better solved using linear elements *P1* than quadratic ones. Although COMSOL allows to adopt diverse discretization orders for different physics, in order to limit the computational power requirements linear shape functions *P1* have been selected for both the velocity and the pressure fields.

COMSOL Multiphysics comes with an automatic meshing tool, that adapts the computational grid to the specific physics of each problem. However, this predefined function is not always able to distinguish where the mesh needs to be finer and where, instead, refining the grid only increases the computational requirements. A user-defined mesh set-up yields at better results, as it is possible to manually specify, for every mesh domain, the following parameters:

- Maximum and minimum element size
- Maximum allowed element growth rate
- Resolution of narrow regions
- Curvature factor
- Mesh distribution
- Boundary layers number and thickness

This approach allows to use a relatively rough default computational grid and to refine the mesh only where locally needed. This way, it is possible to obtain rather accurate solution while limiting the need for computational resources and the solving time.

In conclusion, it is worth reminding that since each problem has a unique solution, also the numerical solution need to be proved independent from the computational grid. Therefore, in order to validate the results of a CFD simulation it is cardinal to carry out a *mesh refinement study* (MRS), in which the grid size is gradually reduced until a further mesh refinement does not alter the simulation outcomes.

9.2.3 Solvers

If from a physical perspective the Navier-Stokes equations are an expression of the conservation laws, from a mathematical standpoint they are partial differential equations (PDE), that is equations containing unknown multi-variable functions together with their partial derivatives.

To this day, the analytical solution of the Navier-Stokes equations is still an open problem. The huge interest revolving around this set of equations has pushed the *Clay Mathematics Institute* to classify it as one of the seven *Millennium Prize Problems* and to award 1 million of USD for its solution. In practice, the Navier-Stokes equations are solved by means of numerical analysis tools, the most diffused methods being finite differences (FDM), in disuse because of its inaccuracy, finite elements (FEM) and finite volume (FVM). COMSOL Multiphysics is a finite element software.

FVM has been the first method applied to CFD and is still widely used because of its velocity. The grid is generated subdividing the spacial domains into cells, where the governing equations in integral form are imposed. FEM, traditionally reserved for structural analysis, is gaining consensus even in the field of CFD because it is more stable and accurate than FVM, the drawback being longer solving times. The nodes are situated at the vertexes of each discrete element and their number depends on the order of the Langrange polynomial.

COMSOL Multiphysics name derives from its capacity to efficiently deal with multi-physics problems, i.e. situations in which multiple different interdependent physics need to be simultaneously solved over the same domain. A heat exchanger, involving at least heat transfer, fluid flow and structural analysis, is a remarkable example of multi-physics model.

Depending on how much the different physics influence each other, there are two possible solution approaches [78; 79]:

1. Fully coupled approach

   It is necessary when there is a 2-ways coupling, i.e. a strong interaction, between the physics. Solving for all the physics in parallel, this approach is very memory and time demanding and should be therefore used only when indispensable.

2. Segregated approach

   It solves the different physics in series, yielding at satisfactory results only when the coupling between different physics is weak or unidirectional. Several iterations are required before reaching the convergence, but each step is less resource demanding than the fully coupled approach, so that in most cases this second method produces faster solutions.

As proved in Chapter 4, temperature strongly influences the mixtures thermo-physical properties and consequently the flow field. On the contrary, this only mildly affects the heat transfer and hence the temperature distribution. Also, the mechanical stresses, which are dependent on pressure and temperature, only marginally affect the heat transfer and the fluids flow. In conclusion, a heat exchanger model can be considered as a weakly coupled multi-physics system. Then, an efficient segregated solver can be used, which solves first for the velocity field and the pressure and only then for the temperature.

In order to solve the system of equations shown in Equation 9.12, Comsol offers again two possible families of solvers [80]:

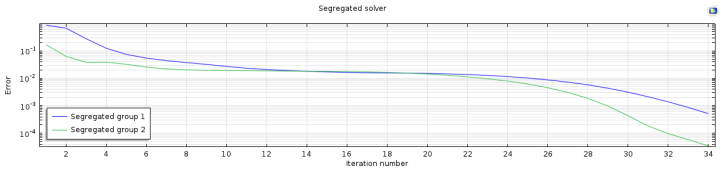

Figure 54: Example of MUMPS convergence plot

$$\boldsymbol{K}(u) \cdot \boldsymbol{u} = \boldsymbol{f} \tag{9.12}$$

1. Direct solvers

These solvers search for the solution in a one step process, simply inverting the stiffness matrix K as shown in Equation 9.13. This method, in spite of being robust, is very memory intensive, as the RAM scaling relative to the number of DOFs is approximately quadratic [74]. However, when the size of the problem is limited and the matrix is sparse, this class of solvers provides a fast and cost-effective solution.

$$\boldsymbol{u} = [\boldsymbol{K}(u)]^{-1} \cdot \boldsymbol{f} \tag{9.13}$$

Among the solvers available in Comsol, MUMPS has been preferentially used because it is not excessively memory intensive and, when the RAM is over, it allows to store a part of the solution on an external storing device (*out-of-core* option). Figure 54 shows a typical convergence plot obtained using a MUMPS solver.

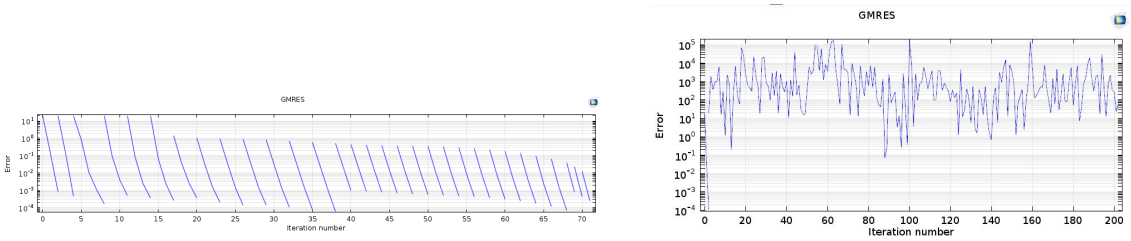

(a) Successful (b) Failure

Figure 55: Examples of GMRES convergence plot

2. Iterative solvers

These solvers approach the solution gradually, until convergence, defined as the achievement of a relative error smaller than 10^{-3}, is reached. Since memory requirements scale linearly with the number of DOFs, these methods are less resource demanding than direct solvers [74]. Among Comsol iterative solvers, the most frequently used has been the GMRES (*Generalized Minimum Residual Method*), which offers superior performances when dealing with non-symmetric matrices. *Geometric Multigrid* is a subroutine used to accelerate the convergence of the GMRES basic iterative method, by rapidly finding a solution on a coarser mesh and then correcting the fine mesh solution accordingly [81].

The biggest inconvenient of indirect solvers is that they need a manual set-up and are intrinsically less robust than direct methods. In fact, even if the problem is mathematically well-posed, they may still fail to find the solution if the mesh is not fine enough or the initial conditions are too far from the actual solution, as shown in Figure 55 (b).

Based on the above, it is evident that whenever possible it is preferable to use a direct solver. As a matter of fact, most of the simulations have been solved with MUMPS. GMRES, which has been used for simulations featuring more than two millions of DOFs, has sometimes failed to converge because of a not sufficiently fine mesh. In fact, it is worth highlighting that while a linear problem always converges in one single step, regardless of the mesh quality, non linear systems are extremely mesh dependent and may never converge.

The bottom level solver used to solve the non-linear equations system is the damped *Newton-Raphson* method [82]. Developed as a solver for linear systems, this tool, thanks to the addition of numerical damping, allows to iteratively find the solution even for strongly non-linear systems such as those described by the Navier-Stokes equations.

As a final remark, it is noteworthy to remember that in Comsol it also exists a parametric solver, which allows to significantly reduce the solving time while performing parametric sweeps. If the variable parameter is not of geometrical nature or related to the mesh, the parametric solver exploits the previous solution as initial guess for the following study thus substantially reducing the number of iterations to convergence. In conclusion, COMSOL solvers hierarchy is schematically represented in Figure 56.

9.2.4 Simulation set-up

Before starting a simulation, a geometrical CAD file and suitable boundary conditions need to be defined. Moreover, in spite of the previous hypothesis of stationarity, because of the strong non-linearity of the Navier-Stokes equations, also initial conditions, interpretable as a first solution guess, need to be specified.

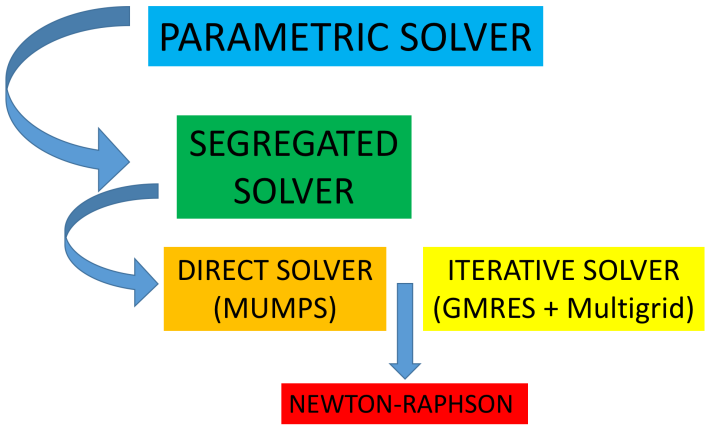

Figure 56: COMSOL Multiphysics solvers hierarchy

9.2.4.1 Geometric model

The geometry, which needs to include both the solid and fluid domains, has been parametrically defined directly on COMSOL boolean drawing environment. Since CFD simulations tend to be very resource-demanding, both in terms of computational power and solving time, reducing the model dimensions and exploiting any existing geometrical symmetry is mandatory to be able to solve the simulation without needing a supercomputer.

To this aim, only a reduced portion of the actual heat exchanger will be object of simulation. In fact, the results obtained in Chapter 8 suggest that, since the final HE includes about 10 layers, the border effects are negligible. As a consequence, hereafter the simulation domain will be limited to just one layer of the complete heat exchanger.

This miniaturized computational domain can be further reduced by subdividing it into two pieces, symmetric relative to the HE longitudinal mid-plane, and by splitting each fluid domain

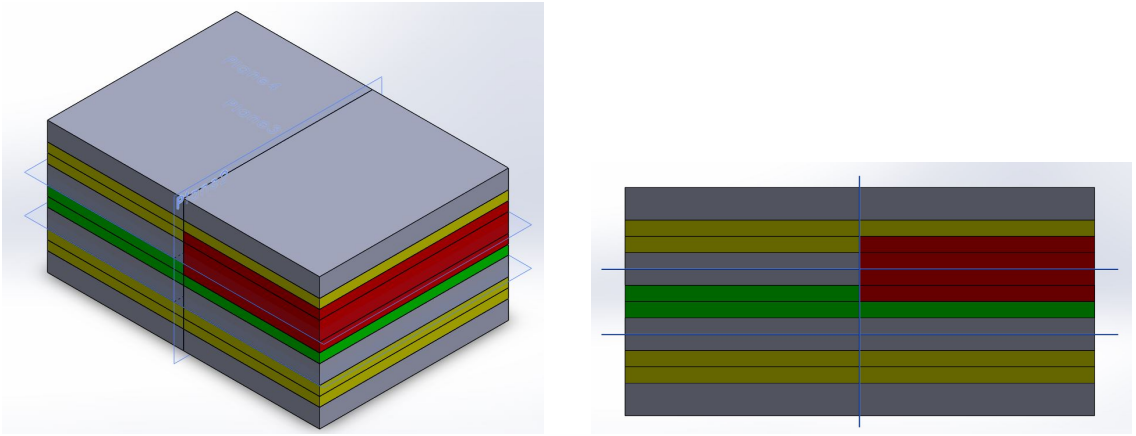

(a) Isometric view (b) Frontal view

Figure 57: The final reduced CFD computational domain, highlighted in red, includes only a quarter of one of the N_H hot fluid layers shown in green, a quarter of one of the N_C cold fluid layers represented in yellow and half of one of the N_W gray solid plates.

in two equal parts. Considering the generic heat exchanger geometry shown in Figure 57, it is possible to appreciate the existence of the symmetry planes which justify the model reduction procedure above described. In conclusion, the final computational domain represented in red in Figure 57, since it is approximately 60 times smaller than the full heat exchanger, allows to tremendously reduce the need for computational resources.

Another crucial information in terms of geometric model is the modification of the physical fluid domains by including the additional fluid regions shown in yellow in Figure 58. These purely virtual domains preceding the inlets and following the outlets, because of their characteristic shape, will be referred to as *spikes* and are necessary for the sake of the simulation accuracy.

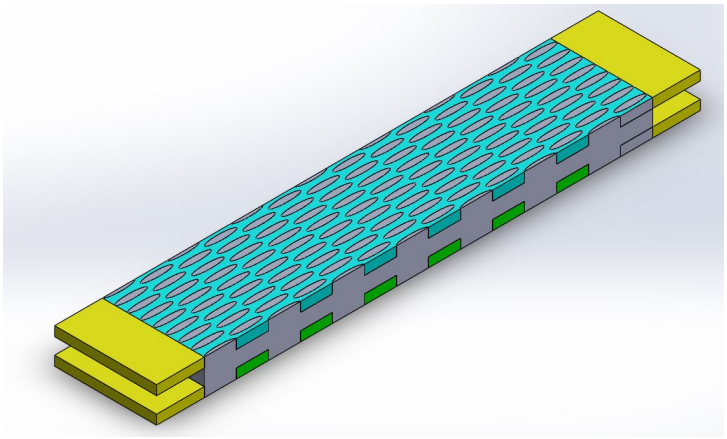

Figure 58: Modified simulation geometry after the *spikes* addition.

In fact, at the very beginning, while running simulations without adopting such a modified geometry, in spite of the apparent numerical conservation of energy, the cold side outlet temperatures were always substantially higher than expectable. Countless verifications of the model demonstrated that this behavior was due to the existence of non-physical heat fluxes induced by the strong temperature gradients existing around the inlet sections. These fluxes caused the software to mess up with the outlet temperatures, i.e. with the fluids enthalpies, so to numerically fix the energy balance.

Adding the spikes shown in Figure 58, i.e. sort of lungs for better flow mixing and gradients resolution, completely solved energy conservation issues. After trying several spike lengths S, a value of 4 mm, later implemented on all the tested geometries, was found to be the best compromise between the simulation accuracy and the longer solving time due to the addition of further computational domains.

9.2.4.2 Boundary conditions

Defining suitable boundary conditions (BCs) is crucial to obtain accurate simulation results. At the same time, some approximations have to be made so to limit the required computational power and the solving time. Considering a heat exchanger, it is possible to distinguish two main categories of boundary conditions:

1. Thermal
2. Flow

Hereafter follows a brief description of which BCs have been selected and how these have been implemented on the COMSOL Multiphysics environment.

Thermal boundary conditions

As previously mentioned, heat exchangers can be considered adiabatic devices. In fact, despite the high temperature difference between the system and the surrounding environment, a proper thermal insulation almost completely annihilates the heat losses. Hence, all the external surfaces wrapping up the heat exchanger, except for the fluid ports and the symmetry boundaries, will be modeled as ideal thermal insulators.

Through a symmetry plane, because of its same definition, there is no heat transfer, meaning that from a thermal standpoint symmetry boundary conditions are absolutely equivalent to an insulation condition.

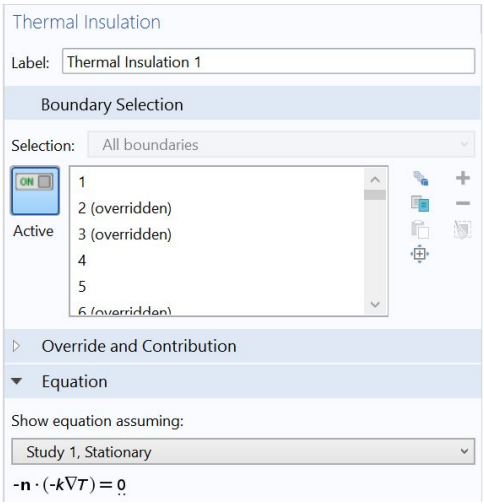

(a) Thermal insulation

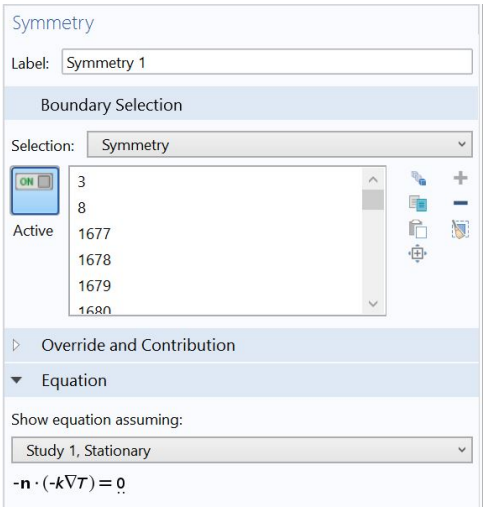

(b) Symmetry

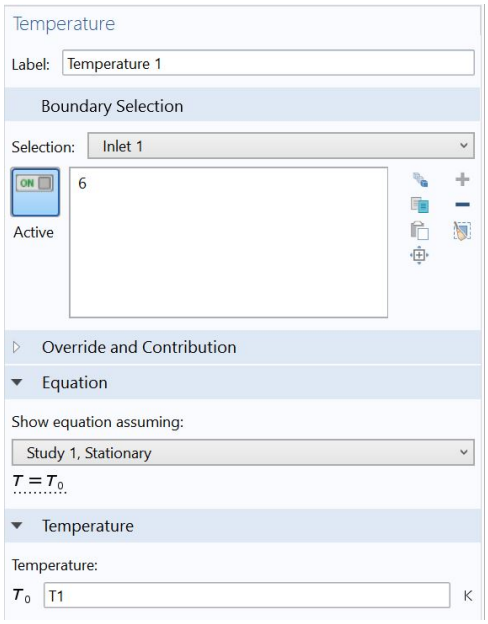

(c) Temperature

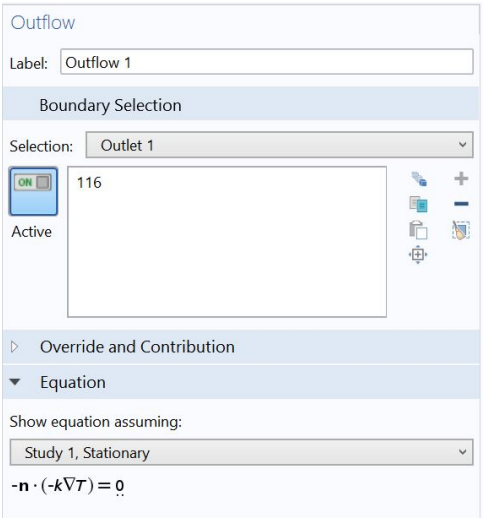

(d) Outflow

Figure 59: COMSOL Multiphysics thermal boundary conditions

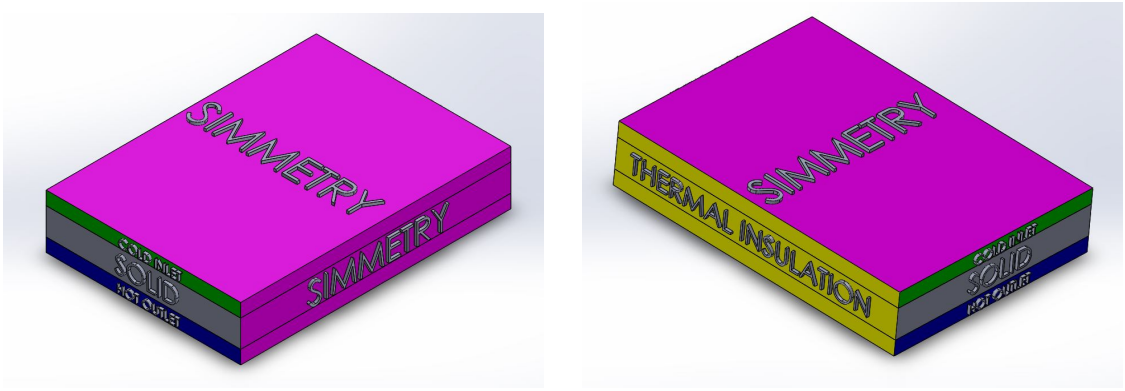

(a) Right view (b) Left view

Figure 60: Thermal boundary conditions

Since the mixture inlet temperatures do not vary under steady-state conditions, they will be modeled by imposing a constant temperature on the inlet boundaries. Finally, in correspondence of the outflow, the temperature gradient and consequently the thermal flux is zeroed.

Figure 59 summarizes the four different boundary conditions implemented on Comsol Multiphysics heat transfer module, while Figure 60, again representing a generic heat exchanger model, highlights to which geometrical boundaries the previously defined BCs refer.

Flow boundary conditions

In order to properly define a flow, it is necessary to specify on which boundaries the mixtures enters and leaves the system, i.e. the inlets and outlets, and where solid walls prevent its motion.

It is intuitive that every external surface, except the fluid ports and the symmetry boundaries, and the inner solid surfaces will be modeled as walls. From a mathematical standpoint, this *no slip* condition corresponds to prescribing a nil fluid velocity at the walls.

Symmetry boundary conditions naturally prescribe that the velocity field is the same on opposite sides of the symmetry plane. Mathematically, a zero normal fluid velocity is then imposed on the symmetry boundary.

Considering an inflow boundary, because of the continuity equation displayed in Equation 9.14, for well-defined fluid and geometrical properties, it is equivalent to impose the volumetric flow rate $\dot{V}$, the mass velocity G or the mass flow rate $\dot{m}$. Due to the available input data, this last option will be hereafter used to impose a fluid flow.

$$\dot{m} = \dot{V} \cdot \rho = A \cdot v \cdot \rho = G \cdot A \tag{9.14}$$

The outlet boundaries have been instead modeled by imposing a zero relative pressure and by suppressing the back-flow. Figure 61 summarizes the four different boundary conditions implemented on COMSOL Multiphysics laminar flow module.

9.2.4.3 Initial conditions

As a rule, initial conditions are required only for time dependent problems. However, considering the strong non-linearity of the Navier-Stokes equations, reasonable initial conditions, which the solvers interpret as a first solution guess, are required even for stationary simulations. In fact, in absence of a good starting point, the solving time increases exponentially and it is even possible that the solver will fail to find the solution. Then, both the initial velocity and temperature fields need to be specified as simulation input. Since the main computational difficulty lies in solving the fluid velocity field, it is cardinal to provide an initial velocity information coherent with the real flow direction.

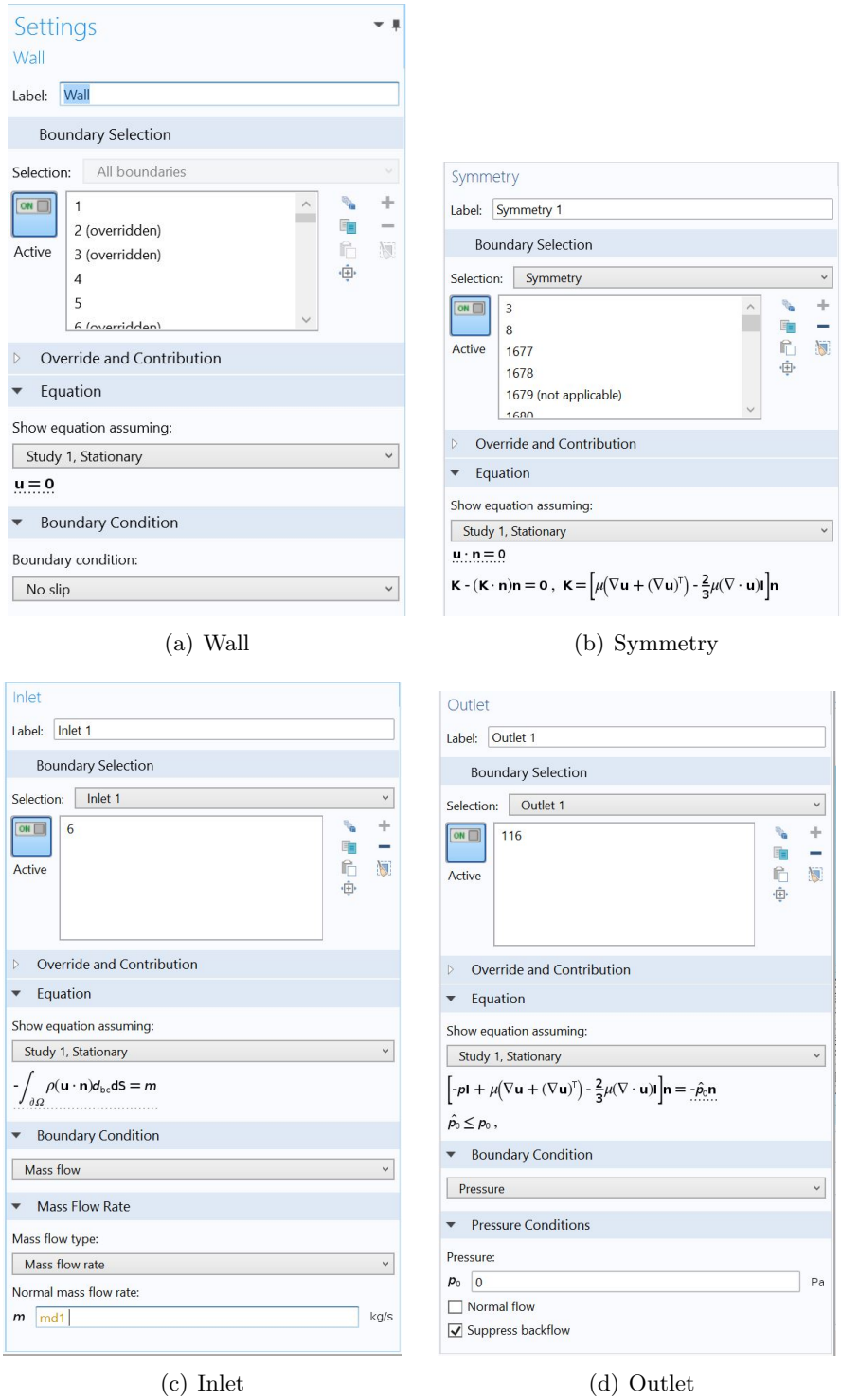

(a) Wall (b) Symmetry

(c) Inlet (d) Outlet

Figure 61: Comsol Multiphysics flow boundary conditions

9.3 Fin geometries

The heat exchanger design result of the MATLAB sizing procedure object of Chapter 8 is the natural candidate as first geometric model for CFD simulations. This geometry, represented in Figure 62 (a), features a modified version of offset-strip fins, in which, thanks to the manufacturing process by AM, the flat parts connecting consecutive fins have been removed. It is intuitive that such a geometry, characterized by rectangular and sharp-cornered fins, while being very performing from a thermal standpoint and resulting in a very high effectiveness ε, also induces very high pressure drops. Since these losses are higher than the limit value previously defined, this fin geometry is not compatible with HELMETH design requirements.

A natural modification of rectangular fins consists in smoothing the corners, in particular by rounding the fin tips as shown in Figure 62 (b). This second fin geometry, while determining a slight reduction in terms of thermal performances, allows to drastically cut the pressure drops, which are easily maintained below the prescribed limit of 10 mbar.

Finally, an elliptical fin design, represented in Figure 62 (c), has been evaluated to further reduce the pressure losses while improving, relative to a rounded geometry, the thermal performances and therefore the heat exchanger effectiveness ε.

To sum up, the performances of the following three fin geometries have been accurately characterized by means of extensive CFD simulations:

1. Rectangular
2. Rounded
3. Elliptical

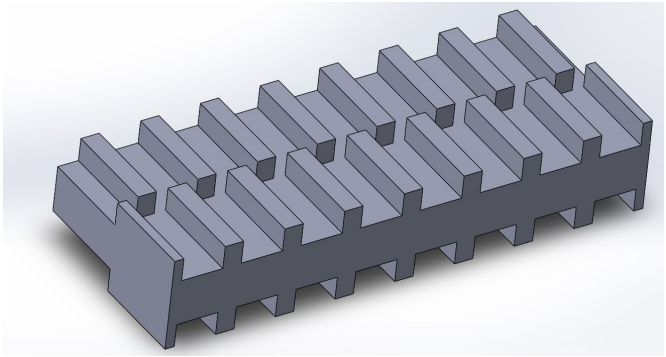

(a) Rectangular

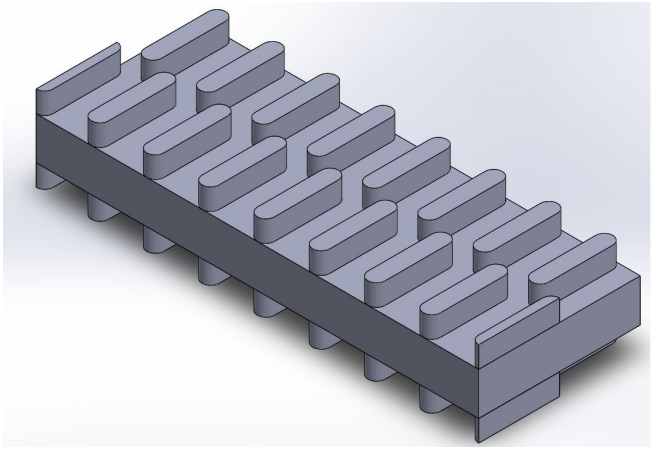

(b) Rounded

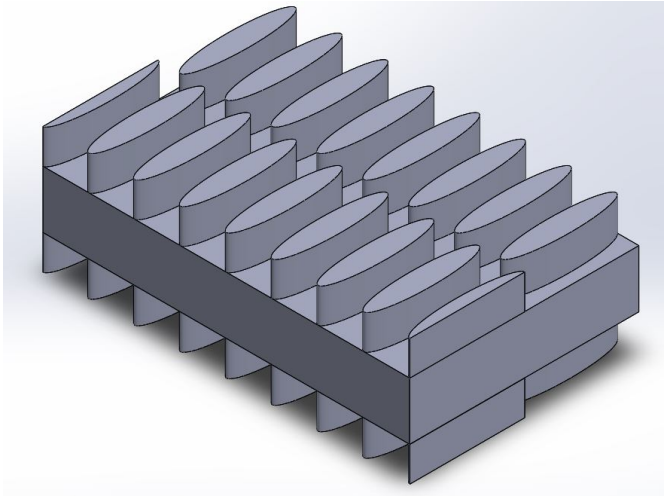

(c) Elliptical

Figure 62: Fin geometries object of CFD simulations

For each of these three fin geometries, using the outcomes of several parametric sweep studies as guidelines, it has been possible to define an optimum heat exchanger design. However, for reasons of conciseness, only the results relative to the most performing elliptical fins design will be analyzed in detail. The knowledge gained through the CFD testing of rectangular and rounded fin geometries will instead allow to draw, at the end of this chapter, a comparison between the thermo-hydraulic performances of different heat exchanger layouts and eventually to confirm that the choice of elliptical fins is motivated.

9.3.1 Elliptical fins geometry

Most of the planar geometrical parameters describing individual elliptical fins and their relative positioning in a fin array are graphically reproduced in Figure 65. Including also the third spacial dimension, the geometric quantities of importance for an elliptical fins heat exchanger can be summarized as:

- Fin length l_s
- Fin width a
- Transversal fins pitch p
- Free flow width $s = p - a$
- Longitudinal fins pitch p_v
- Fins overlap $ov = b - p_v$
- Fin height t

Depending on the relative value between the fin length l_s and the fin longitudinal pitch p_v, it is possible to distinguish three cases: overlap ov, gap and perfect alignment consecutive fin rows. Simulation evidence has suggested that the most performing designs do not feature a gap nor a partial overlap, but rather an alignment of consecutive rows of fins.

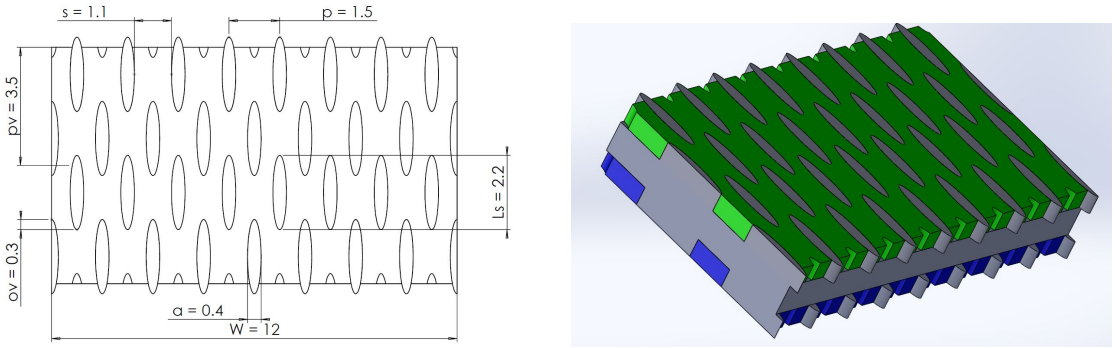

(a) 2-D view (b) 3-D view

Figure 63: Elliptical fins overlap

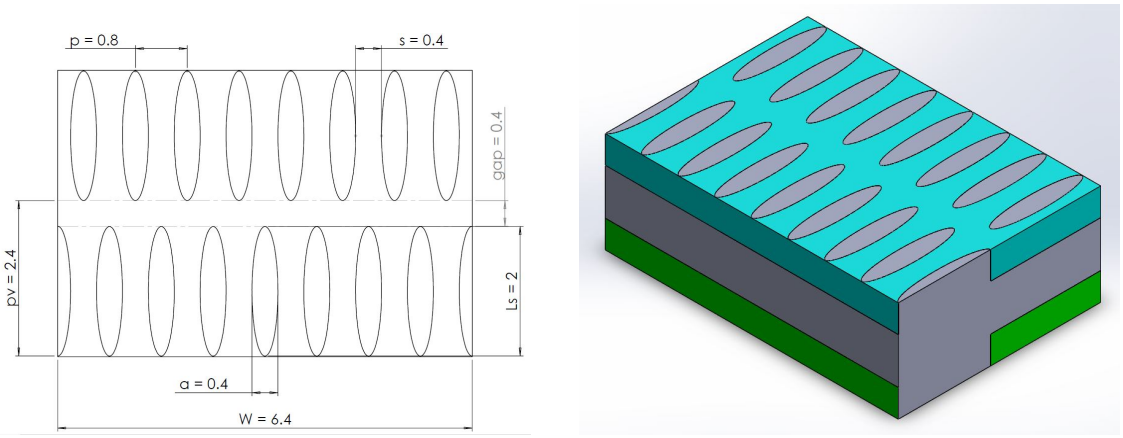

(a) 2-D view (b) 3-D view

Figure 64: Elliptical fins gap

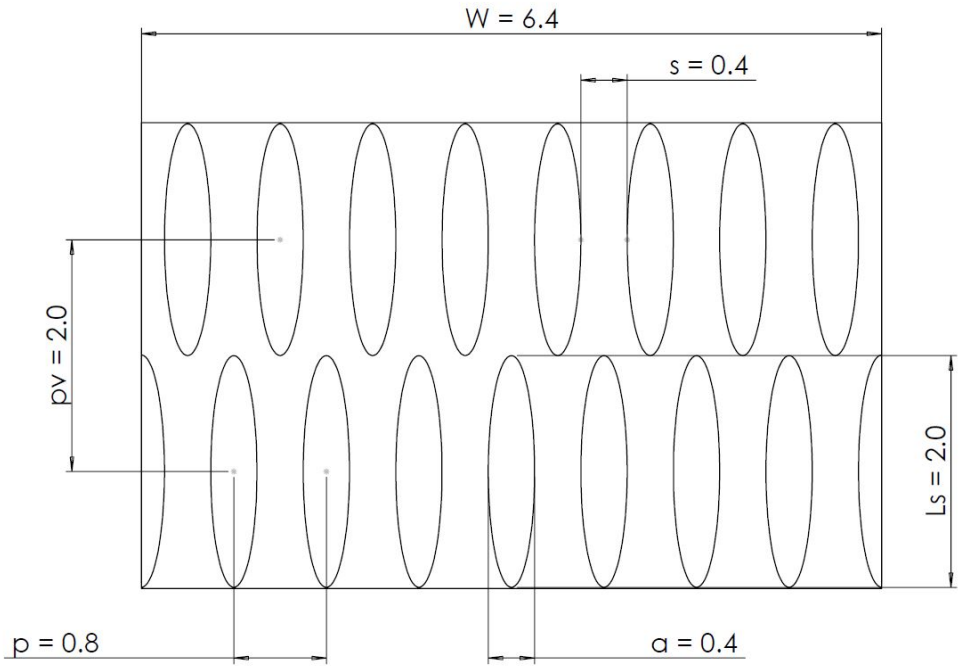

Figure 65: 2-D elliptical fins array

In fact, overlapping fins, represented in Figure 63, only mildly improves the heat transfer, while greatly increasing the pressure drops due to the smaller available minimum free flow area. On the contrary, leaving a gap between fins, as shown in Figure 64, does not sensibly affect heat transfer nor the pressure losses, simply producing an unnecessary increment of the heat exchanger length and worsening the surface area density β.

On these grounds, the geometric condition of exact consecutive fin rows alignment is assumed as reference design solution for all the simulations hereafter reported.

9.4 Results

Having concluded the first introductory part about heat exchangers CFD simulation, this section is completely dedicated to the presentation of the results whereby obtained. In the following, the numerical outcomes relative to the most promising elliptical fin shape, whose geometry has already been defined above, will be described, first presenting the outcomes of a parametric sweep study and then analyzing the performances of what is deemed to be the best design. Finally, after having assessed the simulation accuracy, the CFD geometric model will be scaled to the actual heat exchanger dimensions.

It is worth highlighting that the optimum heat exchanger design hereafter described is the result of an optimization process relying on hundreds of CFD simulations, which have allowed to assess the effect of every geometric parameter on the HE performances and to truly optimize the final heat exchanger design.

9.4.1 Parametric sweep study

The purpose for performing a parametric sweep study, as anticipated in Chapter 8, is revealing the system sensitivity to a particular parameter. The quantities selected for this sweep analysis include most of the heat exchanger geometric parameters, including its length, and the mass velocity G, while the output variables used to evaluate the device performances are the outlet temperatures and the pressure drops. Since the objective of this parametric sweep study is the identification of trends rather than the evaluation of a specific HE design performances, in the following a rather short, i.e. low effectiveness, heat exchanger geometric model will be used so to reduce the simulations solving time.

TABLE XX: INPUTS OF THE CFD PARAMETRIC SWEEP STUDY

a [mm]	l_s [mm]	s [mm]	t [mm]	t_w [mm]	L [mm]	G $\left[\frac{kg}{m^2 \cdot s}\right]$
1.9	0.4	0.4	0.6	1.0	19.0	12

Table XX reports the reference values for each of the parametric sweep study variables. It is important to highlight that the flow is imposed by means of the mass velocity G rather than by a mass flow rate $\dot{m}$. This choice allows, regardless of the free flow area value, which will vary during the parametric sweep study, to maintain constant the inlet flow velocity and therefore to have exactly the same thermo-fluid dynamic conditions for every simulation.

Fin width

Figure 66 suggests a reduced sensitivity to the fin width a, both in terms of heat transfer and pressure losses. In fact, as evidenced by Figure 66 (a) the cold side outlet temperature variation over the whole range of fin widths, inferiorly bounded to 0.2 mm because of manufacturing constraints and superiorly limited to 0.8 mm, is smaller than three degrees. The fact that the cold side outlet temperature minimum is aligned with the hot side outlet temperature maximum is an evidence that energy conservation law is respected.

Figure 66 (b) highlights how, adopting thinner fins, the pressure drops for both the HE sides decrease until a critical fin thickness of 0.6 mm is reached, after which the cold side pressure losses start increasing again. Considering that the free flow width s is assumed to be constant, the overall effect of increasing the fin thickness a is a larger heat exchanger. Therefore, even if

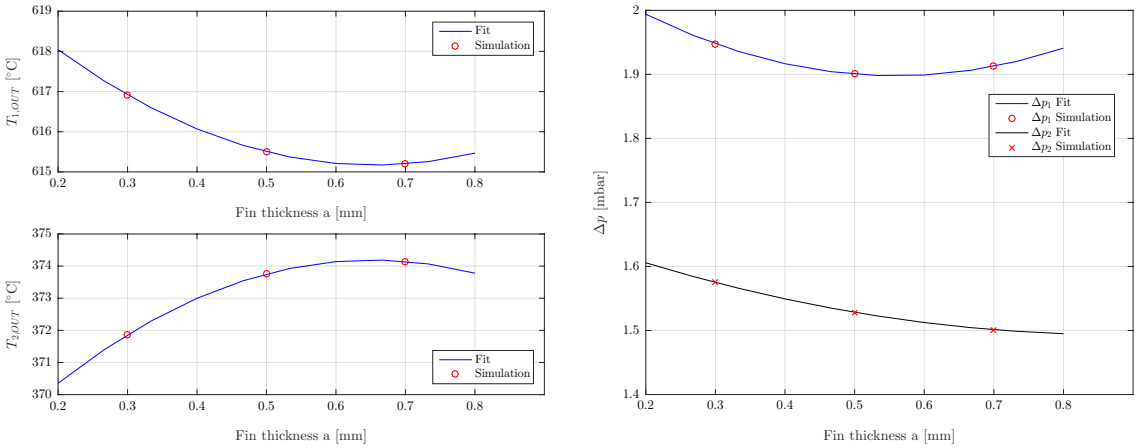

(a) Outlet temperatures (b) Pressure drops

Figure 66: Effect of fin width a

from an hydraulic standpoint fin widths ranging between 0.4 and 0.7 mm are almost equivalent, in terms of compactness it is convenient so select the smaller value of 0.4 mm.

Fin length

Figure 67 (a) shows that shorter fins, triggering more frequent fluid detachments and consequently improving the mixing, substantially enhance heat transfer determining higher cold side outlet temperatures. However, as proved by Figure 67 (b), the more frequent fluid-fin detachment also determines much higher pressure losses.

While the effect in terms of heat transfer is monotonic and almost linear, the quadratic pressure behavior shows the presence of a minimum, which can be explained by considering that the total pressure losses are the sum of two contributions following opposite trends:

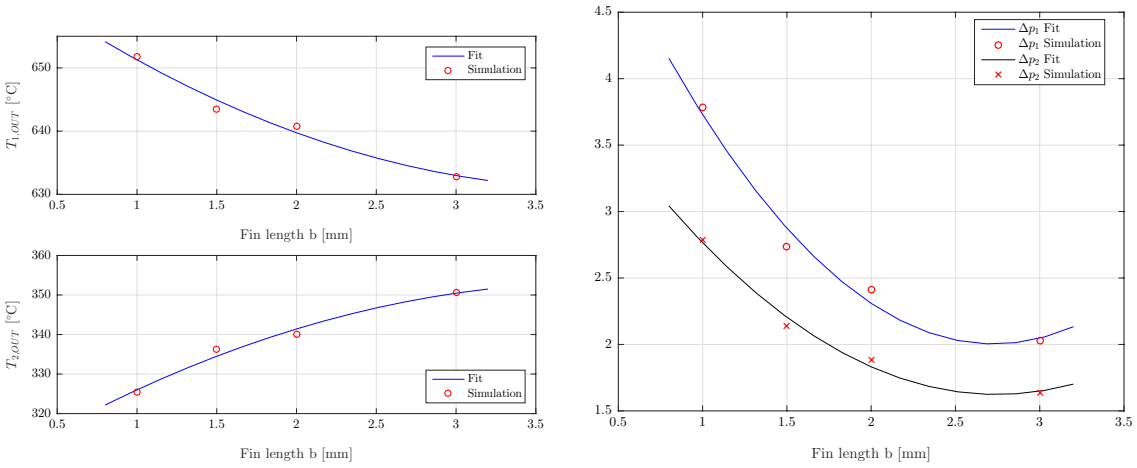

(a) Outlet temperatures

(b) Pressure drops

Figure 67: Effect of fin length l_s

1. Since the heat exchanger length L is supposed constant, a change in the fin length directly affects the number of fin rows, which in turns determines the frequency of fluid-fins collisions and the resulting pressure drops.
2. Pressure losses due to wall friction, on the contrary, increase with the fin length l_s, as a consequence of the higher contact area.

In conclusion, even if using very short fins would be an attractive mean to boost heat transfer, because of the quadratic behavior of pressure drops it is not convenient to design fins shorter than 2 mm.

Free flow width

Decreasing the free flow width, as shown in Figure 68 (a), the cold side outlet temperature can increase of as much as 60 $°C$, because of the higher heat transfer area per unit of fluid

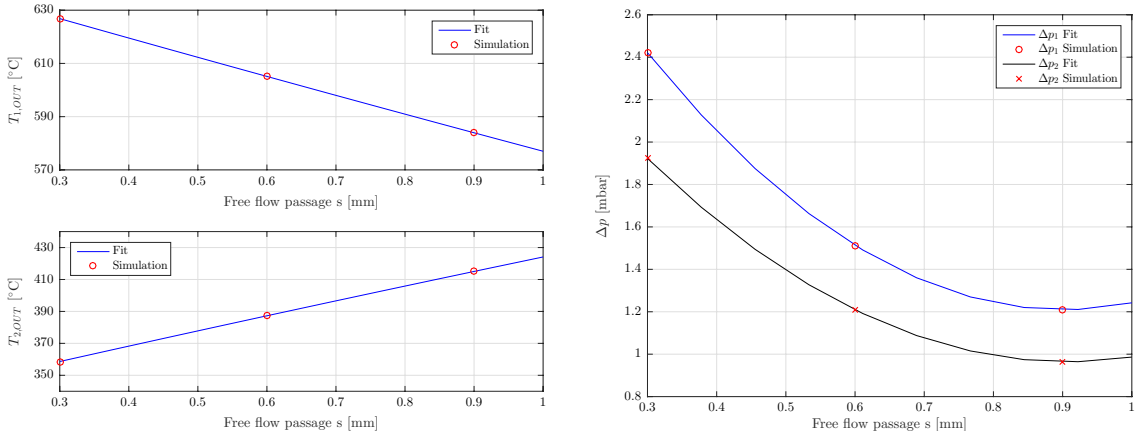

(a) Outlet temperatures

(b) Pressure drops

Figure 68: Effect of free flow width s

volume. In other words, by adopting narrower passages every fluid particle, being closer to a hot surface, can be more easily heated up.

Unfortunately, Figure 68 (b) shows that by reducing the free flow width pressure drops increase as well, with a non linear behavior. In conclusion, considering the strong variability of outlet temperatures, is spite of the higher pressure losses, it is advisable to select values of free flow width s lower than 0.5 mm.

Fin height

Figure 69 (a) proves how increasing the fin height induces moderate positive effects in terms of heat transfer. However, the temperature trend is non monotonic, meaning that for elevated fin heights the cold outlet temperatures begins decreasing. Heat transfer is also affected by the mass velocity G, which shifts leftwards the temperature maximum.

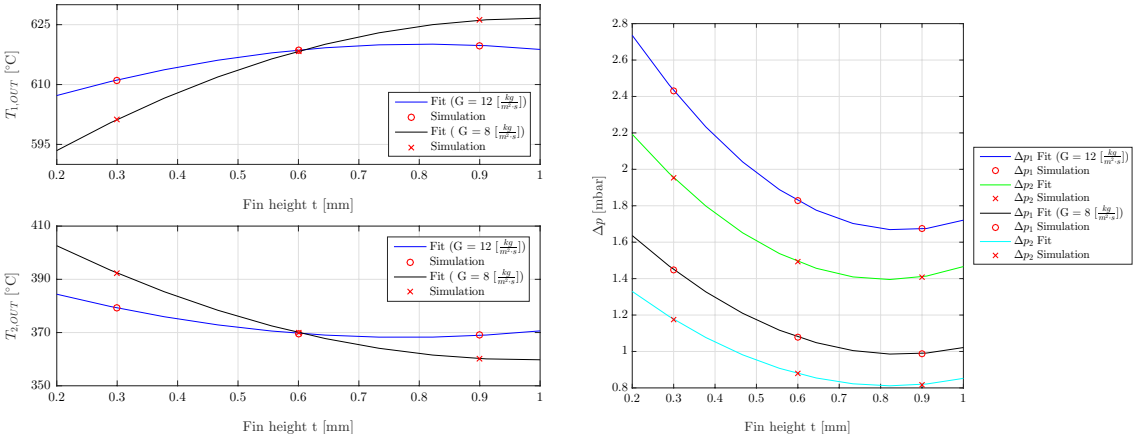

(a) Outlet temperatures (b) Pressure drops

Figure 69: Effect of fin height t

A reduced fin height increases the wall friction between fluid and plates, ultimately leading to the higher pressure drops shown in Figure 69 (b). Pressure losses trend, beyond being non linear, is also non monotonic. The inversion in behavior for fins higher than 0.9 mm can be explained by considering that the fin lateral surface increment triggers higher losses by wall friction. It is almost unnecessary to remark that larger mass velocities G, coherently with the theory introduced in Chapter 8, determine higher pressure drops.

In conclusion, fin heights around 0.6 mm seem to be the most convenient chose.

Plate thickness

Figure 70 (a) confirms the intuition that reducing the plate thickness t_w improves heat transfer, resulting in higher cold side outlet temperatures, while Figure 70 (b) proves that this geometrical parameter has a risible influence on pressure drops.

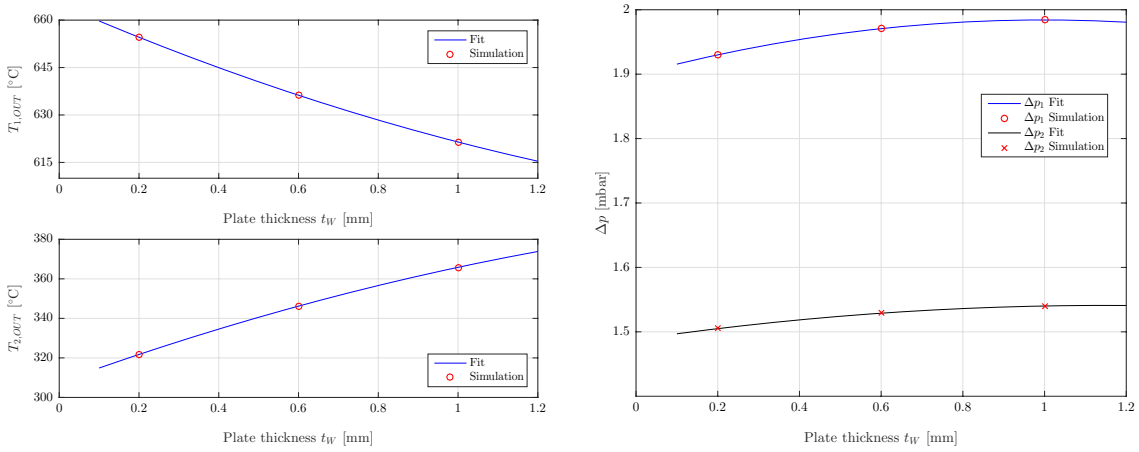

(a) Outlet temperatures

(b) Pressure drops

Figure 70: Effect of plate thickness t_w

In spite of the attractiveness of using thin plates, because of the manufacturing constraints articulated in Chapter 2, the minimum allowed plate thickness is 1 mm.

Mass velocity

Before analyzing the effects of mass velocity G on the HE thermo-hydraulic performances, it is worth reminding that, according to the definition reported in Equation 9.15, a variation in the mass velocity determines a corresponding change in the inlet velocity.

$$G = \frac{\dot{m}}{A_0} = \rho \cdot v \tag{9.15}$$

Figure 71 proves that heat transfer sensitivity to mass velocity G is remarkable and second only to free flow width s, with temperature excursions as high as 50 $°C$ for the short HE and close to 30 $°C$ for the long one.

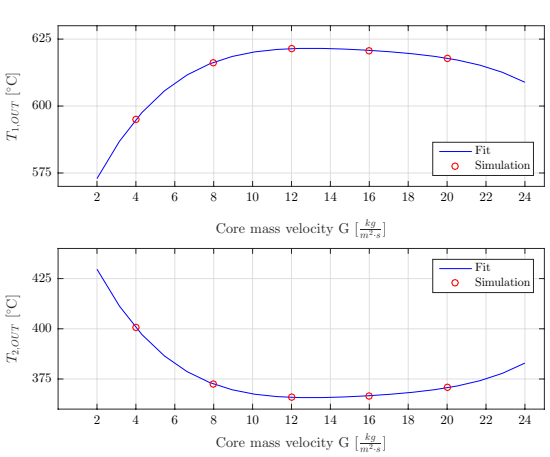

(a) Outlet temperatures (L = 40 mm)

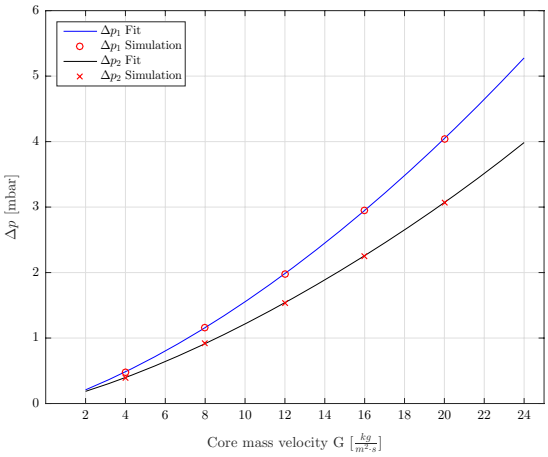

(b) Pressure drops (L = 40 mm)

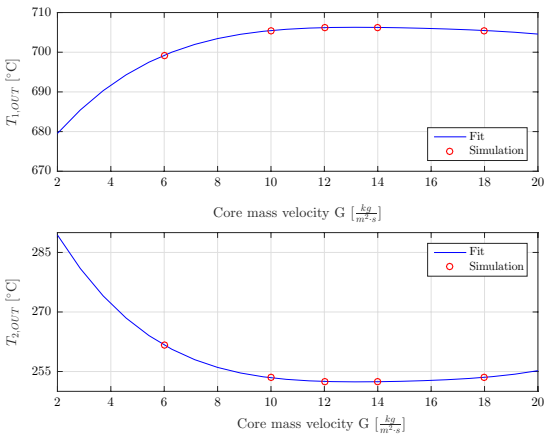

(c) Outlet temperatures (L = 68 mm)

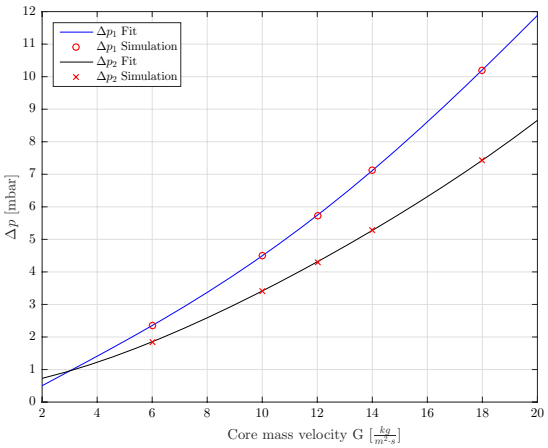

(d) Pressure drops (L = 68 mm)

Figure 71: Effect of mass velocity G

While the pressure drops dependence on the mass velocity is quadratic and monotonic, the cold side temperature plot shows a maximum, which can be explained by taking into account the two following opposite phenomena:

1. Higher mass velocities cause higher flow velocity which, in turn, improve the effectiveness of the convective heat transfer mechanism.
2. As mass velocity increases, the fluid residence time τ in the heat exchanger decreases, thus worsening the heat transfer.

The velocity in correspondence of the maximum is such that, further increasing it, the improvement in terms of convective heat transfer coefficient does not counterbalance the reduced residence time anymore.

Observing better Figure 71, it emerges how in longer heat exchangers the outlet temperatures remains substantially constant increasing the core velocity. In other words, devices having higher effectiveness ε are less sensitive to core velocity G. Figure 71 also confirms a linear dependence of pressure losses on the flow length.

In conclusion, considering the quadratic scaling of pressure drops with the core velocity, values in the range going from 12 to 15 $\frac{kg}{m^2 \cdot s}$ apparently represent the best compromise between the thermal performance and the pressure losses.

Heat exchanger length

Finally, Figure 72 allows to numerically assess the heat exchanger performances sensitivity to its length L. In particular, Figure 72 (b) certifies the substantially linear pressure drops scaling with length, confirming the results produced by previous analyses and the validity of the formulas introduced in Chapter 8.

As derived in Chapter 6, the maximum thermodynamically allowed cold side outlet temperature is bounded to 724 $°C$. This limit allows to better understand the temperature profiles shown in Figure 72 (a) and the effectiveness ε plot represented in Figure 72 (c), where the curves slope, i.e. the gain deriving from building a longer heat exchanger, asymptotically tends to zero. As a matter of fact, a device as short as 40 mm already allows to reach an effectiveness close to 90 %, while a 68 mm long HE approaches a 97 % effectiveness.

On these grounds, with limited benefits in terms of heat transfer on one side and higher pressure drops and fixed costs in terms of material on the other, it is evident that, from an economic standpoint, it is inconvenient to produce extremely effective devices. In conclusion, from an industrial standpoint it is definitely not worth adopting lengths higher than 70 mm.

9.4.2 Optimum design

Using the parametric sweep outcomes as guidelines, it has been possible to shorten the design process by selecting design parameters that are more likely to satisfy the heat exchanger requirements specified in Chapter 8. Starting from these values, after having further explored the effect of geometrical modifications on the HE performances, an optimum heat exchanger design, whose analysis is the object of this section, has been identified.

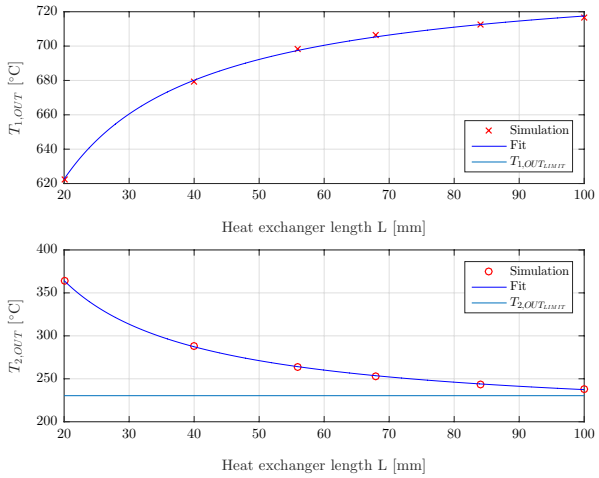

(a) Outlet temperatures

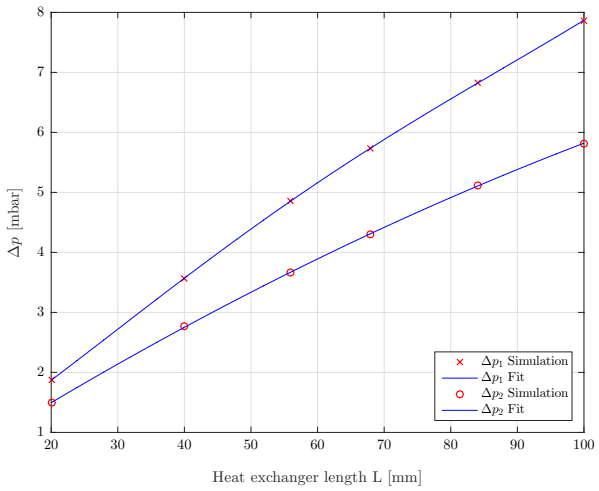

(b) Pressure drops

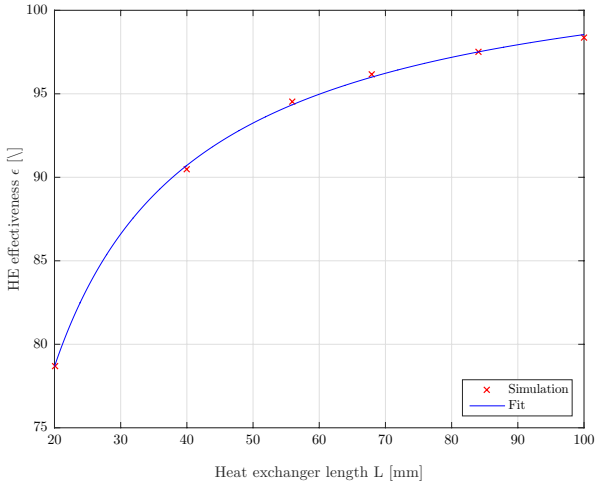

(c) HE effectiveness

Figure 72: Effect of the heat exchanger length L

TABLE XXI: LONGITUDINAL SIMULATION GEOMETRY

$l_s\,[mm]$ [mm]	$p\,[mm]$	ov [mm]	N [/]	L_{HE} [mm]	S [mm]	L_{SIM} [mm]
2.0	2.0	0.0	34	68.0	4.0	76.0

TABLE XXII: TRANSVERSAL AND VERTICAL SIMULATION GEOMETRY

a [mm]	s [mm]	$p_t\,[mm]$	N_C [/]	W [mm]	$A_0\,[mm^2]$	b [mm]	$t_w\,[mm]$	H_{SIM} [mm]
0.4	0.4	0.8	8	6.4	1.92	1.2	1.0	2.2

9.4.2.1 Simulation set-up

Geometry

The numerical values of the geometric parameters defining the optimum heat exchanger geometry are reported in Table XXI and Table XXII, while Table XXIII lists the thermo-fluid dynamics simulation input. These values apply for both fluid sides. The boundary conditions used in the simulation are exactly those described earlier in this chapter, with the fluid ports being positioned as represented in Figure 73. In this figure it is also possible to spot, in yellow, the so-called *spikes*, whose role has been previously clarified.

Finally, Figure 74 shows a detailed graphical representation of one of the 17 two-rows fin modules composing the full-length model, which has been created on Solidworks platform and then imported into the Comsol environment, as shown in Figure 75.

TABLE XXIII: THERMO-FLUID DYNAMICS SIMULATION INPUT

$T_{1,in}\,[°C]$	$T_{2,in}\,[°C]$	p [bar]	G $\left[\frac{kg}{m^2 \cdot s}\right]$	$\dot{m}_1\,[\frac{mg}{s}]$	$\dot{m}_2\,[\frac{mg}{s}]$
230.35	850.00	15.0	12.0	23.040	11.617

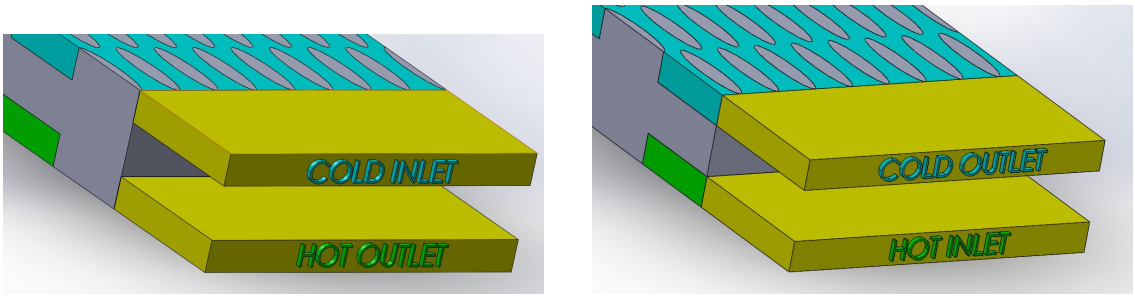

(a) Front view (b) Rear view

Figure 73: Position of the fluid ports

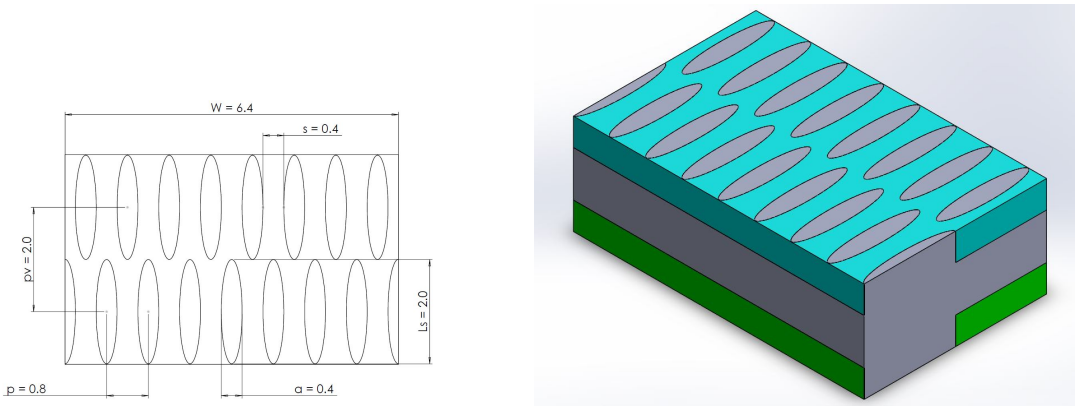

(a) 2-D view (b) 3-D view

Figure 74: Elliptical fin 2-rows module

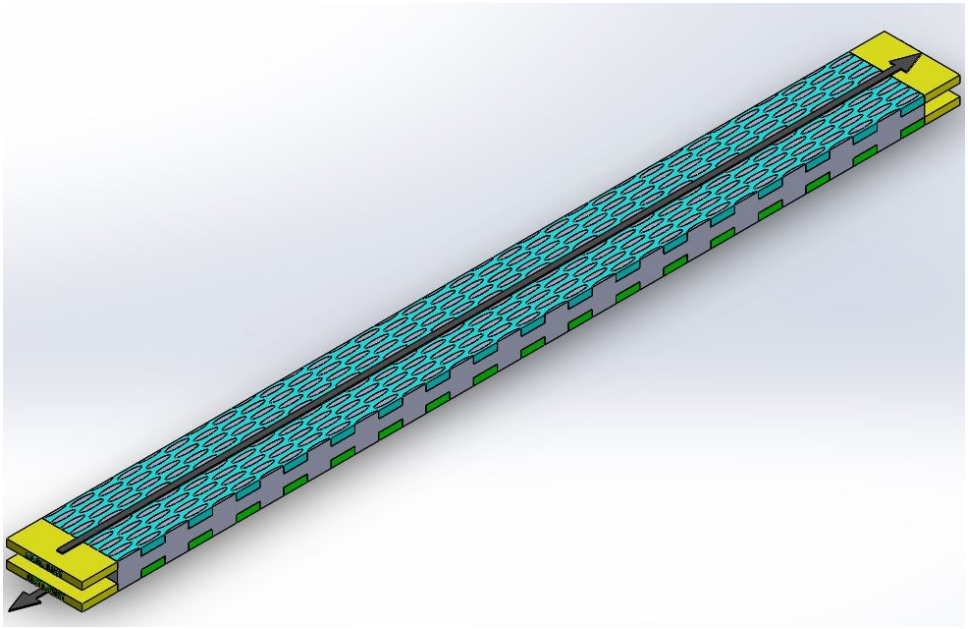

(a) Solidworks: the arrows indicate the flow directions

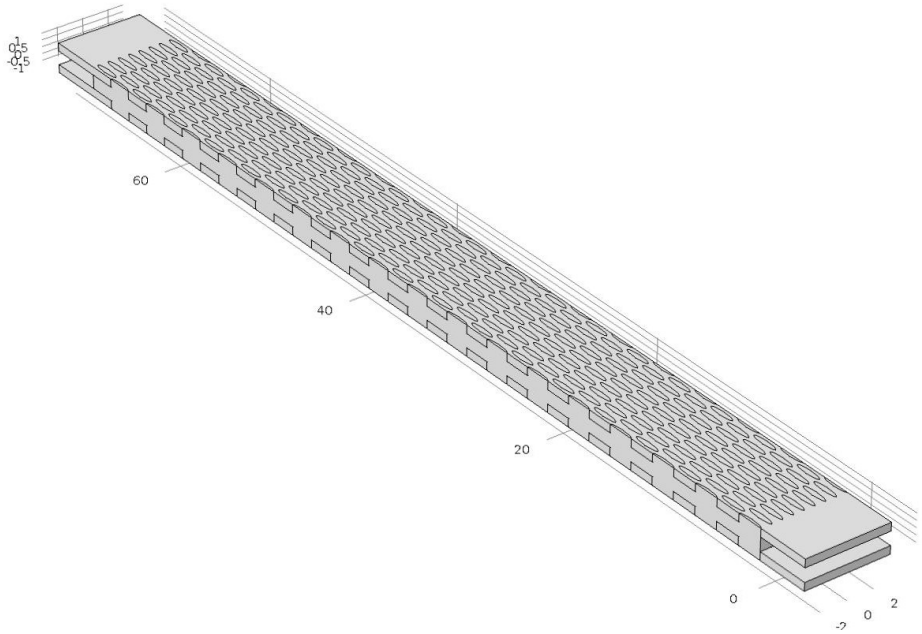

(b) Comsol

Figure 75: Simulation full geometric model

Mesh

In order to solve the CFD simulation, the COMSOL geometry represented in Figure 75 (b) needs to be meshed, producing Figure 76 (a). Looking at this figure, it stands out that the mesh is not homogeneous, in particular being substantially denser in the fluid domains than in solid regions. This is not true for the *spikes*, where the mesh is not as fine as in other fluid domains because these regions have no fins, which means that heat transfer is already over and the velocity field solution is less problematic.

Figure 76 (b), displaying a detail of the heat exchanger side mesh, highlights the difference between the rather rough solid domains mesh and the finer fluid computational grid, which also includes boundary layer meshes to help solving the strong gradients induced by the Navier-Stokes equations. The reason why the solid domain mesh does not need to be very dense is that Inconel 718 conductive heat transfer mode originates an almost linear temperature distribution.

Figure 76 (c), which represents the HE outer top surface mesh, shows that the computational grid is more dense at the interface between consecutive fin rows, again because there the gradients to solve for are stronger. The fins, in spite of their reduced dimensions, as conductive solid bodies do not need very fine mesh.

Finally, Figure 76 (d) highlights how the boundary mesh elements, because of their high aspect ratio, have the lowest mesh quality. Overall, the average mesh quality is equal to 0.55 and the discretized model includes about 6 millions of DOFs, which require almost 50 Gb of RAM to store the system matrix and to solve it.

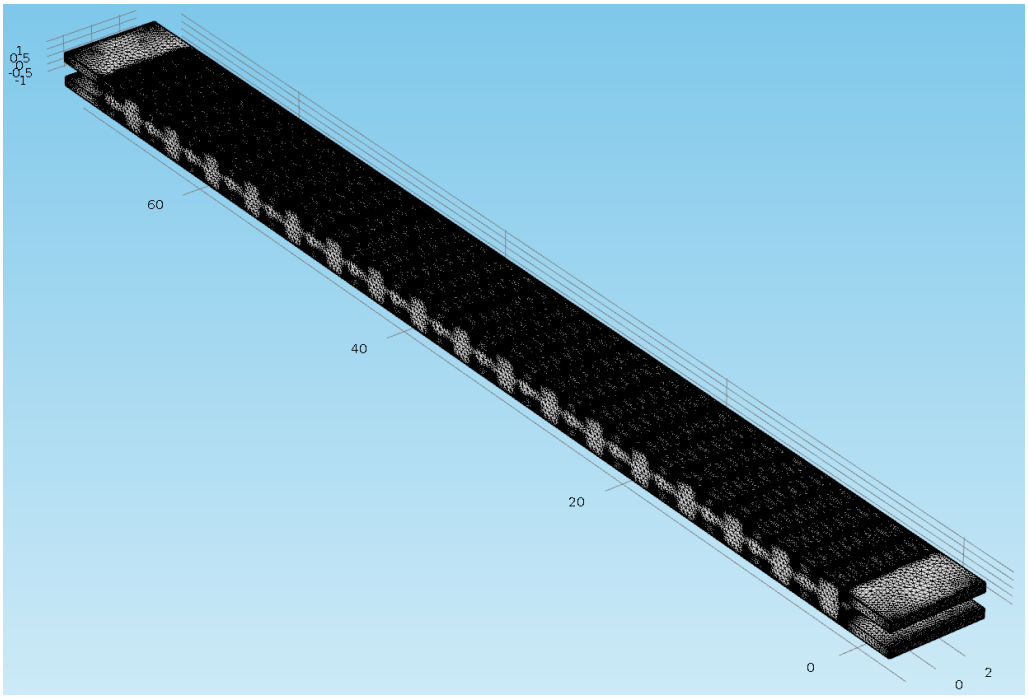

(a) Complete model

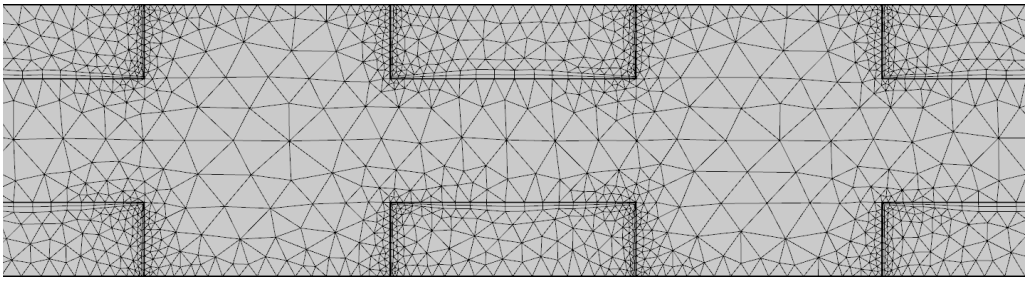

(b) Side

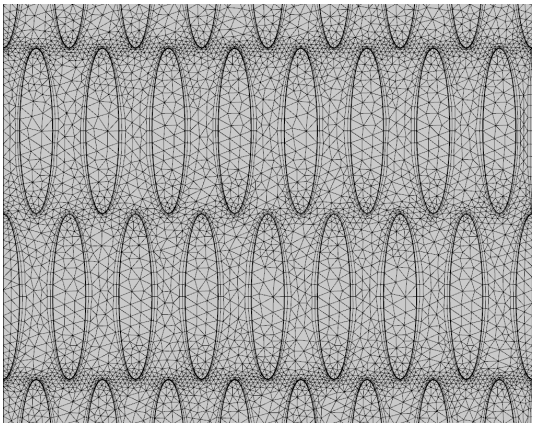

(c) Top

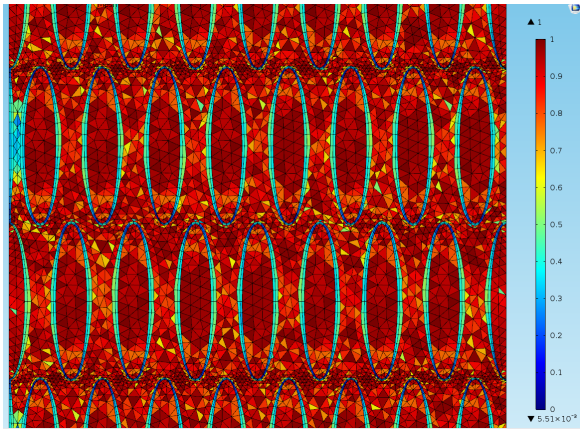

(d) Top mesh quality

Figure 76: Simulation model mesh

TABLE XXIV: HEAT EXCHANGER PERFORMANCES

$T_{1,out}$ [°C]	$T_{2,out}$ [°C]	ε [%]	Δp_1 [mbar]	Δp_2 [mbar]
703.8	255.8	95.9	5.55	4.29

9.4.2.2 Outcomes

As for the parametric sweep study, the most important results derived from the heat exchanger CFD simulation are the outlet temperatures and the pressure drops, which are displayed in Table XXIV. Starting from these data, the HE effectiveness ε calculation, according to its definition shown in Equation 9.16, is straightforward.

$$\varepsilon = \frac{q}{q_{max}} = \frac{T_{2,in} - T_{2,out}}{T_{2,in} - T_{1,in}} \tag{9.16}$$

Since the cold side outlet temperature of 703.8 °C is very close to the thermodynamic limit of 724.1 °C, the heat exchanger results in a very high effectiveness ε, precisely equal to 95.9 %. The results in terms of heat transfer are therefore fully coherent with the design requirements demanding an effectiveness higher than 95 %.

The pressure drops, in spite of the remarkable mass velocity of 12 $\frac{kg}{m^2 \cdot s}$, are well below the prescribed limit of 10 mbar, thanks to the aerodynamic elliptical fin profile. If it is true that in this simulation, differently from the one implemented on MATLAB, the pressure losses in the fluid distribution system are not considered, it is also undeniable that the core losses are low

enough to safely guarantee that the total pressure drops in the heat exchanger are lower than the 10 mbar limit.

After having summarized the HE performances by means of the quantities reported in Table XXIV, hereafter follows a thorough analysis of the CFD simulation results in terms of temperature, velocity and pressure distributions.

Temperature field

Figure 77 displays the temperature distribution on simulation domain outer surface. Because of the counter-flow arrangement, cold and hot regions for both fluids are located at the same device extremities. The almost uniform blue region on the right of Figure 77 confirms that the hot mixture is the limiting heat transfer. In fact, due to its lower heat capacity rate $C_2 = C_{min}$, its outlet temperature is very similar to the cold side inlet one.

On the contrary, looking at the left side of Figure 77, the evident difference in color between cold and hot domains highlights that there the temperature discrepancy is bigger. Figure 78, exhibiting the individual temperature distributions on each side of the heat exchanger, corroborates the validity of this description. In short, as proved by the numerical results of Table XXIV and confirmed by Figure 77, the hot side temperature drop is higher than the cold side temperature rise.

Observing Figure 79, representing the temperature distribution at the outlet of the cold mixture domain, it is possible to notice that fins are substantially hotter than the cold fluid. This is coherent with Fourier's law, Equation 9.7, according to which a temperature gradient is necessary for heat transfer to happen.

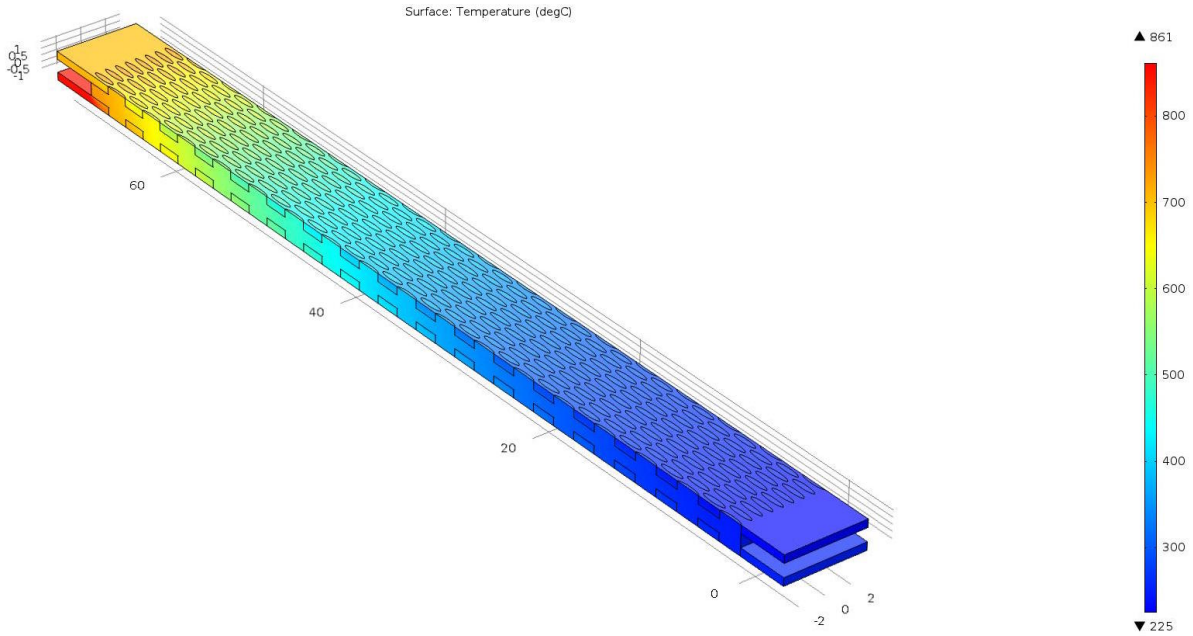

Figure 77: Outer surface temperature distribution

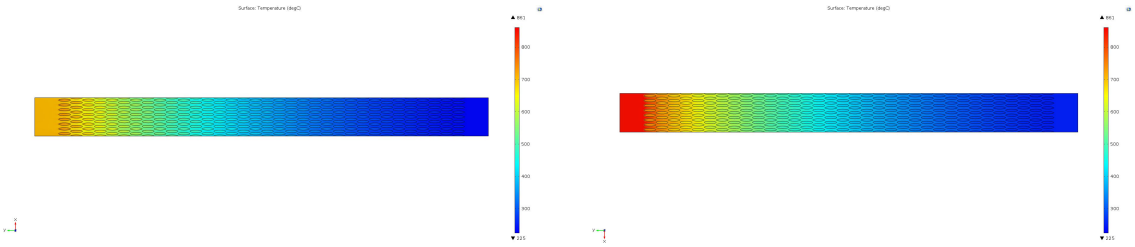

(a) Cold side

(b) Hot side

Figure 78: Individual sides outer surface temperature distribution

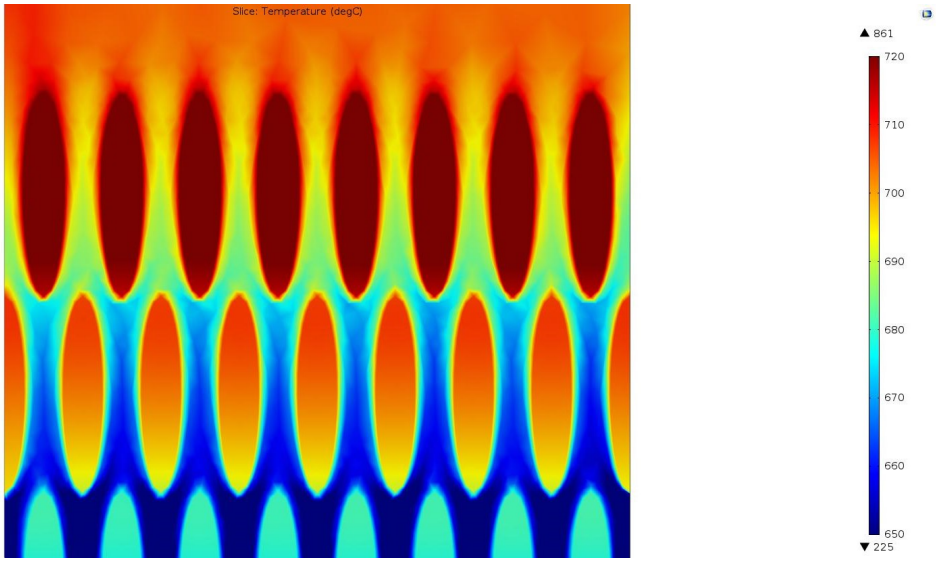

Figure 79: Temperature distribution at the cold side outlet

The longitudinal temperature distribution shown in Figure 80 confirms that the minimum temperature difference between cold and hot fluids takes place at the inlet, with the maximum being instead found in correspondence of the outlet. This consideration, remembering that heat transfer is proportional to the temperature difference, explains why the curves slope increases moving from the inlet to the outlet section. The initial and final flat parts of Figure 80 are motivated by the existence of the previously introduced *spikes*, i.e. virtual domains where fluids are mixed and homogenized.

Figure 80 saw-tooth oscillations reflects the fact that the line along with temperature has been recorded, on the outer surface in correspondence of the mid-plane, alternatively intersects solid and fluid domains. When the cutting line is passing through the solid fins, whose thermal

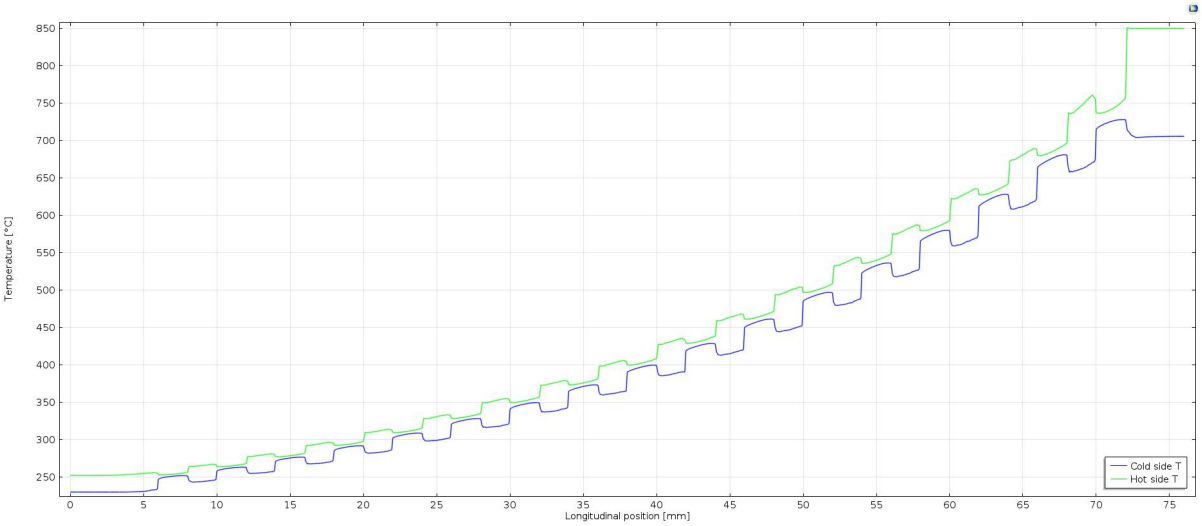

Figure 80: Longitudinal temperature distribution

resistance is negligible, the temperature difference between cold and hot sides is minimum. Vice-versa, the discrepancy is maximum when considering the fluid domains, as gases notoriously have very low heat transfer coefficients.

After having considered the longitudinal temperature distribution, it is worth analyzing its transversal variability, specifically at the interface between consecutive fin rows, Figure 81 (b), and in correspondence of each fins row transversal mid-plane, Figure 81 (a). First, as evinced from the analysis of previous Figure 80, the plate temperature, because of the high thermal conductivity of Inconel 718, is relatively constant. Second, the left figure multi-colored temperature field is related to the fluid-fin detachment and consequent mixing, which do not happen at the fin mid-plane, thus resulting in the less varied distribution shown in the right figure.

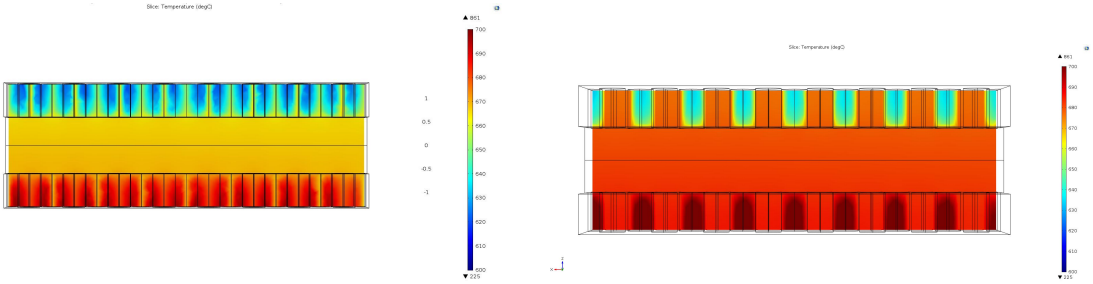

(a) Fins interface (b) Fins mid-plane

Figure 81: 2-D transversal temperature distributions

Third, Figure 81 proves that the cold fluid temperature is substantially higher close to the fins and the plate, as confirmed by Figure 82, which plots the temperature distributions along the heat exchanger width and height. While the fluids temperature is considerably constant along the width, Figure 82 (a), the fins temperature increases moving leftwards, probably because of the different boundary conditions applied on the two sides of the model, wall on the left and symmetry on the right. The fluid-fin temperature difference is not the same for the hot and cold site, amounting respectively to about 15 and 25 $°C$. These values are roughly confirmed by the vertical temperature distribution plot shown in Figure 82 (b), which also confirms that the plate temperature is practically constant.

Observing the isothermal surfaces represented in Figure 83, it is possible to notice that the surfaces slope increases moving leftwards. Also, the distance between consecutive surfaces decreases approaching the heat exchanger end. Remembering that the temperature difference between consecutive isothermal surfaces is constant by definition, it is then clear that both

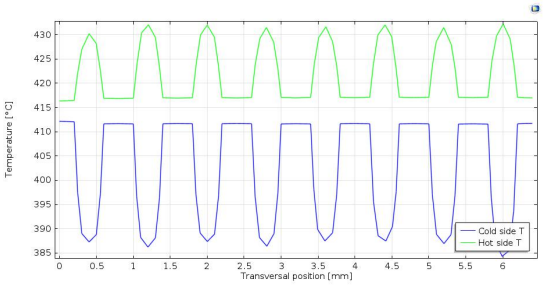

(a) Temperature along the heat exchanger width

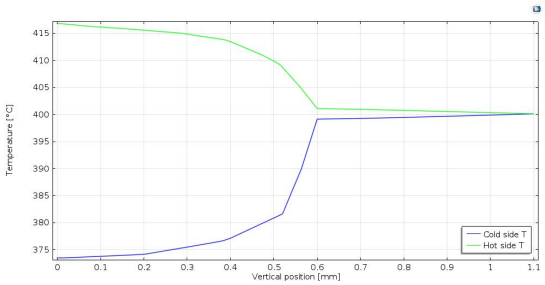

(b) Temperature along the heat exchanger height

Figure 82: 1-D transversal temperature distributions

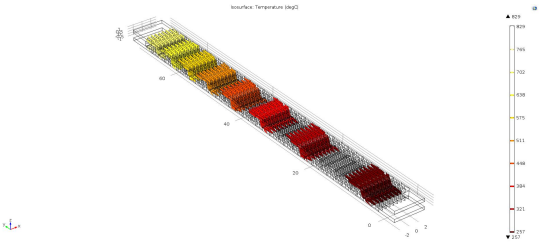

(a) Complete HE

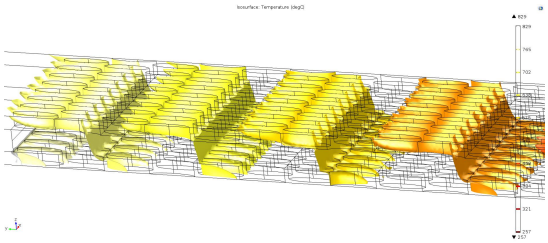

(b) End region

Figure 83: Isothermal surfaces

these information are indicators of the HE terminal region improved heat transfer condition, thanks to the locally higher temperature gradients.

The far isothermal surfaces on the right of Figure 83 (a) confirms the remark first illustrated describing Figure 72, i.e. that the gain produced by choosing a longer heat exchanger is rather limited and therefore achieving too high HE effectiveness ε is not always cost-effective.

TABLE XXV: SIMULATION MEAN TEMPERATURES

$\overline{T}_1[°C]$	$\overline{T}_2[°C]$	$\overline{T}_{1,v}[°C]$	$\overline{T}_{2,v}[°C]$	$\overline{T}_{1,b}[°C]$	$\overline{T}_{2,b}[°C]$	$T_{1,max}[°C]$	$T_{2,min}[°C]$
467.1	552.9	419.0	457.0	383.2	413.8	733.1	249.5

Finally, while developing the $\varepsilon - NTU$ based sizing procedure in Chapter 8, it was announced that using the arithmetical mean temperature, the only available one at that design stage, was not physically correct. The simulation data, shown in Table XXV, indeed confirms that arithmetical (Equation 9.17), volumetric (Equation 9.18) and bulk (Equation 9.19) mean temperatures values are different. In particular, the bulk mean temperature, carrying a physical meaning, is substantially lower than the value obtained by simply taking the arithmetical average.

$$\overline{T} = \frac{T_{in} + T_{out}}{2} \tag{9.17}$$

$$\overline{T}_v = \frac{\int_V T \, dV}{\int_V dV} \tag{9.18}$$

$$\overline{T}_b = \frac{\int_V \rho \cdot T \, dV}{\int_V \rho \, dV} \tag{9.19}$$

A maximum cold side fluid temperature about 28 $°C$ higher than the mean outlet temperature reported in Table XXIV can be explained only by considering the transversal temperature

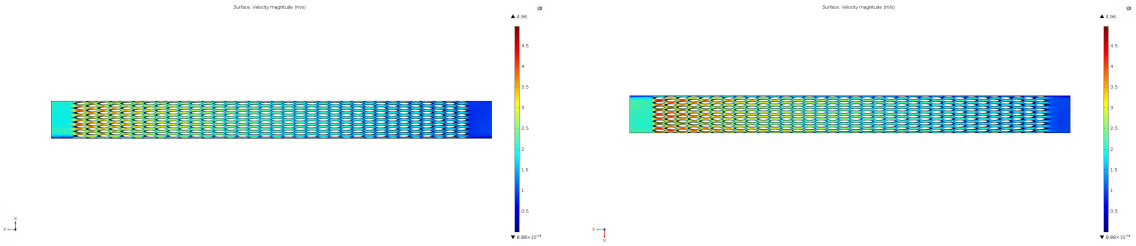

(a) Cold side (b) Hot side

Figure 84: Outer surface velocity fields

variability previously shown in Figure 81. The existence of such numerically relevant gradients also confirms the necessity of adding the *spikes* to the physical fluid domains, in order to smooth the gradients and produce a mixture with uniform properties. On the contrary, the hot side difference between minimum and mean outlet temperature is negligible, due to the fact that the hot fluid outlet, as proved by Figure 77, is already almost isothermal with the cold fluid inlet.

Velocity field

Figure 84 shows the velocity fields on the heat exchanger outer surface. Since the fin geometry and therefore the free flow area does not change along the heat exchanger length, according to the continuity equation, Equation 9.14, because of density reductions, velocity increases with temperature. From Figure 84 it also emerges that the *spikes*, whose thermal function has already been demonstrated, are necessary to reduce the strong velocity gradients and produce a uniform flow.

TABLE XXVI: SIMULATION FLOW VELOCITIES

$v_{1,max}\left[\frac{m}{s}\right]$	$v_{2,max}\left[\frac{m}{s}\right]$	$\overline{v}_1\left[\frac{m}{s}\right]$	$\overline{v}_2\left[\frac{m}{s}\right]$	$v_{1,in}\left[\frac{m}{s}\right]$	$v_{2,in}\left[\frac{m}{s}\right]$	$v_{1,out}\left[\frac{m}{s}\right]$	$v_{2,out}\left[\frac{m}{s}\right]$
4.296	4.962	1.519	1.541	0.709	1.578	1.439	0.721

The reason why the maximum velocity, reported in Table XXVI along with other relevant velocity information extracted from the simulation, is reached on the hot side, in spite of its mass flow rate $\dot{m}_2$ being about half of the cold one $\dot{m}_1$, is that the hot mixture density, as proved in Chapter 4, is substantially lower and its temperature always higher than the for the cold side. Table XXVI also reveals that the mean volumetric velocity is practically equal for the two mixtures, meaning that their residence time τ in the heat exchanger is substantially the same.

The order of magnitude for the velocities being units of meters per second, the flow regime is always laminar. This result is coherent with what foreseen in Chapter 8 and the choice of a laminar flow interface in the simulation set-up is therefore validated.

In Figure 85, where the cold side velocity field is plotted for two different longitudinal coordinates, it is possible to better appreciate temperature related effects. In fact, close to the inlet section, Figure 85 (a), velocities are much lower than in correspondence of the heat exchanger terminal section, Figure 85 (b). In both cases, where the free flow section decreases, i.e. around the fin mid-plane, the flow is accelerated, in agreement with Equation 9.14. Finally,

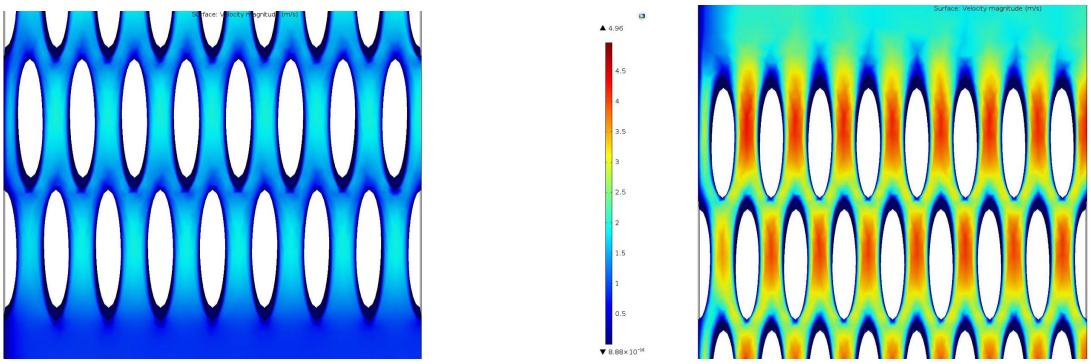

(a) Inlet region (b) Outlet region

Figure 85: Inlet and outlet cold flow velocity fields

Figure 85 proves that the velocity field is well resolved around the fin, where velocity gradually tends to zero as prescribed by the no-slip boundary condition.

A careful observation of Figure 85 also reveals that the velocity profiles on the left and right heat exchanger boundaries are indeed different. In fact, on the left, where a no-slip wall boundary condition has been prescribed, the velocity tends to zero, while on the opposite boundary, where the applied boundary condition is symmetry, the velocity value is finite. As a matter of fact, only the velocity component normal to the boundary is zeroed on the symmetry plane, as shown in Figure 86 (a). This figure also clarifies that a normal velocity component is created only when a fin forces the flow to split into two components having opposite directions and similar module. Figure 86 (b) suggests instead that the velocity magnitude is almost constant along the heat exchanger width, showing just slightly lower values close to the left wall, where a no-slip boundary condition applies.

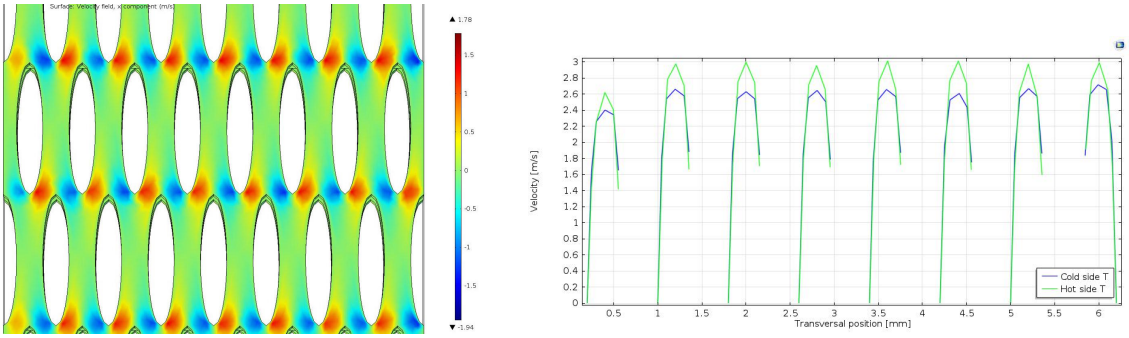

(a) Normal velocity component (b) Velocity along the heat exchanger width

Figure 86: Transversal velocity distribution

Figure 87 (a), representing the velocity magnitude as a function of the longitudinal coordinate, confirms that, due to density related effects, the velocity increases along the heat exchanger length. The cold side velocity, coherently with Table XXVI results, is always lower than the hot side one. The particular *up and down* shape is due to the non constant free flow area associated with an elliptical fin geometry, while the zero-velocity segments account for the fin presence.

Figure 87 (b), whose focus is on the tangential velocity component, shows similar trends for both fluids but with opposite signs due to the heat exchanger counterflow configuration.

In Figure 88 is given evidence of the temperature variability along the fin height. Because of the laminar flow and of the no-slip wall condition, in spite of the fact that approaching the hot plate temperatures are higher, as shown in Figure 88 (b), the velocity tends to zero near the plate. Moving away from the solid plate, despite the lower temperature, as certified by

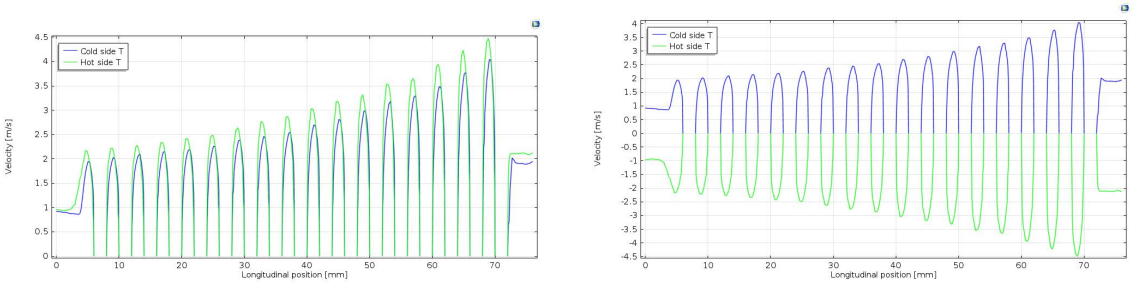

(a) Velocity magnitude (b) Tangential velocity component

Figure 87: Velocity along the heat exchanger length

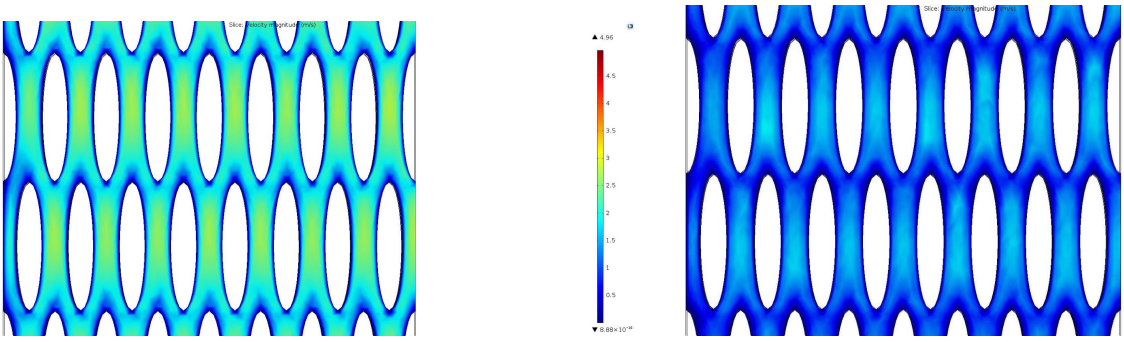

(a) Outer surface (b) Plate-contact surface

Figure 88: Cold flow velocity field at different depths

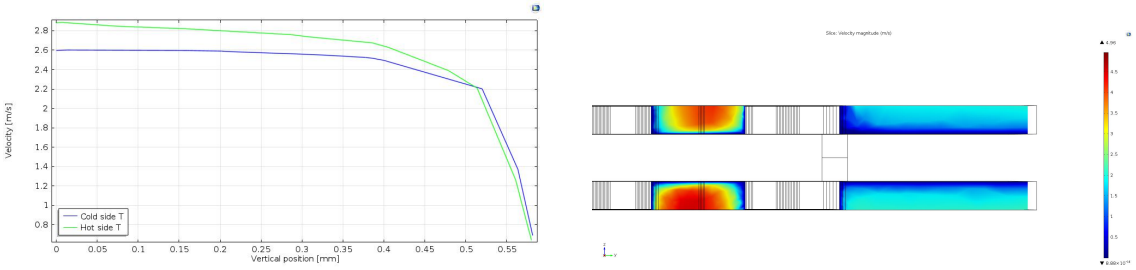

(a) 1-D plot (b) 2-D distribution

Figure 89: Temperature distribution along the fin height

both Figure 88 (a) and Figure 89, velocity increases. The fluid particles having the highest local velocity, as shown in Figure 89 (b), are then those lying on the fin mid-plane and farthest from the Inconel plate.

Finally, the cold flow streamlines represented in Figure 90 allow to visualize the trajectory followed by fluid particles because of the fin elliptical shape. In particular, Figure 90 proves that the fluid-fin detachments are frequent but never sudden and this is precisely what allows to achieve high thermal performances while containing the pressure drops.

Pressure field

Figure 91 shows that the hot side pressure losses per unit of length are almost constant, i.e. the curve slope does not substantially change, while for the cold flow specific pressure losses increase toward the heat exchanger outlet. This is likely due to the high velocities and the non-uniform flow profile that characterizes the cold side outlet region.

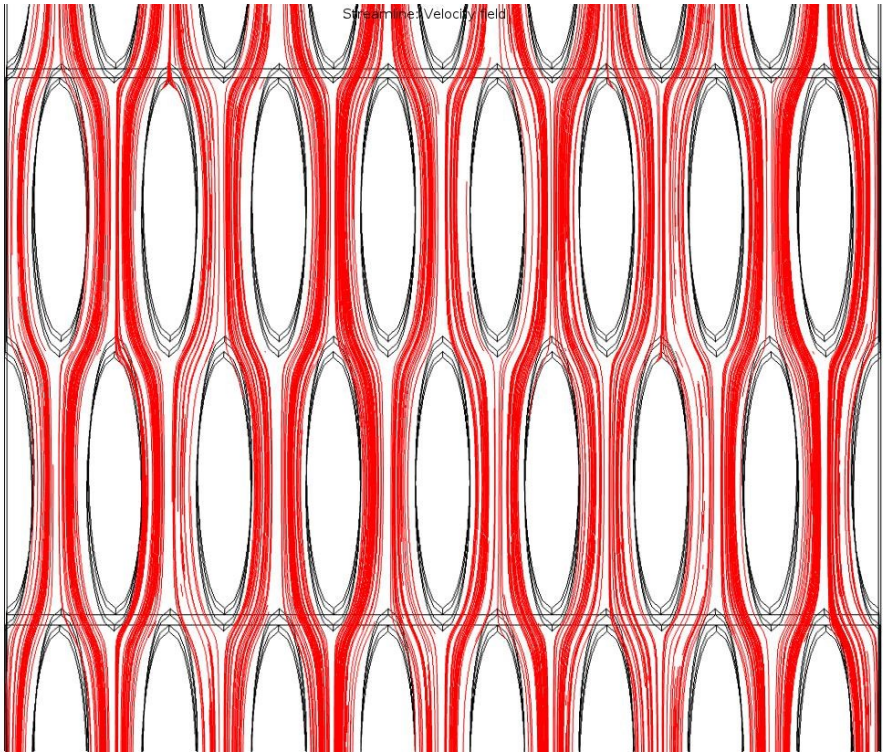

Figure 90: Cold flow streamlines

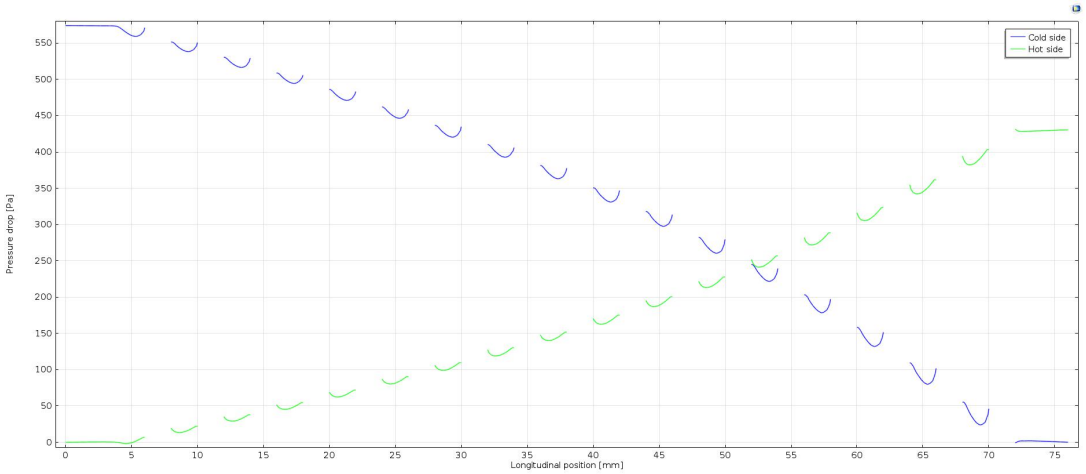

Figure 91: Back-pressure along the heat exchanger length

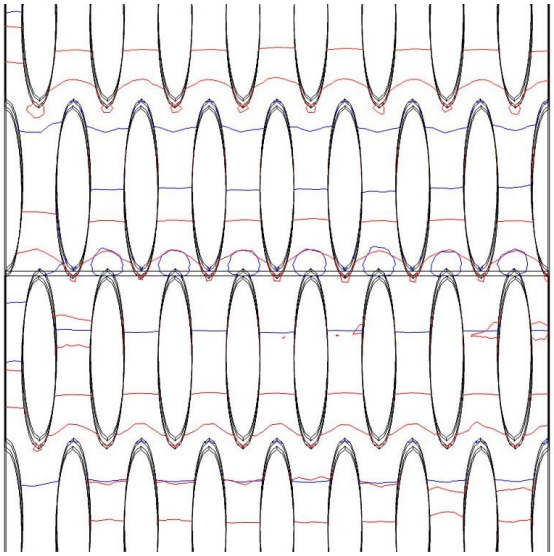

Figure 92: Cold side isobaric curves

Figure 92 allows instead to assess that the fluid-fin collisions mechanism is more important than the fluid-wall friction toward the generation of pressure drops. In fact, the distance between consecutive isobaric surfaces is in fact smaller close to fin tips than along the fin length, meaning that pressure losses are concentrated at the fin extremities. In absolute terms, though, thanks to the extremely aerodynamic elliptical profile, pressure drops are reduced and well below the 10 mbar design limit.

9.4.2.3 Model scaling and characterization

After having validated the simulation results and assessed that the heat exchanger performances meet the design requirements, it is necessary to scale up the reduced CFD geometrical model and determine the actual HE size that allows to deal with the total mass flow rate defined

in Chapter 3. While this process requires to enlarge the free flow area and consequently the frontal area, the device length, related to the thermal performances, will not be modified.

Once the final dimensions of the device are available, several parameters describing the heat exchanger geometry will be calculated, with the two-fold objective of assessing the device compactness and comparing it with the design produced in Chapter 8. The whole procedure, for the sake of accuracy and repeatability, has been implemented on MATLAB.

Heat exchanger size

Having defined the parameters determining the elliptical fin geometry, it is straightforward to calculate the cold and hot free flow areas by means of Equation 9.20, where $N_{ch,\mathrm{CFD}}$ is the number of flow channels used in the CFD model and A_{ch} is the free flow area of each individual channel. The frontal area, Equation 9.21, is simply the product of the CFD model height W_{CFD} and width W_{CFD}. Then, the free flow to frontal area ratio σ follows based on Equation 9.22.

$$A_{0,\mathrm{CFD}} = N_{ch,\mathrm{CFD}} \cdot A_{ch} = N_{ch,\mathrm{CFD}} \cdot (s \cdot t) \tag{9.20}$$

$$A_{fr,\mathrm{CFD}} = W_{\mathrm{CFD}} \cdot H_{\mathrm{CFD}} \tag{9.21}$$

$$\sigma = \frac{A_{0,\mathrm{CFD}}}{A_{fr,\mathrm{CFD}}} \tag{9.22}$$

Knowing the total cold side mass flow rate $\dot{m}_1$, defined in Chapter 3, and having selected an optimum value for the mass velocity G, the required free flow area is computed according to

Equation 9.23. The corresponding frontal area is then obtained, Equation 9.24, starting from the free flow to frontal area ratio σ above derived.

$$A_0 = \frac{\dot{m}_1}{G} \tag{9.23}$$

$$A_{fr} = \frac{A_0}{\sigma} \tag{9.24}$$

$$S = \sqrt{A_{fr}} \tag{9.25}$$

As already mentioned in Chapter 8, without additional constraints, there is no reason not to choose a square front shape, whose side is calculated in Equation 9.25. However, in order to guarantee the device manufacturability, the actual heat exchanger dimensions need to be integer multiples of the fin and plate dimensions. Since the HE length L does not change scaling up the CFD model, hereafter only the definitive width W and height H will be derived.

Labeling again with N_H, $N_C = N_H + 1$ and $N_W = 2 \cdot N_C$ respectively the number of hot layers, cold layers and solid plates, the first quantity can be derived using Equation 9.26 and then the exact heat exchanger height H is computed according to Equation 9.27.

$$N_H = ceil\left[\frac{S - 2t - 2t_w}{4t + 2t_w}\right] \tag{9.26}$$

$$H = 2t \cdot (N_C + N_H) + N_W \cdot 2t_w \tag{9.27}$$

Since the frontal area is available, knowing the height determines, Equation 9.28, the width value as well. However, since also this dimension needs to be a multiple of the fin dimensions, precisely of the fin transversal pitch p, the number of free flow channels N_c along the heat exchanger width is calculated first, Equation 9.29, and then the actual width W is computed based on Equation 9.30.

$$W = \frac{A_{fr}}{H} \tag{9.28}$$

$$N_c = ceil\left[\frac{W}{p}\right] \tag{9.29}$$

$$W = N_c \cdot p \tag{9.30}$$

Knowing all the heat exchanger final dimensions, the actual frontal area A_{fr} and volume V_{HE} follow according to Equation 9.31 and Equation 9.32 respectively.

$$A_{fr} = W \cdot H \tag{9.31}$$

$$V_{HE} = A_{fr} \cdot L \tag{9.32}$$

Table XXVII reports the numerical results, based on the fin dimensions defined in Table XXI and Table XXII, of the scaling procedure above described. The total number of fluid layers, 19, is high enough to consider negligible the border effects and thus validate the use of a reduced

TABLE XXVII: DEFINITIVE HEAT EXCHANGER DIMENSIONS

L [mm]	W [mm]	H [mm]	N_C [/]	N_H [/]	N_{ch} [/]	A_{fr} $[mm^2]$	V $[cm^3]$
68.0	41.6	42.8	10	9	52	1780.5	121.1

model for CFD simulations. Even if the frontal area is not exactly square anymore, the aspect ratio is still very close to the unit, as graphically proved in Figure 93.

In Figure 94 it is possible to appreciate the final heat exchanger design, whose dimensions are 68 x 41.6 x 42.8 mm. It is worth highlighting that this matrix-like structure contains as many as 34.238 elliptical fins, some of which can be spot in Figure 95.

Heat exchanger characterization

Knowing the final heat exchanger size, the following parameters describing the device geometry will be derived:

1. The finned to total heat transfer area ratio f_s
2. The surface area density β
3. The heat transfer area to heat exchanger volume ratio α
4. The hydraulic diameter D_H

Considering the CFD reduced geometric model, the finned to total heat transfer area ratio f_s derivation is straightforward. The elliptical fin geometry is fully defined by its lateral and base surface areas, calculated using respectively Equation 9.33 and Equation 9.34 (Ramanujan, 1914), while the plate area follows from Equation 9.35.

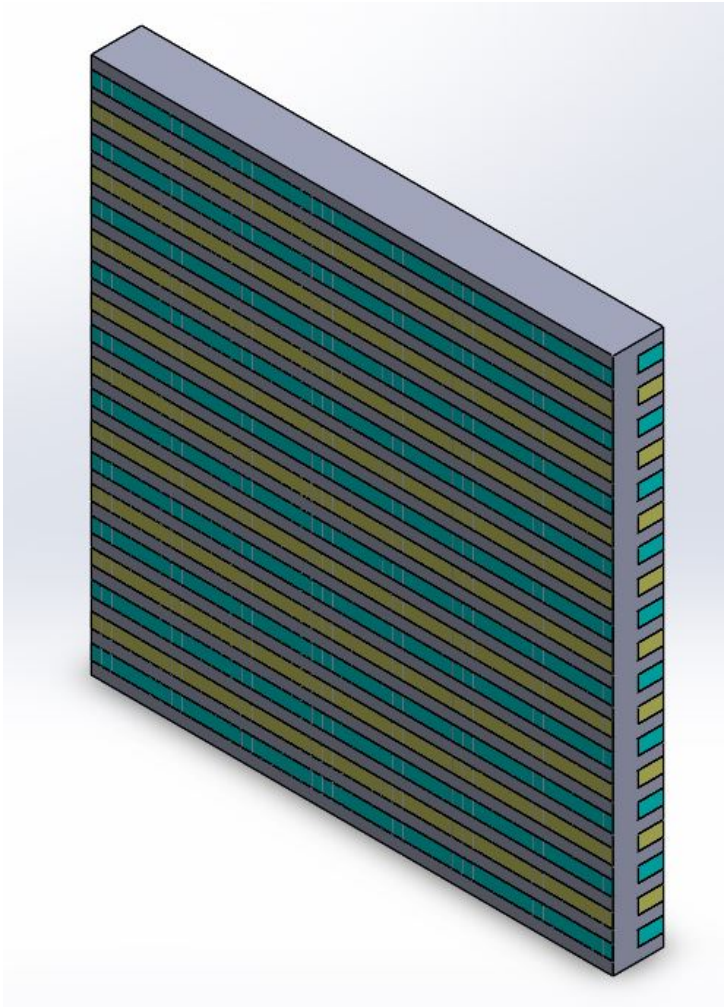

Figure 93: Heat exchanger frontal area
Cold mixture layers shown in cyan, hot mixture layers in yellow

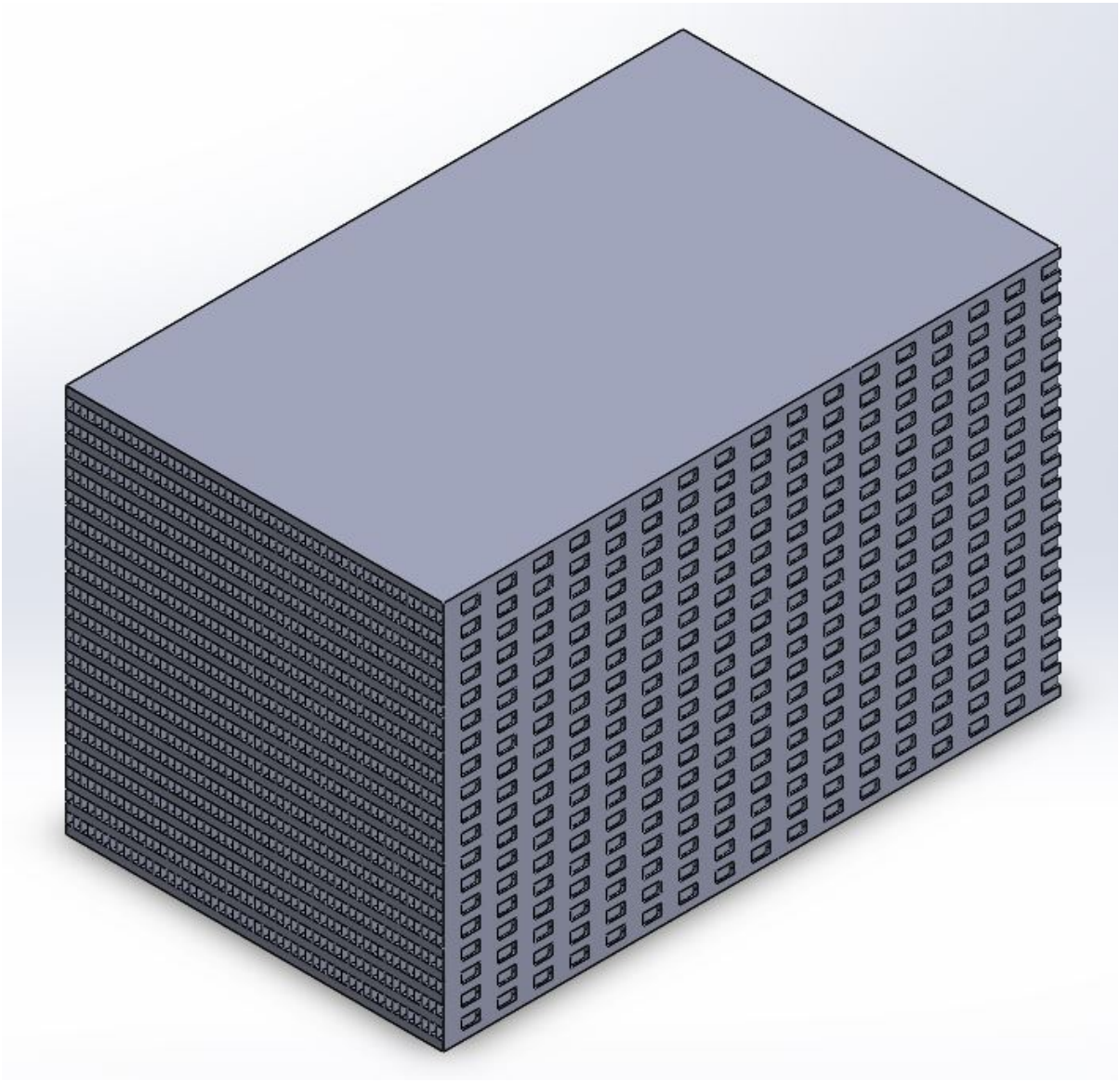

Figure 94: Definitive heat exchanger

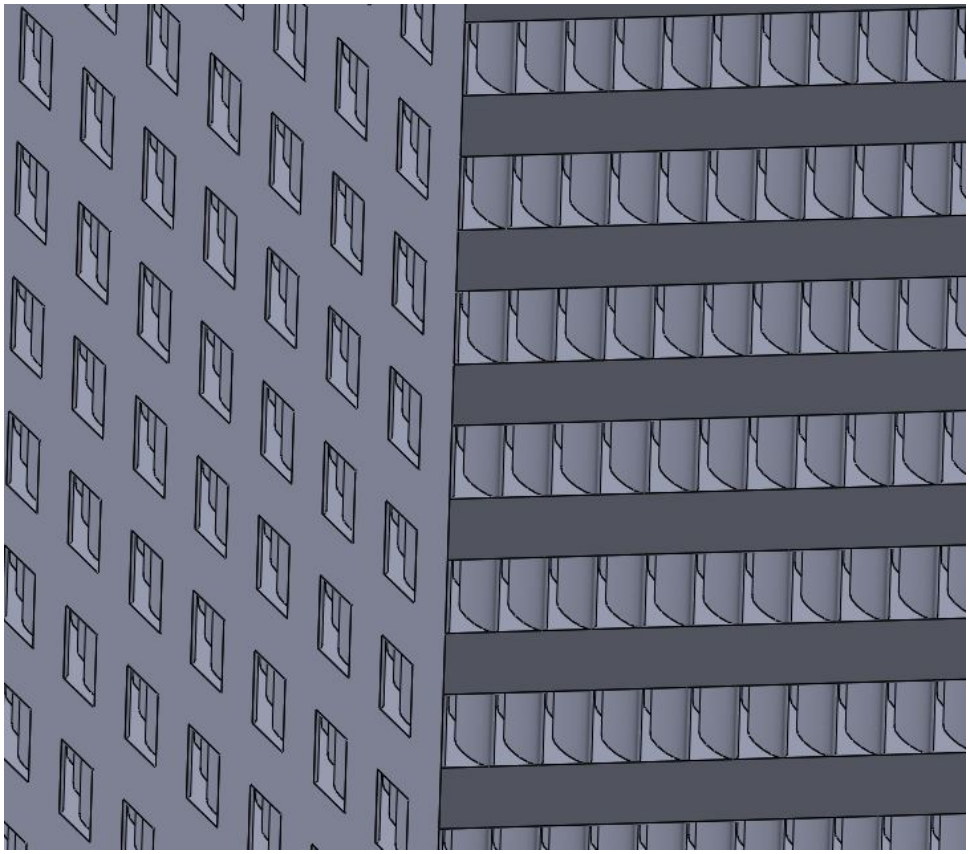

(a)

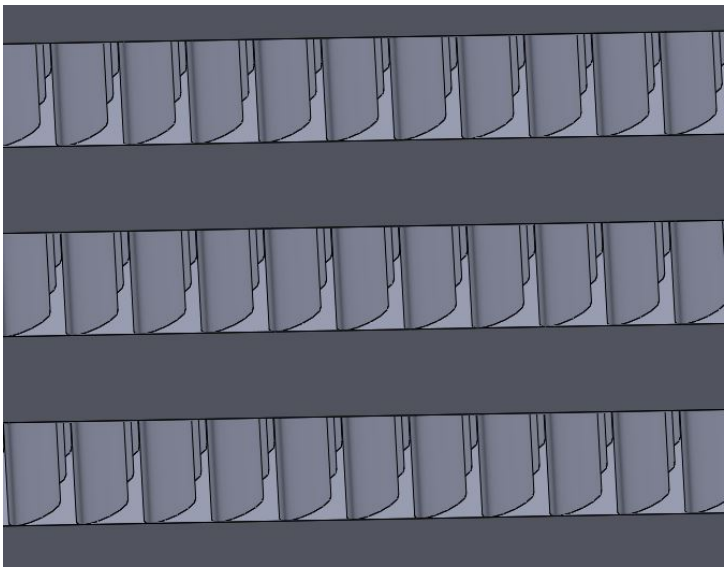

(b)

Figure 95: Heat exchanger final matrix-like structure

$$A_{fin,lat} = 2t \cdot \pi \cdot \left[3 \cdot (a+b) - \sqrt{10 \cdot a \cdot b + 3 \cdot (a^2 + b^2)}\right] \tag{9.33}$$

$$A_{fin,base} = \pi \cdot a \cdot b \tag{9.34}$$

$$A_{plate} = W \cdot L \tag{9.35}$$

The number of fins per layer can be calculated starting from the number of channels and of fin rows according to Equation 9.36.

$$N_{fin} = (N_{ch} + 1) \cdot N_{rows} \tag{9.36}$$

It is then possible to calculate the primary, secondary and total heat transfer surface areas, as shown in Equation 9.37, Equation 9.38 and Equation 9.39 respectively.

$$A_p = 2 \cdot (A_{plate} - N_{fin} \cdot A_{fin,base}) \tag{9.37}$$

$$A_s = N_{fin} \cdot A_{fin,lat} \tag{9.38}$$

$$A_{tot} = A_p + A_s; \tag{9.39}$$

Finally, the finned to total heat transfer area ratio can be computed according to its definition, Equation 9.40.

$$f_s = \frac{A_{secondary}}{A_{total}} \tag{9.40}$$

After having calculated the volume between two plates, Equation 9.41, the surface are density β is easily computed according to its definition, Equation 9.42.

$$V_p = A_{plate} \cdot 2t \tag{9.41}$$

$$\beta = \frac{A_t}{V_p} \tag{9.42}$$

The heat transfer area to heat exchanger volume ratio α calculation is straightforward. In fact, the heat exchanger volume V_{HE} is already known, while the total HE heat transfer areas for the cold and hot sides can be calculated by means of Equation 9.43 and Equation 9.44 respectively.

$$A_1 = N_C \cdot A_{total} \tag{9.43}$$

$$A_2 = N_H \cdot A_{total} \tag{9.44}$$

$$\alpha = \frac{A}{V_{HE}} \tag{9.45}$$

Finally, the hydraulic diameter D_H is derived based on its definition, Equation 9.46.

TABLE XXVIII: HEAT EXCHANGER GEOMETRIC CHARACTERIZATION

σ_1 [/]	σ_2 [/]	f_s [/]	β $\left[\frac{m^2}{m^3}\right]$	α_1 $\left[\frac{m^2}{m^3}\right]$	α_2 $\left[\frac{m^2}{m^3}\right]$	D_H [mm]
0.136	0.136	0.722	3638	1020	918	0.275

$$D_H = \frac{4A_0 \cdot L}{A} \tag{9.46}$$

The numerical values for the 4 parameters above derived, descriptive of the heat exchanger characteristics, are reported in Table XXVIII. A surface area density β as high as 3600 allows to classify the device as an ultra-compact heat exchanger [83], in spite of the unfavorable free flow to frontal area ratio σ, due to the high plate minimum thickness, 1 mm, imposed by AM. The secondary to total heat transfer area ratio f_s value, higher than 70 %, suggests the cardinal importance of fins role toward heat transfer enhancement. Finally, the hydraulic diameter D_H much lower than 1 mm, beyond once more confirming the initial hypothesis of laminar flow regime, allows to classify the HE as a micro heat exchanger [57].

9.4.2.4 Simulation validation

After having analyzed the CFD simulation results, in this section the outcomes validity and accuracy will be assessed by means of the following two tools:

1. Mesh refinement study
2. Respect of the mass and energy conservation principles

Mesh refinement study

As anticipated earlier in this chapter, in order to validate the results of a CFD simulation it is cardinal to carry out a *mesh refinement study* (MRS), in which the grid size is gradually reduced until a further mesh refinement does not alter the simulation outcomes.

Because of computational power limitations, it has not been possible to test models having more than 6 millions of DOFs and therefore prove the complete independence of the physical solution on the computational grid. However, the results in terms of outlet temperatures and pressure drops represented in Figure 96 (a) and Figure 96 (b) respectively are sufficient to validate the simulation results.

In fact, Figure 96 (a) proves that by increasing the number of DOFs solved for of a factor 6, both the cold and hot side outlet temperature variations remains below 5 $°C$. Moreover, considering only the simulations with at least 2 millions of DOFs, the temperature variability falls below 2.5 $°C$.

Figure 96 (b) allows to conclude that when the number of DOFs is higher than 3 millions, the pressure drops remain substantially constant regardless of the mesh density. What is more, if an error is committed, it is on the safe side, as the trend for pressure losses is monotonically decreasing with the mesh side.

On these grounds, considering even the remarkable dimensions of the CFD model object of simulation, i.e. almost 1000 mm^3, and the fact that CFD simulations are reputed accurate only within 5 % [63], it is possible to conclude that the results obtained solving a 6 millions of DOFs model are essentially mesh independent and carry physical meaning.

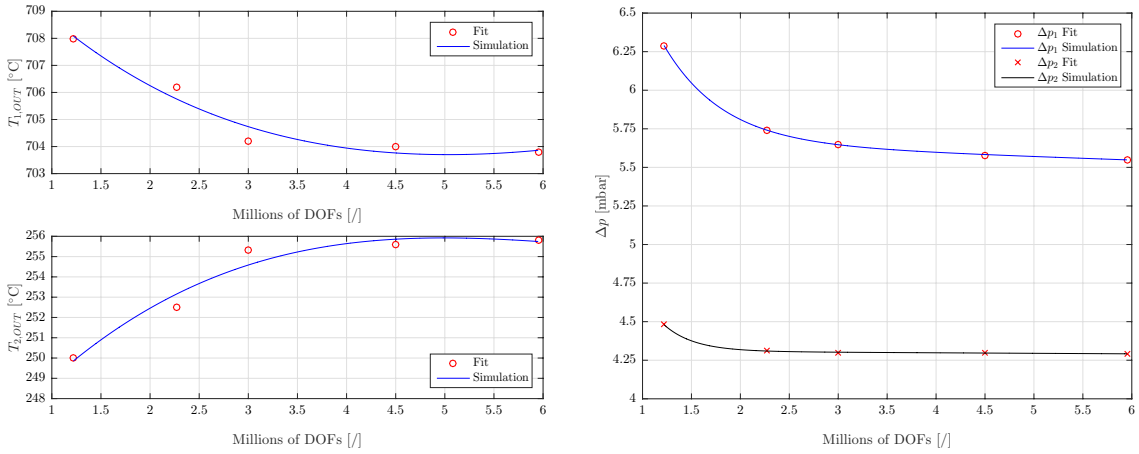

(a) Outlet temperatures

(b) Pressure drops

Figure 96: Mesh refinement study results

Conservation laws

CFD simulations cannot always guarantee precisely energy and mass conservation, since these physical principles are imposed by numerical means. As a consequence, it is mandatory to check that energy and mass balances are respected.

The mass flow rates can be calculated by means of Equation 9.47, where S denotes one of the four fluid ports. Table XXIX shows that mass is conserved very accurately, the relative error being lower than 0.05 %.

$$\dot{m} = \iint_S \rho \boldsymbol{u} \cdot \boldsymbol{n} \, dS \tag{9.47}$$

TABLE XXIX: SIMULATION MASS CONSERVATION

$\dot{m}_{1,in}\,[\frac{mg}{s}]$	$\dot{m}_{1,out}\,[\frac{mg}{s}]$	$\Delta 1$ [%]	$\dot{m}_{2,in}\,[\frac{mg}{s}]$	$\dot{m}_{2,out}\,[\frac{mg}{s}]$	$\Delta 2$ [%]
23.040	23.048	-0.035	11.617	11.621	-0.043

TABLE XXX: SIMULATION ENERGY CONSERVATION

$\dot{E}_{1,in}\,[W]$	$\dot{E}_{1,out}\,[W]$	$q_1\,[W]$	$\dot{E}_{2,in}\,[W]$	$\dot{E}_{2,out}\,[W]$	$q_2\,[W]$	Error [W]	Error [%]
9.461	29.669	20.208	28.064	7.862	20.202	0.006	0.03

Because of the initial hypothesis of adiabatic heat exchanger, the power $\dot{E}$ entering and leaving the thermodynamic system is directly proportional to the flow energy content, as shown in Equation 9.48, where H_0 is the total enthalpy. According to the numerical results reported in Table XXX, even energy conservation is accurately respected, with an error lower than 0.03 %.

$$\dot{E} = \iint_S H_0 \, \rho \, \boldsymbol{u} \cdot \boldsymbol{n} \, dS \tag{9.48}$$

Knowing the flow power $\dot{E}$ and remembering that the HE heat duty can always be calculated as the product between an enthalpy difference and a mass flow rate as shown in Equation 9.49, it is straightforward to compute the enthalpy difference for both mixtures according to Equation 9.50.

With this information available, knowing precisely the inlet temperature and therefore the corresponding mixture enthalpy h_{in}, it is possible to derive the outlet enthalpy h_{out} using Equation 9.51 and then the related temperature by iterative means. The $\pm$ sign in Equation 9.51 is motivated by the fact that enthalpy increases for the cold mixture while decreasing for the hot mixture.

$$q = \dot{m} \cdot \Delta h \tag{9.49}$$

$$\Delta h = \frac{q}{\dot{m}} \tag{9.50}$$

$$h_{out} = h_{in} \pm \Delta h \tag{9.51}$$

The numerical results reported in Table XXXI show a complete agreement between the simulation outlet temperature, based on a numerical application of energy conservation, and of the temperature derived applying the procedure previously explained. With errors as low as 0.3 $^{\circ}C$, it is possible to conclude that physical conservation principles are respected from a numerical standpoint and therefore the simulation results can be trusted.

9.5 Heat Exchangers Benchmark

A smart way to gage the actual heat exchanger performances is to compare it with other possible designs. In this section, heat exchangers featuring the following five different fin geometries will be compared in terms of thermal performance, i.e. outlet temperatures and effectiveness, and pressure drops:

TABLE XXXI: SIMULATION ENTHALPY BALANCE

	$\Delta h \left[\frac{kJ}{kg \cdot K}\right]$	$T_{in}\,[°C]$	$h_{in} \left[\frac{kJ}{kg \cdot K}\right]$	$h_{out} \left[\frac{kJ}{kg \cdot K}\right]$	$T_{out}\,[°C]$	$T_{out,SIM}\,[°C]$	Error $[°C]$
Cold	877.1	230.35	1959.8	2836.9	703.5	703.8	0.3
Hot	1739.0	850.00	3428.1	1689.1	256.0	255.8	0.2

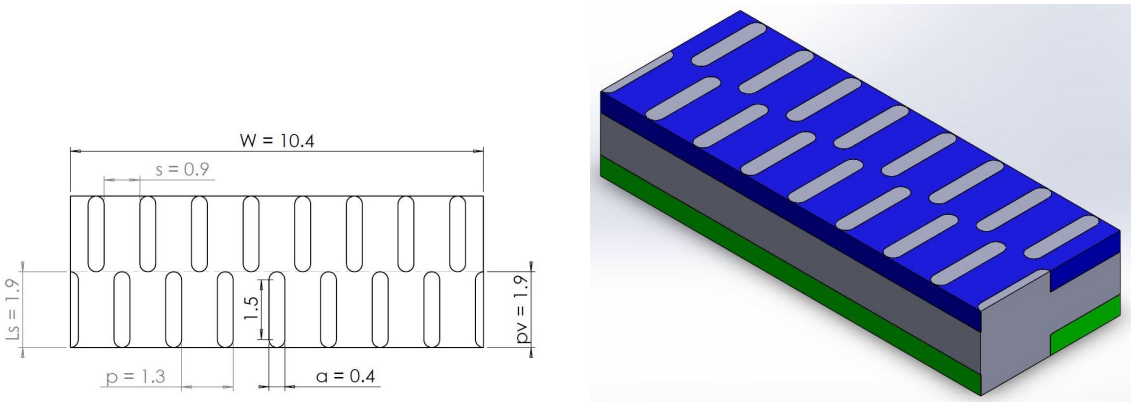

(a) 2-D view

(b) 3-D view

Figure 97: Rounded fins heat exchanger

1. Elliptical fins, Figure 74
2. Rounded fins, Figure 97
3. Rectangular fins, Figure 98
4. Straight fins, Figure 99 (a)
5. No fins, Figure 99 (b)

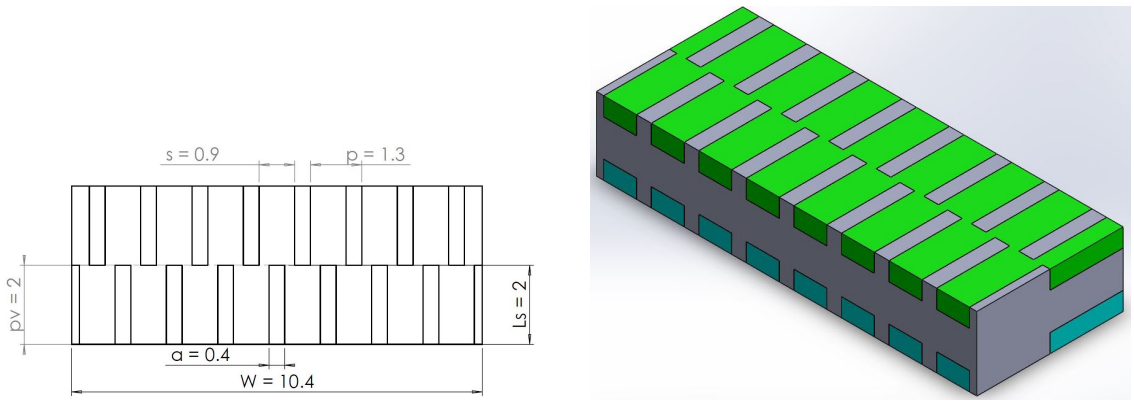

(a) 2-D view (b) 3-D view

Figure 98: Rectangular fins heat exchanger

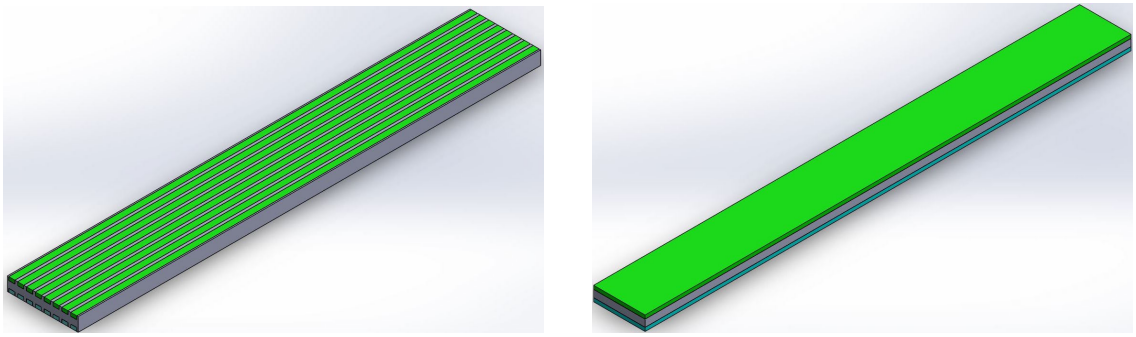

(a) Straight fins (b) No fins

Figure 99: Heat exchangers 3-D views

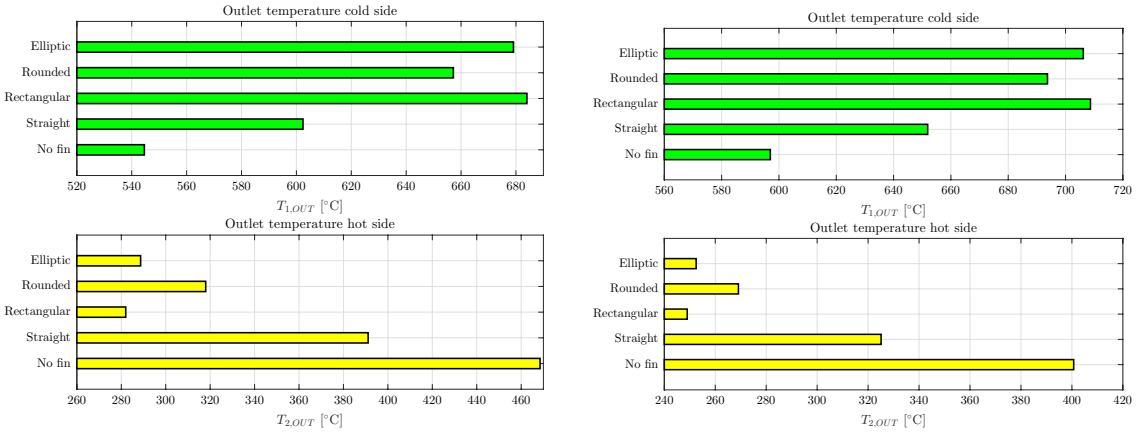

(a) L = 40 mm (b) L = 68 mm

Figure 100: Outlet temperatures for different heat exchangers length

The first four designs are examples of unmixed/unmixed heat exchanger designs, while the last one, without fins, is clearly a mixed/mixed HE. These geometries have been tested under similar conditions, precisely imposing the same length, either 40 mm or 68 mm, and the same core velocity G to every thermal device.

Figure 100 and Figure 101, representing respectively the outlet temperatures and the heat exchanger effectiveness ε, prove that the initial choice of adopting rectangular fins, as an evolution of the offset-strip geometry introduce in Chapter 8, makes sense from a thermal standpoint, as these fins enjoy the highest effectiveness ε of the lot. At the same time, the performance of elliptical and rounded fins is not that different, with the elliptical design being almost as effective as the rectangular one. On the contrary, heat exchangers having a lower or nil finned to total heat transfer area ratio f_s have substantially lower performances. In particular, the

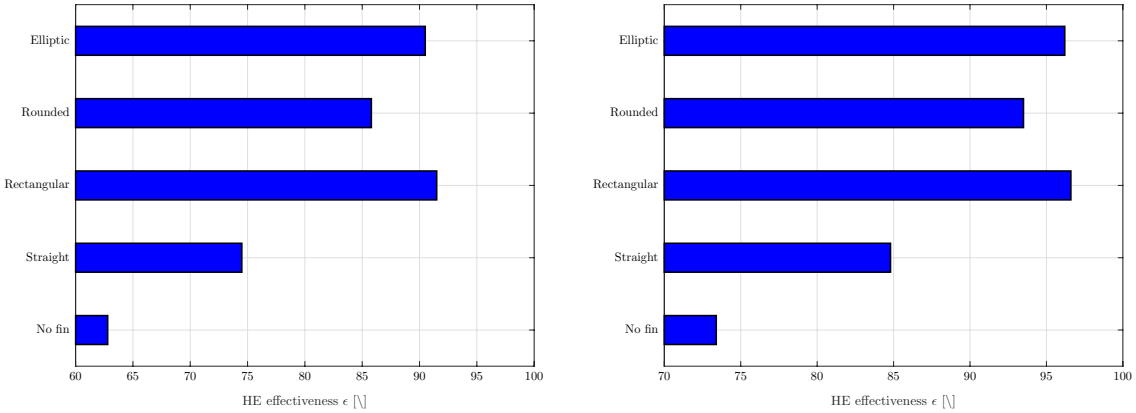

(a) L = 40 mm (b) L = 68 mm

Figure 101: Effectiveness ε for different heat exchangers length

mixed/mixed design cold side outlet temperature trails by almost 150 $°C$ relative to the most effective designs, demonstrating the need for a finned structure. As expected, an increment of the device length improves the cold side outlet temperatures, but without significantly affecting the different designs ranking.

If the rectangular fins are effective in terms of heat transfer, they are absolutely not efficient while considering pressure drops. This is the reason why they have never been seriously considered for the final heat exchanger design. Figure 102 proves that, just by smoothing the rectangular fins extremities, i.e. by producing rounded fins, pressure drops are drastically reduced and that an elliptical fin design allows to further reduce the losses. The last two kinds of designs produce very reduced pressure drops, because they never trigger fluid-fin detachments.

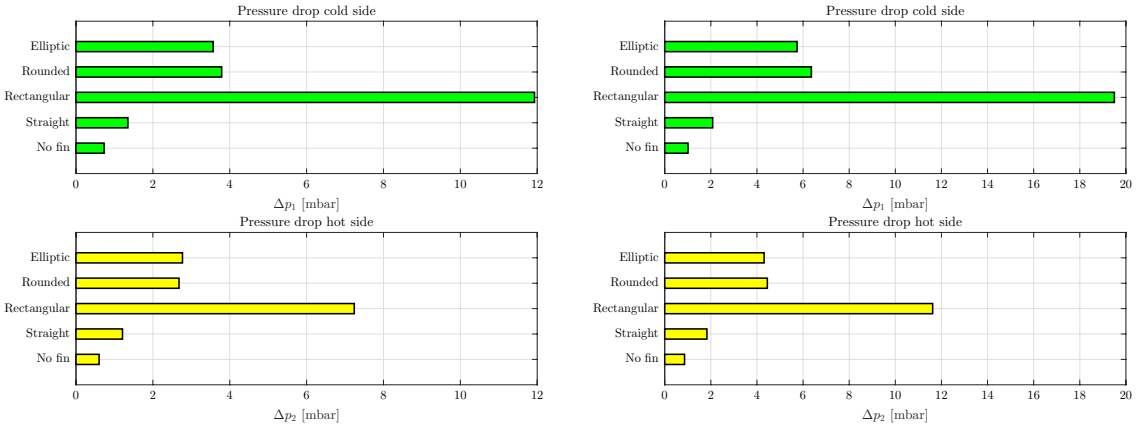

(a) L = 40 mm (b) L = 68 mm

Figure 102: Pressure drops for different heat exchangers length

This consideration confirms that the wall friction contribution to the total pressure losses is substantially smaller than the one associated with fluid-fins collisions.

Finally, Figure 103 summarizes the results of the comparison for the three most interesting fin geometries, namely elliptical, rounded and rectangular, by building a performance index that takes into account both the heat transfer effectiveness and the pressure drops. In particular, since the inlet temperature is the same for every device, the cold side temperature increment divided by the cold side pressure drops is evidently a good index for the overall performance of a heat exchanger. The results highlight that elliptical fins yield at the best combined performance, with rounded fins trailing by about 10 %. Rectangular fins, on the contrary, score very low because of the enormous pressure drops they induce.

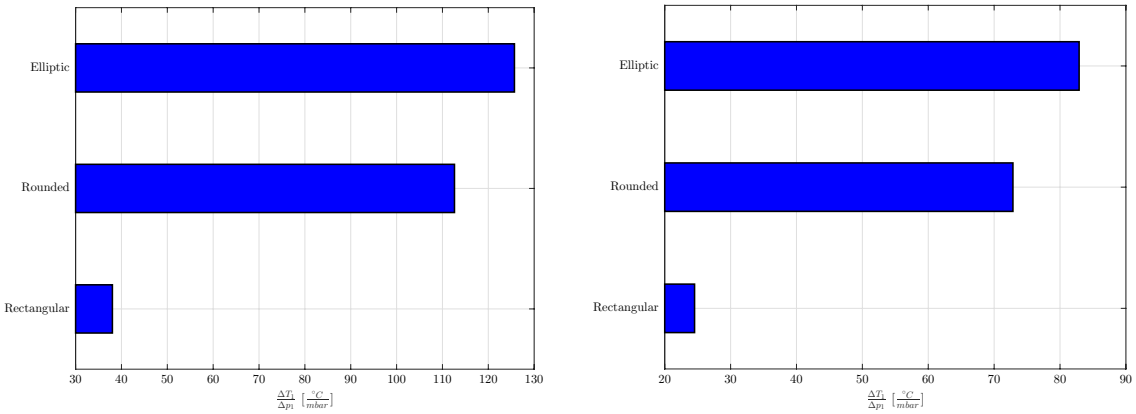

(a) L = 40 mm (b) L = 68 mm

Figure 103: Performance index for different heat exchangers length

In conclusion, this benchmark confirms the suitability of the elliptical fins choice as reference design for the heat exchanger optimization.

9.6 COMSOL/MATLAB Optimum Designs Comparison

As a conclusion of the heat exchanger design activity, it is worth comparing the results produced by the MATLAB sizing procedure object of Chapter 8 and by the COMSOL CFD simulations carried out in this chapter.

In brief, the first design procedure is based on the 0-D concentrated parameters $\varepsilon - NTU$ method, which in turn relies on several assumptions and many semi-empirical correlations. Computational fluid dynamics tools, instead, determine a 3-D distributed parameter model that find its roots in the continuum mechanics. Relying on the Navier-Stokes and on other constitutional equations, a CFD simulation provides as solutions the complete 3-D vectorial

velocity field and the scalar temperature and pressure distributions. As anticipated in this chapter introduction, in order to draw significant comparisons, all these detailed information needs to be condensed into concentrated parameters, such as the heat exchanger effectiveness. In conclusion, the comparison of the two best heat exchangers designs so far produced will be based on the following quantities:

- Effectiveness ε
- Mass velocity G
- Dimensions (length, width and height)
- Compactness index β
- Finned to total heat transfer area ratio f_s

The pressure drops are not a good meter of comparison for several reasons. First, within the MATLAB sizing procedure, pressure losses are treated as a design constraint: the iterative procedure goes on until the actual pressure drops do not exactly meet the limit value imposed as input. On the contrary, the pressure drops in a CFD model are determined as a result of the simulation and can be as low as the fin design allows. Moreover, because of the geometric model used for the CFD simulations, the pressure drops whereby calculated only account for the core losses. On the contrary, the MATLAB implemented sizing procedure includes the losses associated with the flow distribution system as well. Finally, as previously demonstrated, the pressure drops associated with rectangular fins, i.e. an offset-strip geometry evolution, are substantially higher than those produced by the elliptical fins considered for the CFD design.

TABLE XXXII: MATLAB AND COMSOL OPTIMUM HEAT EXCHANGERS DESIGNS COMPARISON

	ε [%]	$G\left[\frac{kg}{m^2 \cdot s}\right]$	L [mm]	W [mm]	H [mm]	$\beta\left[\frac{m^2}{m^3}\right]$	f_s [/]
$\varepsilon - NTU$	95.9	14.4	70.0	36.8	38.4	3990	0.731
CFD	95.9	12.0	68.0	41.6	42.8	3638	0.722

The results of this comparison are represented in Table XXXII. The two heat exchangers, having equally high effectivenesses ε, yield exactly at the same excellent thermal performance. It is worth highlighting that the ratio of finned to primary heat transfer surface area is practically equal as well. As a matter of fact, this consideration confirms one more time that the finned surfaces extension is of cardinal importance toward the achievement of cold side outlet temperatures close to the thermodynamic limit.

In terms of dimensions, the heat exchanger designed following the $\varepsilon - NTU$ method, while having a smaller frontal area, is slightly longer than the other. This is due to the fact that, the pressure drops being higher, i.e. the pressure losses are imposed to be equal to 10 mbar, the allowed mass velocity G is correspondingly higher and, as a consequence, for the same free flow to frontal area ratio σ, the frontal area A_{fr} can be smaller.

Finally, even if the compactness index β is still high enough to refer to both designs as ultra compact heat exchangers, the surface area density β of the HE designed by CFD tools is about 10 % lower than for the other one.

In conclusion, it is possible to state that the best heat exchanger designs produced by the two methods taken into account yield substantially at equally positive outcomes. This result leads to the following two conclusive remarks :

1. It is useful to start with the simpler and less resource-demanding $\varepsilon - NTU$ method to find the preliminary heat exchanger dimensions, before going on with a more accurate, meaningful but also time-consuming CFD design.
2. The $\varepsilon - NTU$ method validity for heat exchangers design is demonstrated one more time. In spite of its apparent simplicity, building on decades of experimental correlations, this method produces rather accurate overall results without being as resources demanding as CFD tools.

CHAPTER 10

FUNCTIONALIZED HEAT EXCHANGER

10.1 Concept

The optimum heat exchanger design introduced in Chapter 9, with an effectivenesses ε as high as 96 %, undoubtedly offers excellent thermal performances. Moreover, the elliptical fins geometry induces reduced pressure drops and leads to a very compact construction, whose surface area density β exceeds 3600 $^{m^2}/_{m^3}$. In brief, this heat exchanger satisfactorily meets all the design requirements specified in Chapter 8.

Nonetheless, in spite of the heat exchanger extremely high effectiveness, the cold side outlet temperature of 704 $°C$ remains considerably lower than the *Solid oxide electrolyser cell* (SOEC) nominal operative temperature, equal to 850 $°C$. In fact, as derived in Chapter 6, because of the heat exchanger regenerative layout and, in particular, of the hot and cold mass flow rates being coupled through the SOEC, the cold side thermodynamic limit outlet temperature is approximately equal to 724 $°C$, well below the desired target of 850 $°C$. As a matter of fact, before entering the co-electrolytic SOEC, the binary water and carbon dioxide mixture needs to undergo a last step of electrical heating, which naturally adds up to the plant variable costs.

In order to improve the P2G plant overall efficiency, it is worth reminding that the methanation reactions taking place downstream of the heat exchanger, as hinted at in Chapter 1, are strongly exothermal. As a consequence, triggering part of these reactions directly in the heat

exchanger, rather than concentrating the entire carbon hydrogenation process into the adiabatic multi-reactor TREMP™ methanation module introduced in Figure 9, allows a further improvement of the system thermal performances. In fact, adding a contribution related to chemical reactions to the *physical* heat flux determined by the system thermal disequilibrium, the greater available energy input allows to push the cold side outlet temperature well beyond the thermodynamic limit of 724 $°C$.

Since for chemical methanation reactions to happen heterogeneous[1] catalytic surfaces are required, the heat exchanger design needs to be accordingly modified or, using a technical term, *functionalized*[2]. While dealing with carbon monoxide and dioxide hydrogenation reactions, in most cases the choice falls on Ni-based catalysts supported by silica or alumina structures, which might incorporate specific promoters as well [84; 85].

If in theory it would be possible to design a single device able to simultaneously operate as heat exchanger and reactor, in practice there are several reasons for which this is not feasible:

1. As stated in Chapter 1, the methanation reaction is favored at low temperature and high pressure. The 850 $°C$ SOEC outlet temperature, although improving the reaction kinetics, does not help from a thermodynamic standpoint.

---

[1]Heterogeneous catalysts, which generally outperform homogeneous ones, act in a different phase than the reactants. Considering the methanation reactions, the catalyst is solid while the reacted elements are gaseous.

[2]The term *functionalization* refers to the modification of a heat exchanger design that enables the achievement of tasks different than pure heat transfer, for instance the development of chemical reactions.

2. Since the SOEC outlet mixture actual composition is very similar to the equilibrium one defined in Table V, which already includes 2.4 % of methane, considering *Le Châtelier's principle*, there is no reason to expect further methanation reactions even in presence of suitable catalysts.

3. Commercial catalysts do not endure temperatures higher than 700 $°C$, because of sintering phenomena that rapidly degrade the performances and ultimately lead to the catalyst destruction [86; 87].

On these grounds, it is not plausible to design a single device combining chemical reactions and heat transfer at high temperature. *Le Châtelier's principle* (1884), which reads as [88]

"When any system at equilibrium is subjected to change in concentration, temperature, volume, or pressure, then the system readjusts itself to (partially) counteract the effect of the applied change and a new equilibrium is established."

suggests that one quantity among concentration, temperature and pressure[1] needs to change in order to enable the methanation reactions development. Since the mixture concentration cannot be easily modified, due to the difficulties in adding or removing any chemical species, and the pressure, a part from the negligible pressure drops, is practically constant, the only remaining free variable is the temperature. In conclusion, carbon can be successfully hydrogenated to methane only provided that the temperature substantially decreases relative to the SOEC outlet level of 850 $°C$.

---

[1] A change in volume is in fact equivalent to a variation of pressure conditions

Figure 104 (a) confirms that the equilibrium methane fraction, and consequently the thermal power released by the exothermal Sabatier reactions shown in Figure 104 (b), increases non-linearly by reducing the temperature. The data represented in Figure 104, referred to the SOEC outlet mixture whose composition and mass flow rate $\dot{m}_2$ have been defined in Table V and Table VI respectively, are the output of an *Aspen Plus* equilibrium simulation. In fact, although the methanation process is well described by the Sabatier reactions, because of the simultaneous hydrogenation of both carbon monoxide, Equation 10.1, and dioxide, Equation 10.2, and since the reaction enthalpy is temperature dependent, it is not possible to precisely derive the thermal power by analytical means, i.e. simulation tools are instead required.

$$CO + 3\,H_2 \rightleftharpoons CH_4 + H_2O \qquad \Delta\overline{h}^0_{298K} = -206\frac{kJ}{mol} \tag{10.1}$$

$$CO_2 + 4\,H_2 \rightleftharpoons CH_4 + 2\,H_2O \qquad \Delta\overline{h}^0_{298K} = -165\frac{kJ}{mol} \tag{10.2}$$

It has already been explained why a single device combining high temperature methanation and heat transfer cannot work. Hereafter, instead, follow the reasons for which it is not convenient to build a unique device where only the surfaces far enough from the SOEC outlet, i.e. at lower temperatures, are functionalized:

1. Thermal management: remembering that the heat exchanger compactness is one important design requirement, it is clear that concentrating the strongly exothermal reactions in the terminal device region is likely to cause the presence of dangerous hot spots.

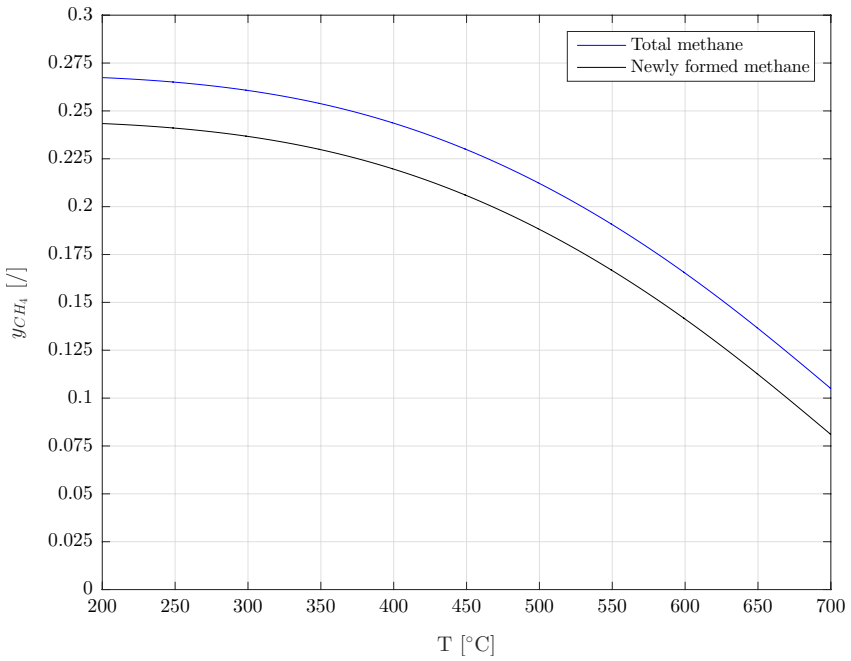

(a) Methane molar fraction

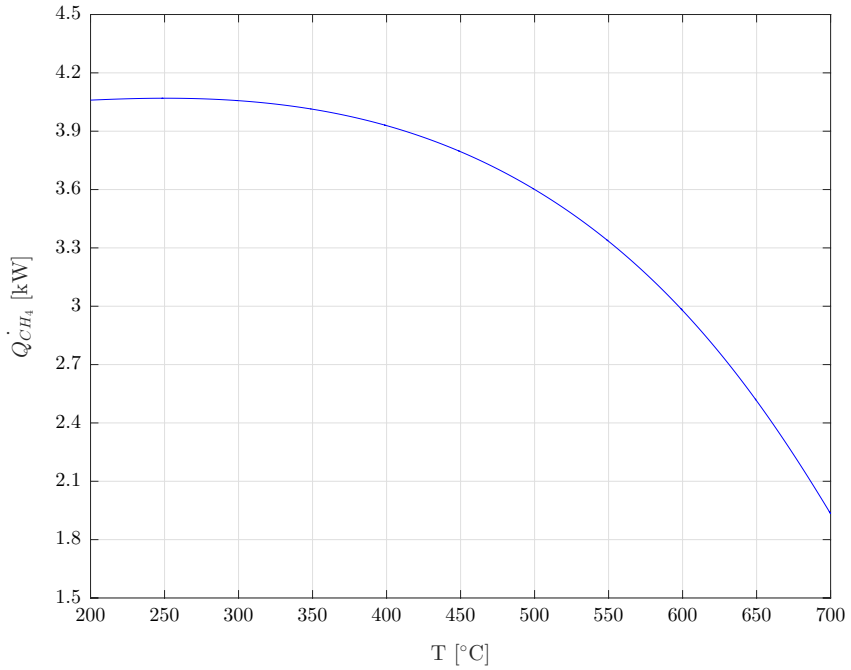

(b) Thermal power produced by the exothermal methanantion reactions

Figure 104: Methanation outputs as a function of temperature

2. Heat transfer: concentrating the chemical reactions close to the hot side outlet could determine an overheating of the cold side inlet and a subsequent inversion[1] of the heat flux moving toward the other heat exchanger extremity.

3. Design optimization: the elliptical fin geometry defined in Chapter 9, while being very performing from a thermo-hydraulic standpoint, is not suitable for catalysts application.

Based on these considerations, it is possible to conclude that, in order to efficiently exploit the methanation exothermal reactions toward the final aim of increasing the SOEC inlet temperature, a two-stages layout, including the components hereafter described, is more suitable than a single device:

1. A *traditional* heat exchanger exploiting the hot SOEC outlet mixture to finalize the SOEC inlet heating. The design of such a device is likely to be very similar to the highly effective one described in Chapter 9, the only difference being the operative temperature range, with the cold side inlet being substantially hotter than 230 $°C$.

2. A *hybrid* heat exchanger, combining chemical reactions with heat transfer processes. In particular, the operative temperature of this second stage being considerably lower than 850 $°C$, the methanation reactions are favored both by the existence of a disequilibrium

---

[1]The *Second Law of Thermodynamics* affirms that "Heat can never pass from a colder to a warmer body without some other change, connected therewith, occurring at the same time." (Clausius, 1854). It is therefore evident that if, due to excessive heating, the *cold* side becomes hotter than the *hot* side, heat transfer direction reverts.

relative to the SOEC outlet conditions (*Le Châtelier's principle*) and for thermodynamic reasons, due to a combination of high pressures and lower temperatures.

Figure 105 summarizes the two paradigms so far introduced in order to maximize the SOEC inlet mixture heating, namely:

a) A single stage consisting of a *physical* heat exchanger where no chemical reactions take place and whose cold side outlet temperature, even supposing a unitary device effectiveness, cannot exceed the thermodynamic limit of 724 $°C$. In practice, as demonstrated in Chapters 8 and 9, this temperature is just slightly higher than 700 $°C$.

b) A two-stages layout, featuring in series a low temperature *hybrid* heat exchanger where the heat produced by the hot side methanation reactions heats up the cold side and a high temperature *physical* heat exchanger which ultimates the cold mixture heating, increasing the temperature well beyond the 724 $°C$ limit.

If it is true that the design of this second solution is more challenging than the previous one because of the introduction of chemical reactions, it is also worth anticipating that the gain in terms of thermal performances, which will be better gaged in the next section, is remarkable as well. As highlighted in Figure 105 (b), adopting a two-stage layout the cold side outlet temperature is a function of the intermediate temperature between the two stages, which from now on will be referred to as *coupling temperature*. Hereafter, the centrality of this parameter on the system performances definition will be carefully explored.

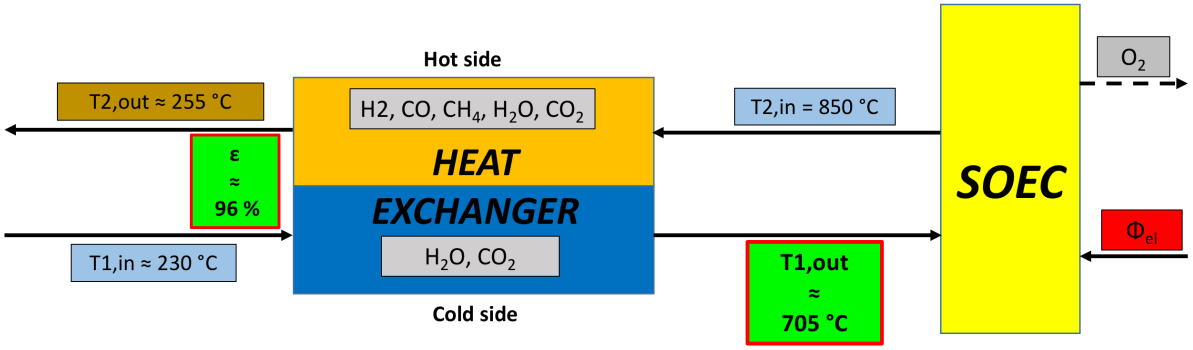

(a) Single stage: *physical* heat exchanger

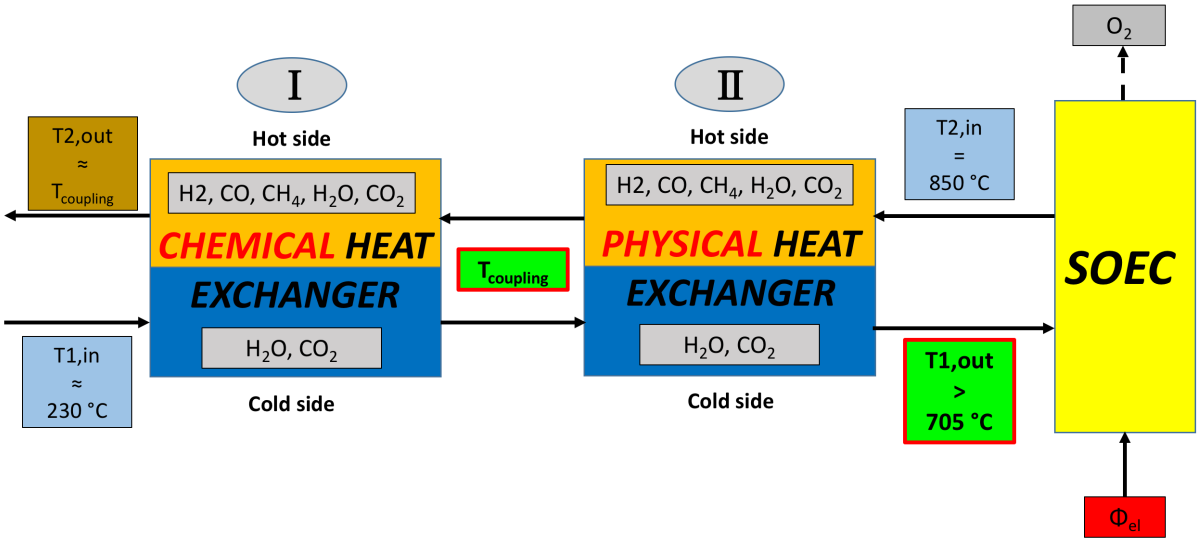

(b) Two-stages: *physical and chemical* heat exchangers

Figure 105: Alternative paradigms for the SOEC inlet mixture heating

10.2 Performances

It is important to highlight since the beginning that what follows will be derived under the assumption of isothermality of the first heat exchanger hot side. This means that in this first stage, the cold fluid heating is supposed to be entirely due to the exothermal methanation reactions, rather than to a hot side cooling, as it happens instead in the second stage.

Considering the existence of a finite approach point temperature difference Δ between the hot and cold sides, the *physical* heat exchanger allows to heat up the cold mixture from just below the coupling temperature $T_{coupling}$ up to its final outlet temperature $T_{1,out,II}$. Assuming, for the sake of calculation simplicity, a unitary heat exchanger effectiveness ε, which is not too far from the reality as an effectiveness higher than 96 % has already been achieved in Chapter 9, the final cold side outlet temperature follows the application of the conveniently simplified *First law of thermodynamics* (FLT) reported in Equation 10.3.

$$\dot{Q}_{II} = C_1 \cdot \Delta T_{1,II} = C_2 \cdot \Delta T_{2,II} \tag{10.3}$$

By remembering that the heat capacity rates ratio C^* is practically constant and equal to 0.8 regardless of the temperature range considered, as proved by Figure 27, it is straightforward to derive the cold side temperature increment $\Delta T_{1,II}$ as a function of the hot side drop $\Delta T_{2,II}$, defined in Equation 10.5 coherently with Figure 105 (b) layout, by means of Equation 10.4.

$$\Delta T_{1,II} = \frac{C_2}{C_1} \cdot \Delta T_{2,II} = C^* \cdot \Delta T_{2,II} \approx 0.8 \cdot \Delta T_{2,II} \tag{10.4}$$

$$\Delta T_{2,II} = T_{2,in,II} - T_{coupling} = 850 - T_{coupling} \quad [^{\circ}C] \tag{10.5}$$

The cold side outlet temperature $T_{1,out,II}$ can be then derived according to Equation 10.6.

$$T_{1,out,II} = T_{1,in,II} + \Delta T_{1,II} = (T_{coupling} - \Delta) + \Delta T_{1,II} \tag{10.6}$$

Combining Equation 10.4 to Equation 10.6, it is possible to derive approximate expressions for the final cold side outlet temperature $T_{1,out,II}$ and for the second stage temperature increment $\Delta T_{1,II}$ as a function of the coupling temperature $T_{coupling}$. Observing Equation 10.7 and Equation 10.8, it is clear that the expected behavior is linear for both quantities and that the coupling temperature determines opposite effects on $T_{1,out,II}$, which increases, and on $\Delta T_{1,II}$, which on the contrary decreases.

$$T_{1,out,II} = T_{coupling} \cdot (1 - C^*) + (C^* \cdot T_{2,in,II} - \Delta) \tag{10.7}$$

$$\Delta T_{1,II} = -C^* \cdot T_{coupling} + C^* \cdot T_{2,in,II} \tag{10.8}$$

Implementing the above described procedure on MATLAB, so to take into account the fact that the heat capacity rates ratio C^* is not exactly constant with temperature as previously assumed, produces the results represented in Figure 106, which confirm the linearity of the

trend. These plots refer to the ideal case in which the approach point temperature difference Δ is nil.

It is evident that increasing the coupling temperature $T_{coupling}$, on one side determines a corresponding cold side outlet temperature $T_{1,out,II}$ rise, while on the other side triggers a reduction of the second stage temperature increment $\Delta T_{1,II}$. Considering the following two limit cases allows to better gage the system performances:

1. $T_{coupling} = T_{1,in,I} \approx 230°C$

   If the coupling temperature coincides with the first stage cold side inlet temperature, it is trivial to conclude that no heat transfer can take place in the first stage heat exchanger. In other words, the two-stages layout represented in Figure 105 (b) degenerates into the well-known system shown in Figure 105 (a). Remembering the assumption of unitary heat exchanger effectiveness ε, it follows that the maximum SOEC inlet temperature is bounded exactly to 724 $°C$.

2. $T_{coupling} = T_{2,in,II} = 850°C$

   When the coupling temperature coincides with the second stage hot side inlet temperature, the layout degenerates again into a single device, which in this second scenario is an ideal hybrid heat exchanger where both high temperature chemical reactions and heat transfer successfully coexist. In this second limit case, the maximum cold side outlet temperature can be as high as 850 $°C$, i.e. coincident with the hot side inlet temperature.

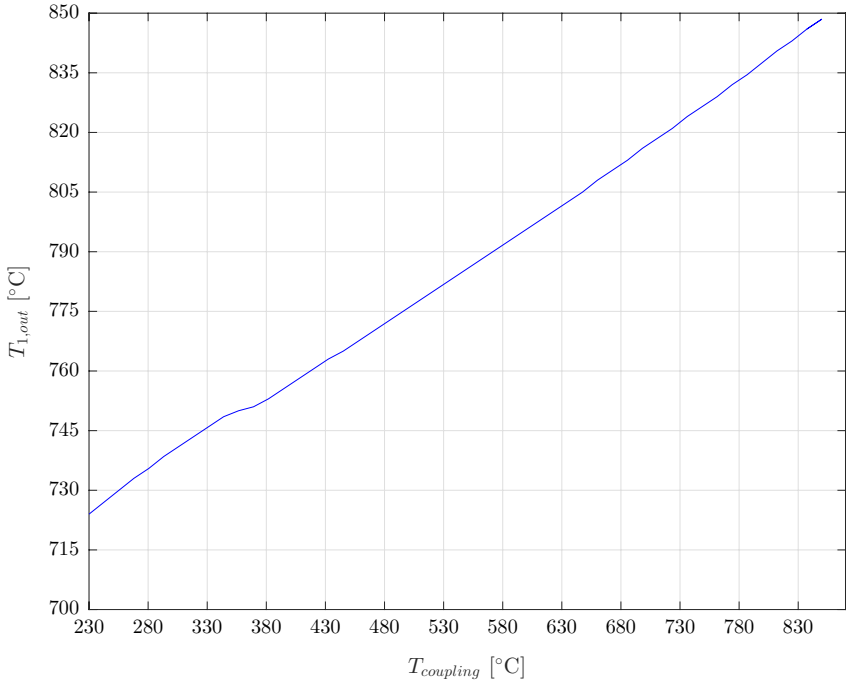

(a) Outlet temperature

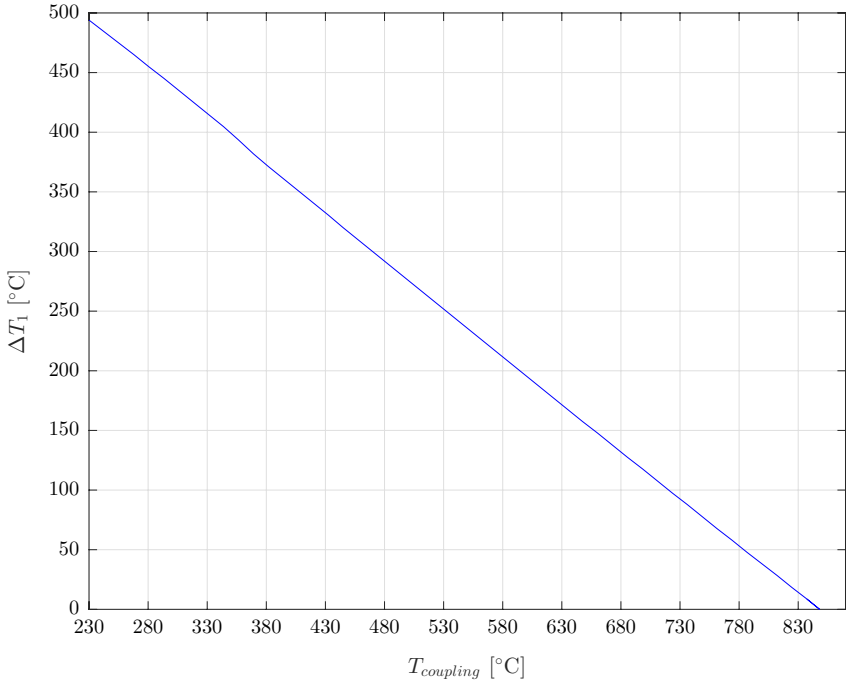

(b) Temperature increment

Figure 106: Second stage heat exchanger cold side

Needless to say, the actual two-stage layout will have performances intermediate between the two extreme cases above described, not allowing to reach, as in the second case, a cold side outlet temperature $T_{1,out,II}$ equal to 850 $°C$ but also improving the first scenario of 724 $°C$.

Having assessed the convenience to select a coupling temperature as high as possible, it is cardinal to remember that commercial catalysts do not operate at temperatures higher than 700 $°C$ because of sintering phenomena, therefore practically limiting the cold side outlet temperature $T_{1,out,II}$ to values lower than 810 $°C$.

Moreover, in order to extend the catalysts life, it is wiser to select even lower values for the coupling temperature, for instance 600 $°C$. Under these operative conditions, Figure 106 (a) proves that the cold side outlet temperature $T_{1,out,II}$ is still approximately equal to 785 $°C$, that is 80 $°C$ higher than what achieved in Chapter 9 adopting the single-stage layout represented in Figure 105 (a).

10.3 Feasibility

While deriving the two-stages layout performances in the previous section, the following assumption has been implicitly made: whatever the coupling temperature $T_{coupling}$, the heat generated by the methanation reactions in the first stage is sufficiently high to heat up the cold mixture to the coupling temperature. This section aims precisely at confirming this hypothesis, so to validate the results previously obtained.

The first stage required heat duty $\dot{Q}_{1,I,required}$, considering one more time the layout shown in Figure 105 (b) and remembering the existence of a finite approach point temperature difference Δ, can be calculated by applying the opportunely simplified FLT represented in Equation 10.9.

$$\dot{Q}_{1,I,required} = C_1 \cdot \Delta T_{1,I} = C_1 \cdot (T_{coupling} - \Delta - T_{1,in,I}) \tag{10.9}$$

The available thermal power $\dot{Q}_{1,I,available}$ as a function of temperature can be instead easily obtained by interpolating the simulation results plotted in Figure 104 (b). It is worth noticing that the values thus obtained refer to a unitary reactant utilization, i.e. to a complete hydrogenation of both carbon monoxide and dioxide.

At this point, it is possible to compare the required and the available heat fluxes as a function of the coupling temperature by taking their ratio as shown in Equation 10.10. This ratio can also be interpreted as an expression for the reactant utilization, i.e. how much methane must be produced, in relative terms, as a function of the temperature. As energy can not be created out of nothing, the range of temperatures where this parameter assumes values greater than the unit do not evidently have any physical meaning.

$$r_{CH_4} = \frac{\dot{Q}_{required}}{Q_{available}} \tag{10.10}$$

On these grounds, the results shown in Figure 107, plotting the reacted methane fraction r_{CH_4} as a function of the coupling temperature, prove that the maximum thermodynamically allowed coupling temperature is approximately equal to 665 $°C$. This limit value derives from the fact that the required and available thermal powers have opposite trends as a function of temperature: while the first one monotonically increases with $T_{coupling}$, the second one decreases non linearly as a consequence of the reduced equilibrium molar fraction, as shown in Figure 104.

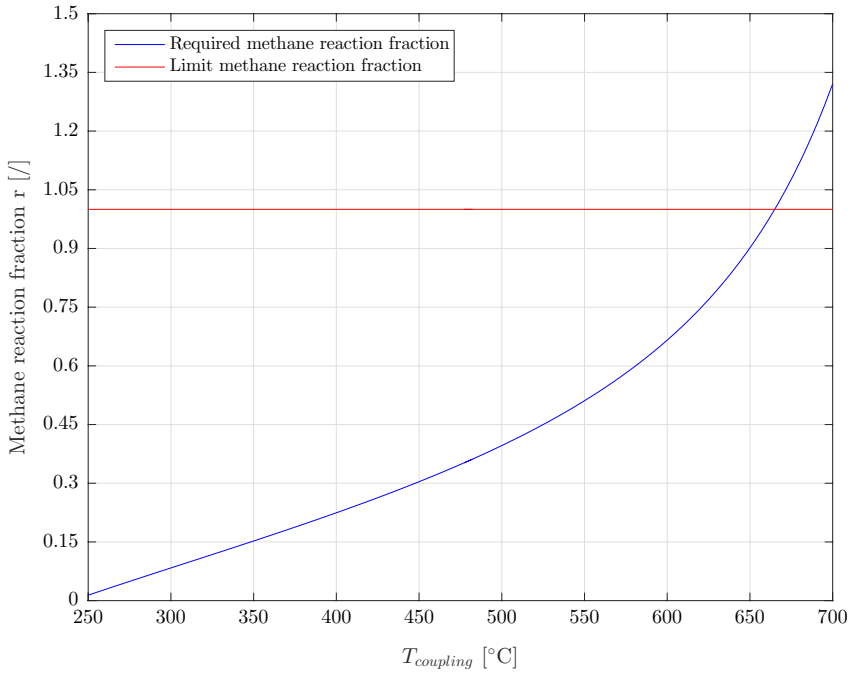

Figure 107: Thermodynamic feasibility of the first stage heat transfer

In practice, however, the technological limit is lower than the thermodynamic one, because of the impossibility to achieve unitary reactant utilizations, especially at high temperatures where the catalysts performance are reduced. The previously mentioned value of 600 $°C$ for the coupling temperature, requiring a reactant utilization factor equal to 65 %, in spite of representing already a remarkable design challenging, is technologically feasible and allows to reach a cold side outlet temperature of 795 $°C$.

In conclusion, adopting a two-stages layout where the first functionalized stage catalyzes methanation reactions allows to substantially increase the SOEC inlet temperature, up to almost 800 $°C$, and therefore to improve the P2G overall efficiency.

CHAPTER 11

CONCLUSIONS

The thesis objective, i.e. the design of a compact high-temperature heat exchanger to be used in a P2G methanation plant and produced by addictive manufacturing, has been successfully reached by means of two independent but complimentary design methods, namely:

1. The Chapter 8 sizing procedure based on the renowned $\varepsilon - NTU$ method.
2. The Chapter 9 CFD tools.

The first lean and cost-effective method has allowed to rapidly identify an optimum heat exchanger design and to estimate its size. The heat exchanger 96 % effectiveness ε, combined with a β value close to 4000 $^{m^2}/_{m^3}$, which indicates an ultra-compact construction, and with pressure drops limited to 10 mbar on both fluid sides, allow to completely meet the demanding HELMETH design requirements.

CFD simulations, starting from the geometric model previously produced, have allowed to optimize the original offset-strip fin geometry, resulting in an elliptical fin shape that drastically cuts the pressure drops. In fact, the *optimum* heat exchanger design, whose effectiveness ε is again equal to 96 %, induces pressure losses as low as 5.5 and 4.3 mbar on the cold and hot side respectively, with evident savings in terms of pumping power. In conclusion, this second device, which, thanks to a β value higher than 3600 $^{m^2}/_{m^3}$, can be still classified as an ultra-compact heat exchanger, thoroughly satisfies the HELMETH technical specifications.

In the perspective of further improving the P2G plant overall efficiency in which this heat exchanger operates heating up the inlet SOEC mixture, Chapter 10 has explored the convenience of *functionalizing* the heat exchanger surfaces by including suitable heterogeneous catalysts able to catalyze methanation processes. In fact, these reactions, because of their exothermal nature, would allow to boost the heat exchanger energy input and consequently increase the SOEC inlet temperature, resulting in evident electrical heating cost savings.

In this context, it has also been proved that the adoption of an innovative two-stages layout, featuring first a low temperature *functionalized* device followed by a *classical* heat exchanger whose design resembles the one described in Chapter 9, allows to maximize the cold side outlet temperature, therefore yielding at the best P2G plant overall efficiency.

In conclusion, the results of this thesis can be summarized in the successful design of an ultra-compact, highly effective heat exchanger and in the exploration of future possibilities to further enhance the P2G performances by combining chemical methanation reactions and heat transfer within a single *functionalized* heat exchanger.

APPENDICES

Appendix A

MATLAB SCRIPTS

Appendix A (continued)

CONSTANT PRESSURE SPECIFIC HEAT

```
function [Cp] = CpGasNIST(T,M)

% This function calculates the costant pressure specific heat Cp of
 each gaseous specie as a function of T, measured in Kelvin.
% Hp: pressure effect is negliglible, only T dependence
% NIST polynominal-wise fit formula used for all species but water

% Cp = A + B * t + C * t^2 + D * t^3 + (E)/t^2;

% Water Cp is calculated through a digital Mollier's diagram, as a
 function of both temperature and pressure

% System pressure [bar]

p = 15;

% Selection between different gases based on their molar mass M

switch M

    % Water vapour (Mollier's diagram, requires Celsius)

    case 18

        % Specific heat at constant pressure [J/kg*K]

        Cp = XSteam('Cp_pt',p,T-273.15) * 1000;

    % Carbon dioxide

    case 44

        % Molar weight [g/mol]

        M_CO2 = 44.0095;

        % Fit constants

        A = 24.99735;
        B = 55.18696;
        C = -33.69137;
        D = 7.948387;
        E = -0.136638;

        t = T/1000;

        % Specific heat at constant pressure [J/kg*K]

        Cp = 1000 * (A + B * t + C * t^2 + D * t^3 + E/t^2)/(M_CO2);
```

Appendix A (continued)

```
% Carbon monoxide

case 28

    % Molar weight [g/mol]

    M_CO = 28.0101;

    % Fit constants

    A = 25.56759;
    B = 6.096130;
    C = 4.054656;
    D = -2.671301;
    E = 0.131021;

    t = T/1000;

    % Specific heat at constant pressure [J/kg*K]

    Cp = 1000 * (A + B * t + C * t^2 + D * t^3 + E/t^2)/(M_CO);

% Hydrogen

case 2

     % Molar weight [g/mol]

     M_H2 = 2.01588;

     % Fit constants

     A = 33.066178;
     B = -11.363417;
     C = 11.432816;
     D = -2.772874;
     E = -0.158558;

     t = T/1000;

     % Specific heat at constant pressure [J/kg*K]

     Cp = 1000 * (A + B * t + C * t^2 + D * t^3 + E/t^2)/(M_H2);

% Methane

case 16

     % Molar weight [g/mol]

     M_CH4 = 16.0425;

     % Fit constants
```

Appendix A (continued)

```
            A = -0.703029;
            B = 108.4773;
            C = -42.52157;
            D = 5.862788;
            E = 0.678565;

            t = T/1000;

            % Specific heat at constant pressure [J/kg*K]

            Cp = 1000 * (A + B * t + C * t^2 + D * t^3 + E/t^2)/(M_CH4);

    otherwise

        disp('There was an error, please select one of the available
 molecular species');

end

end
```

Published with MATLAB® R2015b

Appendix A (continued)

COLD MIXTURE CONSTANT PRESSURE SPECIFIC HEAT

```
function [CpMix] = CpCold(T)

% This function calculates the constant pressure specific heat of the
 cold side mixture

% Fluid composition

[x1, ~] = Composition1();
l = length(x1);

% Individual chemical species molar mass [g/mol]

M_H2O = 18;
M_CO2 = 44;

% Heat capacity of individual chemical species at temperature T

Cp_H2O = CpGasNIST(T,M_H2O);
Cp_CO2 = CpGasNIST(T,M_CO2);

Cp = [Cp_H2O, Cp_CO2];

% Mixture heat capacity calculated as the weighted average of
 components heat capacities relative to mass fractions x

CpMix = 0;

for r = 1:l

    CpMix = CpMix + Cp(r) * x1(r);

end

end
```

Published with MATLAB® R2015b

Appendix A (continued)

HOT MIXTURE CONSTANT PRESSURE SPECIFIC HEAT

```
function [CpMix] = CpHot(T)

% This function calculates the constant pressure specific heat of the
 hot side mixture

% Fluid composition

[x2, ~] = Composition2();
l = length(x2);

% Individual chemical species molar mass [g/mol]

M_H2O = 18;
M_CO2 = 44;
M_CO =  28;
M_H2 =   2;
M_CH4 = 16;

% Heat capacity of individual chemical species at temperature T

Cp_H2O = CpGasNIST(T,M_H2O);
Cp_CO2 = CpGasNIST(T,M_CO2);
Cp_CO =  CpGasNIST(T,M_CO);
Cp_H2 =  CpGasNIST(T,M_H2);
Cp_CH4 = CpGasNIST(T,M_CH4);

Cp = [Cp_H2O,Cp_CO2,Cp_CO,Cp_H2,Cp_CH4];

% Mixture heat capacity calculated as the weighted average of
 components heat capacities relative to mass fractions x

CpMix = 0;

for r = 1:l

    CpMix = CpMix + Cp(r) * x2(r);

end

end
```

Published with MATLAB® R2015b

Appendix A (continued)

SPECIFIC ENTHALPY

```
function [h] = EnthalpyGasNIST(T,M)

% This function calculates the specific enthalpy of each gaseous
 specie as a function of T, measured in Kelvin.
% Hp: pressure effect is negliglible, only T dependence
% NIST polynominal-wise fit formula used for all species but water
% Reference temperature for zero enthalpy: 25 Celsius.
% h as integral of the Cp

% h = A * t + (B/2) * t^2 + (C/3) * t^3 + (D/4) * t^4 - (E)/t + F - H;

% Water h is calculated through a digital Mollier's diagram, as a
 function of both temperature and pressure

% System pressure [bar]

p = 15;

% Selection between different gases based on their molar mass M

switch M

    % Water vapour (Mollier's diagram, requires Celsius)

    case 18

        % Specific heat at constant pressure [kJ/kg]

        h = XSteam('h_pt',p,T-273.15);

    % carbon dioxide

    case 44

        % Molar weight [g/mol]

        M_CO2 = 44.0095;

        % Fit constants

        A = 24.99735;
        B = 55.18696;
        C = -33.69137;
        D = 7.948387;
        E = -0.136638;
        F = -403.6075;
        H = -393.5224;

        t = T/1000;
```

Appendix A (continued)

```
        % Difference between standard enthalpy and reference enthalpy
 [kJ/kg]

        dh = 1000 * (A * t + (B/2) * t^2 + (C/3) * t^3 + (D/4) * t^4 -
 E/t + F - H)/(M_CO2);

        % Reference enthalpy at 25 C [kJ/kg]

        h0 = 0;

        % Total enthalpy at temperature T [kJ/kg]

        h = dh + h0;

    % Carbon monoxide

    case 28

        % Molar weight [g/mol]

        M_CO = 28.0101;

        % Fit constants

        A = 25.56759;
        B = 6.096130;
        C = 4.054656;
        D = -2.671301;
        E = 0.131021;
        F = -118.0089;
        H = -110.5271;

        t = T/1000;

        % Difference between standard enthalpy and reference enthalpy
 [kJ/kg]

        dh = 1000 * (A * t +(B/2)*t^2+(C/3)*t^3+(D/4)*t^4-E/t+F-H)/
(M_CO);

        % Reference enthalpy at 25 C [kJ/kg]

        h0 = 0;

        % Total enthalpy at temperature T [kJ/kg]

        h = dh + h0;

    % Hydrogen

    case 2

         % Molar weight [g/mol]
```

Appendix A (continued)

```
        M_H2 = 2.01588;

        % Fit constants

        A = 33.066178;
        B = -11.363417;
        C = 11.432816;
        D = -2.772874;
        E = -0.158558;
        F = -9.980797;
        H = 0.0;

        t = T/1000;

        % Difference between standard enthalpy and reference enthalpy
[kJ/kg]

        dh = 1000 * (A * t + (B/2) * t^2 + (C/3) * t^3 + (D/4) * t^4
- E/t + F - H)/(M_H2);

        % Reference enthalpy at 25 C [kJ/kg]

        h0 = 0;

        % Total enthalpy at temperature T [kJ/kg]

        h = dh + h0;

   % Methane

   case 16

        % Molar weight [g/mol]

        M_CH4 = 16.0425;

        % Fit constants

        A = -0.703029;
        B = 108.4773;
        C = -42.52157;
        D = 5.862788;
        E = 0.678565;
        F = -76.84376;
        H = -74.87310;

        t = T/1000;

        % Difference between standard enthalpy and reference enthalpy
[kJ/kg]

        dh = 1000 * (A * t + (B/2) * t^2 + (C/3) * t^3 + (D/4) * t^4
- E/t + F - H)/(M_CH4);
```

Appendix A (continued)

```
        % Reference enthalpy at 25 C [kJ/kg]

        h0 = 0;

        % Total enthalpy at temperature T [kJ/kg]

        h = dh + h0;

    otherwise

        disp('There was an error, please select one of the available
 molecular species');

end

end
```

Published with MATLAB® R2015b

Appendix A (continued)

COLD MIXTURE SPECIFIC ENTHALPY

```
function [EnthalpyMix] = EnthalpyCold(T)

% This function calculates the cold side mixture specific enthalpy

% Fluid composition

[x1, ~] = Composition1();
l = length(x1);

% Individual chemical species molar mass [g/mol]

M_H2O = 18;
M_CO2 = 44;

% Specific enthalpy of individual chemical species at temperature T

h_H2O = EnthalpyGasNIST(T,M_H2O);
h_CO2 = EnthalpyGasNIST(T,M_CO2);

h = [h_H2O, h_CO2];

% Mixture specific enthalpy calculated as the weighted average of
 components heat capacities relative to mass fractions x

EnthalpyMix = 0;

for r = 1:l

    EnthalpyMix = EnthalpyMix + h(r) * x1(r);

end

end
```

Published with MATLAB® R2015b

Appendix A (continued)

HOT MIXTURE SPECIFIC ENTHALPY

```
function [EnthalpyMix] = EnthalpyHot(T)

% This function calculates the hot side mixture specific enthalpy

% Fluid composition

[x2, ~] = Composition2();
l = length(x2);

% Individual chemical species molar mass [g/mol]

M_H2O = 18;
M_CO2 = 44;
M_CO =  28;
M_H2 =   2;
M_CH4 = 16;

% Specific enthalpy of individual chemical species at temperature T

h_H2O = EnthalpyGasNIST(T,M_H2O);
h_CO2 = EnthalpyGasNIST(T,M_CO2);
h_CO =  EnthalpyGasNIST(T,M_CO);
h_H2 =  EnthalpyGasNIST(T,M_H2);
h_CH4 = EnthalpyGasNIST(T,M_CH4);

h = [h_H2O,h_CO2,h_CO,h_H2,h_CH4];

% Mixture specific enthalpy calculated as the weighted average of
 components heat capacities relative to mass fractions x

EnthalpyMix = 0;

for r = 1:l

    EnthalpyMix = EnthalpyMix + h(r) * x2(r);

end

end
```

Published with MATLAB® R2015b

Appendix A (continued)

DENSITY

```
function [Ro] = RoGas(T,M)

% This function calculates the density of each gaseous specie as a
 function of T, measured in Kelvin.

% Hp: ideal gas equation

% ro = p/(R * T)

% Universal gas constant [J/K*mol]

Ru = 8314;

% System pressure [Pa]

p= 15*10^5;

% Selection between different gases based on their molar mass M

switch M

    % Water vapour (Mollier's diagram, requires Celsius)

    case 18

       % Density [kg/m^3]

       Ro = XSteam('rho_pT',p/10^5,T-273.15);

    % Carbon dioxide

    case 44

       R = Ru/M;

       % Density [kg/m^3]

       Ro = p/(R * T);

    % Carbon monoxide

    case 28

        R = Ru/M;

        % Density [kg/m^3]

        Ro = p/(R * T);

    % Hydrogen
```

Appendix A (continued)

```
    case 2

        R = Ru/M;

        % Density [kg/m^3]

        Ro = p/(R * T);

    % Methane

    case 16

        R = Ru/M;

        % Density [kg/m^3]

        Ro = p/(R * T);

    otherwise

        disp('There was an error, please select one of the available
 molecular species');

end

end
```

Published with MATLAB® R2015b

Appendix A (continued)

COLD MIXTURE DENSITY

```
function [RoMix] = RoCold()

% This function calculates the cold mixture density

% Inlet, outlet, mean temperatures [K]

[T_v1,~,~] = FLT();

% Fluid composition

[~,y1] = Composition1();
l = length(y1);

% Individual chemical species molar mass [g/mol]

M_H2O = 18;
M_CO2 = 44;

% Since T is a vector, need to derive 3 densities using a cycle

RoMix = zeros(1,3);

for z=1:3

    % Density of individual chemical species at temperature T

    Ro_H2O = RoGas(T_v1(z),M_H2O);
    Ro_CO2 = RoGas(T_v1(z),M_CO2);

    Ro = [Ro_H2O, Ro_CO2];

    % Mixture density calculated as the weighted average of component
 densities relative to molar fractions y

        for r = 1:l

            RoMix(1,z) = RoMix(1,z) + Ro(r) * y1(r);

        end
end

end
```

Published with MATLAB® R2015b

Appendix A (continued)

HOT MIXTURE DENSITY

```
function [RoMix] = RoHot()

% This function calculates the hot mixture density

% Inlet, outlet, mean temperatures [K]

[~,T_v2,~] = FLT();

% Fluid composition

[~, y2] = Composition2();
l = length(y2);

% Individual chemical species molar mass [g/mol]

M_H2O = 18;
M_CO2 = 44;
M_CO = 28;
M_H2 = 2;
M_CH4 = 16;

% Since T is a vector, need to derive 3 densities using a cycle

RoMix = zeros(1,3);

for z=1:3

    % Density of individual chemical species at temperature T

    Ro_H2O = RoGas(T_v2(z),M_H2O);
    Ro_CO2 = RoGas(T_v2(z),M_CO2);
    Ro_CO = RoGas(T_v2(z),M_CO);
    Ro_H2 = RoGas(T_v2(z),M_H2);
    Ro_CH4 = RoGas(T_v2(z),M_CH4);

    Ro = [Ro_H2O, Ro_CO2,Ro_CO,Ro_H2,Ro_CH4];

    % Mixture density calculated as the weighted average of component
 densities relative to molar fractions y

    for r = 1:l

        RoMix(1,z) = RoMix(1,z) + Ro(r) * y2(r);

    end
end
end
```

Published with MATLAB® R2015b

Appendix A (continued)

VISCOSITY

```
function [Mu] = MuGas(T,M)

% This function calculates the viscosity of each gaseous specie as a
 function of T, measured in Kelvin.
% Hp: pressure effect is negliglible, only T dependence

% mu = 26.69 * (M * T)^(0.5)/(sigma^(2)) * Omega) [microPoise]
% Sigma, Epsilon from Lennard Jones Potential
% Tstar = T/(Epsilon/k) = T/r
% k: Boltzmann's constant
% Omega : collision integral
% Omega = [A * (Tstar)^(-B)] + C * [exp(-D * Tstar)] + E * [exp * (-F
 * Tstar)]

% System pressure [bar]

p = 15;

% Neufeld's correlation constants to calculate the collision integral

A = 1.16145;
B = 0.14874;
C = 0.52487;
D = 0.77320;
E = 2.16178;
F = 2.43787;

% Negligible viscosity dependence on pressure

K_pressure = 1.00;

% Selection between different gases based on their molar mass M

switch M

    % Water vapour (Mollier's diagram, requires Celsius)

    case 18

       Mu = XSteam('my_pT',p,T-273.15);

    % Carbon dioxide

    case 44
       sigma = 3.941;
       r = 195.2;
       Tstar = T/r;
       Omega = (A*(Tstar)^(-B))+C*exp(-D*Tstar)+E*exp(-F*Tstar);

       % Viscosity [Pa*s]
```

Appendix A (continued)

```
        Mu0 = (26.69 * (M * T)^(0.5)/((sigma^2) * Omega))/10^7;
        Mu = Mu0 * K_pressure;

    % Carbon monoxide

    case 28
        sigma = 3.690;
        r = 91.7;
        Tstar = T/r;
        Omega = (A*(Tstar)^(-B))+C*exp(-D*Tstar)+E*exp(-F*Tstar);

        % Viscosity [Pa*s]

        Mu0 = (26.69 * (M * T)^(0.5)/((sigma^2) * Omega))/10^7;
        Mu = Mu0 * K_pressure;

    % Hydrogen

    case 2
        sigma = 2.827;
        r = 59.7;
        Tstar = T/r;
        Omega = (A*(Tstar)^(-B))+C*exp(-D*Tstar)+E*exp(-F*Tstar);

        % Viscosity [Pa*s]

        Mu0 = (26.69 * (M * T)^(0.5)/((sigma^2) * Omega))/10^7;
        Mu = Mu0 * K_pressure;

    % Methane

    case 16
        sigma = 3.758;
        r = 148.6;
        Tstar = T/r;
        Omega = (A*(Tstar)^(-B))+C*exp(-D*Tstar)+E*exp(-F*Tstar);

        % Viscosity [Pa*s]

        Mu0 = (26.69 * (M * T)^(0.5)/((sigma^2) * Omega))/10^7;
        Mu = Mu0 * K_pressure;

    otherwise

         disp('There was an error, please select one of the available
 molecular species');
end

end
```

Published with MATLAB® R2015b

Appendix A (continued)

COLD MIXTURE VISCOSITY

```
function [MuMix] = MuCold()

% This function calculates the cold mixture viscosity

% Mean temperaure [K]

[T_v1,~,~] = FLT();
T = T_v1(3);

% Fluid composition

[~,y1] = Composition1();
l = length(y1);

% Individual chemical species molar mass [g/mol]

M_H2O = 18;
M_CO2 = 44;

M = [M_H2O,M_CO2];

% Viscosity of individual chemical species at temperature T

Mu_H2O = MuGas(T,M_H2O);
Mu_CO2 = MuGas(T,M_CO2);

Mu = [Mu_H2O, Mu_CO2];

% Matrix initialization

Phi = zeros(l);

% Cycle to find the coefficient Phi(i,j), correlating 2 components of
 the mixture
% Exactly the same as the one for viscosity

% Phi(i,j) = [1 + (mu_i/mu_j)^(0.25) * (M_j/M_i)^(0.25)]^2/[8 * (1 +
 (M_i/M_j)]^(0.5)

for r = 1:l
    for c = 1:l

        Phi(r,c) = ((1 + ((Mu(r)/Mu(c))^(0.25)) * ((M(c)/
M(r))^(0.25)))^(2))/((8 * (1 + (M(r)/M(c))))^(0.5));

    end
end

% Cycle to calculate the viscosity of the mixture
```

Appendix A (continued)

```
% mu = sum(i) (mu_i*y_i)/(sum(j) (y_j*phi(i,j))

MuMix = 0;

for r = 1:l
    s = 0;
    for c = 1:l

        s = s + (y1(c) * Phi(r,c));

    end

    MuMix = MuMix + (Mu(r) * y1(r))/s;

end

end
```

Published with MATLAB® R2015b

Appendix A (continued)

HOT MIXTURE VISCOSITY

```
function [MuMix] = MuHot()

% This function calculates the hot mixture viscosity

% Mean temperaure [K]

[~,T_v2,~] = FLT();
T = T_v2(3);

% Fluid composition

[~, y2] = Composition2();
l = length(y2);

% Individual chemical species molar mass [g/mol]

M_H2O = 18;
M_CO2 = 44;
M_CO = 28;
M_H2 = 2;
M_CH4 = 16;

M = [M_H2O,M_CO2,M_CO,M_H2,M_CH4];

% Viscosity of individual chemical species at temperature T

Mu_H2O = MuGas(T,M_H2O);
Mu_CO2 = MuGas(T,M_CO2);
Mu_CO = MuGas(T,M_CO);
Mu_H2 = MuGas(T,M_H2);
Mu_CH4 = MuGas(T,M_CH4);

Mu = [Mu_H2O,Mu_CO2,Mu_CO,Mu_H2,Mu_CH4];

% Matrix initialization

Phi = zeros(l);

% Cycle to find the coefficient Phi(i,j), correlating 2 components of
 the mixture
% Exactly the same as the one for viscosity

% Phi(i,j) = [1 + (mu_i/mu_j)^(0.25) * (M_j/M_i)^(0.25)]^2/[8 * (1 +
 (M_i/M_j)]^(0.5)

for r = 1:l
    for c = 1:l

        Phi(r,c) = ((1 + ((Mu(r)/Mu(c))^(0.25)) * ((M(c)/
M(r))^(0.25)))^(2))/((8 * (1 + (M(r)/M(c))))^(0.5));
```

Appendix A (continued)

```
    end
end

% Cycle to calculate the viscosity of the mixture

% mu = sum(i) (mu_i*y_i)/(sum(j) (y_j*phi(i,j))

MuMix = 0;

for r = 1:l
    s = 0;
    for c = 1:l

        s = s + (y2(c) * Phi(r,c));

    end

    MuMix = MuMix + (Mu(r)*y2(r))/s;
end

end
```

Published with MATLAB® R2015b

Appendix A (continued)

THERMAL CONDUCTIVITY

```
function [Lambda] = LambdaGas(T,M)

% This function calculates the thermal conductivity of each gaseous
 specie as a function of T, measured in Kelvin.
% Hp: pressure effect is negliglible, only T dependence

% Lambda = (0.115 + 0.354 * (Cp/R)) * [(8.322/100) * (T/M)^(0.5)/
(sigma^2 * Omega)
% Sigma, Epsilon from Lennard Jones Potential
% Tstar = T/(Epsilon/k) = T/r
% k: Boltzmann's constant
% Omega : collision integral
% Omega = [A * (Tstar)^(-B)] + C * [exp(-D * Tstar)] + E * [exp * (-F
 * Tstar)]

% Water k is calculated through a digital Mollier's diagram, as a
 function of both temperature and pressure

% System pressure [bar]

p = 15;

% Universal gas constant [J/mol*K]

Ru = 8314;

% Neufeld's correlation constants to calculate the collision integral

A = 1.16145;
B = 0.14874;
C = 0.52487;
D = 0.77320;
E = 2.16178;
F = 2.43787;

% Thermal conductivity slightly increases with pressure
% This efect is neglected because too small

K_pressure = 1.00;

% Selection between different gases based on their molar mass M

switch M

    % Water vapour (Mollier's diagram, requires Celsius)

    case 18

       % Thermal conductivity [W/m*K]
```

Appendix A (continued)

```
        Lambda = XSteam('tc_pT',p,T-273.15);

    % Carbon dioxide [g/mol]

    case 44

        sigma = 3.941;
        r = 195.2;
        Tstar = T/r;
        Omega = (A * (Tstar)^(-B)) + C * exp(-D * Tstar) + E * exp(-F *
 Tstar);
        Cp = CpGas(T,M);
        R = Ru/M;

        % Thermal conductivity [W/m*K]

        Lambda0 = (0.115 + 0.354 * (Cp/R)) * ((8.322/100) * (T/
M)^(0.5)/((sigma^2) * Omega));
        Lambda = Lambda0 * K_pressure;

    % Carbon monoxide [g/mol]

    case 28

        sigma = 3.690;
        r = 91.7;
        Tstar = T/r;
        Omega = (A * (Tstar)^(-B)) + C * exp(-D * Tstar) + E * exp(-F *
 Tstar);
        Cp = CpGas(T,M);
        R = Ru/M;

        % Thermal conductivity [W/m*K]

        Lambda0 = (0.115 + 0.354 * (Cp/R)) * ((8.322/100) * (T/
M)^(0.5)/((sigma^2) * Omega));
        Lambda = Lambda0 * K_pressure;

    % Hydrogen [g/mol]

    case 2

        sigma = 2.827;
        r = 59.7;
        Tstar = T/r;
        Omega = (A * (Tstar)^(-B)) + C * exp(-D * Tstar) + E * exp(-F *
 Tstar);
        Cp = CpGas(T,M);
        R = Ru/M;

        % Thermal conductivity [W/m*K]

        Lambda0 = (0.115 + 0.354 * (Cp/R)) * ((8.322/100) * (T/
M)^(0.5)/((sigma^2) * Omega));
```

Appendix A (continued)

```
        Lambda = Lambda0 * K_pressure;

    % Methane [g/mol]

    case 16

        sigma = 3.758;
        r = 148.6;
        Tstar = T/r;
        Omega = (A * (Tstar)^(-B)) + C * exp(-D * Tstar) + E * exp(-F *
 Tstar);
        Cp = CpGas(T,M);
        R = Ru/M;

        % Thermal conductivity [W/m*K]

        Lambda0 = (0.115 + 0.354 * (Cp/R)) * ((8.322/100) * (T/
M)^(0.5)/((sigma^2) * Omega));
        Lambda = Lambda0 * K_pressure;

    otherwise

         disp('There was an error, please select one of the available
 molecular species');

end
end
```

Published with MATLAB® R2015b

Appendix A (continued)

COLD MIXTURE THERMAL CONDUCTIVITY

```
function [LambdaMix] = LambdaCold()

% This function calculates the thermal conductivity of the cold side
 mixture

% Mean temperaure [K]

[T_v1,~,~] = FLT();
T = T_v1(3);

% Fluid composition

[~,y1] = Composition1();
l = length(y1);

% Individual chemical species molar mass [g/mol]

M_H2O = 18;
M_CO2 = 44;

% Thermal conductivity of individual chemical species at temperature T

Lambda_H2O = LambdaGas(T,M_H2O);
Lambda_CO2 = LambdaGas(T,M_CO2);

% Viscosity of individual chemical species at temperature T
% Required to calculate the interaction factors phi

Mu_H2O = MuGas(T,M_H2O);
Mu_CO2 = MuGas(T,M_CO2);

% Property vectors for later cycles

M = [M_H2O,M_CO2];
Mu = [Mu_H2O, Mu_CO2];
Lambda = [Lambda_H2O, Lambda_CO2];

% Matrix initialization

Phi = zeros(l);

% Cycle to find the coefficient Phi(i,j), correlating 2 components of
 the mixture
% Exactly the same as the one for viscosity

% Phi(i,j) = [1 + (mu_i/mu_j)^(0.25) * (M_j/M_i)^(0.25)]^2/[8 * (1 +
 (M_i/M_j)]^(0.5)

for r = 1:l
    for c = 1:l
```

Appendix A (continued)

```
        Phi(r,c) = ((1+((Mu(r)/Mu(c))^(0.25)) * ((M(c)/
M(r))^(0.25)))^(2))/(( 8 * (1 + (M(r)/M(c))))^(0.5));

    end
end

% Cycle to calculate the mixture conductivity

% lambda = sum(i) (lambda_i)/[1 + (sum(j) 1.065 * (y_j/y_i)  *
 phi(i,j)]

LambdaMix = 0;

for r = 1:l
    s = 1;
    for c = 1:l

        if c==r
            s = s + 0;
        else
            s = s + (1.065 * (y1(c)/y1(r)) * Phi(r,c));
        end

    end

    LambdaMix = LambdaMix + (Lambda(r)/s);

end

end
```

Published with MATLAB® R2015b

Appendix A (continued)

HOT MIXTURE THERMAL CONDUCTIVITY

```
function [LambdaMix] = LambdaHot()

% This function calculates the thermal conductivity of the hot side
 mixture

% Mean temperaure [K]

[~,T_v2,~] = FLT();
T = T_v2(3);

% Fluid composition

[~, y2] = Composition2();
l = length(y2);

% Individual chemical species molar mass [g/mol]

M_H2O = 18;
M_CO2 = 44;
M_CO = 28;
M_H2 = 2;
M_CH4 = 16;

% Thermal conductivity of individual chemical species at temperature T

Lambda_H2O = LambdaGas(T,M_H2O);
Lambda_CO2 = LambdaGas(T,M_CO2);
Lambda_CO = LambdaGas(T,M_CO);
Lambda_H2 = LambdaGas(T,M_H2);
Lambda_CH4 = LambdaGas(T,M_CH4);

% Viscosity of individual chemical species at temperature T
% Required to calculate the interaction factors phi

Mu_H2O = MuGas(T,M_H2O);
Mu_CO2 = MuGas(T,M_CO2);
Mu_CO = MuGas(T,M_CO);
Mu_H2 = MuGas(T,M_H2);
Mu_CH4 = MuGas(T,M_CH4);

% Property vectors for later cycles

M = [M_H2O,M_CO2,M_CO,M_H2,M_CH4];
Mu = [Mu_H2O,Mu_CO2,Mu_CO,Mu_H2,Mu_CH4];
Lambda = [Lambda_H2O,Lambda_CO2,Lambda_CO,Lambda_H2,Lambda_CH4];

% Matrix initialization

Phi = zeros(l);
```

Appendix A (continued)

```
% Cycle to find the coefficient Phi(i,j), correlating 2 components of
 the mixture
% Exactly the same as the one for viscosity

% Phi(i,j) = [1 + (mu_i/mu_j)^(0.25) * (M_j/M_i)^(0.25)]^2/[8 * (1 +
 (M_i/M_j)]^(0.5)

for r = 1:l
    for c = 1:l

        Phi(r,c) = ((1 + ((Mu(r)/Mu(c))^(0.25)) * ((M(c)/
M(r))^(0.25)))^(2))/((8 * (1 + (M(r)/M(c))))^(0.5));

    end
end

% Cycle to calculate the mixture conductivity

% lambda = sum(i) (lambda_i)/[1 + (sum(j) 1.065 * (y_j/y_i)  *
 phi(i,j)]

LambdaMix = 0;

for r = 1:l
    s = 1;
    for c = 1:l

        if c==r
            s = s + 0;
        else
            s = s + (1.065 * (y2(c)/y2(r)) * Phi(r,c));
        end

    end

    LambdaMix = LambdaMix + (Lambda(r)/s);

end

end
```

Published with MATLAB® R2015b

Appendix A (continued)

COLD MIXTURE PRANDTL NUMBER

```
function [PrMix] = PrCold()

% This function calculates the Prandtl number of the cold side mixture
 at its mean temperature

% Pr = Cp * mu/lambda

% Mean temperaure [K]

[T_v1,~,~] = FLT();
T = T_v1(3);

% Retrieve constant pressure specific heat, viscosity and thermal
 conductivity from other functions

Cp = CpCold(T);
Mu = MuCold();
Lambda = LambdaCold();

% Prandtl number [/]

PrMix = Cp * Mu/Lambda;

end
```

Published with MATLAB® R2015b

Appendix A (continued)

HOT MIXTURE PRANDTL NUMBER

```
function [PrMix] = PrHot()

% This function calculates the Prandtl number of the hot side mixture
 at its mean temperature

% Pr = Cp * mu/lambda

% Mean temperaure [K]

[~,T_v2,~] = FLT();
T = T_v2(3);

% Retrieve constant pressure specific heat, viscosity and thermal
 conductivity from other functions

Cp = CpHot(T);
Mu = MuHot();
Lambda = LambdaHot();

% Prandtl number [/]

PrMix = Cp * Mu/Lambda;

end
```

Published with MATLAB® R2015b

Appendix A (continued)

MIXTURE 1 COMPOSITION

```
function [x1,y1] = Composition1()

% This function defines the composition of the cold side mixture in
 terms of molar and mass fractions
% Mixture 1 is the mixture entering the co-electrolysis SOEC

% Molar masses [g/mol]

M_H2O = 18;
M_CO2 = 44;

M = [M_H2O M_CO2];

% Molar fractions y [/]

y_H2O = 0.825;
y_CO2 = 0.175;

y1 = [y_H2O y_CO2];
z = length(y1);

% Check that the sum of the molar fractions is unitary

if (sum(y1))~=1
    disp('Error in molar balance!');
end

% Mass fractions x [/]

MMix = 0;

for i = 1:z
    MMix = MMix + y1(i) * M(i);
end

x_H2O = y_H2O * M_H2O / MMix;
x_CO2 = y_CO2 * M_CO2 / MMix;

x1 = [x_H2O x_CO2];

end
```

Published with MATLAB® R2015b

MIXTURE 2 COMPOSITION

```
function [x2,y2] = Composition2()

% This function defines the composition of the hot side mixture in
 terms of molar and mass fractions
% Mixture 2 is the mixture leaving the SOEC after co-electrolysis
 happened under the following conditions:
% 1) Reactant utilization RU = 70%
% 2) Pressure p = 15 bar
% 3) Hp: chemical equilibrium


% Molar masses [g/mol]

M_H2O = 18;
M_CO2 = 44;
M_CO =  28;
M_H2 =  2;
M_CH4 = 16;

M = [M_H2O M_CO2 M_CO M_H2 M_CH4];

% Molar fraction y [/]

y_H2O = 0.286;
y_CO2 = 0.053;
y_CO =  0.107;
y_H2 =  0.530;
y_CH4 = 0.024;

y2 = [y_H2O y_CO2 y_CO y_H2 y_CH4];
z = length(y2);

% Check that the sum of the molar fractions is unitary

if (sum(y2))~=1
    disp('Error in molar balance!');
end


% Mass fractions x [/]

MMix = 0;

for i = 1:z
    MMix = MMix + y2(i) * M(i);
end

x_H2O = y_H2O * M_H2O / MMix;
x_CO2 = y_CO2 * M_CO2 / MMix;
x_CO =  y_CO  * M_CO  / MMix;
```

Appendix A (continued)

```
x_H2 =  y_H2  * M_H2  / MMix;
x_CH4 = y_CH4 * M_CH4 / MMix;

x2 = [x_H2O x_CO2 x_CO x_H2 x_CH4];

end
```

Published with MATLAB® R2015b

Appendix A (continued)

MASS FLOW RATES DEFINITION

```
function [md1,md2] = MdotDef()

% This function defines the cold and the hot mass flow rates for later
 use in other functions

% Index 1: cold side
% Index 2: hot side

% Cold side mass flow rate [kg/s]
% Independent variable, allows to scale the HE frontal area

md1 = 3.0/1000;

% Mass flow rates ratio [/]

K = MDotRatio();

% Hot side mass flow rate [kg/s]
% Scaled with respect to the cold side, because of the working
 principle of the SOEC, that routes away most of the available O2,
 reducing the mass flow rate

md2 = K * md1;

end
```

Published with MATLAB® R2015b

Appendix A (continued)

MASS FLOW RATES RATIO

```
function [K] = MDotRatio()

% This function calculates the ratio between the HE hot and cold mass
 flow rates based on an AspenPlus simulation of the SOEC
% (RU = 70%, p = 15 bar, chemical equilibrium)

% Index 1: cold side
% Index 2: hot side

% Cold HE inlet molar flow rate: H2O, CO2 [mol/s]

md1 = 0.740308;

% Hot HE inlet molar flow rate: H2O, CO2, CO, H2, CH4 [mol/s]

md2 = 0.706105;

% Cold HE inlet molar composition

y1_H2O = 0.825;
y1_CO2 = 0.175;

y1 = [y1_H2O, y1_CO2];

% Hot HE inlet molar composition

y2_H2O = 0.286;
y2_CO2 = 0.053;
y2_CO =  0.107;
y2_H2 =  0.530;
y2_CH4 = 0.024;

y2 = [y2_H2O, y2_CO2, y2_CO, y2_H2, y2_CH4];

% Molar masses [g/mol]

M_H2O = 18;
M_CO2 = 44;
M_CO =  28;
M_H2 =  2;
M_CH4 = 16;

MM1 = [M_H2O, M_CO2];
MM2 = [M_H2O, M_CO2, M_CO, M_H2, M_CH4];

% Individual species molar flow rates [mol/s]

Md1 = md1 * y1;
Md2 = md2 * y2;
```

Appendix A (continued)

```
% Individual species mass flow rates [g/s]

Mm1 = Md1 .* MM1;
Mm2 = Md2 .* MM2;

% Mixtures mass flow rates [g/s]

M1 = sum(Mm1);
M2 = sum(Mm2);

% Mass flow rates ratio [/]

K = M2/M1;
```

Published with MATLAB® R2015b

Appendix A (continued)

Table of Contents

PLATE FIN HEAT EXCHANGER GEOMETRY

```
function [Geom_v1, Geom_v2, Geom] = Geometry()

% This is a definition function, where the dimensions defining a PFHE
 are defined u?numerically for later use in other functions.

% Index 1: cold side
% Index 2: hot side
```

INDEPENDENT PARAMETERS

```
% Plate spacing (fluid passage height) [mm]

b1 = 1.2;
b2 = 1.2;

% Plate thickness [mm]
% Due to manufacturing reasons by Selective Laser Melting, this
 thickness cannot be less than 1 mm (otherwise it would be decreased
 so to reduce the thermal resistance of the plate).

t_w = 1.0;

% Fin thickness [mm]
% Can't go below 0.2 mm again due to manufacturing constraints (SLM)

t1 = 0.3;
t2 = 0.3;

% Fin offset [mm]
% Distance between two rows of fins (longitudinal fin pitch)

ls1 = 2.0;
ls2 = 2.0;

% (Transversal) Fin pitch [mm]

p1 = 0.8;
p2 = 0.8;

% Fins density [fins/m]
```

```
Fin_density1 = (1/p1)*1000;
Fin_density2 = (1/p2)*1000;

% Heat transfer area density beta [m^2/m^3]
% Total heat transfer area to total volume between plates ratio
 (referred to one fluid side only)
% Independent design variable, i.e. how compact I want the HE to be

Beta1 = 3600;
Beta2 = 3600;

% Finned area to total heat transfer area ratio [m^2/m^2]

fs1 = 0.75;
fs2 = 0.75;

% Maximum allowed building volume (SLM Machine EOS Xtended270) [cm^3]

Vmax = 25 * 25 * 21.5;
```

DEPENDENT PARAMETERS

```
% Free flow width [mm]

s1 = p1 - t1;
s2 = p2 - t2;

% Fee flow height [mm]
% In a classical offset strip fin HE, hc = b - t; but thanks
 to addictive manufacturing geometry is modified and hc changes
 correspondingly

h1c = b1;
h2c = b2;

% Hydraulic diameter Dh (diameter for non circular sections) [mm]
% Unitary cell approach

Dh1 = (4*s1 * h1c * ls1)/(2*(s1 * ls1 + h1c * ls1 + h1c * t1));
Dh2 = (4*s2 * h2c * ls2)/(2*(s2 * ls2 + h2c * ls2 + h2c * t2));

% Fin length for fin efficiency calculation [mm]
% % Originally in a classical offset strip fin HE, l = b/2 -t; but
 thanks to addictive manufacturing geometry is modified and hc changes
 correspondingly

l1 = b1/2;
l2 = b2/2;

% Heat transfer area to HE volume ratio Alpha [m^2/m^3]
% Function of compactness Beta and "thickness" of the HE layers

Alpha1 = (b1 * Beta1)/(b1 + b2 + 2*t_w);
```

```
Alpha2 = (b2 * Beta2)/(b1 + b2 + 2*t_w);

% Free flow to frontal area ratio Delta [/]
% Factor 1/1000 to have the hydraulic diameter in m instead of mm
% Function of both Beta (through Alpha) and Dh

Delt1 = (Alpha1 * (Dh1/1000))/4;
Delt2 = (Alpha2 * (Dh2/1000))/4;


% Inconel 718 thermal conductivity [W/m*K]
% Fins and plates are of the same material

k_fin = 22;
k_w = k_fin;
```

OUTPUT VECTORS

```
Geom_v1 = [b1 t1 ls1 p1 Fin_density1 Dh1 Beta1 fs1 s1 h1c l1 Alpha1
 Delt1];
Geom_v2 = [b2 t2 ls2 p2 Fin_density2 Dh2 Beta2 fs2 s2 h2c l2 Alpha2
 Delt2];
Geom = [t_w Vmax k_fin k_w];

end
```

Published with MATLAB® R2015b

Appendix A (continued)

NTU

```
function [C1, C2, Cr, NTU] = fNTU()

% This function calculates NTU (Number of Transfer Units) based on the
 Epsilon-NTU method
% Inputs: Epsilon (indipendent design variable), Cr (function of fluid
 properties), HE configuration (plate fin counterflow HE)

% Mass flow rates [kg/s]

[md1,md2] = MdotDef();

% Temperatures (inlet, outlet and mean) [K]

[T_v1,T_v2,~] = FLT();

T_m1 = T_v1(3);             % Cold side mean T
T_m2 = T_v2(3);             % Hot side mean T

% Constant pressure heat capacities evaluated at the arithmetical mean
 temperatures [J/kg*K]
% For a precise result, thermophysical properties should be evaluated
 at the mass-weighted mean temperature (not arithmetical)

Cp1 = CpCold(T_m1);
Cp2 = CpHot(T_m2);

% Heat capacity rates [W/K]

C1 = md1 * Cp1;
C2 = md2 * Cp2;

Cmin = min(C1,C2);
Cmax = max(C1,C2);

% Heat capacity rate ratio [/]

Cr = Cmin/Cmax;

% Heat exchanger effectiveness

Eps = Epsilon();

% Number of (total) Transfer Units for a COUNTERFLOW PFHE

NTU = 1/(1-Cr)*log((1-Cr*Eps)/(1-Eps));

end
```

Published with MATLAB® R2015b

Appendix A (continued)

Table of Contents

ISOENTHALPIC MIXING OF COLD SIDE FLUIDS

```
function [T1_in] = ColdSideMix()

% This script calculates the inlet temperature of a mixture of CO2 and
 H2O as a result of an enthalpic balance
% This mixture represents the cold side fluid of the heat exchanger
 object of analysis

% Pressure: 15 bar

% H2O inlet T: saturated vapour at pressure p = 15 bar
% CO2 inlet T: result of a polytropic compressione up to p = 15 bar
```

INPUT QUANTITIES

```
% Inlet mixture composition (mass fraction x)

[x1,~] = Composition1();
x_H2O = x1(1);
x_CO2 = x1(2);

% Pressures

p0 = 1;                     % Atmospheric pressure     [bar]
p = 15;                     % Heat exchanger pressure  [bar]

% Hp: water is already compressed and vapourized

% Saturation temperature at pressure p [K] (Mollier diagram)

T_H2O = XSteam('Tsat_p',p)+273.15;

% CO2 polytropic compression

beta_total = p/p0;              % compression ratio
beta = sqrt(beta_total);        % 2-stage compression
gamma_CO2 = 1.294;              % adiabatic coefficient
n_comp = 0.80;                  % politropic efficiency of the
 compressor
T_CO2_0 = 293.15;               % room temperature [K]

% Due to compression heating, CO2 T increases
% Final temperature after a 2-stages polytropic compression [K]
```

```
z = ((gamma_CO2 - 1)/gamma_CO2) * (1/n_comp);

T_CO2 = T_CO2_0 * (beta^(z))^2;

% Molar masses of individual chemical species [g/mol]

M_H2O = 18;
M_CO2 = 44;

% Enthalpy balance, yielding at the unique equilibrium temperature of
 the CO2 and H20 mixture

% Steam enthalpy from Mollier Diagram [kJ/kg]
% 0.1 to avoid numerical confusion between vapour and saturated vapour

h_H2O_in = EnthalpyGasNIST(T_H2O+0.1,M_H2O);

% CO2 enthalpy [kJ/kg]

h_CO2_in = EnthalpyGasNIST(T_CO2,M_CO2);

% Enthalpy balance (FLT), weighted with respect to mass fractions

h_in = (x_H2O * h_H2O_in)+(x_CO2 * h_CO2_in);
```

ITERATIVE SOLVER

```
% Since enthalpy is directly linked to temperature, one can
 iteratively find the temperature corresponding to a known enthalpy
% Initial guess for the equilibrium temperature: mean temperature
 Tmean [K]

T1 = (T_CO2 + T_H2O)/2;

% Mixture enthalpy at the trial temperature [kJ/kg]

h = EnthalpyCold(T1);

ea = h - h_in;                                  % Absolute error
er = ea / h_in;                                 % Relative error
tol = 0.005;                                    % Accepted relative error
Dt = 0.5;                                       % Pitch for correcting the
 T
k = 0;                                          % Counter for iterations

% Iterate until the result is accurate within the required tolerance
% Separate in two cases, depending on the sign of the error, in order
 to avoid that the iterative procedure diverges.

% Er>0: must decrease the temperature
% Er<0: must increase the temperature
```

Appendix A (continued)

```
while abs(er) >  tol
    k = k +1;

    if er > 0
        T1 = T1 - Dt;
        h = EnthalpyCold(T1);
        ea = h-h_in;
        er = ea/h_in;
    else
        T1 = T1 + Dt;
        h = EnthalpyCold(T1);
        ea = h-h_in;
        er = ea/h_in;
    end
end

% Inlet temperature cold side of the mixture [K]

T1_in = T1;

end
```

Published with MATLAB® R2015b

Appendix A (continued)

Table of Contents

ENERGY BALANCE

```
function [T_v1,T_v2,q] = FLT()

% This function allows to calculate the outlet temperatures of both
 cold and hot side and the real heat transfer applying the first
 principle of thermodynamics, based on the following inputs:
% Compositions, mass flow rates, inlet temperatures and  HE
 Effectiveness

% Hp: adiabatic system (no heat losses to external environment)

% Index 1: cold side
% Index 2: hot side
```

HEAT TRANSFER

```
% Mass flow rates [kg/s]

[md1,md2] = MdotDef();

% Heat Exchanger desired effectiveness
% Independent variable, chosen at the beginning of the design

Eps = Epsilon();

% Cold side inlet temperature [K]
% From isoenthalpic mixing process of CO2 and H2O

T1_in = ColdSideMix();

% Hot side inlet temperature [K]
% Operative temperature of the SOEC

T2_in = 850 + 273.15;

% Inlet enthalpies [kJ/kg]

h1_in = EnthalpyCold(T1_in);
h2_in = EnthalpyHot(T2_in);

% From previous trials (and looking at the mass flow rates), it is
 evident that the limiting side is the hot side.
```

Appendix A (continued)

```
% Hence the maximum amount of heat power is calculated with reference
 to the hot side.

% Limit hot side outlet enthalpy:
% Enthalpy at the cold side inlet temperature

h2_out_lim = EnthalpyHot(T1_in);

Dh2_lim = h2_in - h2_out_lim;

% Maximum possible heat transwer (thermodynamic limit) [kW]

qmax = md2 * Dh2_lim;

% Maximum real heat transfer, based on Eps definition [kW]

q = qmax * Eps;
```

OUTLET TEMPERATURE COLD SIDE

```
% Cold side outlet enthalpy, from FLT [kJ/kg]

h1_out = h1_in + q/md1;

% Since enthalpy is directly linked to temperature, one can
 iteratively find the temperature corresponding to a known enthalpy

% Initial guess for cold side outlet T: hot side inlet T (limit case).
 In reality less, so the direction of the correction is known

T1 = T2_in;

% Cold side enthalpy at the trial temperature [kJ/kg]

h1 = EnthalpyCold(T1);

ea1 = h1 - h1_out;                              % Absolute error
er1 = ea1 /h1_out;                              % Relative error
tol = 0.001;                                    % Accepted relative
 error
Dt = 0.01;                                      % Pitch for correcting
 the T
k1 = 0;                                         % Counter for iterations

% Iterate until the result is accurate within the required tolerance
% Separation into two cases, depending on the sign of the error, in
 order to avoid that the iterative procedure diverges.

% Er>0: must decrease the temperature
% Er<0: must increase the temperature

while abs(er1) >  tol
    k1 = k1 +1;
```

```
    if er1 > 0
        T1 =  T1 - Dt;
        h1 =  EnthalpyCold(T1);
        ea1 = h1-h1_out;
        er1 = ea1/h1_out;
    else
        T1 =  T1 + Dt;
        h1 =  EnthalpyCold(T1);
        ea1 = h1-h1_out;
        er1 = ea1/h1_out;
    end
end

% Cold side outlet temperature [K]

T1_out = T1;

% Cold side arithmetical mean temperature [K]

T1_m = (T1_in + T1_out)/2;
```

OUTLET TEMPERATURE HOT SIDE

```
% Hot side outlet enthalpy, from FLT [kJ/kg]

h2_out = h2_in - q/md2;

% Initial guess for hot side outlet T: cold side inlet T (limit case).
 In reality more, so the direction of the correction is known

T2 = T1_in;

% Enthalpy at the trial temperature [kJ/kg]

h2 = EnthalpyHot(T2);

% Maintain the same tolerance (tol) and temperature correction factor
 (dT) as for the cold side iteration, as defined above

ea2 = h2 - h2_out;                              % Absolute error
er2 = ea2 /h2_out;                              % Relative error
k2 = 0;                                         % Counter for iterations

% Iterate until the result is accurate within the required tolerance

while abs(er2) >  tol
    k2 = k2 + 1;

    if er2 > 0
        T2 =  T2 - Dt;
        h2 =  EnthalpyHot(T2);
        ea2 = h2-h2_out;
```

Appendix A (continued)

```
        er2 = ea2/h2_out;
    else
        T2 =  T2 + Dt;
        h2 =  EnthalpyHot(T2);
        ea2 = h2-h2_out;
        er2 = ea2/h2_out;
    end
end

% Hot side outlet temperature [K]

T2_out = T2;

% Hot side arithmetical mean temperature [K]

T2_m = (T2_in + T2_out)/2;
```

OUTPUT VECTORS

```
% Temperature vectors with inlet, outlet and mean temperature in [K]

T_v1 = [T1_in T1_out T1_m];
T_v2 = [T2_in T2_out T2_m];

end
```

Published with MATLAB® R2015b

Appendix A (continued)

Table of Contents

PRELIMINAR SIZING OF A COUNTERFLOW OFFSET-STRIP FINS HEAT EXCHANGER

```
function[L,Lato] = HE_Sizing()

% Main reference: Fundamentals of Heat Exchanger design (Shah)
%                 Chapter 9.2, 605 - 622

% Inputs:

% - HE configuration (crossflow)
% - Fin geometry (offset-strip fins)
% - HE material (Inconel 718)
% - HE required effectiveness
% - Maximum allowed pressure drops
% - Cold and hot side inlet temperatures
% - Cold and hot side compositions
% - Cold and hot side mass flow rates

% Output:

% - HE overall dimensions (length, width, height)
```

```
% - Real pressure drops

% The sizing procedure is inherently iterative, meaning that more
 than one round of iterations will be necessary in order to meet the
 thermal
% requirements while having the actual pressure drops corresponding to
 the imposed ones.

% Important note:
% While the pressure drops are explicitely given as design
 requirements,the thermal requirements are hidden inside the required
 heat exchanger effectiveness

% Index 1: cold side
% Index 2: hot side
```

HE INPUT GEOMETRY

```
% Recall input geometric dimensions from the definition file

[Geom_v1, Geom_v2, Geom] = Geometry();

% Plate spacing [mm]

b1 = Geom_v1(1);
b2 = Geom_v2(1);

% Plate thickness [mm]

t_w = Geom(1);

% Fin thickness [mm]

t1 = Geom_v1(2);
t2 = Geom_v2(2);

% Fin offset [mm]

ls1 = Geom_v1(3);
ls2 = Geom_v2(3);

% (Transversal) Fin pitch [mm]

p1 = Geom_v1(4);
p2 = Geom_v2(4);

% Hydraulic diameter [mm]

Dh1 = Geom_v1(6);
Dh2 = Geom_v2(6);

% Heat transfer area density beta [m^2/m^3]
```

Appendix A (continued)

```
Beta1 = Geom_v1(7);
Beta2 = Geom_v2(7);

% Finned area to total heat transfer area ratio [m^2/m^2]

fs1 = Geom_v1(8);
fs2 = Geom_v2(8);

% Free flow width [mm]

s1 = Geom_v1(9);
s2 = Geom_v2(9);

% Fee flow height [mm]

h1c = Geom_v1(10);
h2c = Geom_v2(10);

% Fin length for fin efficiency calculation [mm]

l1 = Geom_v1(11);
l2 = Geom_v2(11);

% Heat transfer area to HE volume ratio Alpha [m^2/m^3]

Alpha1 = Geom_v1(12);
Alpha2 = Geom_v2(12);

% Free flow to frontal area ratio Delta [/]

Delt1 = Geom_v1(13);
Delt2 = Geom_v2(13);

% Maximum allowed building volume

Vmax = Geom(2);

% Inconel 718 thermal conductivity (plate, fins) [W/m*K]

k_fin = Geom(3);
k_w = Geom(4);
```

HE NON-GEOMETRIC INPUTS

```
% Mass flow rates [kg/s]

[md1,md2] = MdotDef();

% Temperatures [K]

[T_v1,T_v2,~] = FLT();

% Mean  T [K]
```

Appendix A (continued)

```
T_m1 = T_v1(3);
T_m2 = T_v2(3);
```

GEOMETRIC SURFACE CHARACTERISTICS 1

```
% Main reference: Fundamentals of Heat Exchanger design (Shah)
%                 Chapter 7.5

% f: Fanning friction factor f = (Dp * rho * gc * Dh)/(2L * G^2)
% j: Colburn factor j = (h/(G * Cp)) * Pr^(2/3)

% Determination of f and j as function of fin geometry and Reynolds
 number

% Manglik and Bergles correlations
% Validity range:
% 120 < Re < 10^4
% 0.5 < Pr < 15

% Problem: Re is not available at this stage of design
% Solution: thanks to the weak dependance of the ratio (j/f) from
 Reynolds (experimental), the error produced using
% the mean value of (j/f) over an entire range of Reynolds number is
 sufficiently small

% Note: individually, both j and f strongly depends on Reynolds, but
 their
% ratio has isntead just a weak dependance

% Selected Reynolds range (guess): 300 -1000

Re = linspace(300,1000,10^3);

% Colburn factor (vector)

j_1 = 0.6522.*Re.^(-0.5403).*(s1/h1c)^(-0.1541).*(t1/
ls1)^(0.1499).*(t1/
s1)^(-0.0678).*(1+5.269*10^(-5).*(Re).^(1.340).*(s1/h1c)^(0.504).*(t1/
ls1)^(0.456).*(t1/s1)^(-1.055)).^(0.1);
j_2 = 0.6522.*Re.^(-0.5403).*(s2/h2c)^(-0.1541).*(t2/
ls2)^(0.1499).*(t2/
s2)^(-0.0678).*(1+5.269*10^(-5).*(Re).^(1.340).*(s2/h2c)^(0.504).*(t2/
ls2)^(0.456).*(t2/s2)^(-1.055)).^(0.1);

% Fanning friction factor (vector)

f_1 =9.6243.*Re.^(-0.7422).*(s1/h1c)^(-0.1856).*(t1/
ls1)^(0.3053).*(t1/
s1)^(-0.2659).*(1+7.669*10^(-8).*(Re).^(4.429).*(s1/h1c)^(0.920).*(t1/
ls1)^(3.767).*(t1/s1)^(0.236)).^(0.1);
f_2 =9.6243.*Re.^(-0.7422).*(s2/h2c)^(-0.1856).*(t2/
ls2)^(0.3053).*(t2/
```

```
s2)^(-0.2659).*(1+7.669*10^(-8).*(Re).^(4.429).*(s2/h2c)^(0.920).*(t2/
ls2)^(3.767).*(t2/s2)^(0.236)).^(0.1);

% Ratio j/f (vector)

r_v1 = j_1./f_1;
r_v2 = j_2./f_2;

% Mean j/f factor over the selected Reynolds range

rm1 = mean(r_v1);
rm2 = mean(r_v2);
```

NTU

```
% Recall global NTU from Epsilon-NTU function
% C: heat capacity rate
% Cr: ratio of heat capacity rates

[C1, C2, Cr, NTU] = fNTU();

% Heat capacity rate [W/K]

Cmin = min(C1,C2);
Cmax = max(C1,C2);

% Determination of NTU for each fluid side
% Hp: consider balancedthermal resistances on the cold and hot side,
 so NTUi = 2 * NTU

ntu1 = 2 * NTU;
ntu2 = 2 * NTU;
```

FLUID PROPERTIES

```
% Density vector:  Tin, Tout, Tmean [kg/m^3]

Ro_v1 = RoCold();
Ro_v2 = RoHot();

% Density at inlet and outlet temperatures [kg/m^3]

Ro_in1 = Ro_v1(1);
Ro_out1 = Ro_v1(2);

Ro_in2 = Ro_v2(1);
Ro_out2 = Ro_v2(2);

% Mean density calculated as harmonic mean between inlet and outlet
 densities

Ro_m1 = (0.5 * ((1/Ro_v1(1)) + (1/Ro_v1(2))))^(-1);
```

```
Ro_m2 = (0.5 * ((1/Ro_v2(1)) + (1/Ro_v2(2))))^(-1);

% Dynamic viscosity [Pa * s]

Mu1 =  MuCold();
Mu2 =  MuHot();

% Prandtl number Pr = (Cp * Mu)/Lambda

Pr1 = PrCold();
Pr2 = PrHot();

% Heat capacities at the mean temperature

Cp1 = CpCold(T_m1);
Cp2 = CpHot(T_m2);
```

ITERATION 0

```
% First iteration of the sizing problem
```

CORE MASS VELOCITY G

```
% Units of measure conversion factor (1 because SI)

gc = 1;

% Assumed overall fin efficiency

n_o = 0.80;

% Maximum allowed pressure drop [Pa](design requirement)
% 10 mbar

DeltaP1 = 1000;
DeltaP2 = 1000;

% Core mass velocities [kg/m^2*s]

G1 = ((2* gc * Ro_m1/Pr1^(2/3)) * (n_o * DeltaP1/ntu1) * (rm1))^(1/2);
G2 = ((2* gc * Ro_m2/Pr2^(2/3)) * (n_o * DeltaP2/ntu2) * (rm2))^(1/2);
```

REYNOLDS NUMBER

```
% Re = (G * Dh)/Mu
% Factor 1/1000 to convert Dh from mm to m

Re1 = G1 * (Dh1/1000)/Mu1;
Re2 = G2 * (Dh2/1000)/Mu2;

% CHECK if Re value falls in the validity range of Manglik and Bergles
 correlations:
```

Appendix A (continued)

```
% 120 < Re < 10^4
% 0.5 < Pr < 15
```

GEOMETRIC SURFACE CHARACTERISTICS 2

```
% Calculation of INDIVIDUAL j and f factors (Re is now available)

% Colburn factor j

j1 = 0.6522*Re1^(-0.5403)*(s1/h1c)^(-0.1541)*(t1/ls1)^(0.1499)*(t1/
s1)^(-0.0678)*(1+5.269*10^(-5)*(Re1)^(1.340)*(s1/h1c)^(0.504)*(t1/
ls1)^(0.456)*(t1/s1)^(-1.055))^(0.1);

j2 = 0.6522.*Re2.^(-0.5403)*(s2/h2c)^(-0.1541)*(t2/ls2)^(0.1499)*(t2/
s2)^(-0.0678)*(1+5.269*10^(-5)*(Re2)^(1.340)*(s2/h2c)^(0.504)*(t2/
ls2)^(0.456)*(t2/s2)^(-1.055))^(0.1);

% Fanning friction factor f

f1 =9.6243*Re1^(-0.7422)*(s1/h1c)^(-0.1856)*(t1/ls1)^(0.3053)*(t1/
s1)^(-0.2659)*(1+7.669*10^(-8)*(Re1)^(4.429)*(s1/h1c)^(0.920)*(t1/
ls1)^(3.767)*(t1/s1)^(0.236))^(0.1);

f2 =9.6243*Re2^(-0.7422)*(s2/h2c)^(-0.1856)*(t2/ls2)^(0.3053)*(t2/
s2)^(-0.2659)*(1+7.669*10^(-8)*(Re2)^(4.429)*(s2/h2c)^(0.920)*(t2/
ls2)^(3.767)*(t2/s2)^(0.236))^(0.1);
```

OVERALL FIN EFFICIENCY

```
% Heat transfer coefficient [W/K*m^2]
% j = (h/(G * Cp)) * Pr^(2/3)

h1 = (j1 * G1 * Cp1)/(Pr1^(2/3));
h2 = (j2 * G2 * Cp2)/(Pr2^(2/3));

% Fin parameter m  = ((h * 2p)/(k * A))^(1/2) for offset-strip fins
 [1/m]
% Factor 1/1000 to convert mm to m

m1 = (((2 * h1)/(k_fin * (t1/1000))) * (1 + (t1/ls1)))^(1/2);
m2 = (((2 * h2)/(k_fin * (t2/1000))) * (1 + (t2/ls2)))^(1/2);

% Fin efficiency n_f = tanh(m * l)/(m * l) [/]
% Factor 1/1000 to convert mm to m

n_f1 = tanh(m1 * (l1/1000))/(m1 * (l1/1000));
n_f2 = tanh(m2 * (l2/1000))/(m2 * (l2/1000));

% Overall surface efficiency n_o = 1 - (1 - n_f) * fs [/]
% Calculated, not assumed

n_o1 = 1 - (1 - n_f1) * fs1;
```

```
n_o2 = 1 - (1 - n_f2) * fs2;

% Thermal resistances [m^2*K/W]

R10 = 1/(n_o1 * h1);
R20 = 1/(n_o2 * h2);

% Hp: fouling and wall resistance negligible
% Fouling is always negliglible, wall resistance no and it will be
 included in the next iterations, when the HE dimensions are available

% Overall heat transfer coefficient [W/K*m^2]

U1 = (R10 + (Alpha1/Alpha2) * R20)^(-1);
```

CORE DIMENSIONS

```
% Total heat transfer areas [m^2]
% NTU = UA/Cmin

A1 = (NTU * Cmin)/U1;
A2 = (Alpha2/Alpha1) * A1;

% Free-flow areas [m^2]
% G = A0/md

A0_1 = md1/G1;
A0_2 = md2/G2;

% Frontal areas [m^2]

% Must be equal in a counterflow HE
% If there is a numerical difference, Afr is the bigger of the two
% Factor 10^4 to convert m^2 to cm^2

A_fr1 = (A0_1/Delt1) * 10^4;
A_fr2 = (A0_2/Delt2) * 10^4;

% Numerical error [m^2]

A_fr_error = abs(A_fr1-A_fr2);

% Unique frontal area [m^2]

A_fr = max(A_fr1, A_fr2);

% Hp: square frontal section A = Lato^2
% Side [cm]

Lato = (A_fr)^(0.5);

% HE longitudinal length [cm]
% Dh = (4A0 * L)/A
```

Appendix A (continued)

```
% Factor 1/10 to convert mm to cm
% Factor 10^4 to convert cm^2 to m^2

L = ((Dh1/10) * A1)/(4 * (A_fr/10^4) * Delt1);

% Heat exchanger volume [cm^3]

Volume = L * A_fr;

% Check: maximum allowed building volume

if Volume > Vmax
    display ('HE is too big to be manufactured by SLM')
    return;
end
```

FANNING FRICTION FACTOR CORRECTION

```
% Main reference: Fundamentals of Heat Exchanger design (Shah)
%                 Chapter 7.6.1

% The Fanning factor previously calculated (f0) refers to isothermal
 properties
% Since in reality temperature varies, f0 must be corrected to f

% Thermal resistances [K/W]

R1 = 1/(n_o1 * h1 * A1);
R2 = 1/(n_o2 * h2 * A2);

% Mean bulk temperature Tm [K]
% Wall temperature Tw [K]
% Hp: negliglible wall resistance

Tw = (T_m1 + (R1/R2) * T_m2)/(1 + (R1/R2));

% Correction coefficients for laminar flow
% f/f0 = (Tw/Tm)^(m)

m1c = 1.0;              % Fluid 1 : cold, heated
m2c = 0.81;             % Fluid 2 : hot, cooled

% Corrected Fanning factors

f1c = f1 * (Tw/T_m1)^m1c;
f2c = f2 * (Tw/T_m2)^m2c;
```

PRESSURE DROPS

```
% Calculation of the actual pressure drop on each fluid side, in order
 to
% see if it matches the imposed one
```

Appendix A (continued)

```
% Pressure loss coefficients

[Ke1,Kc1,Ke2,Kc2] = pLoss(Delt1,Delt2);

a1 = ((1-(Delt1)^2 + Kc1)+2*((Ro_in1/Ro_out1)-1)+f1c*((L*10)/
(Dh1/4))*(Ro_in1/Ro_m1)-(1-(Delt1)^2-Ke1)*(Ro_in1/Ro_out1));
a2 = ((1-(Delt2)^2 + Kc2)+2*((Ro_in2/Ro_out2)-1)+f2c*((L*10)/
(Dh2/4))*(Ro_in2/Ro_m2)-(1-(Delt2)^2-Ke2)*(Ro_in2/Ro_out2));

% Calculate the pressure drops [Pa]
% Factor 10 to convert L from cm to mm

Dp1 = ((G1^2)/(2 * gc * Ro_in1)) * a1;
Dp2 = ((G2^2)/(2 * gc * Ro_in2)) * a2;

% End of the first round of iteration (frontal area, length and real
 pressure drops have been found)
```

ITERATION 1

```
% In case the pressure drops do not meet the imposed pressure drops,
 it is necessary to impose the allowed pressure drop on both fluid
 sides and
% repeat the procedure above explained, starting with the calculation
 of the core mass velocity G [kg/m^2 * s]

G1I = ((DeltaP1/a1) * (2 * gc * Ro_in1))^(1/2);
G2I = ((DeltaP2/a2) * (2 * gc * Ro_in2))^(1/2);
```

REYNOLDS NUMBER

```
% Re = (G * Dh)/Mu
% Factor 1/1000 to convert Dh from mm to m

Re1I = G1I * (Dh1/1000)/Mu1;
Re2I = G2I * (Dh2/1000)/Mu2;

% CHECK if Re value falls in the validity range of Manglik and Bergles
 correlations:
% 120 < Re < 10^4
% 0.5 < Pr < 15
```

GEOMETRIC SURFACE CHARACTERISTICS II

```
% Calculation of INDIVIDUAL j and f factors (Re is now available)

% Colburn factor

j1I = 0.6522*Re1I^(-0.5403)*(s1/h1c)^(-0.1541)*(t1/ls1)^(0.1499)*(t1/
s1)^(-0.0678)*(1+5.269*10^(-5)*(Re1I)^(1.340)*(s1/h1c)^(0.504)*(t1/
ls1)^(0.456)*(t1/s1)^(-1.055))^(0.1);
```

Appendix A (continued)

```
j2I = 0.6522.*Re2I.^(-0.5403)*(s2/h2c)^(-0.1541)*(t2/
ls2)^(0.1499)*(t2/s2)^(-0.0678)*(1+5.269*10^(-5)*(Re2I)^(1.340)*(s2/
h2c)^(0.504)*(t2/ls2)^(0.456)*(t2/s2)^(-1.055))^(0.1);

% Fanning friction factor

f1I =9.6243*Re1I^(-0.7422)*(s1/h1c)^(-0.1856)*(t1/ls1)^(0.3053)*(t1/
s1)^(-0.2659)*(1+7.669*10^(-8)*(Re1I)^(4.429)*(s1/h1c)^(0.920)*(t1/
ls1)^(3.767)*(t1/s1)^(0.236))^(0.1);

f2I =9.6243*Re2I^(-0.7422)*(s2/h2c)^(-0.1856)*(t2/ls2)^(0.3053)*(t2/
s2)^(-0.2659)*(1+7.669*10^(-8)*(Re2I)^(4.429)*(s2/h2c)^(0.920)*(t2/
ls2)^(3.767)*(t2/s2)^(0.236))^(0.1);
```

OVERALL FIN EFFICIENCY

```
% Heat transfer coefficient [W/K*m^2]
% j = (h/(G * Cp)) * Pr^(2/3)

h1I = (j1I * G1I * Cp1)/(Pr1^(2/3));
h2I = (j2I * G2I * Cp2)/(Pr2^(2/3));

% Fin parameter m  = ((h * 2p)/(k * A))^(1/2) for offset-strip fins
 [1/m]
% Factor 1/1000 to convert mm to m

m1I = (((2 * h1I)/(k_fin * (t1/1000))) * (1+(t1/ls1)))^(1/2);
m2I = (((2 * h2I)/(k_fin * (t2/1000))) * (1+(t2/ls2)))^(1/2);

% Fin efficiency n_f = tanh(m * l)/(m * l) [/]
% Factor 1/1000 to convert mm to m

n_f1I = tanh(m1I * (l1/1000))/(m1I * (l1/1000));
n_f2I = tanh(m2I * (l2/1000))/(m2I * (l2/1000));

% Overall surface efficiency n_o = 1 - (1 - n_f) * fs [/]

n_o1I = 1 - (1 - n_f1I) * fs1;
n_o2I = 1 - (1 - n_f2I) * fs2;
```

WALL RESISTANCE

```
% During the iteration 0 wall resistance could not be evaluated
 because no dimensions were available
% Starting from this second iteration, it can instead be evaluated

% L3    stack length (height)
% L2    transversal length (width)
% L1    longitudinal length (length)

% Nh = Np: number of hot side passages
```

Appendix A (continued)

```
% Nc = Np + 1 : number of cold side passages
% Nw = 2 * Nc : number of plates

% L3 = (Np+1) * b1 + (Np) * b2 + 2 * (Np+1) * t_w [mm]

% Hp: square section
% L2=L3=Lato
% Factor 10 to convert cm to mm

NpI = ceil((Lato * 10 - b1 - 2 * t_w)/(b1 + b2 + 2 * t_w));
Lato = ((NpI+1) * b1 + NpI * b2 + 2 * (NpI+1) * t_w)/10;

% Wall conduction area [m^2]
% Factor 10^(-4) to convert cm^2 to m^2

AwI = (2 * (NpI+1) * L * Lato) * 10^(-4);

% Wall resistance [K/W]
% Factor 1/1000 to convert mm to m

RwI = (t_w/1000)/(k_w * AwI);
```

OVERALL HEAT TRANSFER COEFFICIENT

```
% Thermal resistances [m^2*K/W]

R1I0 = 1/(n_o1I * h1I);
R2I0 = 1/(n_o2I * h2I);

% Overall heat transfer coefficient [W/K*m^2]
% Hp: negliglible fouling

U1I = (R1I0 + A1 * RwI + (Alpha1/Alpha2) * R2I0 )^(-1);
```

CORE DIMENSIONS

```
% Total heat transfer areas [m^2]
% NTU = UA/Cmin

A1I = (NTU * Cmin)/U1I;
A2I = (Alpha2/Alpha1) * A1I;

% Free-flow areas [m^2]
% G = A0/md

A0_1I = md1/G1I;
A0_2I = md2/G2I;

% Frontal areas [m^2]
% Must be equal in a counterflow HE
% If there is a numerical difference, Afr is the bigger of the two
% Factor 10^4 to convert m^2 to cm^2
```

```
A_fr1I = (A0_1I/Delt1) * 10^4;
A_fr2I = (A0_2I/Delt2) * 10^4;

% Numerical error [m^2]

A_fr_errorI = abs(A_fr1I-A_fr2I);

% Unique frontal area [m^2]

A_frI = max(A_fr1I, A_fr2I);

% Hp: square frontal section A = Lato^2
% Side [cm]

LatoI = (A_frI)^(0.5);

% HE longitudinal length [cm]
% Dh = (4A0 * L)/A

% Factor 1/10 to convert mm to cm
% Factor 10^4 to convert cm^2 to m^2

LI = ((Dh1/10) * A1I)/(4 * (A_frI/10^4) * Delt1);

% Heat exchanger volume [cm^3]

VolumeI = LI * A_frI;

% Check: maximum allowed building volume

if VolumeI > Vmax
    display ('HE is too big to be manufactured by SLM')
    return;
end
```

FANNING FRICTION FACTOR CORRECTION

```
% Thermal resistances [K/W]

R1I = 1/(n_o1I * h1I * A1I);
R2I = 1/(n_o2I * h2I * A2I);

% Mean bulk temperature Tm [K]
% Wall temperature Tw [K]
% Hp: negliglible wall resistance

TwI = (T_m1 + (R1I/R2I)*T_m2)/(1+(R1I/R2I));

% Corrected Fanning factor

f1cI = f1I * (TwI/T_m1)^m1c;
f2cI = f2I * (TwI/T_m2)^m2c;
```

Appendix A (continued)

PRESSURE DROPS

```
% Calculation of the actual pressure drop on each fluid side, in order
 to
% see if it matches the imposed one

% Entrance and exit pressure loss coefficients depende only on the
 ratio of free flow area to frontal area, which depends only on the
 geometry;
% Therefore Kc and Ke are unchanged from the previous iteration

% Calculate the pressure drops [Pa]
% Factor 10 to convert L from cm to mm

a1I = ((1-(Delt1)^2 + Kc1)+2*((Ro_in1/Ro_out1)-1)+f1cI*((LI*10)/
(Dh1/4))*(Ro_in1/Ro_m1)-(1-(Delt1)^2-Ke1)*(Ro_in1/Ro_out1));
a2I = ((1-(Delt2)^2 + Kc2)+2*((Ro_in2/Ro_out2)-1)+f2cI*((LI*10)/
(Dh2/4))*(Ro_in2/Ro_m2)-(1-(Delt2)^2-Ke2)*(Ro_in2/Ro_out2));

Dp1I = ((G1I^2)/(2 * gc * Ro_in1)) * a1I;
Dp2I = ((G2I^2)/(2 * gc * Ro_in2)) * a2I;

% End of the second round of iteration (frontal area, length and real
 pressure drops have been updated)
```

ITERATION j

```
% In case the pressure drops still do not meet the imposed pressure
 drops, it is necessary to impose the allowed pressure drop on both
 fluid sides again and
% repeat the above procedure
```

LAST ITERATION

```
% ...

% The sizing procedure is considered concluded when both thermal and
 pressure drop requirements are met simultaneously.

end
```

Published with MATLAB® R2015b

Appendix A (continued)

Table of Contents

GEOMETRY POST-PROCESSING AND INPUT DATA CHECK

```
% The aim of this function is to determine the real heat exchanger
 dimensions and to re-calculate some of the quantities describing the
 HE geometry and
% performance, in order to check that the final result is really
 coherent with the input data.

% This function takes as an input the HE geometry and the dimensions
 produced by the iterative sizing procedure

% Index 1: cold side
% Index 2: hot side
```

INPUT DATA

```
% Recall geometric dimensions from the definition file

[Geom_v1, Geom_v2, Geom] = Geometry();

% Plate spacing [mm]

b1 = Geom_v1(1);
b2 = Geom_v2(1);

% Plate thickness [mm]

t_w = Geom(1);

% Fin thickness [mm]

t1 = Geom_v1(2);
t2 = Geom_v2(2);

% Fin offset [mm]

ls1 = Geom_v1(3);
ls2 = Geom_v2(3);

% Free flow width [mm]
```

Appendix A (continued)

```
s1 = Geom_v1(9);
s2 = Geom_v2(9);

% Fee flow height [mm]

h1c = Geom_v1(10);
h2c = Geom_v2(10);

% HE dimensions after sizing procedure

[L_c,Lato_c] = HE_Sizing();
```

REAL HE DIMENSIONS

```
% L_c and Lato_c (c stays for computed) are the numerical results of
 the iterative procedure, but they
% cannot be used as real HE dimensions, because these need to be
 integer multiples of the fin dimensions

% The real length L must be a integer multiple Zl of the fin lengths
 ls1 and ls2
% As cold and hot side fins are equal, let's use ls = ls1

ls = ls1;

% Zl: number of fin rows (l = longitudinal) []

Zl = floor((L_c * 10)/ls);

% Effective HE length [cm]

L = Zl * (ls/10);

% Similarly, the HE height must be compatible with each HE floor
 thickness

% Nh = Np: number of hot side passages
% Nc = Np + 1 : number of cold side passages
% Nw = 2 * Nc : number of plates

% Height = Nc * b1 + Nh * b2 + Nw * t_w [mm]
% Hp: square section

Np = floor((Lato_c * 10 - b1 - 2 * t_w)/(b1 + b2 + 2 * t_w));
Nc = Np;
Nh = Np +1;
Nw = 2 * Nc;

% HE Height H [cm]

H = (Nc * b1 + Nh * b2 + Nw * t_w)/10;
```

Appendix A (continued)

```
% Finally, the HE width must be compatible with the fins pitches p1
 and p2
% Width = Zt * p + t [mm]
% As cold and hot side pitches and thicknesses are equal, let's use p
 = p1 and t = t1

p = p1;
t = t1;

% Number of flow channels Zt (t = transversal) [/]

Zt = floor((L_c * 10 - t)/p);

% HE Width W [cm]

W = (Zt * p + t)/10;

% HE frontal area (reactangular, not excatly square) [cm^2]

Afr = H * W;

% HE volume [cm^3]

V = (L * Afr);
```

HE DERIVED GEOMETRICAL DIMENSIONS

```
% Here primary, secondary, total heat transfer areas, free flow areas
 and volume between plates are calculated for later use

% n = number of fins per row [/]

n = Zt + 1;

% Nf = number of fins per channel [/]

Nf = n * Zl;

% Passage primary heat transfer surface [cm^2]

Ap1 = 2*L * W - 2*(t1/10) * (ls1/10) *  Nfin + 2*(b1/10) * L;
Ap2 = 2*L * W - 2*(t2/10) * (ls2/10) *  Nfin + 2*(b2/10) * L;

% Passage secondary (finned) heat transfer surface [cm^2]

Af1 = Nf * (2*(h1c/10) * (ls1/10) + 2*(t1/10) * (h1c/10));
Af2 = Nf * (2*(h2c/10) * (ls2/10) + 2*(t2/10) * (h2c/10));

% Passage total heat transfer area (primary+secondary) [cm^2]

At1 = Ap1 + Af1;
At2 = Ap2 + Af2;
```

Appendix A (continued)

```
% Total heat transfer area [cm^2]

A1 = At1 * Nc;
A2 = At2 * Nh;

% Total free flow area [cm^2]

A0_1 = Zt * Nc * (s1 * b1)/100;
A0_2 = Zt * Nh * (s2 * b2)/100;

% Volume between plates [cm^3]

Vp1 = ((b1/10) * W * L);
Vp2 = ((b2/10) * W * L);
```

HE INDEXES

```
% Here the following quantities used as input for the design are re-
calculated based on the final geometry:

% -  Finned area to total heat transfer area ratio [m^2/m^2]
% -  Free flow to frontal area ratio Delta [/]
% -  Heat transfer area density beta [m^2/m^3]
% -  Heat transfer area to HE volume ratio Alpha [m^2/m^3]
% -  Hydraulic diameter Dh [mm]

% Finned area to total heat transfer area ratio [m^2/m^2]

fs1 = Af1/At1;
fs2 = Af2/At2;

% Free flow to frontal area ratio Delta [/]

Delt1 = A0_1/Afr;
Delt2 = A0_2/Afr;

% Heat transfer area density beta [m^2/m^3]

Beta_1 = (At1/Vp1) * 100;
Beta_2 = (At2/Vp2) * 100;

% Heat transfer area to HE volume ratio Alpha [m^2/m^3]

Alpha_1 = (A1/V) * 100;
Alpha_2 = (A2/V) * 100;

% Hydraulic diameter Dh [mm]

Dh1 = (4 * A0_1 * (L*10))/A1;
Dh2 = (4 * A0_2 * (L*10))/A1;
```

Published with MATLAB® R2015b

Appendix A (continued)

Table of Contents

COMSOL SIMULATION GEOMETRY (ELLIPTIC FINS)

```
% This script determines the following quantities describing the PFHE:

% 1) The number of fluid passages N required to manage an imposed cold
 side massflow rate md1;
% The HE is geometrically designed to work with a core mass velocity
 G.

% 2)Characteristic HE parameters: surface area density (BETA), heat
 transfer area to heat exchanger volume ratio (ALPHA), free flow to
 frontal
% surface area ratio, finned area percentage.

% NB: this script is meant to be a post-design RATING tool, it is
 notintented for design!

% Index 1: cold side
% Index 2: hot side

% N: number of passages hot side
% N+1: number of passages cold side
% 2N+1: number of fluid passages
% 2(N+1): number of plates

% Frontal area desired shape: square, i.e. height H = width W
```

HE OPTIMAL FIN GEOMETRIC DIMENSIONS

From Comsol simulations

```
% Fin width [mm]

a = 0.40;

% Fin length [mm]

b = 2.00;
```

Appendix A (continued)

```
% Transversal fin pitch [mm]

ph = 0.80;

% Longitudinal fin pitch [mm]

pv = b;

% Free flow semi-height [mm]

t = 0.60;

% Plate thickness [mm]

tw = 1.00;

% Free flow width [mm]

s = ph - a;

% Number of channels [/]

Nh = 5;
Nc = 2 * (Nh-1);

% Plate width [mm];

W = Nc * ph;

% Number of finned blocks (blocks of 2 rows) [/]

Nr = 17;

%Plate length [mm]

L = Nr * (2 * pv);

% Total number of fins (cold side OR hot side) [/]

Nf = Nr * 4 * (Nh-1);

% Free flow area of a channel [mm^2]

Ac = s * t;

% Passage free flow area [mm^2]

A0 = Nc * Ac;

% Frontal area [mm^2]

Af = W * (2*t+tw);
```

Appendix A (continued)

```
% Free flow to frontal surface area ratio [/]

A0_Afr = A0/Af;

% Frontal to free flow area ratio [/]

k = 1/A0_Afr;
```

NUMBER OF FLUID PASSAGES

```
% Cold side mass flow rate [kg/s]

[md1,~] = MdotDef();

% HE optimal core mass velocity (from Comsol simulation) [kg/m^2*s]

G = 12.0;

% Required free flow area (cold OR hot side) [mm^2]

A0r = (md1/G) * 10^6;

% Required frontal area [mm^2]

Afr = k * A0r;

% Number of channels
% H = 2(N+1)*tw+(2N+1)*2t = 2N+2+2.4N+1.2 = 4.4N+3.2
% Hp2: H = W (Square frontal area)
% Afr = H*W = H^2= (4.4N+3.2)^2

z = (sqrt(Afr)-3.2)/4.4;

% Procedure to reduce the rounding error, while keeping N integer
 (can't be decimal obviously)

if (ceil(z)-z) > 0.7
    N = floor(z);
else
    N = ceil(z);
end

% HE real height and width [mm]

H = 4.4 * N + 3.2;

% Real frontal area [mm^2]

Areal = H^2;

% Difference (error) between the theoretical required area and the
 real one [/]
```

Appendix A (continued)

```
error = 100 * (Areal - Afr)/Afr;
```

FINNED AREA PERCENTAGE

```
% Ellipse semiaxis [mm]

a1 = a/2;
b1 = b/2;

% Lateral fin area [mm^2]

Alat = 2*t * (pi * (3*(a1 + b1) - sqrt(10*a1 *b1 + 3*(a1^2 + b1^2))));

% Base fin area [mm^2]

Abase = pi * a1 * b1;

% Plate area [mm^2]

Aplate = W * L;

% Passage primary heat transfer area [mm^2]

Ap = 2*(Aplate - Nf * Abase);

% Passage secondary heat transfer area [mm^2]

As = Nf * Alat;

% Passge total heat transfer area (cold OR hot) [mm^2]

Aht = Ap + As;

% Finned to total heat transfer area ratio

fs = As/Aht;
```

SURFACE AREA DENSITY BETA

```
% Volume between plates [mm^3]

V = Aplate * (2*t);

% Beta [m^2/m^3]
% Beta is equal for hot and cold side because of the fin geometry

Beta = 1000*(Aht/V);
```

ALPHA

```
% Vplate [mm^3]
```

Appendix A (continued)

```
Vplate = Aplate * tw;

% Hot side, cold side number of passages [/]

Nhot = N;
Ncold = Nhot + 1;

% Number of plates [/]

Np = 2 * Ncold;

% Total HE volume [mm^3]

Vtot = (Nhot + Ncold) * V + Np * Vplate;

% Alpha [m^2/m^3]

Alpha_hot =  1000 *  Nhot * (Aht/Vtot);
Alpha_cold = 1000 * Ncold * (Aht/Vtot);
```

HYDRAULIC DIAMETER

```
% No meaning because the fin is elliptical and then A0 changes
 continuously

Dh = 4 * (A0/Aht) * L;
```

Published with MATLAB® R2015b

Appendix A (continued)

METHANATION THERMAL POWER AND METHANE FRACTION

```
function [Q,y] = Methane(T,md)

% This function calculates the power produced by methanation reaction
 at temperature T of a given mass flow rate having the following
 initial molar composition:

% y_H2O = 0.286;
% y_H2 =  0.530;
% y_CO =  0.107;
% y_CO2 = 0.053;
% y_CH4 = 0.024;

% It also calculates the molar fraction of methane that can is present
 equilibrium (considering that at the beginning there is already some)

% Initial amount of methane [/]

[~,y2] = Composition2();
y_0 = y2(5);

% Data from AspenPlus equilibrium simulation and referred to an inlet
 mass flow rate of 1 kg/s

Q_exp = [2684 2689 2690 2689 2682 2671 2653 2629 2597 2558 2509 2450
 2380 2299 2204 2095 1969 1825 1662 1479 1278];

y_exp = [26.74 26.64 26.50 26.31 26.07 25.76 25.37 24.91 24.36
 23.72 22.98 22.14 21.21 20.19 19.06 17.84 16.53 15.12 13.64 12.09
 10.50]/100;

T_exp = 200:25:700;

% Methanation power fit using normalized variables [kW]

[P,~,MU] = polyfit(T_exp,Q_exp,8);

Q = polyval(P,T,[],MU);

% Scaling with respect to actual mass flow rate [kW]

Q  = Q * md;

% Methane molar fraction fit using normalized variables [/]

[P1,~,MU1] = polyfit(T_exp,y_exp,8);

y_tot = polyval(P1,T,[],MU1);
```

Appendix A (continued)

```
% Net amount of methane that can form in the HE at temperature T

y = y_tot - y_0;

end
```

Published with MATLAB® R2015b

Appendix A (continued)

METHANATION REACTION

```
% This function calculates the effective power that can be obtained
 from isothermal methanation with a given mass flow rate
% Hp: HE approximated as isothermal; T is the methanation temperature

function [Q] = PowerCH4(T);

% T: coupling temperature [C]

% Mass flow rates [kg/s]

[~,md2] = MdotDef();

% Methanation power at temperature T [kW]
% Referred to the hot side mass flow rate md2

[Q_available,~] = Methane(T,md2);

% Power needed to heat up cold side to the target temperature [kW]

Q_need = Methanator();

% Needed reaction fraction [/]

f  = Q_need/Q_available;

if f>1
    disp ('More power than available is required, impossible!')
end
```

Published with MATLAB® R2015b

Appendix A (continued)

FIRST STAGE HEAT EXCHANGER

```
function [q] = ColdPower(T)

% This function calculates the power required to heat up the cold side
 mixture from its inlet temperature
% to the coupling temperature minus the approach temperature in the
 first stage heat exchanger

% Conversion factor Celsius Kelvin

c = 273.15;

% Mass flow rates [kg/s]

[md1,~] = MdotDef();

% Cold side temperatures  [C]

T1_in =  ColdSideMix()-c;
T2_out = T;

% Cold side enthalpies [kJ/kg]

h1_in =  EnthalpyCold(T1_in+c);
h1_out = EnthalpyCold(T2_out+c);

Dh1 = h1_out - h1_in;

% Thermal power required by the cold side [kW]

q = md1 * Dh1;

% This thermal power cannot be supplied by the hot side by purely
 physical
% heat exchange; a chemical contribution, deriving from exothermic
% methanation reaction is necessary to meet the cold side outlet T
 target

end
```

Published with MATLAB® R2015b

Appendix A (continued)

SECOND STAGE HEAT EXCHANGER

```
% This function calculates the thermal power available cooling down
 from 850 to
% the coupling T the hot side mixture in the second stage HE
% T: coupling temperature [C]

function [T1_out,DT1] = HeatExchanger(T)

% Conversion factor Celsius Kelvin

c = 273.15;

% Mass flow rates [kg/s]

[md1,md2] = MdotDef();

% Hot side temperatures
% Inlet temperature is fixed and coincides with the outlet temperature
 of the SOEC
% The outlet temperature is instead a functional parameter (coupling
 T)

T2_in =  850;
T2_out = T;

% Hot side enthalpies [kJ/kg]

h2_in  =  EnthalpyHot(T2_in+c);
h2_out =  EnthalpyHot(T2_out+c);

Dh2 = h2_in - h2_out;

% Hot side thermal power [kW]

q = md2 * Dh2;

% Approach temperature
% The lower this value, the higher the HE effectiveness

dT = 0;

% Inlet T cold side

T1_in = T2_out - dT;

% Inlet cold side enthalpy [kJ/kg]

h1_in = EnthalpyCold(T1_in+c);

% Cold side enthalpy increment (FLT)
```

Appendix A (continued)

```
Dh1 = q/md1;

% Cold side outlet enthalpy [kJ/kg]

h1_out = h1_in + Dh1;

% Since enthalpy is directly linked to temperature, one can
 iteratively find the temperature corresponding to a known enthalpy
% Initial guess for cold side outlet T

T1_out = 750;

% Cold side enthalpy at the trial temperature [kJ/kg]

h1 = EnthalpyCold(T1_out+c);

% Iterate until the result is accurate within the required tolerance
% Separation into two cases, depending on the sign of the error, in
 order to avoid that the iterative procedure diverges.

% Er>0: must decrease the temperature
% Er<0: must increase the temperature

ea = h1 - h1_out;                       % Absolute error
er = ea / h1_out;                       % Relative error
tol = 0.001;                            % Accepted relative error
Dt = 0.5;                               % Pitch for correcting the T
k = 0;                                  % Counter for iterations

while abs(er) >  tol
    k = k +1;

    if er > 0
        T1_out = T1_out - Dt;
        h1 = EnthalpyCold(T1_out+c);
        ea = h1 - h1_out;
        er = ea / h1_out;
    else
        T1_out = T1_out + Dt;
        h1 = EnthalpyCold(T1_out+c);
        ea = h1 - h1_out;
        er = ea / h1_out;
    end
end

% Cold side temperature increment

DT1 = T1_out-T1_in;

end
```

Published with MATLAB® R2015b

Appendix B

PERMISSIONS TO USE COPYRIGHTED FIGURES

Appendix B (continued)

University of Illinois at Chicago
College of Engineering
Department of Mechanical and Industrial Engineering

Turin, 11th April 2016

Dear Mr. Owen,

I am writing to request permission to use the following material from your paper "*Convective heat transfer and pressure losses across novel heat sinks fabricated by Selective Laser Melting*" (2008) in my thesis:

- Fig. 3. SLM fabricated heat sinks, base dimensions 50 mm x 100 mm, flow in the z direction. (a) Pin fin 6061, (b) Rectangle, (c) Rect RND, (d) Ellipse, (e) Lattice and (f) close up of Lattice.
- Fig. 6. Diagram of conventionally produced offset strip fins (left) and SLM-fabricated offset strip fins (right).

This material will appear as originally published. Unless you request otherwise, I will use the conventional style of the Graduate College of the University of Illinois at Chicago as acknowledgment.

Thank you for your kind consideration of this request.

Sincerely,

Julien Roux

Frazione Mazod 12
11020, Nus (AO), Italy

The above request is approved.

Approved by: _____ Date:__12 April 2016_

Appendix B (continued)

University of Illinois at Chicago
College of Engineering
Department of Mechanical and Industrial Engineering

THE UNIVERSITY OF ILLINOIS AT CHICAGO
UIC

Turin, 13th April 2016

Dear Ms. Jordan,

I am writing to request permission to use the following picture of EOSINT M 270 DMLS machine, which I found on your website (http://www.eos.info/en), in my thesis:

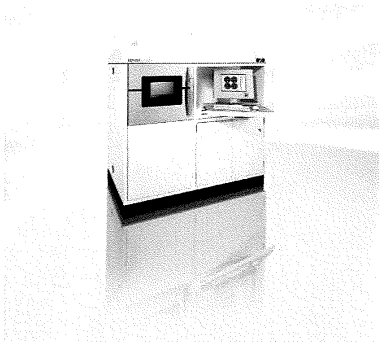

This material will appear as originally published. Unless you request otherwise, I will use the conventional style of the Graduate College of the University of Illinois at Chicago as acknowledgment.

Thank you for your kind consideration of this request.

Sincerely,

Julien Roux

Frazione Mazod 12
11020, Nus (AO), Italy

Image source "EOS" to be added

The above request is approved.

Approved by: C. Jordan, EOS GmbH Date: April 13, 2016

Appendix B (continued)

THE UNIVERSITY OF ILLINOIS AT CHICAGO

University of Illinois at Chicago
College of Engineering
Department of Mechanical and Industrial Engineering

Turin, 5th April 2016

Dear Mr. Giglio,

I am writing to request permission to use the following material from your paper *"Synthetic natural gas via integrated high-temperature electrolysis and methanation: Part I—Energy performance"*, 2015, in my thesis:

- Fig. 1. Power-to-gas pathway through both low-temperature (LT) and high-temperature electrolysis devices. [...] The benefits of a coupled high-T electrolysis and methanation process are investigated in this work.
- Fig. 3. Co-electrolysis plant layout: carbon dioxide is directly co-fed to the SOEC with steam thus yielding a H2 + CO rich syngas. The syngas is catalytically converted to a methane rich stream in downstream methanation reactors. Post-methanation cooling is outlined with two heat exchangers: HE 10 realizes a pre-cooling, whereas HE 11condensates the water into the stream.
- Fig. 8. Co-electrolysis cathode outlet gas molar composition by varying pressure. CH4 molar fraction is zoomed and moved to the right vertical axis. Methane formation increases at high pressure.

This material will appear as originally published. Unless you request otherwise, I will use the conventional style of the Graduate College of the University of Illinois at Chicago as acknowledgment.

Thank you for your kind consideration of this request.

Sincerely,

Julien Roux

Frazione Mazod 12
11020, Nus (AO), Italy

The above request is approved.

Approved by: EMANUELE GIGLIO Emanuele Giglio Date: 05/04/2016

Appendix B (continued)

University of Illinois at Chicago
College of Engineering
Department of Mechanical and Industrial Engineering

THE UNIVERSITY OF ILLINOIS AT CHICAGO
UIC

Turin, 5th April 2016

Dear Sir or Madam,

I am writing to request permission to use the following material from your online blog *This Is ECS-Blog* (http://thisisecs.com/blog/2008/11/04/heat-transfer/) in my thesis:

- Counterflow
- Straight fins
- Offset fins
- Wavy fins

This material will appear as originally published. Unless you request otherwise, I will use the conventional style of the Graduate College of the University of Illinois at Chicago as acknowledgment.

Thank you for your kind consideration of this request.

Sincerely,

Julien Roux

Frazione Mazod 12
11020, Nus (AO), Italy

The above request is approved.

Approved by: _____ Date: APRIL 15, 2016

John W Newman
President, This is ECS

Appendix B (continued)

Permission to Publish and Use COMSOL Multiphysics Images

Phil Kinnane
VP of Business Development
COMSOL, Inc.
100 District Avenue
Burlington, MA 01803 USA
Email: phil@comsol.com
Tel: +1 781-273-3322
Fax: +1 781-273-6603

COMSOL hereby grants you permission to reproduce, publish and distribute the image listed in Schedule A, in your thesis at Politecnico di Torino ("Thesis") as well as in subsequent editions of your Thesis in all media of expression now known or later developed and in all foreign language translations, for distribution throughout the world subject to your compliance with the following terms and conditions:

1. You shall comply with COMSOL's Trademark Guidelines set forth at: http://www.comsol.com/company/trademarks/.
2. You insert the phrase "Image credit: COMSOL." underneath the image in the Thesis.
3. You acknowledge that you are receiving the COMSOL Materials "As Is" without any representations or warranties of any kind including, but not limited to any implied warranties of merchantability, fitness for a particular purpose or non-infringement.

This permission shall last until you receive a written request from COMSOL to terminate this permission, except that no such termination shall operate to revoke permission granted with respect to instances in which the images and/or descriptions have already been placed in circulation. I understand and acknowledge the above requirements,

Signed: Julien Roux

Name: JULIEN ROUX

Date: 04/10/2016

Company/Institution: UNIVERSITY of ILLINOIS at CHICAGO (UIC)

Appendix B (continued)

SCHEDULE A

Image from the COMSOL Blog titled "Meshing Considerations for Linear Static Problems" By Walter Frei published on October 22, 2013:

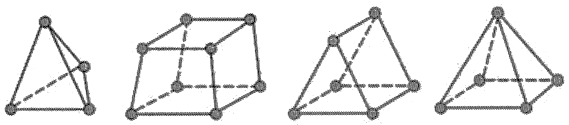

Appendix B (continued)

University of Illinois at Chicago
College of Engineering
Department of Mechanical and Industrial Engineering

Turin, 5th April 2016

Dear Mr. Santarelli,

I am writing to request permission to use the following material belonging to the HELMETH project in my thesis.

From the document "Call topic: SP1-JTI-FCH.2012.2.4 (HELMETH)", 2012:

- HELMETH Logo
- Figure 1: Power-to-Gas concept overview
- Figure 2: Energy demand of hydrogen operation versus operation temperature
- Figure 3: Operation modes of high temperature steam electrolysis
- Figure 6: Operation principle of a solid oxide electrolyser cell (SOEC) for the co-electrolysis of steam/CO2, producing syngas and oxygen
- Figure 11: Cells and stack of SUNFIRE's (staxera) Mk200 (left, 1-2 kW class) and Mk250 (right, 5 kW class) series
- Figure 18: Renewable energy storage systems: capacity and discharge time
- Figure 19: Principle of SOC (Solid oxide cell) technology for the storage of electricity in the natural gas grid.

From the slides "Additive Manufacturing Trials for HELMETH project", March 2015:

- Figures slide 2
- Figure slide 10
- Figure slide 32

This material will appear as originally published (or with changes noted below). Unless you request otherwise, I will use the conventional style of the Graduate College of the University of Illinois at Chicago as acknowledgment.

Thank you for your kind consideration of this request.

Sincerely,

Julien Roux

Frazione Mazod 12
11020, Nus (AO), Italy

The above request is approved.

Approved by: Prof. Massimo Santarelli  Date: 05/04/2016

Appendix B (continued)

University of Illinois at Chicago
College of Engineering
Department of Mechanical and Industrial Engineering

THE UNIVERSITY OF ILLINOIS AT CHICAGO
UIC

Turin, 5th April 2016

Dear Mr. Brown and Mr. Hitchcox,

I am writing to request permission to use the following picture, retrieved from your website at http://hydraulicspneumatics.com/200/TechZone/FluidPowerAcces/Article/False/6451/TechZone-FluidPowerAcces, in my thesis:

- Fig 5. Plate-fin heat exchangers consist of finned chambers separated by flat plates that route fluid through alternating hot and cold passages. Heat is transferred via fins in the passageways, through the separator plate, and into the cold fluids via fin once again.

This material will appear as originally published. Unless you request otherwise, I will use the conventional style of the Graduate College of the University of Illinois at Chicago as acknowledgment.

Thank you for your kind consideration of this request.

Sincerely,

Julien Roux

Frazione Mazod 12
11020, Nus (AO), Italy

The above request is approved.

Approved by: Alan L. Hitchcox Date: April 12, 2016

Alan L. Hitchcox, Editor

Appendix B (continued)

University of Illinois at Chicago
College of Engineering
Department of Mechanical and Industrial Engineering

THE UNIVERSITY OF ILLINOIS AT CHICAGO
UIC

CITED LITERATURE

1. CollaborativeProject: Integrated High-Temperature Electrolysis and Methanation for Effective Power to Gas Conversion, 2012.

2. GSE: Rapporto statistico: energia da fonti rinnovabili, 2014.

3. European Commission: Renewable Energy Directive, April 2009.

4. CollaborativeProject: Integrated High-Temperature Electrolysis and Methanation for Effective Power to Gas Conversion, 5.1 edition, 2015.

5. Specht, M. and Zuberbühler, U.: Power-to-gas: Technology and system operation results. 2013.

6. Guandalini, G.: Seminario "power-to-gas" e idrogeno.

7. Laguna-Bercero, M.: Recent advances in high temperature electrolysis using solid oxide fuel cells: A review. Journal of Power Sources, 203:4–16, 2012.

8. Jensen, S. H., Sun, X., Ebbesen, S. D., Knibbe, R., and Mogensen, M.: Hydrogen and synthetic fuel production using pressurized solid oxide electrolysis cells. International Journal of Hydrogen Energy, 35:9544–9549, 2010.

9. Kopyscinski, J., Schildhauer, T. J., and Biollaz, S. M.: Production of synthetic natural gas (sng) from coal and dry biomass – a technology review from 1950 to 2009. Fuel, 89:1763–1783, 2010.

10. Giglio, E., Lanzini, A., Santarelli, M., and Leone, P.: Synthetic natural gas via integrated high-temperature electrolysis and methanation: Part i—energy performance. Journal of Energy Storage, 1:22–37, 2015.

11. Swickrath, M. J. and Anderson, M.: The development of models for carbon dioxide reduction technologies for spacecraft air revitalization. 42nd International Conference on Environmental Systems, 2012.

CITED LITERATURE (continued)

12. Jensen, S. H., Graves, C., Mogensen, M., Wendel, C., Braun, R., Hughes, G., Gao, Z., and Barnett, S. A.: Large-scale electricity storage utilizing reversible solid oxide cells combined with underground storage of co2 and ch4. Energy and Environmental Science, 8:2471–2479, 2015.

13. Graves, C., Ebbesen, S. D., and Mogensen, M.: Co-electrolysis of co2 and h2o in solid oxide cells: Performance and durability. Solid State Ionics, 192:398–403, 2011.

14. Manotti Lanfredi, A. and Tiripicchio, A.: Fondamenti di chimica. Casa Editrice Ambrosiana, second edition, 2006.

15. Ni, M., Leung, M., and Leung, D.: Technological development of hydrogen production by solid oxide electrolyzer cell (soec). International Journal of Hydrogen Energy, 33:2337–2354, 2008.

16. Sunfire: Deutsch stacks sofc stack integrated stack module (ism) soec electrolysis stack (hydrogen generator) stack test box systems services fuel soec electrolysis stack. `http://www.sunfire.de/en/produkte/stacks/soec-hochtemperatur-dampfelektrolyse`. Retrieved November 5 2015.

17. Rönscha, S., Schneider, J., Matthischke, S., Schlüter, M., Götz, M., Lefebvre, J., Prabhakaran, P., and Bajohr, S.: Review on methanation – from fundamentals to current projects. Fuel, 166:276–296, February 2016.

18. Topsøe, H.: From coal to clean energy. `http://www.topsoe.com/sites/default/files/topsoe_from_coal_to_clean_energy_nitrogen_syngas_march_april_2011.pdf`, March-April 2011. Retrieved March 12 2016.

19. Specifica tecnica sulle caratteristiche chimicofisiche e sulla presenza di altri componenti nel gas naturale. `http://www.snamretegas.it/export/sites/snamretegas/repository/file/Codice_di_rete/01_Area_Capitoli_Codice_di_Rete/Capitolo_11/11_Allegati/allegato__11A__rev1.pdf`, 2003. Retrieved November 10 2015.

20. Fraunhofer: Generative manufacturing methods: Selective laser melting. `http://www.ilt.fraunhofer.de/en/media-center/brochures/b-selective-laser-melting.html`. Retrieved November 19 2015.

CITED LITERATURE (continued)

21. Yadroitsev, I., Krakhmalev, P., and Yadroitsava, I.: Hierarchical design principles of selective laser melting for high quality metallic objects. Additive Manufacturing, 7:45–56, July 2015.

22. Sidambe, A. T.: Biocompatibility of advanced manufactured titanium implants—a review. Materials, 7(12):8168–8188, 2014.

23. Thomas, D.: The Development of Design Rules for Selective Laser Melting. Doctoral dissertation, University of Wales Institute, October 2009.

24. Wong, M., Owen, I., Sutcliffe, C., and Puri, A.: Convective heat transfer and pressure losses across novel heat sinks fabricated by selective laser melting. International Journal of Heat and Mass Transfer, (52):281–288, 2009.

25. Pham, D. and Gault, R.: A comparison of rapid prototyping technologies. International Journal of Machine Tools and Manufacture, 38:1257–1287, 1998.

26. Waterman, N. and Dickens, P.: Rapid product development in the usa, europe and japan. World Class Design to Manufacture, 1(3):27–36, 1994.

27. Wong, M., Tsopanos, S., Sutcliffe, C., and Owen, I.: Selective laser melting of heat transfer devices. Rapid Prototyping Journal, 13(5):291 – 297, 2007.

28. Wong, M., Owen, I., and Sutcliffe, C.: Pressure loss and heat transfer through heat sinks produced by selective laser melting. Heat Transfer Engineering, 30(13):1068–1076, 2009.

29. Tsopanos, S., Sutcliffe, C., and Owen, I.: The manufacture of micro cross-flow heat exchangers by selective laser melting. In Enhanced, Compact and Ultra-Compact Heat Exchangers: Science, Engineering and Technology. ECI, 2005.

30. Thompson, S., Aspin, Z., Elwany, A., Shamsaei, N., and Bian, L.: Additive manufacturing of heat exchangers: A case study on a multi-layered ti-6al-4v oscillating heat pipe. Additive Manufacturing, 2015.

31. Norfolk, M. and Johnson, H.: Solid-state additive manufacturing for heat exchangers. The Journal of The Minerals, Metals and Materials Society, 67(3), 2015.

CITED LITERATURE (continued)

32. EOS: New design structures in heat exchangers increase compactness and effecticeness. http://www.eos.info/industries_markets/industry/other_industrial_applications, 2015. Retrieved February 9 2016.

33. Using additive manufacturing to build high performance heat exchangers. http://www.insidemetaladditivemanufacturing.com/blog/using-additive-manufacturing-to-build-high-performance-heat-exchangers, July 2015. Retrieved February 8 2016.

34. Williams, M., Muley, A., Bolla, J., and Strumpf, H.: Advanced heat exchanger technology for aerospace applications. SAE Technical Paper, 2008.

35. 3DSystems: Us air force contract taps 3d systems to transform manufacturing of aerospace components. https://www.3dsystems.com/sites/www.3dsystems.com/files/5_21_2015_u.s._air_force_contract_taps_3d_systems_to_transform_manufacturing_of_aerospace_components.pdf, May 2015. Retrieved February 9 2016.

36. EOS: Eosint m270. http://dmlstechnology.com/images/pdf/EOSINT_M_270.pdf. Retrieved December 29 2015.

37. SpecialMetalsCorporation: Inconel. http://www.specialmetalswiggin.co.uk/products/by-alloy/inconel. Retrieved April 2 2016.

38. PolitTO: Additive manufacturing trials for helmeth project. March 2015.

39. Trosch, T., Strößner, J., Völkl, R., and Glatzel, U.: Microstructure and mechanical properties of selective laser melted inconel 718 compared to forging and casting. Materials Letters, 164:428–431, 2016.

40. Amato, K., Gaytan, S., Murr, L., Martinez, E., Shindo, P., Hernandez, J., Collins, S., and Medina, F.: Microstructures and mechanical behavior of inconel 718 fabricated by selective laser melting. Acta Materialia, 60:2229–2239, 2012.

41. EOS: Eos nickelalloy in718. http://gpiprototype.com/images/PDF/EOS_NickelAlloy_IN718_en.pdf, 2014. Retrieved March 18 2016.

42. Thermophysical properties of fluid systems. http://webbook.nist.gov/chemistry/fluid/, 2015. Retrieved November 7 2015.

CITED LITERATURE (continued)

43. Poling, B. E., Prausnitz, J. M., and O'Connell, J. P.: The Properties of Gases and Fluids. McGraw-Hill, 2000.

44. Holmgren, M.: Xsteam.

45. Janaf thermochemical tables. `http://www.nist.gov/data/PDFfiles/jpcrd205.pdf`, 1982. Retrieved November 11 2015.

46. Turns, S. R.: An Introduction to Combustion: Concepts and Applications. McGraw-Hill, second edition, 2000.

47. Chase, M.W., J.: Nist-janaf themochemical tables j. phys. chem. ref. data, monograph 9, 1998, 1-1951. Journal of Physical and Chemical Reference Data, 9:1–1951, 1998.

48. Asinari, P. and Chiavazzo, E.: An Introduction to Multiscale Modeling with Applications. Società Editrice Esculapio, 2013.

49. Chapman, S. and Cowling, T. G.: The mathematical theory of non-uniform gases: an account of the kinetic theory of viscosity, thermal conduction, and diffusion in gases. Cambridge University Press, 1932.

50. Jones, J.: On the determination of molecular fields. ii. from the equation of state of a gas. Proceedings of the Royal Society of London Series A, 106:463–477, October 1924.

51. Catania, A.: Complementi di Macchine. Levrotto e Bella, 1988.

52. Banks, J., Carson, J., Nelson, B., and Nicol, D.: Discrete-Event System Simulation. Prentice Hall, 2001.

53. (n.d.): Simulation. `https://en.wikipedia.org/wiki/Simulation`. Retrieved March 22 2016.

54. Sargent, R. G.: Verification and validation of simulation models. In Proceedings of the 2011 Winter Simulation Conference, 2011.

55. (n.d.): Verification and validation of computer simulation models. `https://en.wikipedia.org/wiki/Verification_and_validation_of_computer_simulation_models`. Retrieved March 22 2016.

CITED LITERATURE (continued)

56. Kakaç, S., Liu, H., and Pramuanjaroenkij, A.: Heat Exchangers: Selection, Rating, and Thermal Design. CRC Press, March 2012.

57. Shah, R. K. and Sekulic, D. P.: Fundamentals of Heat Exchanger Design. John Wiley and Sons, Inc., 2003.

58. Vohra, I. A., Aijaj, A., and Saxena, B.: Modern heat exchanger - a review. International Journal of Engineering Research and Technology, 2(2), February 2013.

59. Li, Q., Flamant, G., Yuana, X., Neveu, P., and Luo, L.: Compact heat exchangers: A review and future applications for a new generation of high temperature solar receivers. Renewable and Sustainable Energy Reviews, (15):4855–4875, 2011.

60. Kays, W. and London, A.: Compact Heat Exchangers. Krieger Pub Co, third edition, 1988.

61. Rattanamaung, M.: Plate heat exchanger. `https://commons.wikimedia.org/wiki/File:%E0%B9%80%E0%B8%84%E0%B8%A3%E0%B8%B7%E0%B9%88%E0%B8%AD%E0%B8%87%E0%B9%81%E0%B8%A5%E0%B8%81%E0%B9%80%E0%B8%9B%E0%B8%A5%E0%B8%B5%E0%B9%88%E0%B8%A2%E0%B8%99%E0%B8%84%E0%B8%A7%E0%B8%B2%E0%B8%A1%E0%B8%A3%E0%B9%89%E0%B8%AD%E0%B8%99%E0%B9%81%E0%B8%9A%E0%B8%9A%E0%B9%81%E0%B8%9C%E0%B9%88%E0%B8%99.png`, November 2015. Retrieved March 12 2016.

62. eds. J. G. Segovia-Hernández and A. Bonilla-Petriciolet Process Intensification in Chemical Engineering Design Optimization and Control. Springer, 2016.

63. Shah, R. K.: Advances in science and technology of compact heat exchangers. Heat Transfer Engineering, 27(5):3–22, 2006.

64. Engineering essentials: Heat exchangers. `http://hydraulicspneumatics.com/200/TechZone/FluidPowerAcces/Article/False/6451/TechZone-FluidPowerAcces`, January 2012. Retrieved April 12 2016.

65. This is ecs - blog: Heat transfer. `http://thisisecs.com/blog/2008/11/04/heat-transfer/`, November 2008. Retrieved April 12 2016.

66. Incropera, F. P., Bergman, T. L., Lavine, A. S., and DeWitt, D. P.: Fundamentals of Heat and Mass Transfer. John Wiley and Sons, Inc., 7th edition, 2011.

CITED LITERATURE (continued)

67. Kim, M., Lee, J., Yook, S., and Lee, K.: Correlations and optimization of a heat exchanger with offset-strip fins. International Journal of Heat and Mass Transfer, 54:2073–2079, 2011.

68. Yang, Y. and Li, Y.: General prediction of the thermal hydraulic performance for plate-fin heat exchanger with offset strip fins. International Journal of Heat and Mass Transfer, 78:860–870, 2014.

69. Manglik, R. M. and Bergles, A. E.: Heat transfer and pressure drop correlations for the rectangular offset strip fin compact heat exchanger. Experimental Thermal and Fluid Science, 10(2):171–180, February 1995.

70. COMSOL: COMSOL Multiphysics Reference Manual, 5.0 edition, October 2014.

71. Bhutta, M. M. A., Hayat, N., Bashir, M. H., Khan, A. R., Ahmad, K., and Khan, N. S.: Cfd applications in various heat exchangers design: A review. Applied Thermal Engineering, (32):1–12, 2012.

72. COMSOL: Navier-stokes equations. `https://www.comsol.it/multiphysics/navier-stokes-equations`. Retrieved February 16 2016.

73. Bocchi, F.: How to calculate mass conservation and energy balance. `https://www.comsol.it/blogs/how-to-calculate-mass-conservation-and-energy-balance/`, October 2015. Retrieved January 16 2016.

74. Frei, W.: How much memory is needed to solve large comsol models? `https://www.comsol.com/blogs/much-memory-needed-solve-large-comsol-models/`, October 2013. Retrieved December 27 2015.

75. Huc, N.: Conjugate heat transfer. `https://www.comsol.com/blogs/conjugate-heat-transfer/`, January 2014. Retrieved January 9 2016.

76. Frei, W.: Meshing considerations for linear static problems. `https://www.comsol.com/blogs/meshing-considerations-linear-static-problems/`, October 2013. Retrieved December 27 2015.

77. Frei, W.: Using virtual operations to simplify your geometry. `https://www.comsol.com/blogs/using-virtual-operations-simplify-geometry/`, November 2013. Retrieved December 27 2015.

CITED LITERATURE (continued)

78. Frei, W.: Solving multiphysics problems. https://www.comsol.com/blogs/solving-multiphysics-problems/, December 2013. Retrieved December 27 2015.

79. Frei, W.: Improving convergence of multiphysics problems. https://www.comsol.it/blogs/improving-convergence-multiphysics-problems/, December 2013. Retrieved December 27 2015.

80. Frei, W.: Solution of systems of linear systems of equations. https://www.comsol.com/blogs/solutions-linear-systems-equations-direct-iterative-solvers/, November 2013. Retrieved December 27 2015.

81. Marra, V.: On solvers: Multigrid methods. https://www.comsol.it/blogs/on-solvers-multigrid-methods/, February 2013. Retrieved January 4 2016.

82. Frei, W.: Solving nonlinear static finite element problems. https://www.comsol.com/blogs/solving-nonlinear-static-finite-element-problems/, November 2013. Retrieved December 27 2015.

83. eds. R. K. Shah, M. Ishizuka, T. M. Rudy, and V. Wadekar Preface. ECI, 2005.

84. Aziz, M. A. A., Jalil, A. A., Triwahyono, S., and Ahmad, A.: Co2 methanation over heterogeneous catalysts: recent progress and future prospects. Green Chemistry, 17:2647–2663, January 2015.

85. Hawkins, G.: Theory and operation of methanation catalyst.

86. Rostrup-Nielsen, J., Pedersen, K., and Sehested, J.: High temperature methanation sintering and structure sensitivity. Applied Catalysis A: General, 330:134–138, 2007.

87. Nguyen, T., Wissing, L., and Skjøth-Rasmussen, M.: High temperature methanation: Catalyst considerations. Catalysis Today, 215:233–238, 2013.

88. (n.d.): Le chatelier's principle. https://en.wikipedia.org/wiki/Le_Chatelier%27s_principle. Retrieved April 10 2016.

VITA

NAME	Julien Roux
EDUCATION	
August 2016	Master of Science in Mechanical Engineering, *University of Illinois at Chicago*, Chicago, USA
July 2016	Specialization Degree in Mechanical Engineering, *Polytechnic of Turin*, Turin, Italy
July 2016	ASP Diploma, *Alta Scuola Politecnica*, Italy
October 2014	Bachelor's Degree in Mechanical Engineering, *Polytechnic of Turin*, Turin, Italy
June 2011	Scientific High School Diploma, *Liceo Scientifico E. Berard*, Aosta, Italy
RESEARCH	
2015–2016	Master thesis
	Title: *Design of a compact heat exchanger used in a methanation plant and produced by additive manufacturing*
	CFD design through COMSOL Multiphysics of a high temperature compact heat exchanger serving a solid oxide electrolyser cell (SOEC) in the context of a substitute natural gas methanation plant.
2014	Bachelor thesis
	Title: *Study of the hydraulic jump through experiments on a moving floor canal*
	Comparison between theoretical models and experimental results of turbulence losses due to a hydraulic jump.
SCHOLARSHIPS	
2014–2016	ASP Scholarship
Fall 2015	Italian scholarship for TOP-UIC students
Spring 2015	BCC Scholarship

VITA (continued)

PROJECTS

February 2016	Design and prototyping of innovative products in Fablabs
	Polytechnic of Turin and Université Technique de Compiègne
Fall 2015	Business plan of an educational startup
	Entrepreneurship, UIC
	Design and testing of an analog PID controller
	Mechatronics I, UIC
Spring 2015	Calculation of a two stages helical gear gearbox
	Machine Design, Polytechnic of Turin
	Design of a panel heating system
	Advanced Thermodynamics, Polytechnic of Turin
Spring 2014	Design of a toy company industrial warehouse
	Industrial plants, Polytechnic of Turin

LANGUAGE SKILLS

Italian	Native speaker
English	Full working proficiency
	2014 - IELTS examination (8.0/9)
	Fall 2015 - Exchange semester abroad in Chicago, Illinois
	Since 2014, lessons and exams attended exclusively in English
French	Full working proficiency
	2011 - DALF C1 examination (85/100)
	July 2010 - Study abroad in Bruxelles, Belgium
German	Intermediate level
	2014 - Goethe Zertifikat B1 examination (85/100)
	August 2014 - Study abroad in Bonn, Germany
Latin	Reading and translating only

VITA (continued)

EXPERIENCE	
Spring 2015	Thermal analyst
	OLSA Spa, Torino, Italy
	Design of a smart automotive LED taillight system
Summer 2009	Land-surveyor & CAD drawer
	Geometra Aldo Roux, Nus, Italy
	Land and building surveys. Technical drawing using *Allplan*. Writing technical reports.
Summer 2008	Help plumber
	Muller Emilia Idraulica, Nus, Italy
COMPUTER SKILLS	
General	Microsoft Office (ECDL, 2010), LaTeX
Technical	MatLab & Simulink, COMSOL Multiphysics, SolidWorks, Thermal Hyperlynx, C, Turbo Pascal, IDE
MEMBERSHIPS	
	American Society of Mechanical Engineers (ASME)
	Golden Key Honor Society
	Alumni PoliTO
INTERESTS	
	Mountaineering, Skiing, Basketball, Motorsport, Technology, Reading, Economics